TECHNISCHE UNIVERSITÄT MÜNCHEN

MAX-PLANCK-INSTITUT FÜR ASTROPHYSIK

General Relativistic Collapse of Rotating Stellar Cores in Axisymmetry

Harald Dimmelmeier

Vollständiger Abdruck der von der Fakultät für Physik der Technischen Universität München zur Erlangung des akademischen Grades eines

Doktors der Naturwissenschaften

genehmigten Dissertation.

Vorsitzender:		Univ.-Prof. Dr. Franz von Feilitzsch
Prüfer der Dissertation:		
	1.	Priv.-Doz. Dr. Ewald Müller
	2.	Univ.-Prof. Dr. Manfred Lindner

Die Dissertation wurde am 14.09.2001 bei der Technischen Universität München eingereicht und durch die Fakultät für Physik am 31.10.2001 angenommen.

Max-Planck-Institut für Astrophysik

General Relativistic Collapse of Rotating Stellar Cores in Axisymmetry

Harald Dimmelmeier

Dissertation

Technische Universität München
Physik-Department

Abstract

Numerical studies of core collapse supernovae are an important field of research in astrophysics. They are concerned with such diverse aims as the investigation of the collapse dynamics, the formation of a high-density neutron star, the propagation of shock fronts and heavy element nuclear synthesis in the shock, the explanation of the light curves, the cooling, spin behavior and oscillation modes of the neutron star, pulsar physics and the interaction of the shock with the interstellar medium and the fate of the supernova remnant. Many of these aspects can be modeled using Newtonian gravity.

On the other hand, core collapse of ideal fluids has always been a playground for numerical general relativity. However, numerical simulations of relativistic matter flows which evolve in the presence of strong (and dynamic) gravitational fields are a highly complex problem. To make things worse, the most commonly used formulations of numerical relativity lack long-term stability. Therefore, up to date no numerical simulations of rotational core collapse to a neutron star have been undertaken in general relativity.

In this thesis we present a new approach to this problem: In order to simplify the complexity of the gravitational field equations of general relativity, Wilson and coworkers have proposed an approximation scheme, where the three-metric γ_{ij} is chosen to be conformally flat. This reduces the Einstein equations to a set of 5 coupled elliptic equations. We have adopted this approximation for the equations of spacetime, and have combined it with a modern high-resolution shock-capturing scheme to solve the hyperbolic conservation equations for relativistic hydrodynamics, with an equation of state consisting of a thermal and a polytropic contribution.

Here we introduce an axisymmetric general relativistic hydrodynamic code which is based upon this approach. We have applied this code to simulations of rotational core collapse. A comprehensive set of tests demonstrates the ability of the code to handle a variety of astrophysical situations, including, among others, the propagation of highly relativistic shocks and the evolution of rapidly differentially rotating neutron stars in equilibrium.

We have performed a parameters study of rotational core collapse and have computed the gravitational radiation waveforms for each model. These results extend previous work on rotational supernova core collapse and the resulting gravitational radiation in Newtonian gravity. In most cases, compared to Newtonian simulations the gravitational wave signal is weaker and its spectrum exhibits higher average frequencies, as the inner core is more compact in the deeper gravitational potential in general relativity. The computed wave templates will be useful in the data analysis of the gravitational wave interferometer detectors which are scheduled to become operational in the near future. We present models where relativistic effects qualitatively change the collapse dynamics. We show that in relativistic gravity, core collapse with multiple bounces is only possible for a narrow range of parameters. We further demonstrate that the prospects for detection of gravitational wave signals from supernova core collapse are most likely not enhanced by taking into account relativistic gravity.

Contents

1 Introduction **1**
- 1.1 History of Supernova Research 1
- 1.2 Supernova Classes 3
- 1.3 Physics of Supernova Core Collapse 5
- 1.4 Gravitational Radiation 12
- 1.5 Simulations of Supernova Core Collapse 16
- 1.6 Organization of the Thesis 19
- 1.7 Conventions 20

2 General Relativistic Hydrodynamics **21**
- 2.1 Relativistic Field Equations – $\{3+1\}$ Formalism 21
- 2.2 Conservation Equations 25
- 2.3 The General Relativistic Riemann Problem 27

3 Metric Equations **31**
- 3.1 ADM Evolution and Constraint Equations 33
- 3.2 Problems with the ADM Equations – Alternative Formulations and Approximations 34
- 3.3 Conformally Flat Metric Equations 37
  - 3.3.1 Conformal Flatness Condition 37
  - 3.3.2 Conformal Scaling 40
  - 3.3.3 Derivation of the CFC Metric Equations 42
  - 3.3.4 Properties of the Elliptic System of Metric Equations 46

4 Rotational Core Collapse **47**
- 4.1 Physical Model 47
- 4.2 Equation of State 50
- 4.3 Rotating Relativistic Stars in Equilibrium 52
- 4.4 Initial Models and Collapse Parameters 54

5 Numerical Implementation **57**
- 5.1 Numerical Grid 57
  - 5.1.1 Grid Setup – Logarithmic Radial Spacing 57
  - 5.1.2 Symmetry Conditions 59
  - 5.1.3 Boundary Conditions – Isotropic Schwarzschild Solution 61
- 5.2 Hachisu's Self-Consistent Field Method 63
- 5.3 Atmosphere Treatment at the Surface of the Star 64

5.4 High-Resolution Shock-Capturing Methods 66
    5.4.1 Approximate Solvers for the Riemann Problem – The Numerical Flux . . 68
5.5 Iteration Scheme – Discretization of the Evolution Equations 71
    5.5.1 Time Evolution of the Conserved Quantities 71
    5.5.2 Recovery of the Primitive Quantities 78
5.6 Numerical Solution of the Elliptic Metric System 79
    5.6.1 Finite Differencing – Newton–Raphson Iteration 79
    5.6.2 The Linear Problem 82
    5.6.3 Numerical Methods for Solving the Linear Problem 87
    5.6.4 Computational Performance of the Metric Solver – Metric Extrapolation 91

6 Tests 97
6.1 Relativistic Shock Tube Tests 97
6.2 Rotating Neutron Stars 101
6.3 Spherical Core Collapse 106
6.4 Integral Quantities – Conservation of Rest Mass and Angular Momentum 109
6.5 Excitation of the Thermal Pressure 115
6.6 Quality of the CFC Approximation during Rotational Core Collapse 118
6.7 Convergence and Accuracy Tests 125
    6.7.1 Order of Numerical Convergence 125
    6.7.2 Grid and Metric Resolution Tests – Metric Extrapolation Tests 127

7 Results and Discussion 131
7.1 Collapse and Waveform Types 131
    7.1.1 Type I Collapse Model – Regular Collapse 132
    7.1.2 Type II Collapse Model – Multiple Bounce Collapse 134
    7.1.3 Type III Collapse Model – Rapid Regular Collapse 134
7.2 Homology of the Infall 139
7.3 Central Densities and Time of Bounce 142
7.4 Gravitational Wave Amplitudes 147
7.5 Multiple Bounces 151
7.6 Compactness of the Proto-Neutron Star Core 161
7.7 Rapidly and Highly Differentially Rotating Models 174
7.8 Gravitational Wave Energy Emission and Spectra 182
7.9 Evolution of the Rotation Rate 191
    7.9.1 Problems with the Calculation of the Rotation Rate 199
7.10 Propagation of the Shock Front 200

8 Summary and Outlook 207

A Characteristic Fields 211
A.1 Characteristic Structure of the Conservation Equations 211
A.2 Eigenvalues and Eigenvectors 212

B Source Terms for the Evolution Equations 215
B.1 Energy-Momentum Tensor 216
B.2 Christoffel Symbols 217

C Gravitational Wave Extraction **221**
C.1 Multipole Expansion of the Radiation Field 221
C.2 Standard Quadrupole Formula 223
C.3 First Moment of Momentum Density Formula 224
C.4 Stress Formula 225
C.5 Ambiguities of the Quadrupole Formula in Relativity 230

D Density Evolution and Gravitational Wave Signal Catalogue **235**

E Acknowledgments **243**

References **244**

We are all in the gutter,
but some of us are looking at the stars.

Oscar Wilde, *Lady Windemere's Fan* (1892).

It's the nexus of the crisis
And the origin of storms
Just the place to hopelessly
Encounter time and then came me
...
Astronomy – a star

Blue Öyster Cult, *Astronomy* (1974).

Ich bin kein Freund großer Worte...

Harry Dee.

Chapter 1

Introduction

1.1 History of Supernova Research

Rarely occurring spectacular phenomena in the sky have always been fascinating for human beings. Among the most exciting of these are supernovae, although only a few human beings ever have had the opportunity to see one with the unaided eye. In historical times, the appearance of new stars (or guest stars) has often been attributed to some heavenly omen which was supposed to influence mankind's fate for better, or mostly worse [91]. So the director of the Chinese Imperial Astronomical Bureau, Yang Wei-te, who observed the supernova of 1054, the one which should leave behind the much studied Crab nebula, was smart enough to ensure his employer that this sign in the sky could be deciphered as a promise that a person of great wisdom and virtue was to be found within his realm. He certainly did not want to share the ill fate of his two famous predecessors Hsi and Ho who had been beheaded for not being able to fulfil the Emperor's expectations.

A few centuries later it was sheer coincidence that the emergence of modern Western science and especially astronomy in the Renaissance period was accompanied by the appearance of two supernovae visible in Europe, and that two of the most famous astronomers ever, Tycho Brahe and Johannes Kepler, each witnessed one of them. They were both, in succession, court astronomers and astrologists of King Rudolph II of Bohemia – a combination of professions which has somewhat gone out of fashion in later times. However, at those times of philosophical and scientific clashes between the geocentric and heliocentric view of the Universe, at least among professionals, the notion of a heavenly phenomena as indicators for famine and other catastrophes (in ancient Japan, astronomers had interpreted the supernova of 1181 as a *sign of abnormality, indicating that at any moment we can expect control of the administration to be lost* [91]) had already yielded to the idea of scientifically interesting objects of study. Tycho must have really been struck so much by his noticing of the new star in 1572 that he asked his servants for confirmation of his observation, and as not even that seemed convincing enough for him, he even sought assistance from local peasants who passed by.

As already mentioned, the Renaissance supernova observations and their interpretation also played a role in the struggle for the acceptance of the new heliocentric picture of the Universe. In the Aristotelean philosophy, which still influenced science in late medieval times, the celestial crystal spheres of the planets and fixed stars which was supposed to surround the Earth at the outer boundary of the Universe was thought to be flawless and unchanging. All nonregular heavenly phenomena therefore had to take place in the Earth's atmosphere. When observations of the supernovae exhibited no measurable parallax, the distance to the supernovae had to be extended beyond the Moon's orbit and even the known planets. This dealt a serious blow to the Aristotelian view.

A similar extension in distance for the origin of supernovae was repeated in 1885 when the first extragalactic supernova was discovered. However, since Kepler's supernova in 1604, astronomers had been patiently waiting in vain for another unobscured nearby supernova, although theoretical calculations and the observations in other galaxies were indicating an average galactic supernova birthrate of about one every 20 to 50 years. In 1987, the long waiting was finally rewarded when the light of supernova SN 1987A arrived on Earth. This supernova had exploded in the Large Magellanic Cloud, a satellite of our Milky Way, about 160,000 years ago[a]. This event enhanced interest in supernova research in astronomy and astrophysics, and triggered the publication of a great number of scientific articles; this is similar to what happened after Kepler's supernova, of which Kepler himself said that, as far as its astrological significance was regarded, it would bring good fortune to publishers at least. Today, more than a decade after the explosion of a blue supergiant star was detected as SN 1987A, the field of supernova research is still an interesting and far from completely solved topic in astrophysics, although it has calmed down to the daily scientific routine work again after the boost it got from SN 1987A. New advanced concepts for explosion mechanisms for both thermonuclearly driven supernovae and core collapse supernovae, and the advent of gravitational wave detectors, which will be able to detect galactic supernovae as soon as they are in full operation within the next years, will most probably reveal new insights into the physics of supernovae in the years to come. The supernova explosion mechanism and the prospects of detectability will be discussed in the following sections.

---

[a] Although astrophysicists have now sophisticated models to determine the event rate of galactic supernovae, the corresponding detection rate on Earth is strongly influenced by their galactic distribution, the possible obscuration by dust clouds, and the runtime of the light and the neutrinos.

1.2 Supernova Classes

Supernovae come in two breeds. This was first discovered by Minkowski in 1941 on observational grounds, when he split a sample of 14 extragalactic supernovae into one class of 5, which exhibited distinct hydrogen absorption lines in their spectrum, and into one class of 9, which did not. By now, after the discovery of numerous other supernova explosions, this clearcut split into two single types and therefore explosion scenarios has evolved into the emergence of various subclasses [29, 30], which we want to summarize briefly in the following: If hydrogen Balmer lines are present in the spectrum of the light emitted by the supernova, either as blue-shifted emission lines, or red-shifted absorption lines, we speak of Type II supernovae. Supernovae, whose spectrum exhibits no distinct hydrogen line features, are dubbed Type I supernovae. This class again branches into the subclasses Type Ia (which contain Si absorption lines), Ib (which show no Si, but He lines), and Ic (which have neither Si nor He lines in their spectrum)[b]. The light curve, i.e. the emission of electromagnetic radiation in the visible spectrum versus time, also differs for both types: In a Type Ia supernova, the initial peak in the light emission is followed by an exponential drop over about 3 magnitudes within about 100 days, which gradually goes over into a gentler decline. On the other hand, in Type II supernovae the maximum brightness phase is followed by either a distinct plateau with a subsequent drop by about 4 orders in magnitude in the first 100 days (Type II-P), or by first a steep linear decline in magnitude in the first 100 days (Type II-L). Then the slope flattens and the afterglow decay is less pronounced compared to a Type I supernova. A comprehensive review of supernova light curves can be found in [29].

However, the spectroscopic classification is misleading in terms of the underlying explosion mechanism, as it only yields information about the state of the envelope of the stellar progenitor at the time of the supernova explosion. A useful observation, which has helped to determine the explosion mechanism, is a particular feature of Type II and Type Ib/Ic explosions: The host galaxies of these events are spiral galaxies, where they especially occur in the spiral arms, i.e. in places where the density of young and massive stars is high. Type Ia supernovae however occur in all types of galaxies, but seem to favor elliptic galaxies, i.e. galaxies with an overproportional population number of old stars. This observation indicates that members of the Type Ia have old stars as progenitors, whereas such of Type II and Type Ib/Ic are associated with massive stars, which have a relatively short lifetime.

The exact mechanism of Type Ia explosions is still a somewhat open issue, with several debated possible scenarios, although a standard model has emerged here: These explosions are possibly caused by a thermonuclear deflagration which completely incinerates and subsequently disrupts a compact star in a binary system, which has got rid of its H envelope prior to the supernova explosion due to mass transfer to its companion star. The most likely candidate for a Type Ia progenitor is a carbon-oxygen white dwarf in which a thermonuclear runaway is ignited due to accretion from its companion. As a low mass transfer rate may be needed for a successful explosion [143], the above scenario could explain the increased occurrence of this type in elliptic galaxies, in which the formation rate of new stars is very low. The total energy released in a Type Ia explosion is the thermonuclear energy of its fuel, which amounts about 10^{51} erg.

---

[b] Type II supernovae can also be divided into classes II-L, II-P, IIn, and IIb. However, for Type IIn it is not even known if they are genuine supernovae [30].

Most of this energy is converted to kinetic energy of the stellar material which is ejected by the explosion. As small part (about 10^{48} erg) is emitted in the form of electromagnetic radiation.

The by now well established theory of the Type II and Type Ib/c supernova mechanism predicts those explosions to be the violent end of massive stars in the mass range between $9M_\odot$ (Type II) up to $30M_\odot$ (Type Ib/c), where $M_\odot = 1.98 \times 10^{33}$ g is the solar mass. During their evolution, they have developed an onion-like internal structure of layers consisting of different nuclear composition[c]. When the mass of the interior core, which contains the end products of thermonuclear burning, becomes too large, an instability develops. Following this instability, the dense interior core, which has an average density of about 10^{10} g cm^{-3}, collapses on the timescale of about 100 ms, and forms a neutron star. A part of the gravitational binding energy, which is released during this gravitational core collapse as kinetic energy of the infalling mass shells, is converted into an outward shock wave which drives the explosion of the outer layers of the star. As in the case of Type Ia supernovae, the kinetic energy in the explosion amounts to about 10^{51} erg, and the total electromagnetic radiation energy is of the order of 10^{48} erg.

In thermonuclear explosions, almost all of the liberated total energy couples to the stellar material, which is then ejected. Therefore, by measuring the amount of ejecta, and its velocity, one can infer an estimate of the total energy released in the supernova explosion. This method can not be applied in an analogous way to core collapse supernovae: Here the kinetic energy of the ejecta is only a small fraction of the gravitational binding energy released by the collapse of the stellar core to a neutron star. During the collapse, about 3×10^{53} erg are released as gravitational binding energy, of which less than 1% couple to the stellar matter to form the shock wave. The overwhelming part of the binding energy is deposited in the form of neutrinos, which are emitted during the formation of the neutron star. According to current understanding of supernova core collapse, it is the release of the energy stored in neutrinos which plays a decisive role in driving the supernova explosion. This standard model of core collapse, and the still debated issues arising from it, will be the focus of Section 1.3.

Although astrophysicists now have elaborate models for the engines of the different types of supernova explosions, many of the details are far from being fully understood. Nevertheless, observers and theoretical astrophysicists use Type Ia supernovae as standard candles at high red-shifts to measure the cosmic expansion rate, and thus to test cosmological models and to determine the value of the cosmological constant [9]. In core collapse supernovae, the light curves can be computed without detailed knowledge of the physics in the central explosion engine. However, if it comes to nucleosynthesis and the emission of gravitational radiation (see Section 1.4) and neutrinos from the core collapse, and the explanation of the properties of newborn neutron stars, one must resort to multi-dimensional simulations of the collapse, which is the content of this thesis.

---

[c] During their evolution as giant stars, the Type Ib/c progenitors have been stripped off their H envelopes by a stellar wind or by mass transfer to a companion star. Possibly the Type Ic progenitors have also lost their He envelopes.

1.3 Physics of Supernova Core Collapse

As a result of the interplay between observation and numerical simulations, in the last few decades a rather sophisticated standard scenario of the physics of core collapse supernovae has emerged. This state-of-the-art model combines ideas from very different aspects of physics, including, among others, stellar evolution, hydrodynamics, gravitational physics, and nuclear and particle physics. (For a more detailed review of the standard model of core collapse supernovae and numerical simulations, see e.g. [87, 61]).

As already indicated, the progenitor of a core collapse supernova is a massive star in the mass range of $9M_\odot$ to $30M_\odot$ at the end of its thermonuclear evolution, which lasts for a time of the order of about 10^7 yr. Initially, these stars consist mainly of hydrogen, which is burned to helium by thermonuclear fusion at temperatures above 2×10^7 K. This is the star's main energy source for most of its lifetime. However, in the late evolutionary stages, helium, carbon, neon, oxygen, and finally silicon burning are ignited subsequently[d], with ignition temperatures up to 3×10^9 K for Si [109]. A burning stage usually begins in the central regions of the star, where the concentration of the nuclear burning products of the prior burning stage, and the density and temperature are highest. As a consequence of this burning sequence, the star develops an onion-like structure of concentric layers composed of different nuclei (see Figure 1.1).

In the center, elements of the iron-nickel group, which are the end products of the chain of exothermic fusion reactions[e], accumulate in a so-called iron core. The iron core is surrounded by the silicon shell, the oxygen shell, and the carbon shell. The outermost parts of the stellar structure consist of the helium shell and finally the hydrogen envelope, unless the star has already lost its outermost layer(s) by means of a stellar wind.

Whereas in the outer layers of the star the pressure is still predominantly due to radiation or ionized gas pressure, the iron core is stabilized against gravity by the pressure exerted by degenerate relativistic electrons:

$$P_\mathrm{e} \gg P_\mathrm{ion} \gg P_\mathrm{rad}. \tag{1.1}$$

At the high densities and temperatures encountered in the core, the nuclei, electrons, and photons are in nuclear statistical equilibrium via the strong and electromagnetic interactions. This implies that their collisional mean free paths are much smaller than the characteristic macroscopic scale of the system, i.e. the radius of the iron core. Furthermore, energy transport by heat conduction, and the viscosity of matter can be neglected, i.e. the iron core can be treated as an ideal fluid. (For a more detailed justification of the hydrodynamic ideal gas model, see Section 4.1.) As the pressure of a relativistic degenerate electron gas follows a polytropic relation with an adiabatic index $\gamma = 4/3$, the total pressure in the iron core depends practically only on the density and can be well approximated by a polytropic equation of state (EoS). Due to continuing silicon shell burning, the iron core mass increases until it exceeds the Chandrasekhar mass, which is the maximum mass which can be supported by P_e against

---

[d] During their evolution, stars with masses less than about $9M_\odot$ lose too much mass to be able to reach central temperatures high enough to ignite oxygen. Their final state is a compact white dwarf consisting mainly of carbon and oxygen.

[e] The nucleus ^{56}Fe has the maximum binding energy per nucleon.

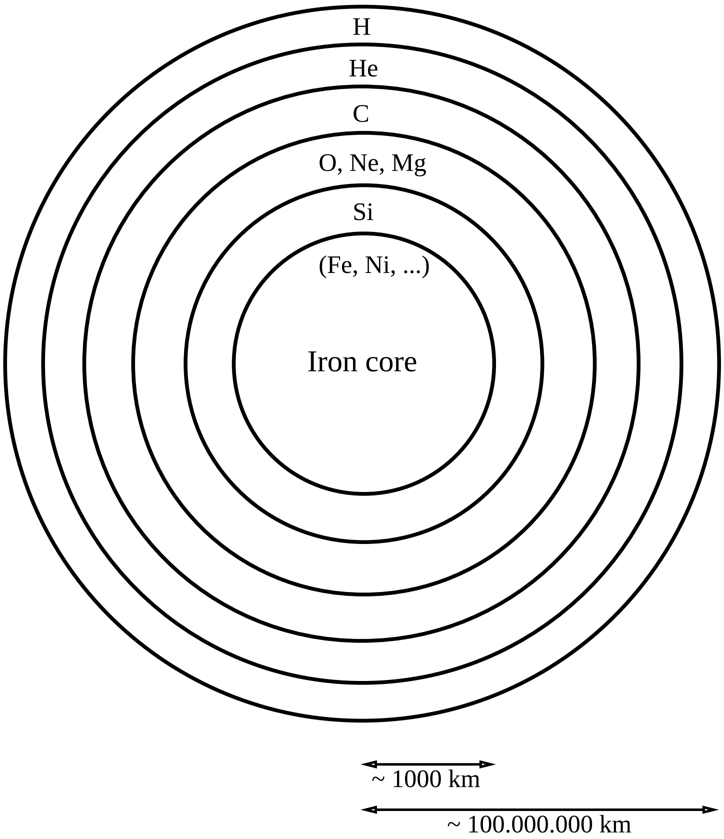

Figure 1.1: *Onion-like shell structure of the progenitor of a Type II core collapse supernova: The iron core in the center is surrounded by the silicon shell, the oxygen shell, the carbon shell, the helium shell, and the hydrogen envelope. Note that the radial scale is arbitrary. (Figure reproduced by courtesy of M. Rampp.)*

gravitational forces[f]:

$$M_{\mathrm{Ch}} = 1.457(2Y_{\mathrm{e}})^2 M_\odot, \tag{1.2}$$

where Y_{e} is the electron fraction (number of electrons per baryon). When the core reaches this limit, the central density $\rho \sim 10^{10}$ g cm^{-3}, the temperature $T \sim 10^{10}$ K, the entropy per nucleon $s \sim 1k_{\mathrm{B}}$, and the electron fraction $Y_{\mathrm{e}} \sim 0.46$. Accordingly, its mass has grown to about $1.5M_\odot$, and its radius is about 1,500 kilometers.

The iron core is marginally stable, and any lowering of its adiabatic index will result in a collapse. The main process which drives the iron core to instability is electron capture by nuclei and free protons. This "neutronization" reduces the degeneracy pressure exerted by the electrons, as Y_{e} is reduced (deleptonization). The electron neutrinos generated in the electron capture processes can leave the iron core unhindered. Photodissociation can also act as a source of instability: At temperatures like the ones in the iron core, highly energetic photons can dissolve Fe nuclei into α particles, and those into free nucleons. This process is endothermic as it consumes nuclear binding energy and effectively cools the core (and thus reduces the pressure and lowers the effective γ). This effect is only significant in very massive stars with main sequence masses greater than about $25M_\odot$, where P_{ion}, which can be reduced by photodissociation, constitutes about 10% of the total pressure.

When the adiabatic index is reduced below 4/3, the iron core becomes unstable against radial oscillations. It starts to collapse on a dynamic timescale of several 10 milliseconds. As long as γ stays below the critical value of 4/3, the collapse cannot be halted. Initially, any neutrinos emanating from electron capture processes can leave the iron core without scattering. However, at matter densities around 10^{11}–10^{12} g cm^{-3}, the opacity of matter due to coherent scattering of neutrinos off nuclei increases considerably and becomes important. When the mean free path of the neutrinos becomes comparable to the dimension of the core, the neutrinos are "trapped" in the core[g]. At even higher densities of about 10^{13} g cm^{-3}, the neutrino–matter reactions reach equilibrium, and the neutrinos fill up their Fermi sea. As a result, the phase space for new neutrinos generated by electron capture is effectively blocked, and thus electron capture is strongly suppressed. Therefore, nuclei, electrons, photons, and neutrinos are in equilibrium, and the collapse proceeds adiabatically with $\gamma \approx$ const. (during the entire collapse, the specific entropy only rises by about $0.5k_{\mathrm{B}}$). This in turn means that the collapse (at least in the nonrotating case) cannot be stopped unless the EoS changes[h]. As the density increases further,

---

[f] Stellar rotation increases the maximum stable mass. Relativistic effects decrease the critical mass.

[g] One can define a neutrino sphere at the radial location where the opacity is unity.

[h] Electron capture and photodissociation at the onset of collapse and during the infall phase will reduce the effective adiabatic index γ to between 1.28 and 1.325. Neutral currents, which have been introduced in the theory of weak interactions by Weinberg, Salam, and Glashow, are crucial in this collapse scenario: They allow for coherent scattering off nuclei, with a cross section given by [109]

$$\sigma_A^{\mathrm{coh}} \approx \frac{\sigma_0}{16}\left(\frac{E_\nu}{m_{\mathrm{e}}c^2}\right)^2 A^2 \left[1 - \frac{Z}{A} + \left(4\sin^2\theta_{\mathrm{W}} - 1\right)\frac{Z}{A}\right]^2, \qquad \text{with } \sigma_0 = 1.76 \times 10^{-44}\ \mathrm{cm}^2, \tag{1.3}$$

where E_ν is the neutrino energy, A is the atomic mass number, Z is the atomic (proton) number, $m_{\mathrm{e}}c^2$ is the electron rest energy, θ_{W} is the Weinberg angle, and σ_0 is the characteristic cross section of weak interactions [128]. This cross section features an effective factor A^2, which increases the opacity dramatically. If neutrinos would continue to leak out during the collapse instead of being in equilibrium, the entropy would increase due to ongoing electron capture, and the equilibrium for the nuclear matter would shift towards free nucleons. This would in turn increase the gas pressure by the ions by a factor $A \approx 56$, which would then dominate the total the separation between the nuclei becomes smaller. When the mean matter density approaches nuclear density, the individual nuclei form extremely massive nuclei with mean atomic mass numbers up to about 500[i].

Until nuclear density is reached in the center of the core, the density and collapse profiles obey the self-similar solutions for a $\gamma = 4/3$ polytrope. In these solutions, the core splits into an approximately homologously falling inner core, in which the matter stays in sonic contact, and into a supersonically falling outer core. The mass of the inner core is approximately the Chandrasekhar mass (1.2) for the now reduced electron fraction Y_e and lies between $0.6M_\odot$ and $0.9M_\odot$. The (negative) velocity of the inner core is proportional to the radius coordinate r. This behavior, which can be derived analytically [46, 144], has been confirmed by numerical simulations.

When the central density exceeds nuclear density at $\rho_\mathrm{nuc} \approx 2.0 \times 10^{14}$ g cm^{-3}, the repulsive part of the nuclear forces between the protons and neutrons becomes important, and the EoS rapidly stiffens. This can be modelled by a jump in γ to about 2.5[j]. This is sufficient to halt the collapse by subsequently stopping the infalling mass shells, beginning in the center. From the bouncing mass shells, acoustic waves start to travel outward through the inner core until they concentrate near the sonic point. Within about 1 ms, the entire inner core has come to a halt, and the pressure waves, which have accumulated at its edge, steepen into a shock wave. This shock starts to propagate through the outer core, and reverses the velocity of the supersonically falling mass shells by passing through them. The initial energy of the shock is approximately equal to the kinetic energy of the inner core just before bounce, which is between 4 and 8×10^{51} erg. This is in principle enough energy to power a supernova explosion. In this *prompt shock* scenario, the shock wave would then eject the stellar envelope and leave behind a hot core of supranuclear density with a radius of about 20 to 30 km, the nascent neutron star (see Figure 1.2). However, it turns out that the shock stalls, because it loses energy due to photodissociation of iron nuclei into α particles and free nucleons, as it propagates outward through the infalling matter. The losses amount to about 2×10^{51} erg per $0.1M_\odot$ of matter which is passed by the shock. Additional energy losses arise from neutrino cooling as soon as the shock breaks through the neutrino sphere[k]. The energy gain by dissipation of kinetic energy from infalling matter is insufficient to compensate the losses. As a consequence, the shock stalls after a few 10 ms at a radius of several 100 km, when all its energy is spent in dissociating the matter[l], and the expanding shock front turns into an accretion shock.

---

pressure and stop the collapse. Such "thermal bounces" have been reported from numerical simulations, where neutrino trapping due to neutral currents was not included.

[i] At intermediate effective mass numbers electron capture is further suppressed due to shell blocking effects in the neutron rich heavy nuclei [43].

[j] The supranuclear γ is approximately bounded in the lower limit by 5/3, which is the adiabatic index for a nonrelativistic Boltzmann gas of nucleons. The upper bound is 3, which is the maximum value for nuclear forces between the nucleons consistent with extrapolations from heavy ion experiments, and theoretical calculations [53].

[k] Neutrinos, which are generated in the heated matter behind the shock front, can then escape much easier; this leads to a sudden rise in the neutrino luminosity.

[l] For small iron core masses the prompt shock energy could in principle be sufficient to drive the shock through the iron core. In the outer layers, where the density and temperature is lower, less energy is lost by dissociation processes.

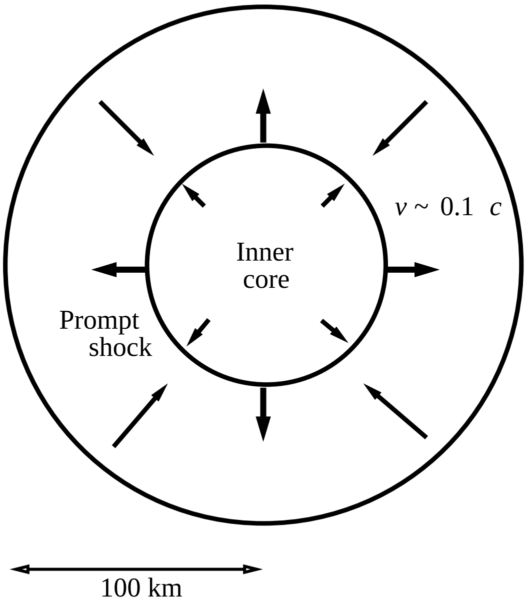

Figure 1.2: *Prompt shock phase of a core collapse supernova: While the inner core reaches a new equilibrium state, the hydrodynamic shock propagates outward through the outer core, where matter continues to fall inward. (Figure reproduced by courtesy of M. Rampp.)*

At that time, in the interior a hot quasi-static proto-neutron star has formed. The electron fraction is still large ($Y_\mathrm{e} \approx 0.3$), and most electrons have not been captured by the protons yet, as the neutrinos are still trapped inside the proto-neutron star. However, around the time when the prompt shock has come to a halt, neutrino diffusion becomes important, i.e. more electrons can be captured, and the proto-neutron star becomes neutron richer. Together with the μ- and τ-neutrinos, which are generated by thermal processes, these e^--neutrinos now leave the proto-neutron star. This neutrino emission cools the proto-neutron star and lets it shrink in size. Neutrino cooling may be enhanced by convective processes; in that case, the hot proto-neutron star virtually boils. When the nascent neutron star has reached its final size of about 10 km, 99% of the core collapse energy, i.e. the binding energy of the neutron star,

$$E_\mathrm{grav} \sim \frac{GM_\mathrm{core}^2}{R} = 3 \times 10^{53} \left(\frac{M_\mathrm{core}}{M_\odot}\right)^2 \left(\frac{R}{10\ \mathrm{km}}\right)^{-1} \mathrm{erg} \tag{1.4}$$

(where R is the radius of the neutron star, and G is the gravitational constant), has been emitted in the form of neutrinos[m]. When the neutrinos pass the region behind the stalled shock front, there is a small, but finite, probability that they scatter off the dissociated nuclei which mainly comprise the matter there. If only about 1% of the neutrinos deposit their energy in the post-shock "heating region", the resulting pressure and temperature increase is sufficient to drive the shock further outwards and cause the supernova explosion. It is now believed that this neutrino heating of the initially stalled prompt shock is the mechanism which ultimately leads to the ejection of the outer layers of the star. It can be shown [61] that (under certain

---

[m] At bounce time, the kinetic energy of the inner core, which is somewhat smaller than 10^{52} erg, is converted into the kinetic energy of the shock. The total released energy of about 10^{53} erg originates from the difference in gravitational energy between the proto-neutron star ($R_\mathrm{pns} \approx 30$ km) and the final neutron star ($R_\mathrm{ns} \approx 10$ km), and the internal energy in the inner core (in the form of neutrinos) which is released as the proto-neutron star cools down.

conditions) the heating by neutrinos behind the shock dominates over the cooling due to thermal emission, which leads to the net energy deposition. This scenario is dubbed *delayed explosion*, as the initially stalled shock is “revived” (see Figure 1.3). The neutrinos necessary to drive the shock are emitted from the collapsed core on the diffusion timescale (about 10 s). The resulting neutrino luminosity is of the order of 10^{52} erg s^{-1}. It is clear that momentum transfer of the neutrinos to the nucleons in the heating region plays no role in reviving the shock, as the neutrino Eddington luminosity (i.e. the flux which is needed to balance the gravitational attraction of nucleons by momentum transfer) is several orders of magnitude higher than the actual neutrino flux.

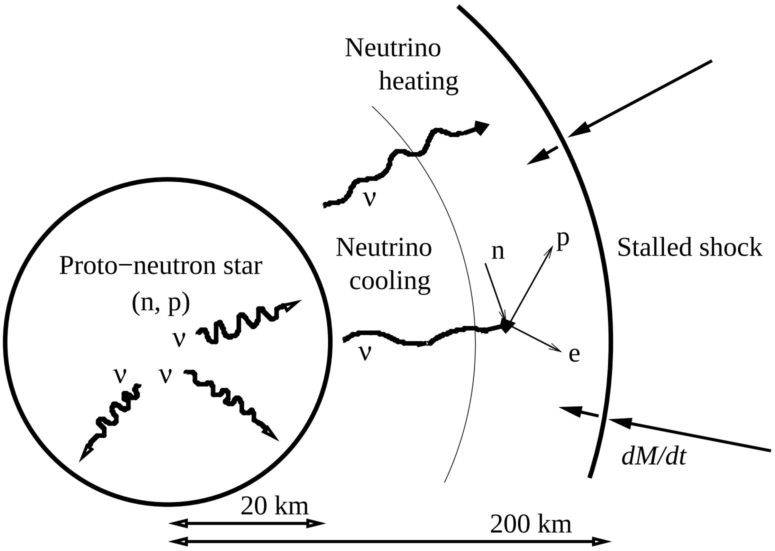

Figure 1.3: *Reviving of the stalled prompt shock in the delayed explosion scenario: The deposition of energy due to neutrino heating behind the stalled prompt shock drives the shock through the outer layers of the star. (Figure reproduced by courtesy of M. Rampp.)*

Finally, a few to many hours after core collapse, the shock front reaches the stellar surface, and the “optical” explosion of the star begins, when the ejected stellar matter expands into the interstellar medium.

In the above scenario, spherical symmetry has been assumed during all stages of core collapse. However, observations, analytical calculations, and numerical simulations suggest that in a core collapse supernova, local and global nonspherical effects might play an important role during the collapse and in the explosion mechanism: Observations indicate that core collapse supernova progenitors possess non-negligible equatorial surface velocities [122], at least while they are on the main sequence. However, the rotation profile inside the star is not well known, as there are no consistent numerical stellar evolution calculations including rotation available up to now. Due to angular momentum conservation during the collapse[n], the rotational velocity of an observer comoving with the fluid will increase significantly. This has several important consequences: First of all, for initially rapidly rotating iron cores, the collapse could be stopped by centrifugal forces before nuclear density is reached. In such a case of a centrifugal bounce, the core can experience several distinct multiple bounces. This scenario has been observed in

---

[n] There are no efficient angular momentum transport mechanisms inside the star on the collapse timescale.

numerical simulations. On the other hand, if the rotation rate, specified by the quantity

$$\beta = \frac{E_{\mathrm{rot}}}{|E_{\mathrm{pot}}|}, \tag{1.5}$$

which measures the ratio between rotational energy E_{rot} and potential energy E_{pot}, rises above 13.8% (27.4%) during the infall phase, an initially axisymmetric matter distribution can develop a secular (dynamical) triaxial instability, respectively[o]. Rotation also affects the form of the shock front, as in a rapidly rotating collapsing iron core the density at a given radius along the rotation axis is reduced compared to the density at same radius in the equatorial plane. Rotation may also lead to the generation of strong magnetic fields due to the winding up of magnetic field lines, which could in turn determine the evolution of the dynamics, or even result in the generation of a second, "magnetohydrodynamic" shock [88].

Other nonspherical effects occur only locally: Even in an initially spherically symmetric matter distribution, convection or Rayleigh–Taylor instabilities can induce vortices in the velocity field. This can modify the neutrino luminosity of the proto-neutron star, the shape of the heating region and the shock front, and thus the nucleosynthesis in the explosive environment behind the shock front[p].

---

[o] These numbers have been obtained by linear stability analysis for homogenous and uniformly rotating MacLaurin spheroids in Newtonian gravity. However, the corresponding nonlinear and relativistic numbers should be similar.

[p] Observations of radioactive ^{56}Ni generated during the explosion of SN 1987A suggest that it was formed in clumps rather than in a uniform angular distribution [62].

1.4 Gravitational Radiation

When Einstein put forth his discovery of wavelike vacuum solutions in general relativity (GR) in 1916, shortly after he established his new theory of gravity, the physical existence of these gravitational wave solutions was debated for long: Even Eddington thought for a long time that these solutions of the linearized Einstein equations were a mere coordinate effect and propagating with the "speed of thought" rather than with the speed of light [25], but it finally emerged and was commonly accepted that they were an invariant, i.e. physical, effect.

Contrary to electromagnetic radiation, which are oscillations propagating through spacetime, gravitational waves are oscillations of spacetime itself. Apart from this fundamental difference, there are other significant properties where electromagnetic and gravitational radiation differ [125]: Whereas electromagnetic radiation emitted by astrophysical sources is easily absorbed or scattered along the line of sight by e.g. interstellar matter or the Earth's atmosphere, gravitational waves are nearly unattenuated after they decouple from the source due to their extremely weak coupling to any intervening matter. Absorption and re-emission of electromagnetic waves is also responsible for the fact that they carry information predominantly about the thermodynamic state of the optically thin outer layers of the source. As their wavelength is typically much smaller than the spatial extension of the source, they give local pictures of the emitting system. Contrary to that, gravitational waves contain information about the global coherent bulk motion of some matter concentration (even if that matter is surrounded by other layers of matter with high optical thickness, but low density), conveyed by wavelengths comparable to the size of the source. The bottom line of this is that the content of information by electromagnetic and gravitational wave brought to us from astrophysical sources is almost "orthogonal", i.e. complementary. Observing gravitational waves from relativistic astrophysical sources like e.g. active galactic nuclei, accretion discs, rotating neutron stars, inspiralling and merging black holes and neutron stars, or rotational supernova core collapse will provide new insights into the dynamics and physical constitution of those systems. Moreover, just like the exploration of the Universe with radio astronomy was revolutionary to astronomy and astrophysics in the second half of the 20th century, gravitational wave astronomy could similarly open a new window onto the Universe in the future.

For nonspherical supernova core collapse in particular this means that with the detection of gravitational waves we could see right through the optically thick envelope of the star and look directly at the collapsing iron core and thus at the engine which drives the explosion of the stellar envelope, hours before the first light emission from the surface of the star. The only other possibility of a "direct" observation of core collapse dynamics in the first few hundred milliseconds of a (Galactic) supernova is the detection of neutrino emission from the nascent neutron star, which has actually been measured for SN 1987A[q] [7]. The price a prospective observer has to pay for this unobscured view to the very heart of the supernova is that gravitational waves are equally elusive to detection as neutrinos: The predominant problem in detecting neutrinos from a galactic supernova is not the number of particles arriving at the Earth. A typical core collapse supernova ejects roughly 10^{57} neutrinos, which translates into a time integrated flux

---

[q] For neutrinos the luminosity, i.e. the *flux* through a unit area, scales like R^{-2}, where R is the distance between the source and the detector. Contrary to that, in the detection of a gravitational wave, its *amplitude* is measured, and thus the luminosity declines like R^{-1}.

of about 10^{11} cm^{-2}, if the supernova is in the galactic center at a distance of 10 kpc. Of this large number of neutrinos, only about 1 per 10^{14} can be detected by the current Cherenkov type neutrino detectors[r].

We now want to estimate the prospects of detecting a gravitational wave with an average amplitude h[s]. The amplitude h, which measures the mean deviation of the actual spacetime from flat spacetime in a region far from the source, can also be seen as a "relative strain" of the gravitational wave on spacetime, which causes a relative, time dependent displacement Δl of two test particles, which are a distance l apart, at a detector site [55]:

$$h = \frac{2\Delta l}{l}. \tag{1.6}$$

Like an electromagnetic radiation field, gravitational radiation can be represented by an expansion into multipoles, where the mass density assumes the role of charge density in electromagnetic radiation. The field itself is then the second time derivative of the series of multipoles. Just as there is no electric monopole in electromagnetic radiation due to charge conservation, the time derivative of the according electric mass monopole of a gravitational wave vanishes due to mass conservation. Additionally, the time derivatives of the electric mass dipole, and the magnetic mass dipole of gravitational radiation also vanish, as the moments correspond to the linear and angular momenta, which are conserved for an isolated source (see Chapter 36 in [85]). The first nonvanishing moment is the mass quadrupole moment Q, and the wave amplitude h is the second time derivative of Q divided by the distance to the source R:

$$h \sim \frac{G}{c^4}\frac{\ddot{Q}}{R}, \tag{1.7}$$

with c being the speed of light. In order to obtain a rough estimate of the emission of gravitational radiation by a compact source like a collapsing iron core, we approximate the quadrupole moment Q by

$$Q \sim ML^2, \tag{1.8}$$

where M is the mass of the source that moves, and L is its typical size. If we neglect any accelerations, and denote the average time for the masses in the system to move from one side to the other by T, we get:

$$\ddot{Q} \sim \frac{2ML^2}{T^2} = 2MV^2 \simeq 4E_{\mathrm{kin}}^{\mathrm{nonspher}}, \tag{1.9}$$

where V is the average internal velocity of the source, and $E_{\mathrm{kin}}^{\mathrm{nonspher}}$ is the nonspherical part of its internal kinetic energy. From this we get for the wave amplitude:

$$h \sim \frac{4GE_{\mathrm{kin}}^{\mathrm{nonspher}}}{c^4 R}. \tag{1.10}$$

---

[r] The Kamiokande experiment reported 11 detections of neutrinos from SN 1987A [92]. The advanced Superkamiokande experiment has an estimated sensitivity increase by a factor of around 50 compared to Kamiokande [127].

[s] A more detailed derivation of gravitational radiation and the quadrupole formula can be found in Appendix C.1.

Thus the gravitational wave's influence on the detector is roughly 4 times the gravitational binding exerted by the mass-equivalent of the source's nonspherical internal kinetic energy. As the signal amplitudes of gravitational waves generated by laboratory devices are out of the scope of any practical detection (see e.g. Section 36.3 in [85]), only energy and mass concentrations in the Universe seem to be promising sources of gravitational waves. As matter concentrations in the Universe are generally bound, from the virial theorem we can infer that the gravitational binding energy of such an astrophysical system is of the order of its internal kinetic energy. Systems with a high kinetic energy thus require a large gravitational binding energy, and, in turn, have to be compact. If the matter in such a compact concentration of mass undergoes a dynamical nonspherical bulk motion, its nonspherical kinetic energy and thus the second time derivative of its quadrupole moment will be large. As a consequence of this, a system of one or more compact objects moving under its self-gravitation will be a strong source of gravitational radiation.

In a core collapse supernova the gravitational energy release during the infall will be mostly put into radial motion, and the energy radiated away in gravitational waves due to quadrupolar motion has a maximum of only about $10^{-7} M_{\odot} c^2$ [147]. This then translates into a gravitational wave amplitude of $h \sim 10^{-23}$ at a distance of 20 Mpc[t]. The frequency of the radiation will be in the so-called high frequency band, and range from about 100 to 1000 Hz, as the typical timescales of the oscillatory motion in the formation of a proto-neutron star lie between 1 and 10 ms. The predicted signal from coalescence and merger of two black holes of several solar masses is in the same frequency range, but its amplitude may be about 4 orders of magnitude larger [33], as the nonsphericity of such a configuration is much higher, and the objects involved are extremely compact. Nevertheless, gravitational wave emission from supernova core collapse is one of the promising sources for ground-based detectors.

There are basically two classes of detectors which are capable of measuring such minute length differences like the ones caused by gravitational waves from an astrophysical source [125]: Resonant mass detectors are massive bars or spheres tuned to a very narrow frequency bandwidth, where their sensitivity is rather high. This type of detector goes back to a prototype by Joseph Weber built in the 1960s. Several of these detector projects are currently operating in various countries (Grail in the Netherlands, Allegro in the U.S.A., Nautilus and Auriga in Italy, Explorer in Switzerland, and Niobe in Australia). However, due to their narrow bandwidth they are not designed to detect the gravitational wave burst signal from supernova core collapse, because that will not be a clean single mode signal but rather a superposition of many frequencies, which will probably vary distinctly with each supernova event.

The best observational tools available in the near future for detecting gravitational waves from core collapse will definitely be ground-based Michelson interferometers, several of which are being built and tested right now on sites in the U.S. (the two LIGO detectors), Italy (the Italian–French collaboration VIRGO), Germany (the joint German–British venture GEO600), Japan (the TAMA project), and Australia (the AIGO detector). Each of these detectors consists of four massive mirror test masses in two perpendicular arms suspended on vibration-isolated

---

[t] The astronomical distance measure 1 parsec (pc) is the distance from which the radius of the Earth's orbit around the Sun appears under an angle of 1°. 1 pc equals 3.26 light years (Ly), where 1 Ly = 9.46×10^{17} cm. The diameter of our Milky Way is approximately 30 kpc, while the distance to the center of the Virgo cluster of galaxies is about 15 Mpc.

supports to damp seismic noise. The separation between the masses can be measured to extremely high precision by a laser, which is split to run through the optical cavities in the two interferometer arms and is reflected by the mirror masses. When a gravitational wave passes through the detector, not only its amplitude, which translates into a displacement of the mirrors[u], can be measured as long as the detector is sensitive enough, but also its polarization can be determined, and the direction to the source can be triangulated by two or more detectors. The current detectors have arm lengths between 300 m and 4 km. It can be hoped that the gravitational wave signal from a Galactic supernova is within the range of detectability [125]. However, even with the help of a neutrino detection as a trigger for (offline) data analysis, which could improve the signal to noise ratio by a factor of 2 [125], the low event rates of only a few per century is a serious obstacle to a successful detection in practice. As advanced detector stages with increased sensitivity (like advanced LIGO) will become operational in the future, the prospects of detection will grow immensely, as these detectors could search for gravitational wave signals from core collapse supernovae out to the Virgo cluster (although they will not be able to utilize a neutrino trigger, as the flux of neutrinos emitted by extragalactic supernovae is too small to be detectable with current experiments). From such observations astrophysicist could scrutinize their current understanding of core collapse supernovae, and significantly extend their knowledge about the detailed physics involved. Already now gravitational wave templates from numerical simulations of rotational core collapse [147] are being used to calibrate data analysis tools for interferometer detectors [99]. As more realistic waveforms for such scenarios become available, it may be possible, given a positive detection of such a gravitational wave signal, to infer detailed information about the dynamics of a particular core collapse supernova from such a signal.

---

[u] To increase sensitivity of the detector, multiple passage of the light in the optical cavities is achieved by means of Fabry–Perot resonant cavities. This adds up the apparent movement of the test masses.

1.5 Simulations of Supernova Core Collapse

As we have laid out in Section 1.3, the aspects of physics which play a role in supernova core collapse are diverse and complicated. Therefore it is futile to try to extract anything but the crudest physics from analytic models. Rather, one has to resort to numerical simulations, which enable astrophysicists to get a handle on such distant and experimentally inaccessible phenomena like supernovae. However, core collapse is a very complicated interplay between hydrodynamic and relativistic gravitational forces, involves neutrino transport and thermonuclear burning fronts with turbulent combustion, and may additionally be influenced by rotation, convection, and magnetic fields. Thus numerical simulations, even such which include the above physics only partially, will be in no way trivial. Furthermore, any numerical treatment has to deal with the problems arising from the huge range of the relevant temporal and spatial scales present in the scenario: While the collapse of the core lasts only for several 10 ms and takes place within a radius of about 1000 km, the shock wave reaches the surface of the star several hours (a factor of $\sim 10^5$) later at the radius of several 10 million kilometers (a factor of $\sim 10^4$)[v].

Despite of all these difficulties, our current understanding of the physics involved in core collapse relies strongly on numerical simulations. Since the early days of computational physics, there have been numerous efforts to numerically simulate this problem. From the first investigations, which were considering spherically symmetric gravitational collapse of an ideal fluid in Newtonian gravity, basically two branches have emerged: On the one hand, the nonrelativistic approaches approximate gravity by a Newtonian potential, and use sophisticated microphysics. The first attempts to simulate core collapse by assuming that a prompt supernova shock is driven by means of energy deposition from neutrinos, have been performed by Colgate and White [20]. This was ruled out by Wilson, whose simulations showed that this scenario would fail due to the small neutrino scattering cross sections [136]. The introduction of neutral currents in the weak interaction lead to an additional weakening of the explosion by effectively reducing the neutrino luminosity of the proto-neutron star [138]. The delayed explosion mechanism due to neutrino heating, which was discovered by Wilson [140], turned out to yield sufficient explosions energies under certain circumstances [13]. However, the outcome of a successful explosion was a marginal effect and depended very much on the specific model. There have been many attempts to include more realistic physics in the simulations to get explosions more naturally. One of the directions has been to solve the Boltzmann equation for the neutrino transport in Newtonian gravity [101], or even in general relativity [71]. While these simulations have been performed in spherical symmetry, other promising approaches are to enhance energy deposition from neutrino heating by means of convection in the proto-neutron star, while keeping the neutrino transport schemes simple. This has been done in two dimensions using SPH [52], and using finite volume hydrodynamics [16]. In a similar work [90], the gravitational wave imprint of convective instabilities induced by neutrino heating has been computed.

---

[v] In one-dimensional hydrodynamic simulations, this problem can be remedied by using Lagrangian coordinates, which comove with the fluid [80]. In multi-dimensional simulations, this is not possible, and one has to use either fixed Eulerian coordinates, or some method of moving the grid with the flow [146]. Another approach is to automatically adapt the grid resolution to the hydrodynamic evolution (adaptive mesh refinement techniques [63]). A completely different method is to avoid finite difference or finite volume methods altogether, and use smoothed particle hydrodynamics (SPH).

In other multi-dimensional Newtonian gravity codes, the influence of microphysics was approximated by an ideal gas EoS, sometimes including a simple model for neutrino treatment. Rotational core collapse simulations in axisymmetry [89, 86, 147] or even without symmetry assumptions [102] have successfully been accomplished and used for approximately calculating the gravitational wave emission from such collapse scenarios. In some two-dimensional simulations magnetic fields were also included [88, 121]. However, even in Newtonian gravity, up to now no simulations which consider rotation, convection and a sophisticated Boltzmann transport for neutrinos have been performed.

The above models have predominantly originated from the astrophysics community. On the other hand, numerical relativists have mostly concentrated their efforts on solving the Einstein equations in vacuum. The most intriguing aspects of the theory of general relativity like black holes or gravitational radiation could be investigated without ever having to take into account the right hand side of Einstein's equations, the tensor of energy-momentum of matter. Even today, a considerable part of numerical relativity is concerned with coalescence and mergers of black holes [54], normal modes of black holes [10], and collapse of gravitational waves to a black hole [2], where no matter at all is present.

Nevertheless, in order to explain the existence of black holes in the Universe, the problem of astrophysical black hole formation has to be addressed, and thus attempts to use relativistic hydrodynamics for simulating core collapse to a black hole or neutron star were undertaken in numerical relativity. This meant that it became necessary to couple matter to the vacuum metric equations and evolve matter flows in a dynamic spacetime. The first simulation of an ideal fluid collapsing to a neutron star in spherical symmetry with a shock front forming has been done in 1966 by May and White [80, 81], who used a formulation of the Einstein equations by Misner and Sharp [84]. In the following decades, more sophisticated models emerged from that, like linear perturbations evolving on a background spacetime in a simulation of spherical core collapse to a neutron star [107, 106], and axisymmetric matter collapse from neutron star density to a black hole by Stark and Piran [117], and recently Shibata [111]. The introduction of modern sophisticated numerical methods from fluid dynamics to numerical relativity [104] and new formulations of the Einstein equations [112, 3] boosted progress in relativistic hydrodynamics simulations. Due to the discovery of gamma ray bursts and jets in active galactic nuclei, interest was triggered in collapsar models and studying the formation of relativistic jets near black holes [6, 74, 82].

Similar to the state-of-the-art astrophysical simulations in Newtonian gravity, current numerical relativistic codes put high demands on numerical techniques and computer resources. To simulate the inspiral and merger of two orbiting neutron stars requires major efforts like the U.S. Grand Challenge or the new E.U. TMR network. However, such research is not only of theoretical interest, but clearly has astrophysical relevance since the actual discovery of the binary pulsar PSR 1913+16 by Hulse and Taylor [59, 58]. Furthermore, the gravitational radiation from such a merger could be among the first to be detected by the new gravitational wave interferometers.

In spite of all the progress in numerical relativity over the last two decades, the advances in GR to simulate rotational core collapse to a neutron star in two or three dimensions – the necessity of which becomes apparent when it comes to explaining the rotation of newborn neutron stars[w] or asymmetries in the supernova explosion – were rather slow and tenacious. Practically all of the attempts so far [145, 139, 93, 28] used the ADM $\{3+1\}$ formulation of numerical relativity (see Section 3.1), which is numerically unstable in the long run.

As a consequence, up to now there exist no successful numerical simulations of rotational core collapse to neutron stars in general relativity, even for simple matter models. On the other hand, simulations which include better microphysics like neutrino transport have been confined to spherical symmetry, or have used Newtonian gravity. There is obviously a need to bridge the gap between these different approaches to the core collapse problem, if one wants to answer these questions:

- What is the quantitative influence of general relativity on the dynamics of core collapse compared to Newtonian gravity?
- How do higher densities and velocities expected in general relativistic simulations change the properties of the rotating neutron star?
- To what extent do general relativistic effects alter the gravitational wave signal?
- What is the behavior of the rotation rate β in a relativistic simulation, and what consequences does that have on the development of dynamical or secular triaxial instabilities in the neutron star?
- Is the prompt shock propagation sensitive to relativistic effects?

These are the issues which we have addressed in this work. It is based upon the parametric study of rotational core collapse of polytropes in Newtonian gravity by Zwerger and Müller [146, 147]. We have extended their work by including general relativistic gravity[x]. As a consequence of the apparent dead end situation in using the ADM formalism for that scenario in numerical relativity, we have chosen to utilize a close approximation of full general relativity. Like Zwerger and Müller, we use a simplified EoS (see Section 4.2).

With the work described in this thesis we have tried to unite in a numerical code a relativistic formulation of the hydrodynamic equations with some of the features of the most advanced multi-dimensional rotational core collapse studies in Newtonian gravity, using modern computational and numerical tools. We believe that it is justified to proceed along this path and eventually, by adding sophisticated microphysics like neutrino transport, arrive at a model to simulate rotational core collapse with all aspects of the relevant physics included. For the time being, the repeated failures of numerical models to produce the desired explosion simply show the shortcomings of such approximate numerical models, but they do not prove that the underlying physical scenario is entirely wrong. However, with improved numerical simulations of core collapse supernovae and realistic gravitational wave templates, astrophysicists will have a tool at hand which allows them to extract important and otherwise unaccessible information from actual observations of the gravitational wave signal from core collapse supernovae.

---

[w] Newborn neutron stars obviously have linear velocities of several 100 km s^{-1}, so they must have been subject to a “kick” during their formation.

[x] A similar direct comparison between Newtonian and general relativistic models of core collapse was done in spherical symmetry by van Riper [130, 131].

1.6 Organization of the Thesis

The thesis is structured as follows:

We briefly recapitulate the ADM $\{3+1\}$ formalism of general relativity in Chapter 2, and explain the derivation of the GR system of hydrodynamic conservation equations from the Einstein equations. We show how the hyperbolic structure of these conservation equations can be exploited to analytically solve the Riemann problem in GR hydrodynamics. Such methods are the foundation of many modern numerical schemes for solving hydrodynamic problems.

In Chapter 3 we present the ADM metric equations, and derive a constrained system of coupled nonlinear elliptic equations for the spacetime under the assumption of conformal flatness. The validity of this approximation is assessed considering our specific astrophysical model.

We describe our physical model, and especially the approximations we use to numerically handle rotational core collapse in Chapter 4. A hybrid equation of state is introduced, which extends a simple polytropic or ideal gas EoS to account more consistently for thermal heating behind shock fronts.

The numerical implementation of the hydrodynamic and metric equations derived in the previous sections is discussed in Chapter 5. The numerical representation of the matter distribution and spacetime on the computational grid is presented, and we explain the numerical application of Riemann solvers in high-resolution shock-capturing schemes. We also introduce the method employed to calculate initial data representing rotating polytropes in equilibrium. We present our specific implementation of a Riemann solver in the evolution method for the hydrodynamic quantities. A detailed discussion of the methods to numerically solve the metric equations follows, as these are the limiting factors in terms of computational efficiency.

Chapter 6 deals with comprehensive tests we have performed with our numerical code. In addition to evolution tests of initial data under various symmetry conditions, it also contains investigations on convergence and conservation features of the code.

The results from applying the computer code to rotational core collapse simulations, the principal object of study in this thesis, are presented in detail in Chapter 7. This chapter also contains a broad discussion of these results, including an analysis of the gravitational wave signals and their prospective use as templates for gravitational wave detection.

The thesis is summarized in Chapter 8, particularly focussing on the applicability of the results and future directions for continuing and extending the work presented here.

In Appendix A, we state the eigenvectors and eigenvalues needed for the solution of the general relativistic Riemann problem. In Appendix B, we list the source terms for the GR hydrodynamic conservation equations. The numerical method for extracting the gravitational radiation content from the spacetime of rotational core collapse is explained in Appendix C. The thesis is completed by a catalogue of the collapse types and gravitational wave signals of all models, which we have obtained from our simulations. This catalogue is contained in Appendix D.

1.7 Conventions

Throughout the thesis, unless otherwise stated, we use geometrized units for all hydrodynamic and metric quantities, i.e. the speed of light c and the gravitational constant G are set to 1.

Greek indices run from 0 to 3, while Latin indices run from 1 to 3. Repeated indices are summed up according to the Einstein summation convention, and the flat Minkowski spacetime metric has the diagonal elements $(-1, +1, +1, +1)$.

Four-vectors v^μ are called time-like if $v_\mu v^\mu < 0$, and space-like if $v_\mu v^\mu > 0$.

Chapter 2

General Relativistic Hydrodynamics

2.1 Relativistic Field Equations – $\{3+1\}$ Formalism

Contrary to Newtonian gravity, where the gravitational forces between massive bodies act in Euclidean space, in Einstein's general theory of relativity, gravity manifests itself as curvature of space and time, which is determined in a nonlinear way by the energy of matter or gravity itself. Cast into a mathematical formulation this is expressed by a theory of pseudo-Riemannian geometry of a continuous four-dimensional spacetime. This spacetime is a manifold $\mathcal{M}$ on which a metric $g_{\mu\nu}$ (and its inverse $g^{\mu\nu}$) with six independent metric functions is defined. The Einstein equations relate the curvature of spacetime, specified in the Einstein tensor $G_{\mu\nu}$, which derives from the Ricci tensor $R_{\mu\nu}$ and scalar $R = R^{\mu}_{\mu}$ as

$$G_{\mu\nu} = R_{\mu\nu} + \frac{1}{2} g_{\mu\nu} R, \tag{2.1}$$

with the energy-momentum tensor $T_{\mu\nu}$ of the mass energy distribution in the spacetime:

$$G_{\mu\nu} = 8\pi T_{\mu\nu}. \tag{2.2}$$

With the help of the Bianchi identities $\nabla^{\nu} G_{\mu\nu} = 0$, where ∇^{ν} is the covariant derivative on Riemannian manifolds, from the Einstein field equations one can derive the relativistic equations of motion, which manifest themselves as divergence equations for the energy-momentum tensor:

$$\nabla^{\nu} T_{\mu\nu} = 0. \tag{2.3}$$

The form (2.3) of the equations is coordinate-free, or covariant. However, to solve these equations numerically, one has to choose a suitable coordinate system. As the concept of absolute space and time is not valid in GR unlike in Newtonian physics, the interpretation of the geometry of coordinates has to be handled with caution.

In numerical relativity, the most widespread form of writing the Einstein equations as an initial value evolution problem was introduced in 1962 by Arnowitt, Deser and Misner [8], based on the $\{3+1\}$ splitting of spacetime by Lichnerowitz [70]. It is known as the ADM $\{3+1\}$

formalism, and their equations derived from the Einstein equations (2.2) have served as the workhorse of numerical relativity for the last four decades. The $\{3+1\}$ splitting is based upon a foliation of the four-dimensional spacetime manifold $\mathcal{M}$ into a continuous sequence of three-dimensional Cauchy hypersurfaces $\Sigma_{\hat{t}}$, where $\hat{t}$ is a scalar time parameter. This decomposition allows for an illustrative geometrical interpretation (see Figure 2.1):

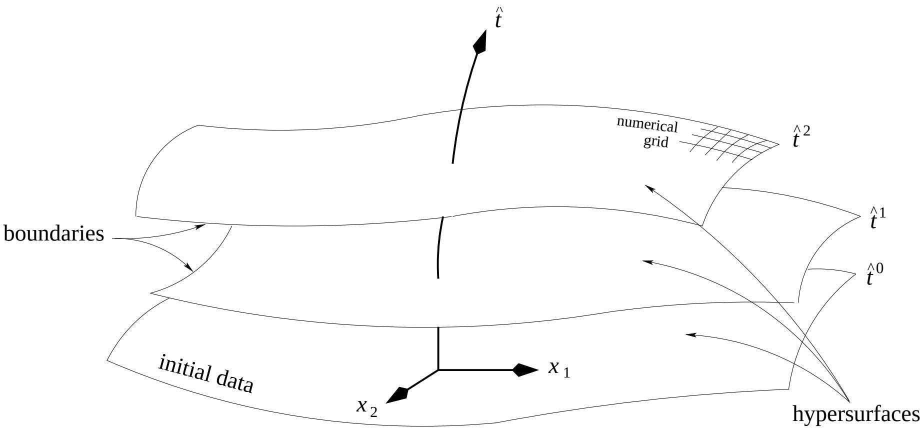

Figure 2.1: *Foliation of spacetime* $\mathcal{M}$ *into hypersurfaces* $\Sigma_{\hat{t}}$ *in the* $\{3+1\}$ *formalism.*

Each of these time slices $\Sigma_{\hat{t}}$ is a space-like hypersurface encompassing the entire three-dimensional space. Thus we have defined a Cauchy problem, i.e. if initial data on some hypersurface $\Sigma_{\hat{t}_0}$ and boundary conditions for all other $\Sigma_{\hat{t}>\hat{t}_0}$ are specified, then the time evolution of the initial data is determined.

The most general metric, which describes a spacetime foliated that way, can be derived as follows: First we introduce a set of coordinates $(x^\mu) = (t, x^i)$ which cover the entire spacetime manifold $\mathcal{M}$. Then the line element ds^2, the interval between two events $\hat{x}^\mu$ and x^μ on infinitesimally separated time slices $\Sigma_{\hat{t}}$ and $\Sigma_{\hat{t}+d\hat{t}}$ in spacetime, is given by the generalization of Pythagoras' theorem to Riemannian geometry:

$$ds^2 = -\begin{pmatrix}\text{proper time between}\\ \text{the hypersurfaces}\end{pmatrix}^2 + \begin{pmatrix}\text{proper distance within}\\ \text{the hypersurface}\end{pmatrix}^2 = -(d\hat{t}\,)^2 + (d\hat{x}^i)^2. \qquad (2.4)$$

In order to find an explicit form for ds^2, one has to take into account that in general the distance between two infinitesimal time slices depends on the location x^i on $\Sigma_{\hat{t}}$. Thus we have

$$d\hat{t} = \alpha dt, \qquad (2.5)$$

where α is called *lapse function.* The position of the spatial coordinate point x^i, when projected to $\Sigma_{\hat{t}+d\hat{t}}$ by the vector normal to $\Sigma_{\hat{t}}$, will be displaced by an amount

$$d\hat{x}^i = dx^i + \beta^i dt \qquad (2.6)$$

by the *shift vector* β^i. With those expressions for $d\hat{t}$ and $d\hat{x}^i$ the time-like contravariant unit vector n^μ normal to the hypersurface $\Sigma_{\hat{t}}$ is given by

$$n^\mu = (\alpha^{-1}, -\alpha^{-1}\beta^i), \qquad n_\mu n^\mu = -1. \qquad (2.7)$$

As in general the coordinates between hypersurfaces are shifted by β^i, the world line of a coordinate observer need not be normal to the hypersurface. Instead, its tangent is given by the time-like unit vector

$$t^\mu = \alpha n^\mu + \beta^\mu. \tag{2.8}$$

After having fixed the coordinate relation between two consecutive time slices, what remains to be done is to specify the curvature of the time slices themselves. That is given by the intrinsic three-dimensional curvature tensor γ_{ij} on a time slice $\Sigma_{\hat{t}}$, which is the spatial part of the tensor

$$\gamma_{\mu\nu} = g_{\mu\nu} + n_\mu n_\nu. \tag{2.9}$$

So in the end the ADM line element is given as

$$ds^2 = g_{\mu\nu} dx^\mu dx^\nu = -\alpha^2 dt^2 + \gamma_{ij}(dx^i + \beta^i dt)(dx^j + \beta^j dt), \tag{2.10}$$

where γ_{ij} describes the intrinsic geometry on a particular time slice, and α and β^i determine the relation between the coordinates on two consecutive time slices.

The four-dimensional spacetime metric $g_{\mu\nu}$ assumes the following form:

$$g_{\mu\nu} = \left(\begin{array}{c|ccc} -\alpha^2 + \beta_i \beta^i & \beta_1 & \beta_2 & \beta_3 \\ \hline \beta_1 & & & \\ \beta_2 & & \gamma_{ij} & \\ \beta_3 & & & \end{array} \right). \tag{2.11}$$

In order to project vector or tensor quantities from the four-dimensional manifold $\mathcal{M}$ onto a three-dimensional hypersurface Σ embedded in $\mathcal{M}$, one uses the projection operator

$$\perp^\mu_\nu = g^\mu_\nu + n^\mu n_\nu. \tag{2.12}$$

With the help of $\perp^i_\mu$ one can get the spatial components S^{ij} of the energy-momentum tensor, or the spatial momenta S^i,

$$S^{ij} = \perp^i_\mu \perp^j_\mu T^{\mu\nu}, \tag{2.13}$$

$$S^i = -\perp^i_\mu T^{\mu\nu} n_\nu, \tag{2.14}$$

whose role in the GR hydrodynamic equations will be discussed in detail later. The explicit formulations of $T^{\mu\nu}$, S^{ij}, and S^i for an ideal fluid EoS can be found in Appendix B.1.

Another metric quantity, which is extensively used in numerical relativity, is the extrinsic curvature K_{ij}. It measures the shear and expansion of neighboring coordinate observers in local proper time [116], and gives information about the embedding of the three-surface $\Sigma_{\hat{t}}$ in the four-dimensional manifold $\mathcal{M}$. The extrinsic curvature is defined as

$$K_{ij} = -\frac{1}{2} \mathcal{L}_{n^\mu} \gamma_{ij}, \tag{2.15}$$

where $\mathcal{L}_{n^\mu}$ is the Lie derivative with respect to the normal vector n^μ, a description for infinitesimal parallel transport in a curved spacetime (for a detailed discussion of the Lie derivative, see e.g. [133]).

The concept of parallel transport and differentiation in a curved spacetime becomes more apparent, if we point out that the derivative of e.g. a tensor $A_{\mu\nu}$ with respect to the coordinates x^λ does not transform as a tensor under coordinate transformations. So instead one introduces the covariant derivative (often denoted by the semicolon operator):

$$A_{\mu\nu;\lambda} = \nabla_\lambda A_{\mu\nu} = \frac{\partial A_{\mu\nu}}{\partial x^\lambda} - \mathit{\Gamma}^\kappa_{\mu\lambda} A_{\nu\kappa} - \mathit{\Gamma}^\kappa_{\nu\lambda} A_{\mu\kappa}. \tag{2.16}$$

The quantities $\mathit{\Gamma}^\lambda_{\mu\nu}$ used in this generalized derivative are called Christoffel symbols, and are defined as

$$\mathit{\Gamma}^\lambda_{\mu\nu} = \frac{1}{2} g^{\kappa\lambda} \left(\frac{\partial g_{\mu\kappa}}{\partial x^\nu} + \frac{\partial g_{\nu\kappa}}{\partial x^\mu} - \frac{\partial g_{\mu\nu}}{\partial x^\kappa} \right). \tag{2.17}$$

Note that the Christoffel symbols also do not behave like tensors under coordinate transformations.

A more detailed discussion of the geometrical interpretation of the ADM $\{3+1\}$ formalism can be found in [116]. The connection between derivatives in curvilinear coordinates in general, the covariant derivative, and the Christoffel symbols is discussed in the book by Landau and Lifshitz [67].

We finish this introduction to the geometrical properties and quantities in the ADM foliation of spacetime by a remark on raising and lowering indices of vectors and tensors: Unless otherwise stated, the indices of quantities defined in the four-dimensional spacetimes like $G_{\mu\nu}$ or the four-velocity u_μ are lowered or raised using the four-metric $g_{\mu\nu}$ or its inverse $g^{\mu\nu}$, respectively. On the other hand, quantities on the embedded three-dimensional hypersurface $\Sigma_{\hat{t}}$ like K_{ij} or v_i are lowered or raised using the three-metric γ_{ij} or its inverse γ^{ij}. Note that in general the components of the inverse three-metric are different from the spatial components of the inverse four-metric: $\gamma^{ij} \neq g^{ij}$.

2.2 Conservation Equations

From the mathematical point of view the relativistic equations of motion (2.3) together with the continuity equation are a set of conservation laws for hydrodynamic quantities. This character becomes more apparent when they are written in the ADM formalism for a fluid obeying an ideal gas EoS:

The hydrodynamic evolution of a relativistic perfect fluid with the rest-mass current J^μ and energy-momentum tensor $T^{\mu\nu}$,

$$J_\mu = \rho u_\mu, \qquad T_{\mu\nu} = \rho h u_\mu u_\nu + P g_{\mu\nu}, \tag{2.18}$$

is determined by a system of local conservation equations, which read:

$$\nabla^\mu J_\mu = 0, \qquad \nabla^\mu T_{\mu\nu} = 0. \tag{2.19}$$

Here u^μ the four-velocity of the fluid. Its 3-velocity, as measured by an Eulerian observer at rest in the space-like hypersurface $\Sigma_{\hat{t}}$ is

$$v^i = \frac{u^i}{\alpha u^0} + \frac{\beta^i}{\alpha}. \tag{2.20}$$

The Lorentz factor, which is defined as $W = \alpha u^0$, satisfies the relation

$$W = \frac{1}{\sqrt{1 - v_i v^i}}. \tag{2.21}$$

Following [11] we now introduce the following set of conserved variables in terms of the primitive hydrodynamic variables (ρ, v_i, ϵ), where ρ is the rest mass density, and ϵ is the internal specific energy:

$$\begin{aligned} D &= J^\mu n_\mu = \rho W, && \text{rest mass density,} && (2.22)\\ S^i &= -\perp^i_\nu T^{\mu\nu} n_\mu = \rho h W^2 v^i, && \text{momentum density,} && (2.23)\\ \tau &= T^{\mu\nu} n_\mu n_\nu - J^\mu n_\mu = \rho h W^2 - P - D, && \text{total energy density.} && (2.24)\end{aligned}$$

Here P is the pressure, and $h = 1 + \epsilon + \rho/P$ is the relativistic specific enthalpy.

Then the local conservation laws (2.19) can be written as a first-order, flux-conservative hyperbolic system of conservation laws:

$$\frac{1}{\sqrt{-g}} \left[\frac{\partial \sqrt{\gamma} \boldsymbol{F}^0}{\partial x^0} + \frac{\partial \sqrt{-g} \boldsymbol{F}^i}{\partial x^i} \right] = \boldsymbol{Q}, \tag{2.25}$$

with the state vector (vector of conserved quantities), flux vector and source vector given by

$$\boldsymbol{F}^0 = (D, S_j, \tau)^T \tag{2.26}$$

$$\boldsymbol{F}^i = \left(D \left(v^i - \frac{\beta^i}{\alpha} \right), S_j \left(v^i - \frac{\beta^i}{\alpha} \right) + \delta^i_j P, \tau \left(v^i - \frac{\beta^i}{\alpha} \right) + P v^i \right)^T, \tag{2.27}$$

$$\boldsymbol{Q} = \left(0, T^{\mu\nu} \left(\frac{\partial g_{\nu j}}{\partial x^\mu} - \mathit{\Gamma}^\lambda_{\mu\nu} g_{\lambda j} \right), \alpha \left(T^{\mu 0} \frac{\partial \ln \alpha}{\partial x^\mu} - T^{\mu\nu} \mathit{\Gamma}^0_{\mu\nu} \right) \right)^T. \tag{2.28}$$

Here $\sqrt{-g} = \alpha\sqrt{\gamma}$, with $g = \det(g_{\mu\nu})$ and $\gamma = \det(\gamma_{ij})$ being the determinant of the four-metric and three-metric, respectively. $\Gamma^{\lambda}_{\mu\nu}$ are the four-dimensional Christoffel symbols (2.17), which represent the gravitational source action of the curved spacetime, and δ^i_j is the Kronecker delta.

These equations are the general relativistic analogue to the mass conservation equation, the Euler equations, and the energy conservation equation in Newtonian gravity. They have been formulated by Banyuls et al. in 1997 [11]. Other conservative formulations of the relativistic hydrodynamic equations have been derived by Eulderink and Mellema [27], or by Papadopoulos and Font [96].

The following list summarizes the evolutionary steps from the Newtonian to the GR hydro equations in flux conservative form.

- In the Newtonian limit, the hydrodynamic equations read:

$$\frac{\partial \rho}{\partial t} + \frac{\partial \rho v^i}{\partial x^i} = 0, \tag{2.29}$$

$$\frac{\partial \rho v_j}{\partial t} + \frac{\partial (\rho v_j v^i + P\delta^i_j)}{\partial x^i} = \rho g_j, \tag{2.30}$$

$$\frac{\partial (\rho\epsilon + \frac{1}{2}\rho v_i v^i)}{\partial t} + \frac{\partial (\rho\epsilon + \frac{1}{2}\rho v_i v^i + P) v^i}{\partial x^i} = \rho g_i v^i. \tag{2.31}$$

- In special relativity, i.e. for flows with characteristic velocities close to the speed of light c on a flat Minkowski spacetime $\eta_{\mu\nu} = (-1, +1, +1, +1)$, the corresponding equations are:

$$\frac{\partial \rho W}{\partial t} + \frac{\partial \rho W v^i}{\partial x^i} = 0, \tag{2.32}$$

$$\frac{\partial \rho h W^2 v_j}{\partial t} + \frac{\partial (\rho h W^2 v_j v^i + P\delta^i_j)}{\partial x^i} = \rho g_j, \tag{2.33}$$

$$\frac{\partial (\rho h W^2 - P - \rho W)}{\partial t} + \frac{\partial (\rho h W^2 - \rho W) v^i}{\partial x^i} = \rho g_i v^i. \tag{2.34}$$

- For a general relativistic system, the matter flow is determined by Equations (2.25) (with the fluxes and sources explicitely written out, and $\hat{v}^i = v^i - \beta^i/\alpha$):

$$\frac{1}{\sqrt{-g}}\left(\frac{\partial \sqrt{\gamma}\rho W}{\partial t} + \frac{\partial \sqrt{-g}\rho W \hat{v}^i}{\partial x^i}\right) = 0, \tag{2.35}$$

$$\frac{1}{\sqrt{-g}}\left(\frac{\partial \sqrt{\gamma}\rho h W^2 v_j}{\partial t} + \frac{\partial \sqrt{-g}(\rho h W^2 v_j \hat{v}^i + P\delta^i_j)}{\partial x^i}\right) = T^{\mu\nu}\left(\frac{\partial g_{\nu j}}{\partial x^\mu} - \Gamma^{\lambda}_{\mu\nu} g_{\lambda j}\right), \tag{2.36}$$

$$\frac{1}{\sqrt{-g}}\left(\frac{\partial \sqrt{\gamma}(\rho h W^2 - P - \rho W)}{\partial t} + \frac{\partial \sqrt{-g}((\rho h W^2 - P - \rho W)\hat{v}^i + P v^i)}{\partial x^i}\right) = \alpha\left(T^{\mu 0}\frac{\partial \ln \alpha}{\partial x^\mu} - T^{\mu\nu}\Gamma^{0}_{\mu\nu}\right). \tag{2.37}$$

2.3 The General Relativistic Riemann Problem

The general relativistic equations (2.35–2.37) for the evolution of an ideal fluid constitute a highly nonlinear problem. In general, nonlinear hyperbolic systems have the property that they allow for weak solutions, i.e. classical solutions in smooth regions which are separated by a finite number of discontinuities (shocks or contact discontinuities[a]). Even an initially smooth density, velocity, and energy distribution can develop shocks after some time, if it is evolved according to such nonlinear hyperbolic equations. This is particularly true for core collapse scenarios, where the core bounce will result in the formation of a shock wave, which then propagates through the envelope of the star.

On the other hand, in a hydrodynamic computer code based on finite difference or finite volume methods (see also Section 5.4), hydrodynamic quantities are represented as discrete data. As a consequence, even a smooth flow is treated as a sequence of piecewise constant data, which are discontinuous at cell interfaces between neighboring grid points. This is a good approximation for regions of smooth flow, and is especially well suited for discontinuities. Now one can regard every such interface in isolation: Each of these cell interfaces then defines a Riemann problem, the simplest initial value problem with discontinuous initial data. Such a problem admits an exact solution. For the Euler equations of classical fluid dynamics such an analytic solution has been developed by Godunov [45]. The extension of this solution to special relativistic flows has been done by Martí and Müller [76][b]. In both cases a general solution of the Riemann problem consists of constant states, which are separated by three distinct classes of waves, depending on the states left and right of the interface: (i) shocks, (ii) contact discontinuities, and (iii) rarefactions[c]. The exact nature of the solution to a particular Riemann problem is determined by the Rankine–Hugoniot conditions across the discontinuity. The solutions of the local Riemann problem are themselves exact solutions of the conservation laws. Therefore a series of such local solutions on a discrete grid constitutes a global solution of the conservation equations for the discrete initial data.

We have already stated in Section 2.2, that the hydrodynamic equations are formulated as a hyperbolic set of conservation problems. This means that the information in this system is propagating with finite velocities (unlike in elliptic equations, which have infinite propagation speeds and therefore instantaneous action), and thus the evolution of the matter flow is governed by the characteristic velocities of the system. This characteristic information is then used to (exactly or approximately) solve the associated Riemann problem for this specific system of conservation equations. The procedure to obtain the characteristic structure is as follows: The Jacobi matrices of the conservation equations (2.25) corresponding to the three spatial directions are

$$\boldsymbol{B}^i = \alpha \frac{\partial \boldsymbol{F}^i}{\partial \boldsymbol{F}^0} \tag{2.38}$$

---

[a] In shocks, all hydrodynamic state variables are discontinuous; in contact discontinuities, the density is discontinuous while the other state variables are continuous.

[b] This method can be extended to flows on a curved spacetime in general relativity: By a local coordinate transformation the spacetime is changed to a locally flat Minkowski spacetime, which then allows for an application of the solution of (locally) special relativistic Riemann problems [98].

[c] In rarefactions, all state vector quantities are continuous, but nonconstant.

($i = 1, 2, 3$), i.e. the derivatives of the flux vectors in each spatial coordinate direction with respect to the state vector.

As the state and the flux vector have five components, to each of the three Jacobi matrices belong five eigenvalues [11],

$$\lambda^i_0 = \alpha v^i - \beta^i, \qquad \text{threefold degenerate,} \tag{2.39}$$

$$\lambda^i_\pm = \frac{\alpha}{1 - v^2 c_\mathrm{s}^2}\left[v^i(1 - c_\mathrm{s}^2) \pm c_\mathrm{s}^2\sqrt{(1 - v^2)(\gamma^{ii}(1 - v^2 c_\mathrm{s}^2) - v^i v^i(1 - c_\mathrm{s}^2))}\right] - \beta^i, \tag{2.40}$$

and a set of right eigenvectors $\boldsymbol{r}$ (which are listed in Appendix A.2). These solve the three linear eigenvalue problems $\boldsymbol{B}^i \boldsymbol{r}^i = \lambda^i \boldsymbol{r}^i$.

From this we can infer that the features in the flow are transported with velocities corresponding to the eigenvalues[d]. This form of the eigenvalues (2.39, 2.40) is again the general relativistic extension of the corresponding form in Newtonian hydrodynamics, where they assume the simple and instructive form

$$\lambda^i_0 = v^i, \qquad \text{threefold degenerate,} \tag{2.41}$$

$$\lambda^i_\pm = v^i \pm c_\mathrm{s}. \tag{2.42}$$

From that it is obvious that in a Newtonian flow information can propagate with the velocity of the flow itself (material waves) or with plus or minus the speed of sound with respect to the flow velocity (acoustic waves).

The information about the propagation velocities (i.e. the eigenvalues λ^i) together with the knowledge about the hydrodynamics states left and right of the interface (i.e. the density ρ, the pressure P, and the internal energy ϵ) is sufficient to analytically solve the Riemann problem.

However, the exact analytic solution of numerous Riemann problems – i.e. one per grid point for each coordinate direction in one time step – during a numerical computation can be costly and therefore time consuming. To cope with this fact, it is often sufficient in numerics to solve the Riemann problem approximately: For this one assumes that the Jacobian matrices are locally constant (for a justification of this assumption in conjunction with numerical codes, see Section 5.4.1). This is effectively a local linearization of the hyperbolic system at each Riemann interface. Then one can utilize the following decomposition of the Jacobi matrix:

$$\boldsymbol{B}^i = \boldsymbol{R}^i \boldsymbol{\Lambda}^i (\boldsymbol{R}^i)^{-1} = \boldsymbol{R}^i \boldsymbol{\Lambda}^i \boldsymbol{L}^i. \tag{2.43}$$

Here $\boldsymbol{R}^i$ is the matrix of right eigenvectors (as columns), $\boldsymbol{\Lambda}^i$ is the diagonal matrix of the eigenvalues λ^i, and $\boldsymbol{L}^i = (\boldsymbol{R}^i)^{-1}$ is the matrix of left eigenvalues (as rows). With the help of this transformation, the approximate Riemann problem can be numerically solved in a straightforward way, which will be shown in Section 5.4.

As the matrix of right and left eigenvectors, and the matrix of eigenvalues are analytically known for the general relativistic hydrodynamic conservation equations (2.25), the numerical solution of the Riemann problem can be accomplished in a fast and easy manner. Modern

---

[d] The curves defined by the tangents along these characteristic velocities in the flow are called *characteristics*.

numerical solvers for hydrodynamic flows often rely upon approximate Riemann solvers. The solutions obtained in that way are for practical purposes almost as good as if the full nonlinear Riemann problem would be solved [24].

Chapter 3

Metric Equations

The system of equations (2.25) determines the evolution of the hydrodynamic quantities in a given spacetime. On the other hand, the evolution of spacetime itself is governed by another set of equations. In order to be able to understand more clearly the mathematical classification of the system of metric equations, at this point we briefly explain the general concept of evolution and constraint equations.

When the evolution of a physical problem is determined by a set of hyperbolic partial differential equations, then it can be mathematically formulated as a Cauchy problem. This means that if the initial data are specified on a time slice $\Sigma_{\hat{t}_0}$, and boundary conditions are given for all subsequent times, then the corresponding differential equations can be separated into a set of evolution and constraint equations. As a simple example, we want to consider the one-dimensional wave equation:

$$\partial_{tt}\phi - \partial_{xx}\phi = 0. \tag{3.1}$$

If we now introduce the following definitions,

$$u = \partial_t \phi, \qquad \gamma = \partial_x \phi, \tag{3.2}$$

the second-order wave equation can be written as a set of three evolution equations,

$$\partial_t \phi = u, \tag{3.3}$$

$$\partial_t u = \partial_x \gamma, \tag{3.4}$$

$$\partial_t \gamma = \partial_x u, \tag{3.5}$$

and one constraint equation,

$$0 = \partial_x \phi - \gamma, \tag{3.6}$$

each with derivatives of first order in t and x.

The evolution equations (3.3–3.5) propagate forward in time the quantities ϕ, u, and γ, while the constraint equation (3.6) must be satisfied at all times (and will be, if the propagation is properly done according to the evolution equations). As in the case of the wave equation (3.1), where there are in total four equations for three unknowns, in general a number n_{u} of unknowns are determined by a system of n_{eq} equations. The n_{u} unknowns can be computed numerically by picking any n_{u} of the n_{eq} equations and solving them[a]. Sometimes, there are n_{u} evolution equations, so it is sufficient to determine the evolution of the unknowns by solving these equations ("free evolution"). The constraint equations will then (in the limit of infinitely good accuracy of the numerical scheme) be satisfied automatically. In practice, this method of numerical evolution is often preferred, as the numerical solution of an evolution equation may be easier and more inexpensive in terms of computer time. The constraint equations, which are normally computationally expensive, are then used to monitor the accuracy of the evolution equations at given times during the evolution. On the other hand, some or all of the constraint equations can be used to solve the system. This method is then called "constrained evolution". From the mathematical point of view, both approaches, the free or constrained evolution, are a valid method for solving such a system. However, in the numerical implementation, one may be preferable to the other method for reasons of computational efficiency, stability, or accuracy.

In general, a system of evolution and constraint equations will not be purely hyperbolic in its nature, but it will be a mixture of equations of hyperbolic, parabolic, and elliptic type, or contain ordinary differential equations. This is why mathematically stringent statements about the behavior of such equation systems, and especially of their numerical representations, are rather difficult to make [42].

---

[a] The system is overdetermined, if $n_{\mathrm{eq}} > n_{\mathrm{u}}$. Then the remaining equations, which have not chosen for determining the evolution of the unknowns, can be used for a consistency check of the numerical evolution.

3.1 ADM Evolution and Constraint Equations

In the ADM formalism (2.11), the Einstein equations can also be written in a mixed evolution and constraint form [145]:

$$
\begin{aligned}
\partial_t \gamma_{ij} &= -2\alpha K_{ij} + \nabla_i \beta_j + \nabla_j \beta_i, && \text{three-metric evolution,} \quad (3.7)\\
\partial_t K_{ij} &= -\nabla_i \nabla_j \alpha + \alpha(R_{ij} + K K_{ij} - 2K_{ik}K^k_j) + \beta^k \nabla_k K_{ij} + && \text{extrinsic curvature evolution,}\\
&\quad + K_{ik}\nabla_j \beta^k + K_{jk}\nabla_i \beta^k - 8\pi\alpha\Big(S_{ij} - \frac{\gamma_{ij}}{2}(S - \rho_{\mathrm{H}})\Big), && (3.8)\\
0 &= R + K^2 - K_{ij}K^{ij} - 16\pi\rho_{\mathrm{H}}, && \text{Hamiltonian constraint,} \quad (3.9)\\
0 &= \nabla_i (K^{ij} - \gamma^{ij} K) - 8\pi S^j, && \text{momentum constraint,} \quad (3.10)
\end{aligned}
$$

where $\rho_{\mathrm{H}} = \alpha^2 T^{00}$, R_{ij} is the Ricci curvature tensor of the three-hypersurface $\Sigma_{\hat{t}}$ and R its contraction (the scalar curvature). So the ADM system of equations consists of two times six evolution equations for the three-metric γ_{ij} and the extrinsic curvature K_{ij}, and four constraint equations. As explained before in the example of the wave equation (3.1), the evolution equations can be used to propagate forward in time the 12 unknowns γ_{ij} and K_{ij}, which are given on the initial time slice, whereas the constraint equations provide a check for the accuracy of the numerical solution.

Like any arbitrary spacetime metric on a four-dimensional manifold without symmetries, the ADM metric (2.11) has 10 independent components, as it is symmetric with respect to the diagonal[b]. However, the theory of general relativity has only 6 physical degrees of freedom. As a consequence of this, one is free to choose 4 additional gauge conditions, just like in the vector formulation of Maxwell's theory of electromagnetic fields. So within boundaries[c], gauge choices can be imposed as a set of algebraic relations between the elements of $g_{\mu\nu}$, or, for the ADM system, equivalently between α, β^i, γ_{ij} and K_{ij}. In numerical relativity such gauge conditions are usually adapted to the specific evolution situations in order to ensure nonpathological coordinate behavior or numerical stability of the system. This exploiting of gauge freedom plays an essential role in many numerical simulations, e.g. in the evolution of binary systems or the handling of coordinate and metric singularities, like in the case of black hole singularities. The fundamental concepts about gauge conditions in numerical relativity have been introduced by Smarr and York in 1978 [116][d].

---

[b] Note that the ADM equations (3.7–3.10) have 12 unknowns. This is due to the introduction of the quantities K_{ij}, which are combinations of the components of the metric $g_{\mu\nu}$. They are auxiliary constructs like the quantities u and γ in Equation (3.2), which are used in the wave equation (3.3–3.6).

[c] Depending on the symmetry of the spacetime, certain metric components cannot be subjected to arbitrary gauge conditions.

[d] In numerical simulations, α and β^i are often determined by algebraic equations. One approach would be to set all components of the shift vector β^i to zero, and impose the maximal slicing gauge condition on the lapse function by setting the trace of K to zero, which fixes α.

3.2 Problems with the ADM Equations – Alternative Formulations and Approximations

Since its introduction over 40 years ago, the ADM formalism and the associated system of metric equations have been the workhorse of numerical relativity. Most of the numerical simulations in the literature [108, 34] have been based upon solving the ADM equations (3.7–3.10) with a variety of different approaches to exploit the remaining gauge freedom for relations between the metric components.

However, there exist many essential drawbacks, which have been hampering the use of the ADM equations in numerical applications. Not only is it computationally expensive and complicated to solve the complete set of ADM equations (especially if the elliptic constraint equations have to be solved at every time step), but the ADM formalism of metric equations also seems to have an intrinsic negative property: In many simulation runs severe numerical instabilities are encountered after some evolution time, which often lead to unacceptable constraint violations and cause the computer code to crash in the end. This failure of the ADM equations to guarantee long term stable evolution, particularly if the numerical grid is based on coordinates which result in singularities of some metric components (like polar radial coordinates), has been a serious obstacle in previous simulations of black holes [15], rotational core collapse [145, 28], and other astrophysical scenarios.

Because of this deficiency of the ADM equations, the quest for the *Holy Grail of Numerical Relativity*, defined by Shapiro and Teukolsky in 1985 [110] as a computer code which

(i) evolves an arbitrary spacetime in GR without symmetries,
(ii) avoids or successfully handles singularities,
(iii) can deal with black holes,
(iv) maintains high accuracy, and
(v) runs indefinitely long,

has so far not yet been brought to a successful end for codes based on solving the original ADM equations. At present there is no clear understanding for the underlying reasons of the lack of stability of the ADM equations [42]. As a consequence of this, in the last few years many reformulations of the $\{3+1\}$ equations particularly for the use in numerical relativity have been attempted, like the conformal traceless treatment of the metric equations, first proposed by Shibata and Nakamura [112]. This reformulation has been tested on evolutions of gravitational waves [12], and single black holes, boson stars, and neutron stars [3]. These simulations exhibit better long term stability than the ones where the metric is solved with the help of the ADM formulation; still, they will also eventually develop serious constraint violations or numerical instabilities.

Another approach are alternative formulations of the Einstein equations not based on the ADM formalism. Among these is the characteristic formulation, in which the spacetime is sliced along null hypersurfaces (rather than along time-like hypersurface like in the ADM formalism) [142]. In this formulation, the numerical solution of the vacuum Einstein equations for a single nonrotating black hole exhibits long-term stable behavior [123]. In spherical symmetry, the core collapse of a supermassive star has been simulated [72], and there are ongoing attempts to extend hydrodynamic simulations to two dimensions [114].

For many hydrodynamic applications in astrophysics it is not necessary to solve the full set of Einstein equations to obtain a fair approximation of the actual physics: When simulating cosmological structure formation, the influence of gravity, which leads to the first structures in the early Universe, is so weak that a general relativistic approach to this problem is not necessary. Moreover, the velocities in the matter flows are so small compared to the speed of light c, that not even special relativity is needed for such simulations. Thus, even if the first cosmological matter concentrations form on a curved background spacetime, the gravitational interaction between them can be described to high accuracy by a Newtonian potential [134]. Another example of approximating general relativity by a less complicated physical model in an astrophysical context is the simulation of jets streaming from active galactic nuclei into the intergalactic medium. As such jets propagate with speeds very close to the speed of light (with Lorentz factors of approximately 100), relativistic effects play a crucial role. However, far away from the central engine, which powers the outflow, both external gravitational fields and self-gravity can be completely neglected, and it suffices to solve the much simpler special relativistic equations of fluid dynamics (see [78] for two-dimensional, and [5] for three-dimensional simulations).

On the other hand, there are astrophysical situations, where gravity can neither be neglected nor be sufficiently approximated by a Newtonian potential. Then one can still resort to approximation techniques which better model general relativistic gravity without having to deal with the full machinery of GR: One such example are calculations of inspiralling black hole or neutron star binaries. A common approach to analytically or numerically attack this problem is to represent the two compact objects by "point particles") and expand the Einstein equations in orders of $(v/c)^2$, known as the parameterized post-Newtonian (PPN) formalism [135, 14]. In this method, the exact general relativistic metric is typically expanded in orders 1, 2, 2.5, 3, 3.5, …, which significantly simplifies the Einstein equations, when this expansion is truncated at some power. The resulting PPN metric equations can be regarded as "truncated" Einstein equations. The rationale behind this way of approximating the full Einstein equations is very similar to perturbation theory. Depending on the order of the PPN expansion, the equations include different relativistic effects, like the generation of gravitational waves, the gravitational radiation back-reaction[e], dragging of inertial frames, etc. However, even for point particles, in higher expansion orders the PPN equations become analytically not solvable and increasingly complicated. Still the PPN formalism is endowed with an important property of general relativity, which is a curved spacetime. Therefore it follows the philosophy of the full theory much closer than Newtonian gravity, which suffers from features like infinite propagation speed of information or the artificial split of energy and mass.

Another approximation method, which yields a good modeling of relativity for specific physical systems is the description of the spacetime by a time-independent, i.e. static, metric (Cowling approximation). The application range of this method is confined to systems where the hydrodynamic matter flow exerts only negligible influence on the variation of spacetime with

---

[e] As a consequence of the nonlinearity of the theory of general relativity, gravitational radiation will react back onto the emitting system by curving the spacetime and extracting energy from the source.

time, like accretion onto compact objects [36], or rotating neutron stars in equilibrium [119, 35]. A less restrictive approximation is the fully relativistic evolution of matter on a spacetime which is calculated by linearizing the metric equations. This has been done as well for simulating accretion onto black holes [95] and computing neutron star oscillations [4].

A rather novel approach in general relativity, using a truncated set of metric equations by assuming the *conformal flatness condition* (CFC) for the three-metric, first introduced recently for a coupled set of metric and hydrodynamic evolution equations in numerical relativity by Wilson et al. [141]. Our implementation of the metric equations is based upon this approximation. We will motivate its assumptions and derive the resulting metric equations in the following.

3.3 Conformally Flat Metric Equations

3.3.1 Conformal Flatness Condition

Instead of approximating the full spacetime metric by expanding it in orders of $(v/c)^2$ and then truncating this series, as in the PPN formalism, one can try to impose certain conditions on particular quantities of the metric. Then one can investigate whether, and under which conditions, the resulting set of equations describes a general relativistic hydrodynamic flow properly.

We now want to see which parts of the metric might be best suited for a modification: The lapse function α, which controls the distance between subsequent time slices, should better remain a free parameter at first, as it ensures that the metric evolves in a way such that the numerical grid points do not exhibit pathological behavior, like e.g. getting attracted by a coordinate or physical singularity. Nevertheless, its behavior can be determined by a gauge condition, which then controls the evolution of α, and thus the sequence of time slices, in the desired way. Similarly all shift vector components should be kept as in the general metric, because they are also responsible for the appropriate reaction of the hypersurfaces to the metric evolution. Fixing β^i without prior knowledge of the spacetime geometry during the evolution may result in a too rigid sequence of time slices and coordinates which could turn inadequate to adapt properly to the curvature of spacetime.

These restrictions leave us with the freedom to modify the three-metric γ_{ij}, which describes the curvature of three-dimensional space during the evolution. The simplest possible choice for the three-metric is the flat metric $\hat{\gamma}_{ij}$, which in Cartesian coordinates is $\delta_i^j = \mathrm{diag}\,(1,1,1)$, and in spherical coordinates is

$$\hat{\gamma}_{ij} = \mathrm{diag}\,(1, r^2, r^2 \sin^2\theta) = \begin{pmatrix} 1 & 0 & 0 \\ 0 & r^2 & 0 \\ 0 & 0 & r^2 \sin^2\theta \end{pmatrix}. \tag{3.11}$$

A less restrictive choice, and thus a better approximation to a general three-metric, is given by introducing a conformally flat metric

$$\gamma_{ij} = \phi^4 \hat{\gamma}_{ij} = \begin{pmatrix} \phi^4 & 0 & 0 \\ 0 & \phi^4 r^2 & 0 \\ 0 & 0 & \phi^4 r^2 \sin^2\theta \end{pmatrix}, \tag{3.12}$$

where the conformal factor ϕ depends in general on the coordinates $x^\mu = (t, r, \theta, \varphi)$[f]. It can be shown that any (even time-dependent) spherically symmetric spacetime can be described by a conformally flat metric, with the additional properties that $\beta^i = 0$, and $\phi = \phi(r)$. This holds for any spherically symmetric matter distribution in general relativity, even for a single Schwarzschild black hole spacetime.

---

[f] In the context of curved manifold, two metrics γ_{ij} and $\hat{\gamma}_{ij}$ are called conformal, if they are identical modulo a conformal factor ϕ: $\gamma_{ij} = \phi^4 \hat{\gamma}_{ij}$. If $\hat{\gamma}_{ij}$ is the flat metric, γ_{ij} is called conformally flat. The forth power in the factor ϕ^4 is due to convention.

Therefore, permitting an unconstrained lapse function, shift vector and conformal factor, any spacetime which does not deviate too far from spherical symmetry, should be well approximated by the following four-metric:

$$g_{\mu\nu} = \begin{pmatrix} -\alpha^2 + \beta_i\beta^i & \beta_1 & \beta_2 & \beta_3 \\ \beta_1 & \phi^4 & 0 & 0 \\ \beta_2 & 0 & \phi^4 r^2 & 0 \\ \beta_3 & 0 & 0 & \phi^4 r^2 \sin^2\theta \end{pmatrix}. \tag{3.13}$$

As a consequence of that, the approximation (3.13) for the spacetime metric in a dynamic simulation of a rotational core collapse seems properly justified. Additionally, since all off-diagonal components of the three-metric are zero, this metric simplifies both the metric equations (3.7–3.10) as well as the hydrodynamic equations (2.25), in particular the expressions for the source terms.

Nevertheless, there are obvious limitations to the validity of approximating the exact spacetime by a conformally flat three-metric. An unstopped rotational core collapse proceeds towards a rotating Kerr black hole, for which the approximation would certainly break down: For a Kerr black hole, there exists no coordinate transformation of the Kerr spacetime solution to a conformally flat spacetime [44]. So whereas the exact spacetime even for a nonspherical rotating neutron star only slightly deviates from conformal flatness, a maximally rotating black hole violates conformal flatness considerably. Note however, that the CFC makes no explicit assumptions whether the spacetime is static or dynamic. Therefore we can assume that the deviation of the CFC metric from the exact metric is only determined by the instantaneous deviation of the matter from spherical symmetry; this conjecture is supported by tests, which we present in Section 6.6.

Another issue which needs special consideration is the inability of a conformally flat three-metric to describe the gravitational radiation content of spacetime. We have already mentioned that any spherically symmetric spacetime can be written in such a way that it obeys the CFC. However, due to Birkhoff's theorem, even dynamic matter distributions in spherical symmetry cannot emit gravitational radiation. Furthermore, in polar coordinates, the component γ_{23} of the metric can be identified in the far field with one of the two states of polarization of the gravitational waves radiated away by an isolated source. Gravitational waves are an invariant physical effect rather than a coordinate effect, and hence cannot be transformed away. Therefore, if all off-diagonal elements of the three-metric are zero like in (3.13), then the spacetime metric does not account for gravitational radiation[g]. Nevertheless, as numerical simulations [147] of rotational core collapse indicate that only about 10^{-6} of the total energy is converted to gravitational waves during the collapse, the above restriction is acceptable. But instead of computing gravitational waves directly, one has then to resort to an approximate calculation of the radiation, e.g. in some sort of post-processing step using the quadrupole formula, which is the first order term of the multipole expansion of gravitational radiation [124]. This method and its numerical implementation in our numerical code is explained in Appendix C.

---

[g] We emphasize that the CFC does not just mean "exact general relativity minus gravitational radiation". The CFC yields a spacetime with no gravitational radiation present, but additionally imposes more restrictions than that, as even spacetimes which do not radiate gravitational waves like the Kerr spacetime cannot be exactly described by a conformally flat metric.

The conformal treatment of spacetimes is a line of research in GR on its own: It has been first introduced by Penrose [97] to eliminate the blowing up of the physical metric at space-like infinity. There are many formulations of GR which are based upon this approach [41, 56, 39, 57]. Recently, a conformal treatment has been used to obtain long-term stable numerical evolutions, as described in [3]. On the other hand, there have also been numerous applications of conformally flat metric transformations, mostly in numerical techniques which aim towards obtaining initial data for binary black hole or neutron star evolutions, which are listed in [21].

The extension of the CFC to a numerical evolution scheme as an approximation of the full Einstein equations has first been used by Wilson et al. in 1996 [141][h]. In that work the CFC metric equations, which will be described in Section 3.3.3, have been derived. This new approximation scheme has been applied to computing a sequence of quasi-equilibrium configurations of two equal mass binary neutron stars, using the hydrodynamic evolution equations to obtain the equilibrium state with a relaxation technique. This sequence of orbits has also been used as an approximate estimate of the actual inspiralling motion of the binary system, which would have been obtained if the exact system of metric equations would have been evolved. The metric equations by Wilson et al. have then been used as a basis in other simulations: Cook et al. [22] have compared a sequence of single rapidly rotating neutron stars in equilibrium, and have found that in these cases the largest deviations of the CFC solution from the exact solution are less than 5%, and in general much less than that. Kley and Schäfer [64] have investigated the accuracy of the CFC approximation for rotating infinitesimally thin dust disks. Their comparisons show that the approximate solution is very accurate for moderate values of the central lapse function. For extremely relativistic configurations (with a central value of the lapse function which is much smaller than in any of our simulations), the agreement deteriorates for some of the metric function. The validity tests of the CFC metric in the context of rotational core collapse, which have been performed by us, also indicate that the CFC is a justified approximation for our applications (see Section 6.6).

In this thesis for the first time the coupled set of hydrodynamic and CFC metric equations is solved in a fully dynamic situation, the collapse of a rotating iron core to a neutron star[i]. Comparisons of results obtained by using the CFC with solutions in full general relativity or in the PPN formalism [141, 64, 22], although performed in the context of quasi-equilibrium situations, were very promising. This has motivated us to apply this approximation to the scenario of rotational core collapse.

---

[h] See [32, 79] for corrections.

[i] An approximation of the exact spacetime, which is related to the CFC approximation, was suggested for core collapse simulations by Cardall et al. [18]. The metric in this “Newton-Plus” approximation is the same as the CFC metric (3.13) with the additional requirement that all shift vector components are zero. As the CFC metric has three additional degrees of freedom compared to the Newton-Plus metric, it is a better approximation of the exact ADM metric (2.11). So far no results from numerical simulations of core collapse supernovae using the Newton-Plus formalism have been published.

3.3.2 Conformal Scaling

When one deals with conformal transformations between two metrics of the general form

$$\gamma_{ij} = \phi^4 \hat{\gamma}_{ij} \tag{3.14}$$

(here $\hat{\gamma}$ need not be conformally flat), it is interesting to investigate the transformation (i.e. the conformal scaling) behavior of scalar, vector, tensor, and other quantities associated with the three-metric.

For example, the Ricci scalar curvature scales like this[j]:

$$R = \frac{1}{\phi^4}\left(\hat{R} - \frac{8}{\phi}\hat{\Delta}\phi\right). \tag{3.15}$$

Here $\hat{\Delta}$ is the flat space Laplace operator, which in spherical polar coordinates reads

$$\hat{\Delta} = \frac{\partial^2}{\partial r^2} + \frac{2}{r}\frac{\partial}{\partial r} + \frac{1}{r^2}\frac{\partial^2}{\partial \theta^2} + \frac{\cot\theta}{r^2}\frac{\partial}{\partial\theta}. \tag{3.16}$$

Similarly, we get a rather simple transformation rule for the Christoffel symbols,

$$\mathit{\Gamma}^k_{ij} = \hat{\mathit{\Gamma}}^k_{ij} + \frac{2}{\phi}\left(\delta^k_i \hat{\nabla}_j \phi + \delta^k_j \hat{\nabla}_i \phi - \hat{\gamma}_{ij}\hat{\gamma}^{kl}\hat{\nabla}_l \phi\right), \tag{3.17}$$

which can be easily checked for the transformation between the flat and the conformally flat metric. These transformation rules can be directly derived from the definition of R and $\mathit{\Gamma}^k_{ij}$.

Another useful scaling property is the following one for the Laplacian of a scalar function α multiplied with the conformal factor ϕ:

$$\Delta(\alpha\phi) = \frac{1}{\phi^5}\left(\phi\hat{\Delta}(\alpha\phi) + 2\hat{\gamma}^{ij}\hat{\nabla}_i(\alpha\phi)\hat{\nabla}_j\phi\right). \tag{3.18}$$

This equation can also be rewritten as

$$\hat{\Delta}(\alpha\phi) = \phi^5\left(\Delta\alpha - \alpha\phi\Delta\phi^{-1}\right) = \phi^5\Delta\alpha + \alpha\hat{\Delta}\phi, \tag{3.19}$$

using the identity

$$\Delta(\alpha\phi) = \phi\Delta\alpha - \alpha\phi^2\Delta\phi^{-1} - \frac{2\hat{\gamma}^{ij}}{\phi^5}\hat{\nabla}_i(\alpha\phi)\hat{\nabla}_j\phi, \tag{3.20}$$

and Equation (3.18) applied to $\alpha = 1$:

$$\Delta\alpha = \Delta 1 = 0 = \frac{1}{\phi^5}\hat{\Delta}\phi + \phi\Delta\phi^{-1}. \tag{3.21}$$

Note that for any scalar function s the covariant derivative is independent of the metric:

$$\nabla_i s = \hat{\nabla}_i s. \tag{3.22}$$

---

[j] In the following, the quantities with a hat are computed using the metric $\hat{\gamma}_{ij}$.

For a tensor quantity like the extrinsic curvature K_{ij}, the transformation behavior is in no way trivial: Although the extrinsic curvature is a three-tensor, and its components are lowered and raised with the three-metric, its geometrical meaning has to be seen in relation to the four-metric, as the Lie derivative of the three-metric involves components of the four-metric. So one has to investigate how such a tensor, depending on four-vector components, transforms under a conformal scaling of the three-metric. As a first approach to this problem, we can make a definite statement about the behavior of the covariant derivative of K_{ij}: The momentum constraint (3.10), and therefore $\nabla_i K_{ij}$ and $\nabla_i K^{ij}$, should be invariant under a conformal transformation of the form (3.14). But how do covariant derivatives like the one of K_{ij} react to such a metric transformation?

A mathematically rigorous derivation of the transformation properties for such quantities can be found in the book by Wald [133]. Here we just summarize the most important aspects of conformal scaling. Let d be the dimension of the conformal metrics (in our case $d = 3$). We now assume that d-tensors T_{ij} and T^{ij} scale with a factor ϕ^{2s}:

$$T_{ij} = \phi^{2s}\hat{T}_{ij}, \qquad T^{ij} = \phi^{2s}\hat{T}^{ij}. \tag{3.23}$$

Then the covariant and contravariant derivatives of these tensors exhibit the following transformation behavior:

$$\begin{aligned}
\hat{\nabla}_i\hat{T}_{ij} &= \hat{\nabla}_i(\phi^{-2s}T_{ij}) = \phi^{-2s}\nabla_i T_{ij} + (s+d-2)\phi^{-2s+2}T_{ij}\nabla_i\phi^{-2},\\
\hat{\nabla}_i\hat{T}^{ij} &= \hat{\nabla}_i(\phi^{-2s}T^{ij}) = \phi^{-2s}\nabla_i T^{ij} + (s+d+2)\phi^{-2s+2}T^{ij}\nabla_i\phi^{-2},\\
\hat{\nabla}^i\hat{T}_{ij} &= \hat{\nabla}^i(\phi^{-2s}T_{ij}) = \phi^{-2s+4}\nabla^i T_{ij} + (s+d-4)\phi^{-2s+6}T_{ij}\nabla_i\phi^{-2},\\
\hat{\nabla}^i\hat{T}^{ij} &= \hat{\nabla}^i(\phi^{-2s}T^{ij}) = \phi^{-2s+4}\nabla^i T^{ij} + (s+d)\phi^{-2s+6}T^{ij}\nabla^i\phi^{-2}.
\end{aligned} \tag{3.24}$$

If we want the covariant and contravariant derivative of the tensors to be conformally invariant, then the terms on the right hand sides involving the derivative of the conformal factor ϕ must vanish. This yields values for s in each of the four cases in Equation (3.24):

$$\begin{array}{cccc}
\hat{\nabla}_i T_{ij}: & \hat{\nabla}_i T^{ij}: & \hat{\nabla}^i T_{ij}: & \hat{\nabla}^i T^{ij}: \\[1em]
s=-1 & s=-5 & s=+1 & s=-3 \\
\downarrow & \downarrow & \downarrow & \downarrow \\
T_{ij} = \phi^{-2}\hat{T}_{ij}, & T^{ij} = \phi^{-10}\hat{T}^{ij}, & T_{ij} = \phi^{2}\hat{T}_{ij}, & T^{ij} = \phi^{-6}\hat{T}^{ij}.
\end{array} \tag{3.25}$$

Thus, under the requirement that the momentum constraints have to be conformally invariant, the left two columns of Equation (3.25) yield the transformation behavior of the extrinsic curvature as follows:

$$K_{ij} = \frac{1}{\phi^2}\hat{K}_{ij}, \qquad K^{ij} = \frac{1}{\phi^{10}}\hat{K}^{ij}. \tag{3.26}$$

As we have already pointed out, for this derivation neither of the metrics γ and $\hat{\gamma}$ need to be flat. However, if $\hat{\gamma}$ is the flat metric in Cartesian coordinates, and $\gamma_{ij} = \phi^4\hat{\gamma}_{ij}$, then both all Christoffel symbols and the Ricci scalar vanish: $\hat{\Gamma}^k_{ij} = 0$, $\hat{R} = 0$. Note that for a flat metric in curvilinear coordinates, the Christoffel symbols $\hat{\Gamma}^k_{ij}$ are in general non-zero, but rather a combination of functions of the coordinates. However, the components of the Ricci tensor $\hat{R}_{ij}$ and thus its trace $\hat{R}$ are still zero, i.e. the equation for the conformal scaling of R in Equation (3.15) yields:

$$R = -\frac{8}{\phi^5}\hat{\Delta}\phi. \tag{3.27}$$

3.3.3 Derivation of the CFC Metric Equations

With the definition of the conformally flat three-metric from Section 3.3.1, and the knowledge of the transformation behavior of vectors and tensors under conformal transformations of the three-metric from Section 3.3.2, we can now proceed to investigate the consequences of the CFC on the hydrodynamic and metric equations. As already mentioned in Section 3.3.1, the hydrodynamic equations (2.25) will be simplified, as the characteristic fields and velocities (see Appendix A.2), the energy-momentum tensor (see Appendix B.1), and the four-metric Christoffel symbols (see Appendix B.2) will have a much simpler form. However, the form of the hydrodynamic equations, and particularly their conservative character, will remain unaffected.

This does not hold for the ADM metric equations (3.7–3.10). First of all, as already indicated in Section 3.3.1, we impose one of the usual gauge conditions on the lapse function, the so-called maximal slicing condition, which translates into a condition for the trace of the extrinsic curvature:

$$K = K^i_i = 0. \tag{3.28}$$

This gauge condition is widely used in numerical relativity, as it simplifies the ADM equations considerably.

Furthermore, in the following derivations we make frequent use of the square root of the trace of the three-metric and the four-metric. For a CFC metric, they have the following form:

$$\sqrt{\gamma} = \phi^6 r^2 \sin\theta, \qquad \sqrt{-g} = \alpha\sqrt{\gamma} = \alpha\phi^6 r^2 \sin\theta. \tag{3.29}$$

As we demand that the CFC is fulfilled not only initially but at all times, the time derivative of the trace-free parts of γ_{ij}, i.e. the off-diagonal components, have to vanish:

$$\gamma^{1/3}\frac{\partial}{\partial t}\frac{\gamma_{ij}}{\gamma^{1/3}} = 0. \tag{3.30}$$

With this requirement the evolution equation for the three-metric (3.7) yields a simple expression for the extrinsic curvature showing no explicit time dependence:

$$\begin{aligned} 0 = \gamma^{1/3}\partial_t(\gamma^{-1/3}\gamma_{ij}) &= \partial_t\gamma_{ij} - \frac{2}{3}\gamma_{ij}\partial_t \ln\gamma^{1/2} = \\ &= -2\alpha K_{ij} + \nabla_i\beta_j + \nabla_j\beta_i - \frac{2}{3}\gamma_{ij}\nabla_k\beta^k, \end{aligned} \tag{3.31}$$

where we have used the following relation for the trace of Equation (3.7),

$$\partial_t \ln\gamma^{1/2} = \frac{1}{2}\gamma^{ij}\partial_t\gamma_{ij} = -\alpha K^k_k + \nabla_k\beta^k = \nabla_k\beta^k, \tag{3.32}$$

together with the maximal slicing condition.

So in the end, the extrinsic curvature can be calculated from Equation (3.31) according to

$$K_{ij} = \frac{1}{2\alpha} \left(\nabla_i \beta_j + \nabla_j \beta_i - \frac{2}{3} \gamma_{ij} \nabla_k \beta^k \right). \tag{3.33}$$

Equation (3.32) together with Equation (3.29) yields a relation for the time derivative of the conformal factor ϕ, whose numerical usefulness will be examined in Section 5.5.1:

$$\nabla_k \beta^k = \partial_t \ln \sqrt{\gamma} = \frac{1}{\phi^6} \partial_t \phi^6 = \frac{6 \partial_t \phi}{\phi} \qquad \longrightarrow \qquad \partial_t \phi = \frac{\phi}{6} \nabla_k \beta^k. \tag{3.34}$$

Following Equation (3.17), the three-metric Christoffel symbols in the conformally flat metric can be calculated directly from the conformal factor ϕ, as the flat metric Christoffel symbols are time independent functions of the coordinates r and θ.

Now that we have shown how the conformal flatness condition, applied to the ADM evolution equation for γ_{ij} (3.7), affects (and simplifies) the expressions for three-metric quantities like the extrinsic curvature K_{ij} or the Christoffel symbols $\mathit{\Gamma}^k_{ij}$, we next discuss the influence of the CFC on the other ADM metric equations (3.8–3.10):

Hamiltonian constraint:

Using the transformation condition for the Ricci scalar of the conformally flat metric (3.27), the Hamiltonian constraint (3.7) can be written as

$$0 = R + K^2 - K_{ij} K^{ij} - 16\pi \alpha^2 T^{00} = -\frac{8}{\phi^5} \hat{\Delta} \phi - K_{ij} K^{ij} - 16\pi (\rho h W^2 - P). \tag{3.35}$$

From this follows an equation for the Laplacian of the conformal factor ϕ:

$$\hat{\Delta} \phi = -2\pi \phi^5 \left(\rho h W^2 - P + \frac{K_{ij} K^{ij}}{16\pi} \right). \tag{3.36}$$

Three-metric and extrinsic curvature evolution equations:

As a consequence of the maximal slicing condition (3.28), the time derivative of the trace of K_{ij} must vanish. Thus, the three-metric and extrinsic curvature evolution equations (3.7, 3.8) can be combined with the Hamiltonian constraint (3.9) in the following way:

$$\begin{aligned}
0 &= \partial_t K = \partial_t \left(\gamma^{ij} K_{ij} \right) = \gamma^{ij} \partial_t K_{ij} + K_{ij} \partial_t \gamma^{ij} = \\
&= \gamma^{ij} \Big[-\nabla_i \nabla_j \alpha + \alpha (R_{ij} + K K_{ij} - 2 K_{ik} K^k_j) + \beta^k \nabla_k K_{ij} + K_{ik} \nabla_j \beta^k + K_{jk} \nabla_i \beta^k - \\
&\quad - 8\pi\alpha \left(S_{ij} - \frac{\gamma_{ij}}{2} (S - \rho_{\mathrm{H}}) \right) \Big] + K_{ij} \left(-2\alpha K^{ij} + \nabla^i \beta_j + \nabla^j \beta^i \right) = \\
&= -\Delta\alpha + \alpha \left(R + K^2 - 2 K_{ij} K^{ij} \right) + \beta^k \nabla_k K + K_{ij} \nabla^i \beta^j + K_{ij} \nabla^j \beta^i - \\
&\quad - 8\pi\alpha \left(S - \frac{3}{2} (S - \rho_{\mathrm{H}}) \right) + K_{ij} \left(-2\alpha K^{ij} + \nabla^i \beta^j + \nabla^j \beta^i \right) = \\
&= -\Delta\alpha + \alpha R + 4\pi\alpha (S - 3\rho_{\mathrm{H}}) = 0.
\end{aligned} \tag{3.37}$$

Using the scaling relations for the Laplacian of a scalar function (3.19, 3.20), and the metric equation for ϕ (3.36) together with Equation (3.27), we can rewrite this as

$$\begin{aligned}
0 &= -\frac{1}{\phi^5}\left(\hat{\Delta}(\alpha\phi) - \alpha\hat{\Delta}\phi\right) - \frac{8\alpha}{\phi^5}\hat{\Delta}\phi + 4\pi\alpha(S - 3\rho_{\mathrm{H}}) = \\
&= -\frac{1}{\phi^5}\hat{\Delta}(\alpha\phi) + 14\pi\alpha\left(\rho h W^2 - P + \frac{K_{ij}K^{ij}}{16\pi}\right) + 4\pi\alpha(-2\rho h W^2 - \rho h + 6P) = \\
&= -\frac{1}{\phi^5}\hat{\Delta}(\alpha\phi) + 2\pi\alpha\left(3\rho h W^2 - 2\rho h + 5P + \frac{7K_{ij}K^{ij}}{16\pi}\right). \qquad (3.38)
\end{aligned}$$

Here we have used the ideal fluid expressions for S and ρ_{H} from Appendix B.1.

So we are left with an equation for the Laplacian of the lapse α scaled with the conformal factor ϕ:

$$\hat{\Delta}(\alpha\phi) = 2\pi\alpha\phi^5\left(\rho h(3W^2 - 2) + 5P + \frac{7K_{ij}K^{ij}}{16\pi}\right). \qquad (3.39)$$

Momentum constraint:

For a spatial three-metric obeying the CFC, the momentum constraint equation (3.10) yields an equation for the shift vector β^i. First we manipulate the momentum constraint in the following way, where the transformation properties of the extrinsic curvature according to Equation (3.26) play a crucial role:

$$\begin{aligned}
0 &= \nabla_i(K^{ij} - \gamma^{ij}K) - 8\pi S^j = \\
&= \frac{1}{\phi^{10}}\hat{\nabla}_i\left(\phi^{10}K^{ij}\right) - 8\pi S^j = \frac{1}{\phi^{10}}\hat{\nabla}_i\hat{K}^{ij} - 8\pi S^j = \\
&= \frac{1}{\phi^{10}}\hat{\nabla}_i\left[\frac{\phi^6}{2\alpha}\left(\hat{\nabla}^i\beta^j + \hat{\nabla}^j\beta^i - \frac{2\hat{\gamma}^{ij}}{3}\hat{\nabla}_k\beta^k\right)\right] - 8\pi S^j = \\
&= \frac{1}{2\alpha\phi^4}\left[\hat{\Delta}\beta^j + \hat{\nabla}^j\left(\frac{1}{3}\hat{\nabla}_k\beta^k\right) + \frac{\alpha}{\phi^6}\hat{\nabla}_i\left(\frac{\phi^6}{\alpha}\right)\left(\hat{\nabla}^i\beta^j + \hat{\nabla}^j\beta^i - \frac{2\hat{\gamma}^{ij}}{3}\hat{\nabla}_k\beta^k\right)\right] - 8\pi S^j = \\
&= \frac{1}{2\alpha\phi^4}\left[\hat{\Delta}\beta^j + \hat{\nabla}^j\left(\frac{1}{3}\hat{\nabla}_k\beta^k\right) + \frac{\alpha}{\phi^6}\hat{\nabla}_i\left(\frac{\phi^6}{\alpha}\right)\hat{K}^{ij}\right] - 8\pi S^j. \qquad (3.40)
\end{aligned}$$

Here we have used the abbreviation $\hat{\Delta}\beta^j \equiv \hat{\nabla}_i\hat{\nabla}^i\beta^j$.

Equation (3.40) then translates into a Laplace operator equation for the shift vector:

$$\hat{\Delta}\beta^i = 16\pi\alpha\phi^4 S^i + 2K^{ij}\hat{\nabla}_j\left(\frac{\alpha}{\phi^6}\right) - \frac{1}{3}\hat{\nabla}^i\hat{\nabla}_k\beta^k. \qquad (3.41)$$

In spherical axisymmetric coordinates, the quantity $\hat{\nabla}^i\hat{\nabla}_k\beta^k$ present in Equation (3.41) reads:

$$\begin{aligned}
\hat{\nabla}^i\hat{\nabla}_k\beta^k =& \left(\beta^1_{,rr} + \beta^2_{,r\theta} + \frac{2\beta^1_{,r}}{r} - \frac{2\beta^1}{r^2} + \cot\theta\beta^2_{,r} + \right. \\
&\left. + \frac{\beta^1_{,r\theta}}{r^2} + \frac{\beta^2_{,\theta\theta}}{r^2} + \frac{2\beta^1_{,\theta}}{r^3} + \frac{\cot\theta\beta^2_{,\theta}}{r^2} - \frac{\beta^2}{r^2\sin^2\theta}\right). \qquad (3.42)
\end{aligned}$$

We want to close this derivation of the metric equations for β^i by pointing out that in curvilinear coordinates in general $\hat{\Delta}\beta^j \neq (\hat{\Delta}\beta)^j$, because β^i is a three-vector which behaves not like a scalar with respect to covariant derivatives. For example, in spherical polar coordinates we have

$$\hat{\Delta}\beta^i \neq \frac{\partial^2 \beta^i}{\partial r^2} + \frac{2}{r}\frac{\partial \beta^i}{\partial r} + \frac{1}{r^2}\frac{\partial^2 \beta^i}{\partial \theta^2} + \frac{\cot\theta}{r^2}\frac{\partial \beta^i}{\partial \theta}. \tag{3.43}$$

Rather, the Laplacian of the shift vector obeys the following relations:

$$\begin{aligned}
\hat{\Delta}\beta^1 &= \frac{\partial^2 \beta^1}{\partial r^2} + \frac{2}{r}\frac{\partial \beta^1}{\partial r} + \frac{1}{r^2}\frac{\partial^2 \beta^1}{\partial \theta^2} + \frac{\cot\theta}{r^2}\frac{\partial \beta^1}{\partial \theta} - \frac{2\beta^1}{r^2} - \frac{2\cot\theta\beta^2}{r} - 2\frac{\partial \beta^2}{\partial \theta}, \\
\hat{\Delta}\beta^2 &= \frac{\partial^2 \beta^2}{\partial r^2} + \frac{4}{r}\frac{\partial \beta^2}{\partial r} + \frac{1}{r^2}\frac{\partial^2 \beta^2}{\partial \theta^2} + \frac{\cot\theta}{r^2}\frac{\partial \beta^2}{\partial \theta} - \frac{2}{r^3}\frac{\partial \beta^1}{\partial \theta} + \frac{(1-\cot\theta)\beta^2}{r^2}, \\
\hat{\Delta}\beta^3 &= \frac{\partial^2 \beta^3}{\partial r^2} + \frac{4}{r}\frac{\partial \beta^3}{\partial r} + \frac{1}{r^2}\frac{\partial^2 \beta^3}{\partial \theta^2} + \frac{3\cot\theta}{r^2}\frac{\partial \beta^3}{\partial \theta}.
\end{aligned} \tag{3.44}$$

The solution of the system of metric equations (3.52–3.54) involves the calculation of the extrinsic curvature components. They are given by a combination of metric components, and for (r, θ) coordinates in axisymmetry, the various components of K^{ij} read:

$$K^{11} = \frac{1}{3\alpha\phi^4}\left(2\beta^1_{,r} - \beta^2_{,\theta} - \frac{2\beta^1}{r} - \cot\theta\beta^2\right), \tag{3.45}$$

$$K^{12} = \frac{1}{2\alpha\phi^4}\left(\frac{\beta^1_{,\theta}}{r^2} + \beta^2_{,r}\right), \tag{3.46}$$

$$K^{13} = \frac{1}{2\alpha\phi^4}\beta^3_{,r}, \tag{3.47}$$

$$K^{22} = \frac{1}{3\alpha\phi^4 r^2}\left(-\beta^1_{,r} + 2\beta^2_{,\theta} + \frac{\beta^1}{r} - \cot\theta\beta^2\right), \tag{3.48}$$

$$K^{23} = \frac{1}{2\alpha\phi^4 r^2}\beta^3_{,\theta}, \tag{3.49}$$

$$K^{33} = \frac{1}{3\alpha\phi^4 r^2 \sin^2\theta}\left(-\beta^1_{,r} - \beta^2_{,\theta} + \frac{\beta^1}{r} + 2\cot\theta\beta^2\right). \tag{3.50}$$

The quantity $K^2 = K_{ij}K^{ij}$ used in the equations for ϕ and α is then given by:

$$\begin{aligned}
K_{ij}K^{ij} = \frac{1}{12\alpha^2}\Big[& 6\sin^2\theta(\beta^3_{,\theta})^2 + \frac{8}{r^2}(\beta^1)^2 + 8(\beta^2_{,\theta})^2 + 8(\beta^1_{,r})^2 + 6r^2(\beta^2_{,r})^2 + 6r^2\sin^2\theta(\beta^3_{,r})^2 - \\
& -8\cot\theta\beta^2_{,\theta}\beta^2 + \frac{8\cot\theta}{r}\beta^1\beta^2 - 8\cot\theta\beta^1_{,r}\beta^2 + 8\cot^2\theta(\beta^2)^2 + \frac{6}{r^2}(\beta^1_{,\theta})^2 - \\
& -\frac{16}{r}\beta^1_{,r}\beta^1 + \frac{8}{r}\beta^2_{,\theta}\beta^1 - 8\beta^1_{,r}\beta^2_{,\theta} + 12\beta^1_{,\theta}\beta^2_{,r}\Big].
\end{aligned} \tag{3.51}$$

3.3.4 Properties of the Elliptic System of Metric Equations

Collecting the metric equations (3.36, 3.39, 3.41) derived in Section 3.3.3, we get the following system of equations for the metric degrees of freedom for a conformally flat three-metric:

$$\hat{\Delta}\phi = -2\pi\phi^5 \left(\rho h W^2 - P + \frac{K_{ij}K^{ij}}{16\pi} \right), \tag{3.52}$$

$$\hat{\Delta}(\alpha\phi) = 2\pi\alpha\phi^5 \left(\rho h (3W^2 - 2) + 5P + \frac{7K_{ij}K^{ij}}{16\pi} \right), \tag{3.53}$$

$$\hat{\Delta}\beta^i = 16\pi\alpha\phi^4 S^i + 2K^{ij}\hat{\nabla}_j \left(\frac{\alpha}{\phi^6} \right) - \frac{1}{3}\hat{\nabla}^i\hat{\nabla}_k\beta^k. \tag{3.54}$$

These equations are five Poisson-like equations for the metric components ϕ, α, and β^i. However, while a system of genuine Poisson equations are linear and its equations independent of each other, the single equations (3.52, 3.53, 3.54) of the metric equation system couple to each other via their right hand sides, and in the case of the equations for β^i additionally via the operator $\hat{\Delta}$ acting on the vector β^i. The equations are dominated by the source terms involving the hydrodynamic quantities ρ, P, and v^i, whereas the nonlinear coupling through the other, purely metric, source terms becomes only important for strong gravity.

By approximating the three-metric by a conformally flat one, we have gained the following: The CFC reduces the complexity of solving the full set of Einstein evolution and constraint equations to solving five not explicitely time-dependent equations. Then on each time slice, the metric is solely determined by the instantaneous hydrodynamic state, i.e. the distribution of matter in space. Compared to the general system of evolution equations and metric equations, the number of terms involving time derivatives is reduced significantly. Therefore, the CFC approximation allows for more stable numerical evolution schemes. In our simulations we have never encountered severe problems with numerical instabilities (see Sections 6 and 7).

As already mentioned in Section 3.3.1, the CFC metric equations are equivalent to the Einstein equations in spherical symmetry (and imposing no symmetry restrictions, up to the first post-Newtonian approximation).

Chapter 4

Rotational Core Collapse

4.1 Physical Model

As indicated in Section 1.5, for supernova core collapse a combination of a state-of-the-art microphysical matter model including sophisticated neutrino transport, a fully dynamic general relativistic treatment of spacetime, plus a detailed and consistent initial model from stellar evolution, combined in a multi-dimensional simulation code without the assumption of symmetries is still beyond the scope of feasibility. Therefore, a numerical simulation of this problem can only cover parts of this complicated scenario. In order to reduce the complexity of the problem, we introduce several simplifications in our model:

Hydrodynamic approximation:

In order to justify the use of hydrodynamics to model supernova core collapse, two requirements must be satisfied [90]: First of all, the collisional mean free path λ of any particle has to be small compared to the characteristic macroscopic length scale L of the system. Then one can define a fluid volume element, whose linear dimensions are large compared to λ, but small compared to L. In Section 1.3 we have seen that this can be assumed for electrons, photons, and nucleons during all stages of the collapse. However, the neutrinos are not in equilibrium with the rest of the matter outside the neutrino sphere. For a correct description of the neutrino behavior, a transport scheme must be used. Nevertheless, if one only wants to study the collapse dynamics until the prompt shock stalls, i.e. in a phase where the neutrinos do not yet determine the dynamics of the system, the neutrinos can be completely neglected. The second criterion for the hydrodynamic approach is that the forces between the particles saturate. Then one can define an internal energy, and the pressure of the particles exerted on the walls of a fluid element can be described as an internal force, i.e. instead of being written as a source term, P can be included in the flux term. As a result of the hydrodynamic approximation, we can define a local EoS, which closes the hydrodynamic system of equations.

Equation of state:

Our matter model obeys an ideal gas EoS with the pressure P consisting of a polytropic and a thermal part as in Zwerger and Müller [147]:

$$P = P_{\mathrm{p}} + P_{\mathrm{th}}. \tag{4.1}$$

We neglect any other microphysics like electron capture or neutrino transport. The treatment of matter and its equation of state are discussed in detail in Section 4.2.

Initial model:

As initial configurations we have constructed rotating relativistic polytropic stellar cores in equilibrium [65, 66, 120]. These models are marginally stable, and the collapse is initiated by decreasing the adiabatic index. Our initial data solver allows us to construct both uniformly and differentially rotating polytropes (see Section 4.3).

So far the rotational state of the core prior to its gravitational collapse is not well known, as multi-dimensional evolutionary calculations of rotating stars have not yet been performed [90]. Up to now, only quasi-spherical progenitor models with a phenomenological description of mixing and angular momentum transport are available [51]. Thus, predictions from rotational core collapse rely upon extensive parameter studies, i.e. simulations with a large set of initial configurations. Due to this lack of a specific initial model, we have computed a comprehensive set of rotating polytropes with various rotation profiles and strengths as initial models.

Conformal flatness condition:

We numerically solve the fully general relativistic set of hydrodynamic equations. However, the metric equations are approximated by adopting the conformal flatness condition for the three-metric γ_{ij} (see Chapter 3). This results in a constrained system of elliptic metric equations. Due to the conformally flat three-metric, no gravitational waves are present in the system in the first place. The extraction of gravitational radiation is then done by post-processing the data via the quadrupole formula.

Symmetry assumptions:

The dimensionality of the problem is reduced by assuming both axisymmetry with respect to the rotation axis, and equatorial plane symmetry. The numerical code uses a spherical grid in (r, θ) coordinates with a logarithmic grid spacing in the r-direction, and constant grid spacing in the θ-direction. All derivatives with respect to the φ-direction vanish. We evolve only one quarter of the (r, θ) plane $(0 \leq \theta \leq \pi/2)$.

These assumptions are physically well motivated and do not impose unnecessary restrictions to the ability of our model to address the questions posed in Section 1.5. Simulating rotational core collapse with this model allows us to capture the important dynamics of all phases of the collapse until the prompt shock stalls, and to compute the gravitational wave signal resulting from the bulk motion of the core. According to the work of Zwerger [146], there is a strong correlation between the collapse dynamics, which may be strongly influenced by relativistic effects, and the gravitational wave signal. We are therfore convinced that including relativistic gravity in a rotational core collapse simulation, while imposing the above simplifications, will yield important results which are a basis to determine the parameters of the initial state and the collapse dynamics of the iron core in a core collapse supernova event from an observed gravitational wave signal (as described in Section 1.4).

4.2 Equation of State

For the initial model of a rotating iron core in equilibrium, the polytropic relation between the pressure P and the rest mass density ρ,

$$P = K\rho^{\gamma_{\text{ini}}}, \tag{4.2}$$

with $\gamma_{\text{ini}} = 4/3$ and $K = 4.8974894 \times 10^{14}$ (in cgs units) [146, 109], is a fair approximation of the density and pressure stratification. It is also consistent with the EoS of an iron core supported against gravity by relativistic leptons (see Section 1.3). Following along the path of practically all general relativistic hydrodynamic simulations, in the infall phase we assume the matter of the core to obey an ideal gas EoS for a compressible inviscid fluid,

$$P = (\gamma - 1)\rho\epsilon. \tag{4.3}$$

Note that during the collapse phase, which we initiate by lowering the adiabatic index γ_{ini} to γ to model the onset of instability in a real iron core by electron capture and photodissociation, the density profile of the fluid is still well described by the polytropic relation (4.2) (see Section 6.5).

In the bounce and shock propagation phases of the collapse scenario, the appropriate thermodynamic modeling of the fluid behavior becomes more complicated: A necessary condition for the polytropic relation (4.2) to hold is that no shocks are present. In the shock front, kinetic energy is dissipated into internal (thermal) energy. A polytropic EoS cannot account for this dissipation of kinetic energy, which contributes to the total pressure. In order to approximate this effect, we assume that the total pressure consists of a polytropic and a thermal part, $P = P_{\text{p}} + P_{\text{th}}$, where P_{p} mimics the pressure exerted by the degenerate electron gas, while P_{th} is due to a thermal distribution of ions [146].

The polytropic part, where

$$P_{\text{p}} = K\rho^{\gamma}, \tag{4.4}$$

still undergoes only adiabatic processes, for which we have:

$$d\epsilon_{\text{p}} = -P_{\text{p}} d\left(\frac{1}{\rho}\right) \quad \rightarrow \quad d\epsilon_{\text{p}} = \frac{P_{\text{p}}}{\rho^2} d\rho \quad \rightarrow \quad \epsilon_{\text{p}} = \frac{P_{\text{p}}}{\rho(\gamma - 1)}. \tag{4.5}$$

We now assume that the polytropic index γ jumps from γ_1 to γ_2 for densities larger than nuclear matter density ρ_{nuc}[a]; this approximates the effective stiffening of the EoS and the resulting increase in pressure at a density, where the matter composition changes and the proto-neutron star forms. Then by requiring the pressure and internal energy to be continuous at the transition density ρ_{nuc}, we get the following general solution for the polytropic internal energy:

$$\epsilon_{\text{p}} = \begin{cases} \dfrac{K}{\gamma_1 - 1}\rho^{\gamma_1 - 1} & \text{for } \rho \leq \rho_{\text{nuc}}, \\ \dfrac{K}{\gamma_2 - 1}\rho^{\gamma_2 - 1}\rho_{\text{nuc}}^{\gamma_1 - \gamma_2} + \dfrac{(\gamma_2 - \gamma_1)K}{(\gamma_2 - 1)(\gamma_1 - 1)}\rho_{\text{nuc}}^{\gamma_1 - 1} & \text{for } \rho > \rho_{\text{nuc}}. \end{cases} \tag{4.6}$$

---

[a] The values for γ_1 and γ_2, which we have used in our simulations, are given in Section 4.4.

The thermal part of the pressure, which is due to shock heating, is given by

$$P_{\mathrm{th}} = (\gamma_{\mathrm{th}} - 1)\rho\epsilon_{\mathrm{th}}, \tag{4.7}$$

where $\gamma_{\mathrm{th}} = 1.5$. This describes a mixture of relativistic ($\gamma = 4/3$) and nonrelativistic ($\gamma = 5/3$) components of an ideal fluid. The thermal internal energy can then be determined by

$$\epsilon_{\mathrm{th}} = \epsilon - \epsilon_{\mathrm{p}}. \tag{4.8}$$

From these equations, we can construct a single EoS for all densities, which is continuous at ρ_{nuc} for the total pressure P and the individual contributions P_{p} and P_{th}:

$$P = \left(K - (\gamma_{\mathrm{th}} - 1)\frac{K}{\gamma - 1}\right)\rho^{\gamma} + (\gamma_{\mathrm{th}} - 1)\rho\epsilon - \frac{(\gamma_{\mathrm{th}} - 1)(\gamma - \gamma_1)}{(\gamma_1 - 1)(\gamma_2 - 1)} K \rho_{\mathrm{nuc}}^{\gamma_1 - 1}\rho. \tag{4.9}$$

It is this equation which we employ as the EoS during all stages of the collapse.

The sound speed for this sum of polytropic and thermal pressure has the usual form of an ideal fluid, where the pressure terms simply add:

$$c_{\mathrm{s}}^2 = \frac{1}{h}\left(\chi + \kappa\frac{P}{\rho^2}\right) = \frac{\gamma P_{\mathrm{p}} + \gamma_{\mathrm{th}} P_{\mathrm{th}}}{\rho h}. \tag{4.10}$$

Here χ and κ are given by

$$\chi = \left.\frac{\partial P}{\partial \rho}\right|_{\epsilon}, \qquad \kappa = \left.\frac{\partial P}{\partial \epsilon}\right|_{\rho}. \tag{4.11}$$

As we have mentioned before, during the infall phase, where no shocks are present, the matter flow exhibits a polytropic profile. In practice this means for our hybrid EoS that the thermal part of the EoS does not contribute, and its associated pressure is therefore negligible. After shock formation, we expect the thermal pressure to rise as the shock front passes by. We will come back to this behavior of the pressure in Section 6.5.

Compared to the more conventional formulations based on purely polytropic or purely ideal fluid equations of state, our approach has the advantage that it represents the (already simplified) microphysics of the problem in a better way, while it keeps the hydrodynamic and metric equations simple.

4.3 Rotating Relativistic Stars in Equilibrium

From observations of supernova remnants and neutron stars one can infer that rotation may play a crucial role in the core collapse scenario [122]. However, as pointed out in Section 4.1, up to date there are no realistic models for the final evolutionary stages of a massive star, i.e. the progenitor of a core collapse supernova, which include rotation in a consistent way. Due to the lack of an initial model with a definite rotation state, we proceed along the lines of the previous Newtonian rotating core collapse simulations by Zwerger and Müller [147], who constructed a set of differentially rotating polytropes in equilibrium as pre-collapse iron core models.

While Zwerger and Müller have used Newtonian iron core models, our initial models are obtained from a consistent general relativistic method for solving the equilibrium equations for rotating polytropic matter distributions. The appropriate general metric to describe rotating axisymmetric relativistic matter configurations in equilibrium is

$$ds^2 = -e^{2\hat{\nu}}dt^2 + e^{2\hat{\alpha}}(dr^2 + r^2 d\theta^2) + e^{2\hat{\beta}} r^2 \sin^2\theta (d\phi - \omega dt)^2, \tag{4.12}$$

with the metric quantities $\hat{\nu}$, $\hat{\alpha}$, $\hat{\beta}$, and ω.

Note that this metric is not conformally flat. It has been shown [44] that the Kerr metric or any other equivalent metric which describes the spacetime of a rotating black hole (the limit a rotating matter configuration with infinite central density) cannot be written in a conformally flat way. This result also holds in general for any spacetime of a rotating star in equilibrium.

The only nonvanishing 3-velocity component is v^3, the velocity of the fluid as measured by a zero angular momentum observer (ZAMO). Thus the Lorentz factor is given by $W = 1/\sqrt{1 - v_3 v^3}$. With the definitions $u^0 = We^{-\hat{\nu}}$, and $u^3 = \Omega W e^{-\hat{\nu}}$, where Ω is the angular velocity of the fluid as measured from infinity, the four-velocity becomes:

$$u^\mu = \frac{W}{\hat{\alpha}}(1, 0, 0, \Omega). \tag{4.13}$$

Thus we get for the φ-component of the 3-velocity:

$$v^3 = \frac{u^3}{u^0 e^{\hat{\nu}}} - \frac{\omega}{e^{\hat{\nu}}} = e^{-\hat{\nu}}(\Omega - \omega); \quad v_3 = e^{2\hat{\beta} - \hat{\nu}} r^2 \sin^2\theta (\Omega - \omega); \quad v_\varphi \equiv \sqrt{v_3 v^3} = e^{\hat{\beta} - \hat{\nu}} r \sin\theta (\Omega - \omega). \tag{4.14}$$

Here v_φ is the proper rotation velocity with respect to the ZAMO. The specific angular momentum of the fluid $j \equiv u^0 u_3$ is given by

$$j = W^2 e^{2(\hat{\beta} - \hat{\nu})} r^2 \sin^2\theta (\Omega - \omega) = \frac{v_3 v^3}{(1 - v_3 v^3)(\Omega - \omega)}. \tag{4.15}$$

Using the Einstein equations we can derive the equation of hydrostatic equilibrium for a rotating mass distribution in axisymmetry, where the angular velocity Ω depends on r only:

$$\frac{\nabla P}{\rho h} + \nabla \hat{\nu} - \frac{v_\varphi}{1 - v_\varphi^2} \nabla v_\varphi + j \nabla \Omega = 0. \tag{4.16}$$

This is the relativistic generalization of the corresponding Newtonian equation

$$\frac{\nabla P}{\rho} + \nabla\Phi - v_\varphi \nabla v_\varphi + j\nabla\Omega = 0, \tag{4.17}$$

where Φ is the Newtonian gravitational potential, obeying Poisson's equation $\Delta\Phi = 4\pi\rho$.

We now specify a rotation law where j depends only on Ω (integrability condition):

$$j = A^2(\Omega - \Omega_\mathrm{c}), \tag{4.18}$$

where Ω_c is the value of Ω at the center, and A is a constant positive parameter. In the Newtonian approximation, the following rotation law follows from (4.18):

$$\Omega = \frac{\Omega_\mathrm{c}}{1 + \frac{d^2}{A^2}} = \begin{cases} \Omega_\mathrm{c} & \text{for } A \to \infty \quad \text{(rigid rotation)}, \\ \dfrac{A^2\Omega_\mathrm{c}}{d^2} & \text{for } A \to 0 \quad (j = -A^2\Omega_\mathrm{c} = \text{const.}). \end{cases} \tag{4.19}$$

with $d = r\sin\theta$ being the distance to the rotation axis.

With the use of the rotation law (4.18), we can integrate the equilibrium equation (4.16), and obtain:

$$\ln h + \hat{\nu} - \frac{1}{2}\ln(1 - v^2) + \frac{1}{2}A^2(\Omega - \Omega_\mathrm{c})^2 = \text{const.} \tag{4.20}$$

Again, this is the relativistic generalization of the Newtonian equation

$$h + \Phi + \frac{A^2\Omega_\mathrm{c}}{2\left(1 + \frac{d^2}{A^2}\right)} = \text{const.} \tag{4.21}$$

For the four-metric components $\hat{\alpha}$, $\gamma = \hat{\beta} + \hat{\nu}$, $\delta = \hat{\nu} - \hat{\beta}$ and ω we get 4 coupled partial differential equations [65]:

$$\Delta\delta e^{\gamma/2} = S_\delta, \tag{4.22}$$

$$\left(\Delta + \frac{1}{r}\partial_r - \frac{1}{r^2}\partial_\theta\right)\gamma e^{\gamma/2} = S_\gamma, \tag{4.23}$$

$$\left(\Delta + \frac{2}{r}\partial_r - \frac{2}{r^2}\partial_\theta\right)\omega e^{(\gamma-2\delta)2} = S_\omega, \tag{4.24}$$

$$\partial_\theta\hat{\alpha} = S_\mu, \tag{4.25}$$

where S_δ, S_γ, S_ω, and S_μ are source terms which in general depend on all four metric functions.

In order to solve the system of equations (4.22–4.25), the first three PDEs are converted from their differential form into an integral representation using a two-dimensional Green's function. The Green's function in then approximated by an expansion into Legendre polynomials. In discretized form, these equations are solved in an iterative scheme until convergence is obtained. During each iteration, the equation for $\hat{\alpha}$ is integrated.

4.4 Initial Models and Collapse Parameters

For a given adiabatic index γ_{ini}, the initial models, which are constructed by applying the HSCF method to solve the equilibrium equations for a rotating polytrope (see Section 5.2), are determined by three parameters, as described in Section 4.3: The central density $\rho_{\mathrm{c\,ini}}$, the degree of differential rotation A, and the rotation rate β_{ini}. In Section 1.3 we have stated that the central density of the iron core is about 10^{10} g cm^{-3}. We adopt this value for $\rho_{\mathrm{c\,ini}}$ in all initial models.

Due to the lack of a specific rotating iron core model from stellar evolution (see Section 4.1), we have chosen to follow Zwerger [146] and treat A and β as free parameters in computing the initial models. In accordance to that work, we use the values for A and β given in Table 4.1, and employ the same nomenclature.

Initial model	A [10^8 cm]	β_{ini} [%]	Model possible	Model used	Initial model	A [10^8 cm]	β_{ini} [%]	Model possible	Model used
A1B1	50.0	0.25	√	√	A3B1	0.5	0.25	√	√
A1B2	50.0	0.5	√	√	A3B2	0.5	0.5	√	√
A1B3	50.0	0.9	√	√	A3B3	0.5	0.9	√	√
A1B4	50.0	1.8	×	×	A3B4	0.5	1.8	√	√
A1B5	50.0	4.0	×	×	A3B5	0.5	4.0	√	√
A2B1	1.0	0.25	√	×	A4B1	0.1	0.25	√	√
A2B2	1.0	0.5	√	×	A4B2	0.1	0.5	√	√
A2B3	1.0	0.9	√	×	A4B3	0.1	0.9	√	×
A2B4	1.0	1.8	√	√	A4B4	0.1	1.8	√	√
A2B5	1.0	4.0	√	×	A4B5	0.1	4.0	√	√

Table 4.1: *Nomenclature of initial models and corresponding values for the free parameters. The parameter A quantifies the degree of differential rotation, and β_{ini} is the rotation rate. Note that the combination of parameters for models A1B4 and A1B5 are not possible, as these polytropes would rotate with more than the Kepler speed in the outer regions close to the equator, which would lead to mass shedding. We have selected 13 initial models from this set.*

With the initial models fixed, the only other free parameters in the collapse models are γ_1, the adiabatic index during the infall phase, and γ_2, the adiabatic index at supranuclear matter densities (see Section 4.2). As in [146], we set $\gamma_2 = 2.5$, which is inside the plausible limits for matter at supranuclear matter densities. The values for γ_1 are parameterized as $\{1.325, 1.320, 1.310, 1.300, 1.280\}$. In our simulations we have evolved the 26 models listed in Table 4.2[b]. One of the models (A3B2G4$_{\mathrm{soft}}$) was run with $\gamma_2 = 2.0$ for testing the influence of a softer supranuclear EoS on the collapse dynamics. The nuclear density is set to $\rho_{\mathrm{nuc}} = 2.0 \times 10^{14}$ g cm^{-3} in all simulations. Additionally to the models specified in Table 4.2, we use the model A3B4G3 for test purposes in Section 6.6.

---

[b] Note that not all initial models will collapse for any value of γ_1, as some are stabilized against infall by rotation even for $\gamma < \gamma_{\mathrm{ini}}$. We have not considered such models.

If $\rho_{\mathrm{c\,ini}}$, A, β_{ini}, γ_1, and γ_2 are specified for a particular collapse model, the evolution is completely determined by those parameters, provided that the numerical grid resolution, and the parameters which control the accuracy of the numerical scheme, are also fixed.

Collapse model	A [10^8cm]	β [%]	γ_1	γ_2
A1B1G1	50.0	0.25	1.325	2.5
A1B2G1	50.0	0.5	1.325	2.5
A1B3G1	50.0	0.9	1.325	2.5
A1B3G2	50.0	0.9	1.320	2.5
A1B3G3	50.0	0.9	1.310	2.5
A1B3G5	50.0	0.9	1.280	2.5
A2B4G1	1.0	1.8	1.325	2.5
A3B1G1	0.5	0.25	1.325	2.5
A3B2G1	0.5	0.5	1.325	2.5
A3B2G2	0.5	0.5	1.320	2.5
A3B2G4$_{\mathrm{soft}}$	0.5	0.5	1.300	2.0
A3B2G4	0.5	0.5	1.300	2.5
A3B3G1	0.5	0.9	1.325	2.5
A3B3G2	0.5	0.9	1.320	2.5
A3B3G3	0.5	0.9	1.310	2.5
A3B3G5	0.5	0.9	1.280	2.5
A3B4G2	0.5	1.8	1.320	2.5
A3B5G4	0.5	4.0	1.300	2.5
A4B1G1	0.1	0.25	1.325	2.5
A4B1G2	0.1	0.25	1.320	2.5
A4B2G2	0.1	0.5	1.320	2.5
A4B2G3	0.1	0.5	1.310	2.5
A4B4G4	0.1	1.8	1.300	2.5
A4B4G5	0.1	1.8	1.280	2.5
A4B5G4	0.1	4.0	1.300	2.5
A4B5G5	0.1	4.0	1.280	2.5

Table 4.2: *Nomenclature of collapse models, which have been simulated, and corresponding values for the initial model and collapse parameters. A is the degree of differential rotation,* β_{ini} *is the rotation rate,* γ_1 *is the adiabatic index at subnuclear densities, and* γ_2 *is the adiabatic index at supranuclear matter densities.*

Chapter 5

Numerical Implementation

5.1 Numerical Grid

5.1.1 Grid Setup – Logarithmic Radial Spacing

In computational fluid dynamics, and especially in numerical relativity, the choice of the coordinates and their adaption to the geometry of a given problem is of crucial importance. Since the early attempts of axisymmetric simulations of ideal fluids in general relativity over 20 years ago, the issue of coordinate problems has always been a challenge. At those times, due to insufficient computer power it was out of question to use a three-dimensional Cartesian grid to simulate axisymmetric problems. But even if this is now possible with modern computers, Cartesian coordinates are not well suited for such geometries as they do not exploit the existence of an azimuthal Killing vector, i.e. a rotational symmetry, to reduce the dimensionality of the problem to two dimensions.

For axisymmetric problems, both cylindrical and polar coordinates are suitable. These coordinate systems share a common disadvantage: The coordinate origin at the center $r = 0$, and for polar coordinates the rotation axis $\theta = 0$, are distinguished from the other coordinate points. Often the equations contain terms involving geometrical quantities like e.g. $\hat{\gamma}^{22} = r^{-1}$, which becomes infinite at the origin, or $\hat{\gamma}^{33} = r^{-1} \sin^{-1} \theta$, which becomes infinite at the axis. Thus the reduction of the problem from three to two dimensions is paid for by having to deal with coordinate pathologies due to singularities at specific points. This fact was the reason for the failure of axisymmetric relativistic ADM codes to provide long term stability [145, 28, 15]. Attempts to solve the axisymmetric problem are nowadays made by going towards three dimensions in Cartesian coordinates, now that larger and faster computers are available.

Still, polar coordinates are by definition the most appropriate ones for axisymmetric situations[a]. Thus we have chosen to use a polar grid, with special analytical and numerical

---

[a] Cylindrical coordinates, which are another obvious choice for axisymmetric problems, are not so well suited for our simulations, as we often use spherically symmetric matter configurations for tests purposes, which are much more precisely handled by polar coordinates.

precautions taken to avoid ill coordinate behavior close to the center and the axis. The setup of our (r, θ)-grid is as follows:

- As we have no azimuthal dependence for any variable, the coordinate φ never shows up explicitely. However, there are motions in the φ-direction, and the associated velocity v_3 and momentum S_3 are nonzero.
- For any meridional plane we assume symmetry with respect to the equator at $\theta = \pi/2$. Therefore, θ spans the interval between 0 and $\pi/2$. Within this range, the grid is equally spaced in θ, with θ_j denoting the cell centers $(1 \leq j \leq n_\theta)$.
- The radial grid points r_i run from the center to the outer boundary and are also located at cell centers. They are logarithmically spaced.
- Each cell (r_i, θ_j) is bounded by interfaces at $r_{i-\frac{1}{2}}$, $r_{i+\frac{1}{2}}$, $\theta_{j-\frac{1}{2}}$, and $\theta_{j+\frac{1}{2}}$.
- The spacing between two neighboring cell centers or interfaces in the θ-direction is $\Delta\theta = \theta_{j+1} - \theta_j = \theta_{j+\frac{1}{2}} - \theta_{j-\frac{1}{2}}$.
- The difference between cell centers in the r-direction is $\Delta r_{i+\frac{1}{2}} = r_{i+1} - r_i$, whereas the difference between radial interfaces is $\Delta r_i = r_{i+\frac{1}{2}} - r_{i-\frac{1}{2}}$. The logarithmic spacing translates into the following relation: $\Delta r_{i+\frac{1}{2}} / \Delta r_{i-\frac{1}{2}} = a_i$. The radial spacing of the three innermost cells is enlarged in order to increase the maximum possible time step; for $i > 3$, $a_i = \text{const.}$ Note that the radial distances from cell center to inner and outer interface are identical, i.e. $r_{i+\frac{1}{2}} - r_i = r_i - r_{i-\frac{1}{2}}$, but unless $a_i = 1$ we have $r_i - r_{i-\frac{1}{2}} \neq r_{i-\frac{1}{2}} - r_{i-1}$.

With this we have defined a grid of finite volume cells, where the cell centers and interfaces are located at points

$$\begin{array}{llll}
(r_i, \theta_j), & i = 1, \ldots, n_r, & j = 1, \ldots, n_\theta, & \text{cell centers,} \\
(r_{i+\frac{1}{2}}, \theta_i), & i = 0, \ldots, n_r, & j = 1, \ldots, n_\theta, & \text{radial interface points,} \\
(r_i, \theta_{j+\frac{1}{2}}), & i = 1, \ldots, n_r, & j = 0, \ldots, n_\theta, & \text{angular interface points,} \\
(r_{i+\frac{1}{2}}, \theta_{j+\frac{1}{2}}), & i = 0, \ldots, n_r, & j = 0, \ldots, n_\theta, & \text{cell corners.}
\end{array} \tag{5.1}$$

Here n_r and n_θ are the number of radial and angular grid points, respectively. Note that $r_{\frac{1}{2}} = 0$ is the origin, $r_{n_r+\frac{1}{2}} = R$ defines the outer boundary, $\theta_{\frac{1}{2}} = 0$ coincides with the rotation axis, and $\theta_{n_\theta+\frac{1}{2}} = 0$ denotes the equatorial plane. In the simulations of all models, we choose a resolution of $n_r = 200$ radial grid points, and $n_\theta = 30$ grid points for the numerical grid; this corresponds to an angular resolution of 3°. The radial differences Δr_i in the innermost cells are set to about 500 m, which fixes the logarithmic spacing factor a_i. This grid resolution is sufficient to resolve the important features of core collapse dynamics (see Section 6.7.2).

A sketch of the polar grid and the relation between cell centers and interfaces is shown in Figure 5.1.

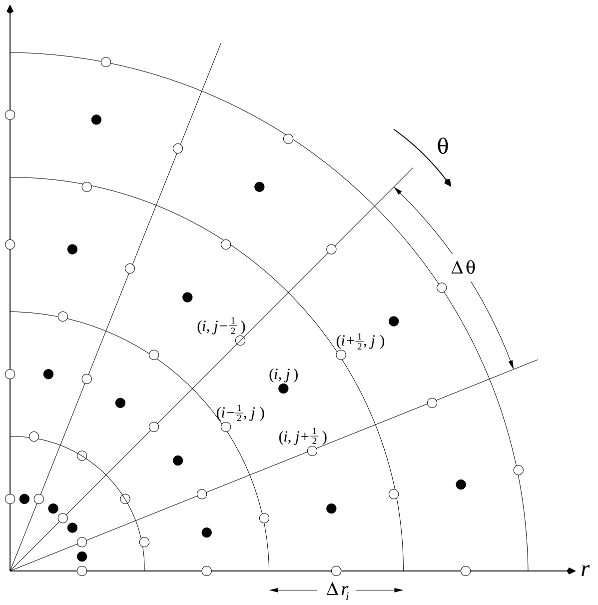

Figure 5.1: *The numerical grid in polar coordinates* (r, θ)*. The angular spacing* $\Delta\theta$ *is equidistant, while the radial one* Δr_i *is logarithmic. The hydrodynamic and metric quantities are assigned to cell centers (black circles), while the fluxes are assigned to cell interfaces (white circles).*

5.1.2 Symmetry Conditions

Due to the symmetry conditions stated in Section 5.1.1, we evolve only one quadrant of the actual spacetime domain. As a consequence of this, in the numerical code we have to impose symmetry conditions for both hydrodynamic and metric quantities across the center ($r = 0$), the rotation axis ($\theta = 0$), and the equatorial plane ($\theta = \pi/2$). The quantities, which have to be continued across the symmetry boundaries, are the hydrodynamic state variables ρ, v_i and ϵ, and the metric quantities ϕ, α and β^i[b]. Typically, a quantity is being mirrored either symmetrically or antisymmetrically across a symmetry boundary, depending on whether it should be continuous across the boundary, or zero at the boundary. We combine those two options in the following notation for a quantity $q_{i,j}$:

$$q_{-\frac{1}{2},j} = \pm_{\mathrm{c}} q_{\frac{1}{2},j}, \qquad q_{i,n_\theta+\frac{1}{2}} = \pm_{\mathrm{e}} q_{i,n_\theta-\frac{1}{2}}, \qquad q_{i,-\frac{1}{2}} = \pm_{\mathrm{p}} q_{i,\frac{1}{2}}, \tag{5.2}$$

where

$$\pm = \begin{cases} + & \text{symmetric,} \\ - & \text{antisymmetric,} \end{cases} \tag{5.3}$$

and the subscripts c, e, p refer to the center, equator, and pole, respectively.

The symmetry conditions for the scalar quantities ρ, ϵ, ϕ and α are trivial: Like their Newtonian counterparts ρ, ϵ and Φ they have to be continuous across all boundaries; thus the corresponding symmetry conditions are symmetric (+) at all boundaries. However, contrary to

---

[b] In the code, these symmetry conditions are implemented in the form of "ghost zones", which extent beyond the regular grid across the symmetry boundaries. These zones are needed in the reconstruction procedure for the calculation of the numerical fluxes, and in the metric solver (see Equation 5.88).

Newtonian hydrodynamics, the symmetry conditions for the vector quantities are nontrivial, as they occur both in covariant and contravariant form. We want to explain this with the following example: Consider the angular velocity v_3, which is a component of a covariant vector. Its contravariant form, which also occurs in the hydrodynamic equations, is $v^3 = \gamma^{33} v_3 = \phi^{-4} r^{-2} \sin^{-2}\theta v_3$. Obviously, the factor $r^{-1}\sin^{-1}$ in this expression changes sign at the rotation axis, and additionally becomes infinite at both the center and the axis. Then the question arises, whether a symmetry condition should be imposed on the covariant or the contravariant component of the velocity vector, and which one this should be. This problem can be resolved by defining “physical” velocities (the same can be done for the shift vector components β^i):

$$v_r = \sqrt{v_1 v^1} = \phi^{-2} v_1 = \phi^2 v^1, \tag{5.4}$$

$$v_\theta = \sqrt{v_2 v^2} = \phi^{-2} r^{-1} v_2 = \phi^2 r v^2, \tag{5.5}$$

$$v_\varphi = \sqrt{v_3 v^3} = \phi^{-2} r^{-1} \sin^{-1}\theta v_3 = \phi^2 r \sin\theta v^3. \tag{5.6}$$

As these velocities are bounded by the speed of light $c = 1$ $(0 \leq |v_r|, |v_\theta|, |v_\varphi| \leq 1)$, and directly occur up in the Lorentz factor, $W = 1/\sqrt{1 - v_r^2 - v_\theta^2 - v_\varphi^2}$, they can be regarded are the general relativistic analogue of the ordinary hydrodynamic velocities. For these velocities, we can then specify the usual symmetry conditions from Newtonian hydrodynamics. The symmetry conditions for covariant or contravariant components follow immediately from these conditions together with the symmetry behavior of the geometrical terms in the three-metric components γ_{ij} and γ^{ij}:

	v_r	v_θ	v_φ	v_1	v_2	v_3	β^1 v^1	β^2 v^2	β^3 v^3
center	$-$	$-$	$-$	$-$	?	?	$-$	$+$	$+$
pole	$+$	$-$	$-$	$+$	$-$	?	$+$	$-$	$+$
equator	$+$	$-$	$+$	$+$	$-$	$+$	$+$	$-$	$+$

(5.7)

For the symmetry conditions summarized in this table we have demanded that all velocities should vanish at the center (no mass flow across the center); additionally, the meridional velocity v_θ should be zero along the rotation axis and in the equatorial plane (no mass flow across these boundaries), and the azimuthal velocity v_φ should be zero along the rotation axis. These entries are set to $(-)$, all others, where the velocities are continuous, are set to $(+)$. The shift vector components β^i are treated according to the velocity vector components, as the shift vector corresponds to a “coordinate velocity”. An entry labeled with (?) states that the corresponding symmetry condition cannot be specified unambiguously with this method[c].

---

[c] In practice, the symmetry conditions are imposed on the “physical” velocities. Any covariant or contravariant components in the ghost zones are then calculated from these velocities by lowering or raising the index with the three-metric.

5.1.3 Boundary Conditions – Isotropic Schwarzschild Solution

As the computational grid covers only the part of the (in principle spatially infinite) spacetime up to the outer boundary at $r_{n_r+\frac{1}{2}}$, we have to impose boundary conditions for the hydrodynamic and metric quantities there[d]. In the case of hydrodynamic quantities, this is a trivial task: We simply extrapolate the interior values to the ghost zones.

The metric quantities cannot be extrapolated, as the elliptic equations for the metric define a boundary value problem. Here the boundary values are not given by the metric equations either a priori or during the solution process, but rather are free parameters which influence the solution of the equations. Therefore we have to determine the boundary conditions by matching the interior metric to an exterior spacetime metric. One possibility is to assume that the exterior spacetime is given by the Schwarzschild solution for a spherically symmetric vacuum spacetime. The quality of this approximation will be good enough for all practical purposes, if the spacetime at the boundary does not deviate too much from spherical symmetry. This is true for iron core initial data, and also holds for rotational core collapse, as the radius of the boundary is fixed at the initial iron core radius of about 1,500 km, while the radius of the (possibly highly nonspherical) neutron star is much smaller.

The usual Schwarzschild solution in vacuum in Schwarzschild coordinates $(t, \hat{r})$ has the line element

$$ds^2 = -\left(1 - \frac{2M_{\mathrm{grav}}}{\hat{r}}\right) dt + \frac{d\hat{r}}{1 - \frac{2M_{\mathrm{grav}}}{\hat{r}}} + \hat{r}^2 d\Omega^2. \tag{5.8}$$

However, this radial coordinate is inappropriate for matching this spacetime to the interior geometry, which uses an isotropic radial coordinate, i.e. one that has the same conformal factor in front of all three diagonal spatial metric components. Thus, in the exterior we introduce a new isotropic coordinate r as well, with

$$\hat{r} = r\left(1 + \frac{2M_{\mathrm{grav}}}{r}\right)^2 \qquad \longleftrightarrow \qquad r = \frac{1}{2}\left(\hat{r} - M_{\mathrm{grav}} + \sqrt{\hat{r}^2 - 2M_{\mathrm{grav}}\hat{r}}\right). \tag{5.9}$$

Then with

$$d\hat{r} = dr\left(1 + \frac{M_{\mathrm{grav}}}{2r}\right)\left[\left(1 + \frac{M_{\mathrm{grav}}}{2r}\right) - \frac{2M_{\mathrm{grav}}}{r}\right], \tag{5.10}$$

the line element in isotropic coordinates becomes

$$ds^2 = -\frac{\left(1 - \frac{M_{\mathrm{grav}}}{2r}\right)^2}{\left(1 + \frac{M_{\mathrm{grav}}}{2r}\right)^2} dt^2 + \left(1 + \frac{M_{\mathrm{grav}}}{2r}\right)^4 (dr^2 + r^2 d\Omega^2). \tag{5.11}$$

For a vanishing shift vector, this metric can be exactly matched to the conformally flat interior metric (3.12):

$$\alpha = \frac{\left(1 - \frac{M_{\mathrm{grav}}}{2r}\right)}{\left(1 + \frac{M_{\mathrm{grav}}}{2r}\right)}, \qquad \phi = 1 + \frac{M_{\mathrm{grav}}}{2r}, \qquad \beta^i = 0. \tag{5.12}$$

---

[d] As for the symmetry conditions, the boundary conditions are in practice established by ghost zones.

As the gravitational mass $M_{\rm grav}$ is conserved (see also Section 6.4), and as β^i is close to zero at the outer boundary[e], we choose to employ the matching to the isotropic Schwarzschild metric as an outer boundary condition for the metric coefficients α, ϕ and β^i.

However, we point out that these boundary conditions are only an approximation to the exact vacuum spacetime solution, since no rotating spacetime can be described by a conformally flat metric (see Section 3.3.1). By matching the interior spacetime to the spherically symmetric isotropic Schwarzschild solution, we neglect effects like frame dragging ($\beta^3 \neq 0$), which would in general be present in the vacuum spacetime region outside the computational domain. Still, such effects or the deviation from spherical symmetry are only significant for extremely relativistic and rapidly rotating configurations. Still, a natural improvement of this boundary condition would be to use the values from the initial data solver at the outer boundary as boundary conditions. This would definitely give better boundary conditions at least for spacetimes which are highly relativistic and nonspherical even at the boundary, like the one for a rapidly rotating neutron star on a grid, whose boundary is close to the neutron star radius.

---

[e] Note that the metric components g_{0i} are zero in the isotropic Schwarzschild metric.

5.2 Hachisu's Self-Consistent Field Method

Hachisu's self-consistent field (HSCF) method [65, 66] for relativistic stars is a numerical method to iteratively solve the equilibrium equations for a rotating relativistic polytrope (4.15, 4.18, 4.20, 4.22–4.25)[f]. The only free parameters of this method are ρ_c (central density), $r_\mathrm{p}/r_\mathrm{e}$ (ratio of equatorial to polar radius) and A (rotation law parameter). In the following, we briefly summarize this method.

One starts with a spherically symmetric constant density distribution (interior Schwarzschild solution). This solution is then iterated until the equilibrium equations are satisfied. To obtain the correct shape of the rotating star, the equilibrium equation (4.20) and the rotation law (4.18) are evaluated at three points: P, the outer boundary of the star at the polar axis; W, the point with the maximum density in the equatorial plane; and Q, the outer boundary of the star in the equatorial plane. Using a Newton–Raphson method, the quantities $\Omega(\mathrm{P})$, $\Omega(\mathrm{W})$, $\Omega(\mathrm{Q})$, Ω_c, r_e and the r.h.s. integration constant of (4.20) are computed for a given metric, which is then recalculated. This iteration is repeated until convergence. For a different choice of the three points P, W and Q, one can also obtain toroidal rotating matter configurations in equilibrium.

As we have already pointed out, the metric for a rotating relativistic star in equilibrium cannot be written in a conformally flat way. Thus, in order to match the initial data obtained with the HSCF method, which uses the metric (4.12), to the conformally flat metric (3.12), we apply the approximation $\hat{\alpha} = \hat{\beta}$[g]. By virtue of this assumption, the metric (4.12) becomes conformally flat, and its components relate to the CFC metric components as follows:

$$\alpha = e^{\hat{\nu}/2}, \qquad \phi = e^{\hat{\alpha}/2} = e^{\hat{\beta}/2}, \qquad \beta^3 = -\omega. \tag{5.13}$$

The error arising from this approximation is only a few percent even for rapidly and differentially rotating (and therefore strongly deformed) neutron star models (see Section 6.2).

Finally, we map the initial models obtained with the HSCF method onto the grid which we use in the evolution code (see Section 5.1.1). As the initial data solver uses an equidistant grid with a Schwarzschild-like radial coordinate $\hat{r}$ (a generalization of the one in Equation (5.9) to non-vacuum spacetimes) and an angular coordinate $\mu = \cos\theta$, this mapping procedure, which involves interpolation of both hydrodynamic and metric quantities, introduces additional numerical errors. However, this has no negative influence on the ability of the evolution code to maintain stability of e.g. a rotating iron core or neutron star in equilibrium (see Section 6.2).

---

[f] The HSCF method is the relativistic extension of the self-consistent field method for stars in Newtonian gravity described in [49]. Other, older methods for obtaining equilibrium configurations can be found for Newtonian rotating polytropic models in [26], for Newtonian neutron star models in [40], and for relativistic homogenous bodies in [17]. A recent improvement of the HSCF method is the RNS code [120], which uses a compactified radial coordinate to cover the entire spacetime.

[g] As this approximation is equivalent to assuming conformal flatness for the metric of the rotating star, its range of validity is the same as for the CFC metric (3.13) used in the dynamic evolution.

5.3 Atmosphere Treatment at the Surface of the Star

One common problem of many hydrodynamic codes is their inability to handle regions where the density is zero (or very small compared to the typical densities in the system). However, polytropic density distributions in stellar models have the property that the density has a very sharp drop at the boundary of the star; this fall-off actually defines the stellar surface. For spherically symmetric stars, this rapid drop in density does not result in numerical problems as the exterior boundary of the grid can always be put at a radius where the density is sufficiently large to be properly handled by the numerical scheme.

On the other hand, in multidimensional simulations, particularly for strongly rotating matter configurations, the deformed stellar surface does not coincide with a coordinate line of the computational grid. For rapidly rotating neutron stars in equilibrium [65, 120, 119], the axis ratio (i.e. the ratio between polar and equatorial radius) can be as low as 0.7. Putting the boundary of the numerical grid at a fixed radius within the star will cut off a large portion of the star in the vicinity of the equator. Defining the boundary of the grid at the maximum grid radius (which is outside the stellar matter) will also not help, as in those parts of the grid the density is zero, and the hydrodynamic scheme is destined to fail.

$f_{\mathrm{atm\,thr}}$	f_{atm}	EoS	v^i
10^{-5}	10^{-5}	$P = K\rho_{\mathrm{atm}}^{\gamma}$	0

Table 5.1: *Parameters for the low density atmosphere model in our core collapse simulations.* $f_{\mathrm{atm\,thr}}$ *has a value between* 5×10^{-4} *and* 1×10^{-4} *for the extremely differentially rotating models A4.*

As a remedy for this we introduce a low density atmosphere outside the stellar matter distribution. In practice we choose a matter model for the atmosphere which is given in Table 5.1. An atmosphere will be assumed in all regions where the density ρ is below a threshold of some fraction $f_{\mathrm{atm\,thr}}$ in the maximum density of the initial matter distribution prior to collapse:

$$\rho_{\mathrm{atm\,thr}} = f_{\mathrm{atm\,thr}}\rho_{\mathrm{max\,ini}}. \tag{5.14}$$

The density ρ_{atm} of the atmosphere is again a fraction f_{atm} of $\rho_{\mathrm{atm\,thr}}$ (which gives additional flexibility by e.g. setting the atmosphere density to a lower value than the threshold density, which defines the stellar surface):

$$\rho_{\mathrm{atm}} = f_{\mathrm{atm}}\rho_{\mathrm{atm\,thr}}. \tag{5.15}$$

This atmosphere is not only set up initially, but also reset after each evolution step in the simulation. This ensures that the region covered by the atmosphere adapts automatically to the collapse dynamics, as the “shape” of the matter distribution may change during the evolution. However, in practice it turns out that the shape of the atmosphere region will not change much.

For the values specified in Table 5.1 and an initial maximum density $\rho_{\mathrm{max\,ini}} = 10^{10}$ g cm^{-3}, this translates into a homogenous atmosphere with a density $\rho_{\mathrm{atm}} = 1$ g cm^{-3} obeying a polytropic EoS. For all practical purposes this can be considered as a low density atmosphere, which has no influence on the dynamics of the core collapse. The only tradeoff is a slight loss of angular momentum to the atmosphere from regions of the star which are close to the boundary (see Section 6.4).

Figure 5.2 shows density profiles at the equator and along the polar axis for a differentially rotating neutron star. The neutron star's parameters are listed in Table 6.2 in Section 6.2, and it possesses an axis ratio of 0.7. Beyond its surface, the neutron star is surrounded by a low density atmosphere of the type described above.

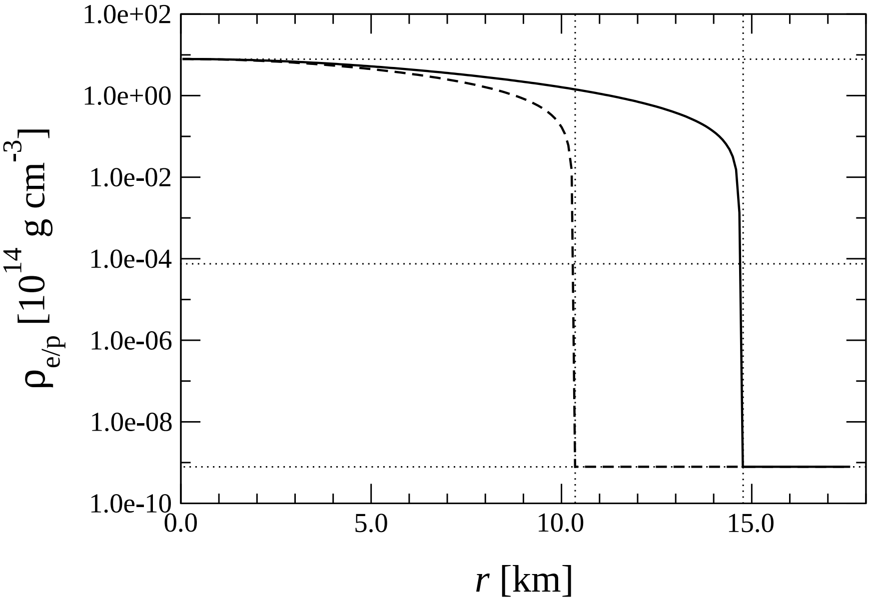

Figure 5.2: *Profiles of the equatorial density* ρ_{e} *(solid line) and polar density* ρ_{p} *(dashed line) for a rapidly rotating neutron star model in equilibrium: Due to its rapid rotation, its polar radius* $R_{\mathrm{p}} \approx 10.4$ km *is only 70% of its equatorial radius* $R_{\mathrm{e}} \approx 14.8$ km *(indicated by the vertical dotted lines). The neutron star is surrounded by an artificial low density atmosphere. The horizontal lines specify (from top to bottom) the central density* $\rho_{\mathrm{c}} \approx 7.9 \times 10^{14}$ g cm^{-3}*, the threshold density* $\rho_{\mathrm{atm\,thr}} = f_{\mathrm{atm\,thr}} \rho_{\mathrm{c}}$*, and the atmosphere density* $\rho_{\mathrm{atm}} = f_{\mathrm{atm}} \rho_{\mathrm{atm\,thr}}$.

5.4 High-Resolution Shock-Capturing Methods

Whereas Section 2.3 was devoted to an introduction of the general relativistic Riemann problem and the spectral decomposition of the Jacobi matrices (2.38) of the hyperbolic conservation laws (2.25), we will now apply these concepts to construct numerical algorithms for solving the evolution equations.

Many modern computational codes which simulate gas dynamics rely upon Godunov type methods. In such codes the evolution equations for the hydrodynamics are discretized in finite volumes, which are bounded by cell interfaces. The hydrodynamic quantities at the cell centers represent the corresponding average value within the cell. An interpolation method is used to construct values at cell interfaces from these cell centered mean quantities. From those reconstructed quantities, the numerical fluxes through the cell boundaries are computed, which then, together with the source terms, determine the time evolution of the cell averaged quantities. The evolution is propagated forward in time by solving local Riemann problems at each cell interface. The maximum numerical time step is limited by the criterion that waves propagating from neighboring cells must not interfere with one another, i.e. that characteristics originating from the cell interfaces do not cross within one time step.

A numerical implementation based upon the solution of local Riemann problems is called high-resolution shock-capturing (HRSC) scheme. Unlike finite difference codes which have problems with weak solutions of the evolution equations containing shocks, the fact that HRSC schemes are based on (exactly or approximately) solving discontinuous Riemann problems results in the ability to capture shocks accurately and resolve them within only a few grid points. Additionally, such methods guarantee, when written in conservation form, the convergence of the numerical solution to the physical solution of the problem, and the correct propagation speeds of discontinuities.

In general the solution of a Riemann problem can contain shock waves (where all hydrodynamic quantities are discontinuous), contact discontinuities (where some hydrodynamic quantities are discontinuous), and rarefaction waves (where all hydrodynamic quantities are continuous) between states where the quantities are constant. A solution of the Riemann problem which contains all three of these features is shown schematically in the top part of Figure 5.3. In the bottom part of that figure the representation of the smooth physical solution by the piecewise constant numerical quantities in grid cells, which define the local Riemann problems, is demonstrated.

The solution of the local Riemann problem depends on the fluxes of density, momentum, and energy which cross the cell interfaces. Therefore, it is important to numerically approximate these fluxes as accurately as possible. First we have to specify how the values of the hydrodynamic quantities at the left (L) and right (R) side of the cell interfaces,

$$q^{\mathrm{L}}_{i-\frac{1}{2},j}, \quad q^{\mathrm{R}}_{i+\frac{1}{2},j}, \qquad \text{in } r\text{-direction}, \tag{5.16}$$

$$q^{\mathrm{L}}_{i,j-\frac{1}{2}}, \quad q^{\mathrm{R}}_{i,j+\frac{1}{2}}, \qquad \text{in } \theta\text{-direction}, \tag{5.17}$$

are reconstructed from the corresponding cell averages $q_{i,j}$, which are defined at cell centers. Note that all components of the state vector (2.22) and the primitive variables have to recon-

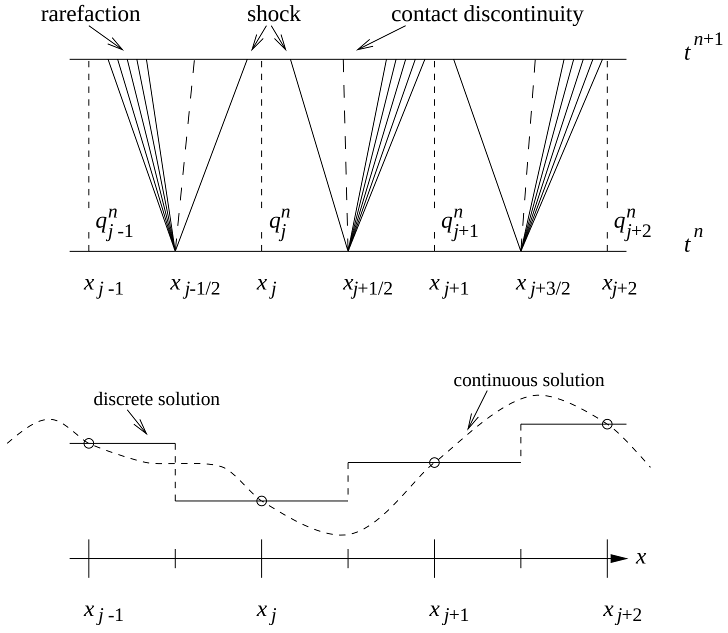

Figure 5.3: *Riemann problems in numerical hydrodynamics: The representation of a continuous solution by a discrete solution is shown in the lower panel. The discrete states* q_i^n *define a series of Riemann problems. The analytic solutions to this class of problems admit shocks, rarefaction waves, and contact discontinuities (upper panel). (Figure reproduced by courtesy of J.A. Font.)*

structed at the interfaces.

The simplest way of reconstruction is to assume constant functions within a zone, which means that the zone interface values are set equal to the values $q_{i,j}$ at the cell centers. This piecewise constant reconstruction, which is only first order accurate in space, was originally proposed by Godunov in 1959 [45] in the development of his exact Riemann solver.

Higher order reconstruction methods were gradually introduced, including second order accurate MUSCL (monotonic upstream schemes for conservation laws [129]), or third order accurate PHM (piecewise hyperbolic methods) and PPM (piecewise parabolic methods [19]), and their respective derivatives. Higher order schemes include methods to detect and sharpen discontinuities, or monotonize numerical artifacts in the post-shock flow. Common to them is that they try to reproduce the physical profiles of the quantities by the numerical reconstruction at the cell interfaces as accurately as possible without introducing numerically unstable features. The key property in these methods to accomplish this is to require monotonicity, which avoids local maxima; this again suppresses the growth of unphysical numerical high frequency oscillations [68].

In our code we have implemented Godunov, MUSCL, and PPM type reconstruction. Except in accuracy tests, however (see Section 6.1), for our simulations we only use PPM reconstruction due to its superior numerical accuracy compared to lower order reconstruction methods.

We can obtain the numerical flux from the reconstructed values at the interfaces computed according to the above methods, together with the characteristic information from the Riemann problem. This is demonstrated in the following. As expressed in the conservation equations (2.25), any change in a state variable is completely determined by the flux through the cell boundaries (and additional sources). This is reflected by this numerical scheme, and owing to this property the HRSC methods are called *flux conservative*.

5.4.1 Approximate Solvers for the Riemann Problem – The Numerical Flux

When nonlinear hyperbolic evolution equations – like the general relativistic hydrodynamic equations – are simply discretized according to some straightforward finite difference scheme, it is unavoidable that either the solution is diffused considerably at discontinuities (in first order methods), or that spurious numerical oscillations develop behind shock fronts (in second order schemes). To damp out such unwanted oscillations in those conventional evolution schemes, artificial viscosity terms are introduced in the equations to "break" their hyperbolic character. This concept was first put forward by von Neumann and Richtmyer [132]. The additional effective "viscosity" term is particularly aimed at damping out high frequency oscillations while (ideally) not affecting flows with small wave numbers. As it is not present in the original evolution equations, it is called "artificial". This purely numerical construct stabilizes the evolution behavior of computational codes by preventing post-shock oscillations at the prize of smearing out shocks fronts across several grid zones. Another disadvantage of this approach is that the amount of artificial viscosity needed is usually problem and resolution dependent. For the particular case of the relativistic hydrodynamic equations, artificial viscosity schemes have severe problems when entering the ultrarelativistic regime [94]. Recent developments in this direction for non-grid-based schemes such as SPH are given in [115].

Conservative codes, which are based on high-resolution shock-capturing schemes for finite volume methods, do not need such artificial viscosity terms. In these schemes the wave structure of the system is used to compute the numerical fluxes through the interfaces and to solve the exact or approximate Riemann problem. There are numerous ways for constructing the numerical fluxes (like Roe, HLLE, Shu and Osher's ENO solvers, etc., for an overview see [126]) which all involve characteristic information from the structure of the Riemann problem. We have chosen to adopt the numerical flux introduced recently by Donat and Marquina [24], which is called *Marquina flux* for short.

Like many flux construction methods this method involves the averaging of state variables left and right of the interface. The characteristic information is contained in a term called *numerical viscosity*. This viscosity term is a result of the characteristic information of the hyperbolic system of conservation laws, and automatically adds as much viscosity to the evolution scheme as necessary. Contrary to artificial viscosity, this numerical viscosity needs no adjustable parameters and is in general considerably smaller.

The Marqunia flux is based upon Roe's formulation of the numerical flux [103] (which is introduced below), and has improved features where the Roe flux produces pathological behavior [24].

Roe flux formula:

In this formulation the numerical flux at cell interfaces in r- and θ-direction is given as the average of the reconstructed fluxes left ($\boldsymbol{F}^{\mathrm{L}}$) and right ($\boldsymbol{F}^{\mathrm{R}}$) of the interface plus the numerical viscosity term:

$$\boldsymbol{F}^1 = \frac{1}{2}\left(\boldsymbol{F}^{1\,\mathrm{R}} + \boldsymbol{F}^{1\,\mathrm{L}} - \sum_{k=1}^{5} \tilde{\boldsymbol{r}}_k^1 |\tilde{\lambda}_k^1| \tilde{\alpha}_k^1\right), \tag{5.18}$$

$$\boldsymbol{F}^2 = \frac{1}{2}\left(\boldsymbol{F}^{2\,\mathrm{R}} + \boldsymbol{F}^{2\,\mathrm{L}} - \sum_{k=1}^{5} \tilde{\boldsymbol{r}}_k^2 |\tilde{\lambda}_k^2| \tilde{\alpha}_k^2\right). \tag{5.19}$$

All quantities with a tilde depend on the "Roe mean", which is some function f of the left and right states of the state vector $\boldsymbol{F}^0$ at the interface: $\tilde{\boldsymbol{F}}^0 = f(\boldsymbol{F}^{0\,\mathrm{L}}, \boldsymbol{F}^{0\,\mathrm{R}})$.

In Equations (5.18, 5.19), $\tilde{\lambda}_k^l$ are the five eigenvalues (2.39, 2.40) of the Jacobi matrices (2.38) as numbered in Equation (A.13), and $\tilde{\boldsymbol{r}}_k^l$ are the five right eigenvectors (A.6, A.8) as numbered in Equation (A.12). The superscript $l = 1, 2$ denotes the r- and θ-direction, respectively. Note that the fluxes in the r- and θ direction are defined at the corresponding interfaces:

$$\boldsymbol{F}^1 = \boldsymbol{F}^1_{i+\frac{1}{2},j}\left(\boldsymbol{F}^{0\,\mathrm{L}}_{i+\frac{1}{2},j}, \boldsymbol{F}^{0\,\mathrm{R}}_{i+\frac{1}{2},j}\right), \qquad \boldsymbol{F}^2 = \boldsymbol{F}^2_{i,j+\frac{1}{2}}\left(\boldsymbol{F}^{0\,\mathrm{L}}_{i,j+\frac{1}{2}}, \boldsymbol{F}^{0\,\mathrm{R}}_{i,j+\frac{1}{2}}\right). \tag{5.20}$$

The quantities $\tilde{\alpha}_k^l$ are called wave strengths, and are defined implicitly as

$$\boldsymbol{F}^{0\,\mathrm{R}} - \boldsymbol{F}^{0\,\mathrm{L}} = \sum_{k=1}^{5} \tilde{\alpha}_k^1 \tilde{\boldsymbol{r}}_k^1, \qquad \boldsymbol{F}^{0\,\mathrm{R}} - \boldsymbol{F}^{0\,\mathrm{L}} = \sum_{k=1}^{5} \tilde{\alpha}_k^2 \tilde{\boldsymbol{r}}_k^2. \tag{5.21}$$

If the hyperbolic system is locally linear, then the Jacobi matrices are constant, and the matrix of right eigenvectors can be inverted: $\boldsymbol{L} = \boldsymbol{R}^{-1}$. As a consequence of such a property of the Riemann problem, the wave strengths can be written as

$$\tilde{\alpha}_k^1 = \tilde{\boldsymbol{l}}_k^1\left(\boldsymbol{F}^{0\,\mathrm{R}} - \boldsymbol{F}^{0\,\mathrm{L}}\right), \qquad \tilde{\alpha}_k^2 = \tilde{\boldsymbol{l}}_k^2\left(\boldsymbol{F}^{0\,\mathrm{R}} - \boldsymbol{F}^{0\,\mathrm{L}}\right), \tag{5.22}$$

and can thus be calculated analytically in a rather simple way.

Marquina flux formula:

This improved flux formula has a structure which is very similar to Roe's flux formula (5.18, 5.19), but differs in the numerical viscosity term, which does not depend on "Roe averaged" reconstructed state vector quantities, but rather has a clear split into left and right states:

$$\boldsymbol{F}^1 = \frac{1}{2}\left(\boldsymbol{F}^{1\,\mathrm{R}} + \boldsymbol{F}^{1\,\mathrm{L}} - \sum_{k=1}^{5}\left(\boldsymbol{r}_k^{1\,\mathrm{R}}|\lambda_k^1|_{\max}\alpha_k^{1\,\mathrm{R}} - \boldsymbol{r}_k^{1\,\mathrm{L}}|\lambda_k^1|_{\max}\alpha_k^{1\,\mathrm{R}}\right)\right), \tag{5.23}$$

$$\boldsymbol{F}^2 = \frac{1}{2}\left(\boldsymbol{F}^{2\,\mathrm{R}} + \boldsymbol{F}^{2\,\mathrm{L}} - \sum_{k=1}^{5}\left(\boldsymbol{r}_k^{2\,\mathrm{R}}|\lambda_k^2|_{\max}\alpha_k^{2\,\mathrm{R}} - \boldsymbol{r}_k^{2\,\mathrm{L}}|\lambda_k^2|_{\max}\alpha_k^{2\,\mathrm{R}}\right)\right). \tag{5.24}$$

Here the function $|x|_{\max}$ is the maximum of the right and left reconstructed values of a quantity x: $|x|_{\max} = \max\left(x^{\mathrm{R}}, x^{\mathrm{L}}\right)$.

If we again assume that the system is linear and thus the Jacobi matrices are constant, we can invert the matrix of right eigenvectors. We define the wave strengths as

$$\alpha_k^{1\,\mathrm{L}} = \boldsymbol{l}_k^{1\,\mathrm{L}}\boldsymbol{F}^{0\,\mathrm{L}}, \quad \alpha_k^{1\,\mathrm{R}} = \boldsymbol{l}_k^{1\,\mathrm{R}}\boldsymbol{F}^{0\,\mathrm{R}}, \qquad \alpha_k^{2\,\mathrm{L}} = \boldsymbol{l}_k^{2\,\mathrm{L}}\boldsymbol{F}^{0\,\mathrm{L}}, \quad \alpha_k^{2\,\mathrm{R}} = \boldsymbol{l}_k^{2\,\mathrm{R}}\boldsymbol{F}^{0\,\mathrm{R}}, \tag{5.25}$$

and rewrite the flux formula as

$$\boldsymbol{F}^1 = \frac{1}{2}\left(\boldsymbol{F}^{1\,\mathrm{R}} + \boldsymbol{F}^{1\,\mathrm{L}} - \Delta\boldsymbol{q}^1\right), \tag{5.26}$$

$$\boldsymbol{F}^2 = \frac{1}{2}\left(\boldsymbol{F}^{2\,\mathrm{R}} + \boldsymbol{F}^{2\,\mathrm{L}} - \Delta\boldsymbol{q}^2\right), \tag{5.27}$$

where the numerical viscosity vector $\Delta\boldsymbol{q}^l$ can be written as the difference of the products of the right eigenvector matrix, the diagonal eigenvalue matrix, the left eigenvector matrix, and the state vector, evaluated right and left of the interface:

$$\Delta\boldsymbol{q}^l = \boldsymbol{q}^{l\,\mathrm{R}} - \boldsymbol{q}^{l\,\mathrm{L}} = \boldsymbol{R}^{l\,\mathrm{R}}\left|\boldsymbol{\Lambda}^{l\,\mathrm{R}}\right|_{\max}\boldsymbol{L}^{l\,\mathrm{R}}\boldsymbol{F}^{0\,\mathrm{R}} - \boldsymbol{R}^{l\,\mathrm{L}}\left|\boldsymbol{\Lambda}^{l\,\mathrm{L}}\right|_{\max}\boldsymbol{L}^{l\,\mathrm{L}}\boldsymbol{F}^{0\,\mathrm{L}}. \tag{5.28}$$

The analytic expressions for the right and left eigenvectors in r- and θ-direction are given in Appendix A.2. Using these equations, the numerical Marquina flux terms can be calculated in a straight-forward and computationally inexpensive way.

We want to close this introduction to approximate solvers with a short reflection on the justification of the use of approximate Riemann solvers. In Section 2.3 we have especially emphasized the fact that the hydrodynamic evolution equations are nonlinear. However, approximate Riemann solvers are based on Jacobi matrices which are assumed to be locally constant. This assumption does not neglect the nonlinearity of the hyperbolic conservation laws, as the equations are linearized *locally*. This is similar to the linearization of equations in a numerical discretization scheme, where the solution of an arbitrary analytic equation is approximated by a locally linear function. Indeed, as suggested by Donat and Marquina [24], one can assume that the discretization of the analytic equations, and the reconstruction process at the cell interfaces already leads to some local loss of nonlinear information, so that the use of an approximate instead of an exact numerical Riemann solver will probably not have a significant impact on the accuracy of the numerical solution. Then the clear advantage of an approximate Riemann solver in terms of considerable savings in computational effort is decisive for choosing this method in the calculation of the numerical flux.

5.5 Iteration Scheme – Discretization of the Evolution Equations

5.5.1 Time Evolution of the Conserved Quantities

To integrate the hydrodynamic evolution equations (2.25) forward in time, we have implemented a Runge–Kutta multi-step scheme for the discretized equations. In general, we have to integrate a system with the following structure:

$$\frac{\partial\sqrt{\gamma}\boldsymbol{F}^0}{\partial t}+\frac{\partial\sqrt{-g}\boldsymbol{F}^1}{\partial r}+\frac{\partial\sqrt{-g}\boldsymbol{F}^2}{\partial\theta}-\sqrt{-g}\boldsymbol{Q}=0. \quad (5.29)$$

This can be transformed into two analytically equivalent forms,

$$\frac{\partial\boldsymbol{F}^0}{\partial t}+\frac{\partial(\alpha\boldsymbol{F}^1)}{\partial r}+\frac{\partial(\alpha\boldsymbol{F}^2)}{\partial\theta}+\alpha\left(\boldsymbol{F}^0\frac{\partial\ln\sqrt{\gamma}}{\alpha\partial t}+\boldsymbol{F}^1\frac{\partial\ln\sqrt{\gamma}}{\partial r}+\boldsymbol{F}^2\frac{\partial\ln\sqrt{\gamma}}{\partial\theta}-\boldsymbol{Q}\right)=$$
$$\frac{\partial\boldsymbol{F}^0}{\partial t}+\frac{\partial\tilde{\boldsymbol{F}}^1}{\partial r}+\frac{\partial\tilde{\boldsymbol{F}}^2}{\partial\theta}+\alpha\tilde{\boldsymbol{Q}}=0, \quad (5.30)$$

or,

$$\frac{\partial\boldsymbol{F}^0}{\partial t}+\frac{1}{\sqrt{\gamma}}\frac{\partial(\alpha\sqrt{\gamma}\boldsymbol{F}^1)}{\partial r}+\frac{1}{\sqrt{\gamma}}\frac{\partial(\alpha\sqrt{\gamma}\boldsymbol{F}^2)}{\partial\theta}+\alpha\left(\boldsymbol{F}^0\frac{\partial\ln\sqrt{\gamma}}{\alpha\partial t}-\boldsymbol{Q}\right)=$$
$$\frac{\partial\boldsymbol{F}^0}{\partial t}+\frac{1}{\sqrt{\gamma}}\frac{\partial\hat{\boldsymbol{F}}^1}{\partial r}+\frac{1}{\sqrt{\gamma}}\frac{\partial\hat{\boldsymbol{F}}^2}{\partial\theta}-\alpha\hat{\boldsymbol{Q}}=0, \quad (5.31)$$

where the spatial derivatives of $\ln\sqrt{\gamma}$ are given by

$$\partial_r\ln\sqrt{\gamma}=\frac{4}{\phi}\frac{\partial\phi}{\partial r}+\frac{2}{r}, \qquad \partial_\theta\ln\sqrt{\gamma}=\frac{4}{\phi}\frac{\partial\phi}{\partial\theta}+\cos\theta. \quad (5.32)$$

Note that for a CFC metric, we can rewrite $\partial_t\sqrt{\gamma}$ in a form without any explicit time dependence by virtue of Equation (3.34). In the above equations, we have made use of the definitions $\tilde{\boldsymbol{F}}=\alpha\boldsymbol{F}$ and $\hat{\boldsymbol{F}}=\alpha\sqrt{\gamma}\boldsymbol{F}$, and have grouped the source terms in $\tilde{\boldsymbol{Q}}$ and $\hat{\boldsymbol{Q}}$.

Both forms differ in the sense that expression (5.30) contains more source terms compared to expression (5.31)[h]. These source terms stem effectively from the coordinate choice and the above algebraic conversion of the conservation equations, and do not emanate from actual physical processes. The additional source terms act like ficticious forces (e.g. like a Coriolis force term) on the system[i]. This can lead to numerical inaccuracies, as these forces tend to

---

[h] Note that the fluxes in both expression (5.29) and expression (5.30) are written in divergence form. However, this is not immediately apparent in this form of writing the equations, as the appropriate geometrical terms involving r and θ are hidden in $\sqrt{\gamma}$ and the covariant form of the fluxes.

[i] We point out that such source terms as in Equation (5.30) do not contain derivatives of the evolved (or primitive) hydrodynamic quantities, contrary to earlier non-conservative formulations of the relativistic hydrodynamic equations (c.f. Wilson [137]). For Cartesian coordinates and Minkowski spacetime, in our formulation the derivatives of geometrical terms in the sources $\tilde{\boldsymbol{Q}}$ vanish.

spoil the conservative character of HRSC schemes. More on that issue can be found at then end of this section and in Section 6.4.

The standard method to integrate forward in time such a system of equations, where the data are stored only on one time slice (contrary to e.g. staggered leap frog schemes), are Runge–Kutta integration schemes of various orders. There are different numerical implementations of these schemes like the midpoint method, or the Heun (or modified trapezoidal) method [1, 100]. We have chosen to use a scheme which was constructed by Shu and Osher [113]. It has a Courant number of 1[j] and is total variation diminishing (TVD – for further discussion of this property, see [50]). For an evolution equation of the form

$$\frac{\partial f}{\partial t} = g(f), \tag{5.33}$$

where the function f is defined as f^n and f^{n+1} at the old and new time slice with a time difference of Δt^n, the scheme has the following implementation:

$$\left.\begin{aligned} \overset{(1)}{f}{}^{n+1} &= f^n + \Delta t^n\, g(f^n), \\ f^{n+1} &= \frac{1}{2}\left(f^n + \overset{(1)}{f}{}^{n+1} + \Delta t^n\, g(\overset{(1)}{f}{}^{n+1})\right), \end{aligned}\right\} \qquad \text{2nd order} \tag{5.34}$$

$$\left.\begin{aligned} \overset{(1)}{f}{}^{n+1} &= f^n + \Delta t^n\, g(f^n), \\ \overset{(2)}{f}{}^{n+1} &= \frac{1}{4}\left(3f^n + \overset{(1)}{f}{}^{n+1} + \Delta t^n\, g(\overset{(1)}{f}{}^{n+1})\right), \\ f^{n+1} &= \frac{1}{3}\left(f^n + 2\overset{(2)}{f}{}^{n+1} + 2\Delta t^n\, g(\overset{(2)}{f}{}^{n+1})\right). \end{aligned}\right\} \qquad \text{3rd order} \tag{5.35}$$

In the time evolution we use quantities which are defined at a specified time t^n at cell centers ($q^n_{i,j}$), and cell interfaces with respect to the r-direction ($q^n_{i+\frac{1}{2},j}$) and to the θ-direction ($q^n_{i,j+\frac{1}{2}}$).

The metric quantities ϕ, α and β^i are needed and defined both at cell centers and at cell interfaces:

$$\begin{array}{ccccccc} \phi^n_{i,j}, & \alpha^n_{i,j}, & \beta^{1\,n}_{i,j}, & \beta^{1\,n}_{i,j}, & \beta^{1\,n}_{i,j}, & \sqrt{\gamma^n_{i,j}}, & \hat{g}^n_{i,j}, \\ \phi^n_{i+\frac{1}{2},j}, & \alpha^n_{i+\frac{1}{2},j}, & \beta^{1\,n}_{i+\frac{1}{2},j}, & \beta^{1\,n}_{i+\frac{1}{2},j}, & \beta^{1\,n}_{i+\frac{1}{2},j}, & \sqrt{\gamma^n_{i+\frac{1}{2},j}}, & \hat{g}^n_{i+\frac{1}{2},j}, \\ \phi^n_{i,j+\frac{1}{2}}, & \alpha^n_{i,j+\frac{1}{2}}, & \beta^{1\,n}_{i,j+\frac{1}{2}}, & \beta^{1\,n}_{i,j+\frac{1}{2}}, & \beta^{1\,n}_{i,j+\frac{1}{2}}, & \sqrt{\gamma^n_{i,j+\frac{1}{2}}}, & \hat{g}^n_{i,j+\frac{1}{2}}, \end{array} \tag{5.36}$$

where $\hat{g} \equiv \sqrt{-g}$, $\gamma = \phi^4 r^2 \sin\theta$, and $-g = \alpha\phi^4 r^2 \sin\theta$.

---

[j] This value for the Courant number can be derived mathematically. However, in most practical numerical applications, the actual Courant number used in the calculation of the time step has to be reduced in order to ensure numerical stability.

The discretized state vector quantities,

$$\boldsymbol{F}^{0\,n}_{i,j} = \begin{pmatrix} D^n_{i,j} \\ S^n_{1\,i,j} \\ S^n_{2\,i,j} \\ S^n_{3\,i,j} \\ \tau^n_{i,j} \end{pmatrix}, \tag{5.37}$$

and the discretized source vectors of Equations (5.30) and 5.31),

$$\tilde{\boldsymbol{Q}}^n_{i,j} = \begin{pmatrix} -D^n_{i,j}\dfrac{\partial \ln\sqrt{\gamma}}{\alpha\partial t} - D^n_{i,j}\hat{v}^1\dfrac{\partial \ln\sqrt{\gamma}}{\alpha\partial r} - D^n_{i,j}\hat{v}^2\dfrac{\partial \ln\sqrt{\gamma}}{\alpha\partial\theta} \\ Q^n_{2\,i,j} - S^n_{1\,i,j}\dfrac{\partial \ln\sqrt{\gamma}}{\alpha\partial t} - (S^n_{1\,i,j}\hat{v}^1 + P)\dfrac{\partial \ln\sqrt{\gamma}}{\alpha\partial r} - S^n_{1,i,j}\hat{v}^2\dfrac{\partial \ln\sqrt{\gamma}}{\alpha\partial\theta} \\ Q^n_{3\,i,j} - S^n_{2\,i,j}\dfrac{\partial \ln\sqrt{\gamma}}{\alpha\partial t} - S^n_{2\,i,j}\hat{v}^1\dfrac{\partial \ln\sqrt{\gamma}}{\alpha\partial r} - (S^n_{2\,i,j}\hat{v}^2 + P)\dfrac{\partial \ln\sqrt{\gamma}}{\alpha\partial\theta} \\ Q^n_{4\,i,j} - S^n_{3\,i,j}\dfrac{\partial \ln\sqrt{\gamma}}{\alpha\partial t} - S^n_{3\,i,j}\hat{v}^1\dfrac{\partial \ln\sqrt{\gamma}}{\alpha\partial r} - S^n_{3\,i,j}\hat{v}^2\dfrac{\partial \ln\sqrt{\gamma}}{\alpha\partial\theta} \\ Q^n_{5\,i,j} - \tau^n_{i,j}\dfrac{\partial \ln\sqrt{\gamma}}{\alpha\partial t} - (\tau^n_{i,j}\hat{v}^1 + Pv^1)\dfrac{\partial \ln\sqrt{\gamma}}{\alpha\partial r} - (\tau^n_{i,j}\hat{v}^2 + Pv^2)\dfrac{\partial \ln\sqrt{\gamma}}{\alpha\partial\theta} \end{pmatrix}, \tag{5.38}$$

$$\hat{\boldsymbol{Q}}^n_{i,j} = \begin{pmatrix} -D^n_{i,j}\dfrac{\partial \ln\sqrt{\gamma}}{\alpha\partial t} \\ Q^n_{2\,i,j} - S^n_{1\,i,j}\dfrac{\partial \ln\sqrt{\gamma}}{\alpha\partial t} \\ Q^n_{3\,i,j} - S^n_{2\,i,j}\dfrac{\partial \ln\sqrt{\gamma}}{\alpha\partial t} \\ Q^n_{4\,i,j} - S^n_{3\,i,j}\dfrac{\partial \ln\sqrt{\gamma}}{\alpha\partial t} \\ Q^n_{5\,i,j} - \tau^n_{i,j}\dfrac{\partial \ln\sqrt{\gamma}}{\alpha\partial t} \end{pmatrix}, \tag{5.39}$$

are defined at cell centers, while the numerical fluxes in the r- and θ-direction are composed of flux differences at the respective cell interfaces plus the numerical viscosity vector $\boldsymbol{V}$. The explicit form for the numerical flux difference $\Delta\tilde{\boldsymbol{F}}$ in Equation (5.30), and $\Delta\hat{\boldsymbol{F}}$ in Equation (5.31) are as follows:

$$\Delta\tilde{\boldsymbol{F}}^{1\,n}_{i,j} = \begin{pmatrix} \alpha^n_{i+\frac12,j}\bar{D}^n_{i+\frac12,j}\;\bar{\hat{v}}^{1\,n}_{i+\frac12,j} - \alpha^n_{i-\frac12,j}\bar{D}^n_{i-\frac12,j}\;\bar{\hat{v}}^{1\,n}_{i-\frac12,j} \\ \alpha^n_{i+\frac12,j}(\bar{S}^n_{1\,i+\frac12,j}\;\bar{\hat{v}}^{1\,n}_{i+\frac12,j} + \bar{P}^n_{i+\frac12,j}) - \alpha^n_{i-\frac12,j}(\bar{S}^n_{1\,i-\frac12,j}\;\bar{\hat{v}}^{1\,n}_{i-\frac12,j} + \bar{P}^n_{i-\frac12,j}) \\ \alpha^n_{i+\frac12,j}\bar{S}^n_{2\,i+\frac12,j}\;\bar{\hat{v}}^{1\,n}_{i+\frac12,j} - \alpha^n_{i-\frac12,j}\bar{S}^n_{2\,i-\frac12,j}\;\bar{\hat{v}}^{1\,n}_{i-\frac12,j} \\ \alpha^n_{i+\frac12,j}\bar{S}^n_{3\,i+\frac12,j}\;\bar{\hat{v}}^{1\,n}_{i+\frac12,j} - \alpha^n_{i-\frac12,j}\bar{S}^n_{3\,i-\frac12,j}\;\bar{\hat{v}}^{1\,n}_{i-\frac12,j} \\ \alpha^n_{i+\frac12,j}(\bar{\tau}^n_{i+\frac12,j}\;\bar{\hat{v}}^{1\,n}_{i+\frac12,j} + \bar{P}^n_{i+\frac12,j}\bar{v}^{1\,n}_{i+\frac12,j}) - \alpha^n_{i-\frac12,j}(\bar{\tau}^n_{i-\frac12,j}\;\bar{\hat{v}}^{1\,n}_{i-\frac12,j} + \bar{P}^n_{i-\frac12,j}\bar{v}^{1\,n}_{i-\frac12,j}) \end{pmatrix} + \Delta\tilde{\boldsymbol{V}}^{1\,n}_{i,j}, \tag{5.40}$$

$$\Delta\tilde{\boldsymbol{F}}^{2\,n}_{i,j} = \begin{pmatrix} \alpha^n_{i,j+\frac12}\bar{D}^n_{i,j+\frac12}\;\bar{\hat{v}}^{2\,n}_{i,j+\frac12} - \alpha^n_{i,j-\frac12}\bar{D}^n_{i,j-\frac12}\;\bar{\hat{v}}^{2\,n}_{i,j-\frac12} \\ \alpha^n_{i,j+\frac12}\bar{S}^n_{1\,i,j+\frac12}\;\bar{\hat{v}}^{2\,n}_{i,j+\frac12} - \alpha^n_{i,j-\frac12}\bar{S}^n_{1\,i,j-\frac12}\;\bar{\hat{v}}^{2\,n}_{i,j-\frac12} \\ \alpha^n_{i,j+\frac12}(\bar{S}^n_{2\,i,j+\frac12}\;\bar{\hat{v}}^{2\,n}_{i,j+\frac12} + \bar{P}^n_{i+\frac12,j+\frac12}) - \alpha^n_{i,j-\frac12}(\bar{S}^n_{2\,i,j-\frac12}\;\bar{\hat{v}}^{2\,n}_{i,j-\frac12} + \bar{P}^n_{i-\frac12,j-\frac12}) \\ \alpha^n_{i,j+\frac12}\bar{S}^n_{3\,i,j+\frac12}\;\bar{\hat{v}}^{2\,n}_{i,j+\frac12} - \alpha^n_{i,j-\frac12}\bar{S}^n_{3\,i,j-\frac12}\;\bar{\hat{v}}^{2\,n}_{i,j-\frac12} \\ \alpha^n_{i,j+\frac12}(\bar{\tau}^n_{i,j+\frac12}\;\bar{\hat{v}}^{2\,n}_{i,j+\frac12} + \bar{P}^n_{i,j+\frac12}\bar{v}^{2\,n}_{i,j+\frac12}) - \alpha^n_{i,j-\frac12}(\bar{\tau}^n_{i,j-\frac12}\;\bar{\hat{v}}^{2\,n}_{i,j-\frac12} + \bar{P}^n_{i,j-\frac12}\bar{v}^{2\,n}_{i,j-\frac12}) \end{pmatrix} + \Delta\tilde{\boldsymbol{V}}^{2\,n}_{i,j}. \tag{5.41}$$

$$\Delta\hat{\boldsymbol{F}}^{1\,n}_{i,j} = \begin{pmatrix} \hat{g}^n_{i,j+\frac12}\bar{D}^n_{i+\frac12,j}\;\bar{\hat{v}}^{1\,n}_{i+\frac12,j} - \hat{g}^n_{i,j-\frac12}\bar{D}^n_{i-\frac12,j}\;\bar{\hat{v}}^{1\,n}_{i-\frac12,j} \\ \hat{g}^n_{i,j+\frac12}(\bar{S}^n_{1\,i+\frac12,j}\;\bar{\hat{v}}^{1\,n}_{i+\frac12,j} + \bar{P}^n_{i+\frac12,j}) - \hat{g}^n_{i,j-\frac12}(\bar{S}^n_{1\,i-\frac12,j}\;\bar{\hat{v}}^{1\,n}_{i-\frac12,j} + \bar{P}^n_{i-\frac12,j}) \\ \hat{g}^n_{i,j+\frac12}\bar{S}^n_{2\,i+\frac12,j}\;\bar{\hat{v}}^{1\,n}_{i+\frac12,j} - \hat{g}^n_{i,j-\frac12}\bar{S}^n_{2\,i-\frac12,j}\;\bar{\hat{v}}^{1\,n}_{i-\frac12,j} \\ \hat{g}^n_{i,j+\frac12}\bar{S}^n_{3\,i+\frac12,j}\;\bar{\hat{v}}^{1\,n}_{i+\frac12,j} - \hat{g}^n_{i,j-\frac12}\bar{S}^n_{3\,i-\frac12,j}\;\bar{\hat{v}}^{1\,n}_{i-\frac12,j} \\ \hat{g}^n_{i,j+\frac12}(\bar{\tau}^n_{i+\frac12,j}\;\bar{\hat{v}}^{1\,n}_{i+\frac12,j} + \bar{P}^n_{i+\frac12,j}\bar{v}^{1\,n}_{i+\frac12,j}) - \hat{g}^n_{i,j-\frac12}(\bar{\tau}^n_{i-\frac12,j}\;\bar{\hat{v}}^{1\,n}_{i-\frac12,j} + \bar{P}^n_{i-\frac12,j}\bar{v}^{1\,n}_{i-\frac12,j}) \end{pmatrix} + \Delta\hat{\boldsymbol{V}}^{1\,n}_{i,j}, \tag{5.42}$$

$$\Delta\hat{\boldsymbol{F}}^{2\,n}_{i,j} = \begin{pmatrix} \hat{g}^n_{i,j+\frac12}\bar{D}^n_{i,j+\frac12}\;\bar{\hat{v}}^{2\,n}_{i,j+\frac12} - \hat{g}^n_{i,j-\frac12}\bar{D}^n_{i,j-\frac12}\;\bar{\hat{v}}^{2\,n}_{i,j-\frac12} \\ \hat{g}^n_{i,j+\frac12}\bar{S}^n_{1\,i,j+\frac12}\;\bar{\hat{v}}^{2\,n}_{i,j+\frac12} - \hat{g}^n_{i,j-\frac12}\bar{S}^n_{1\,i,j-\frac12}\;\bar{\hat{v}}^{2\,n}_{i,j-\frac12} \\ \hat{g}^n_{i,j+\frac12}(\bar{S}^n_{2\,i,j+\frac12}\;\bar{\hat{v}}^{2\,n}_{i,j+\frac12} + \bar{P}^n_{i+\frac12,j+\frac12}) - \hat{g}^n_{i,j-\frac12}(\bar{S}^n_{2\,i,j-\frac12}\;\bar{\hat{v}}^{2\,n}_{i,j-\frac12} + \bar{P}^n_{i-\frac12,j-\frac12}) \\ \hat{g}^n_{i,j+\frac12}\bar{S}^n_{3\,i,j+\frac12}\;\bar{\hat{v}}^{2\,n}_{i,j+\frac12} - \hat{g}^n_{i,j-\frac12}\bar{S}^n_{3\,i,j-\frac12}\;\bar{\hat{v}}^{2\,n}_{i,j-\frac12} \\ \hat{g}^n_{i,j+\frac12}(\bar{\tau}^n_{i,j+\frac12}\;\bar{\hat{v}}^{2\,n}_{i,j+\frac12} + \bar{P}^n_{i,j+\frac12}\bar{v}^{2\,n}_{i,j+\frac12}) - \hat{g}^n_{i,j-\frac12}(\bar{\tau}^n_{i,j-\frac12}\;\bar{\hat{v}}^{2\,n}_{i,j-\frac12} + \bar{P}^n_{i,j-\frac12}\bar{v}^{2\,n}_{i,j-\frac12}) \end{pmatrix} + \Delta\hat{\boldsymbol{V}}^{2\,n}_{i,j}. \tag{5.43}$$

The components of the state vector $\boldsymbol{F}^0$ with overbars are the averages of left and right reconstructed states at the interface, $\boldsymbol{F}^{1\,\mathrm{R}} + \boldsymbol{F}^{1\,\mathrm{L}}$ as in the flux formula (5.23, 5.24) in Section 5.4.1. We also use the following abbreviation: $\hat{v}^i = v^i - \beta^i/\alpha$.

These flux terms contain the characteristic information of the hyperbolic system through the numerical viscosity $\boldsymbol{q}$, according to Section 5.4.1:

$$\Delta\tilde{\boldsymbol{V}}^{1\,n}_{i,j} = \alpha^n_{i+\frac12,j}\boldsymbol{q}^{1\,n}_{i+\frac12,j} - \alpha^n_{i-\frac12,j}\boldsymbol{q}^{1\,n}_{i-\frac12,j}, \tag{5.44}$$

$$\Delta\tilde{\boldsymbol{V}}^{2\,n}_{i,j} = \alpha^n_{i,j+\frac12}\boldsymbol{q}^{2\,n}_{i,j+\frac12} - \alpha^n_{i,j-\frac12}\boldsymbol{q}^{2\,n}_{i,j-\frac12}, \tag{5.45}$$

and

$$
\begin{aligned}
\Delta\hat{\boldsymbol{V}}^{1\,n}_{i,j} &= \hat{g}^{n}_{i+\frac{1}{2},j}\Delta\boldsymbol{q}^{1\,n}_{i+\frac{1}{2},j} - \hat{g}^{n}_{i-\frac{1}{2},j}\Delta\boldsymbol{q}^{1\,n}_{i+\frac{1}{2},j}, &\quad (5.46)\\
\Delta\hat{\boldsymbol{V}}^{2\,n}_{i,j} &= \hat{g}^{n}_{i,j+\frac{1}{2}}\Delta\boldsymbol{q}^{2\,n}_{i,j+\frac{1}{2}} - \hat{g}^{n}_{i,j-\frac{1}{2}}\Delta\boldsymbol{q}^{2\,n}_{i,j+\frac{1}{2}}. &\quad (5.47)
\end{aligned}
$$

The time and space derivatives of the state and flux vectors are discretized to 1st order accuracy for the time derivative and 2nd order accuracy for the spatial derivative as

$$
\begin{gathered}
\frac{\partial \boldsymbol{F}^{0}_{i,j}}{\partial t} = \frac{\boldsymbol{F}^{0\,n+1}_{i,j} - \boldsymbol{F}^{0\,n}_{i,j}}{\Delta t^{n}},\\
\frac{\partial \tilde{\boldsymbol{F}}^{1}_{i,j}}{\partial r} = \frac{\tilde{\boldsymbol{F}}^{1\,n}_{i+\frac{1}{2},j} - \tilde{\boldsymbol{F}}^{1\,n}_{i-\frac{1}{2},j}}{\Delta r_i} = \frac{\Delta\tilde{\boldsymbol{F}}^{1\,n}_{i,j}}{\Delta r_i}, \qquad \frac{\partial \tilde{\boldsymbol{F}}^{1}_{i,j}}{\partial \theta} = \frac{\tilde{\boldsymbol{F}}^{1\,n}_{i,j+\frac{1}{2}} - \tilde{\boldsymbol{F}}^{1\,n}_{i,j-\frac{1}{2}}}{\Delta \theta} = \frac{\Delta\tilde{\boldsymbol{F}}^{1\,n}_{i,j}}{\Delta \theta},\\
\frac{\partial \hat{\boldsymbol{F}}^{2}_{i,j}}{\partial r} = \frac{\hat{\boldsymbol{F}}^{2\,n}_{i+\frac{1}{2},j} - \hat{\boldsymbol{F}}^{2\,n}_{i-\frac{1}{2},j}}{\Delta r_i} = \frac{\Delta\hat{\boldsymbol{F}}^{2\,n}_{i,j}}{\Delta r_i}, \qquad \frac{\partial \hat{\boldsymbol{F}}^{2}_{i,j}}{\partial \theta} = \frac{\hat{\boldsymbol{F}}^{2\,n}_{i,j+\frac{1}{2}} - \hat{\boldsymbol{F}}^{2\,n}_{i,j-\frac{1}{2}}}{\Delta \theta} = \frac{\Delta\hat{\boldsymbol{F}}^{2\,n}_{i,j}}{\Delta \theta}.
\end{gathered}
\quad (5.48)
$$

Thus, the expression (5.31) for the evolution equations can now be written as the following 2nd order Runge–Kutta integration equations:

$$
\begin{aligned}
\overset{(1)}{\boldsymbol{F}}{}^{0\,n+1}_{i,j} &= \boldsymbol{F}^{0\,n}_{i,j} + \Delta t^{n}\left(-\frac{1}{(\phi^{n}_{i,j})^{4} r_i^{2}\sin\theta_j}\left(\frac{\Delta\hat{\boldsymbol{F}}^{1\,n}_{i,j}}{\Delta r_i} + \frac{\Delta\hat{\boldsymbol{F}}^{2\,n}_{i,j}}{\Delta\theta}\right) + \alpha^{n}_{i,j}\hat{\boldsymbol{Q}}^{n}_{i,j}\right),\\
\boldsymbol{F}^{0\,n+1}_{i,j} &= \frac{1}{2}\left[\boldsymbol{F}^{0\,n}_{i,j} + \overset{(1)}{\boldsymbol{F}}{}^{0\,n+1}_{i,j} + \Delta t^{n}\left(-\frac{1}{(\phi^{n}_{i,j})^{4} r_i^{2}\sin\theta_j}\left(\frac{\Delta\overset{(1)}{\hat{\boldsymbol{F}}}{}^{1\,n+1}_{i,j}}{\Delta r_i} - \frac{\Delta\overset{(1)}{\hat{\boldsymbol{F}}}{}^{2\,n+1}_{i,j}}{\Delta\theta}\right) + \alpha^{n}_{i,j}\overset{(1)}{\hat{\boldsymbol{Q}}}{}^{n+1}_{i,j}\right)\right].
\end{aligned}
\quad (5.49)
$$

The 3rd order accurate form is constructed in an analogous way, and reads:

$$
\begin{aligned}
\overset{(1)}{\boldsymbol{F}}{}^{0\,n+1}_{i,j} &= \boldsymbol{F}^{0\,n}_{i,j} + \Delta t^{n}\left(-\frac{1}{(\phi^{n}_{i,j})^{4} r_i^{2}\sin\theta_j}\left(\frac{\Delta\hat{\boldsymbol{F}}^{1\,n}_{i,j}}{\Delta r_i} + \frac{\Delta\hat{\boldsymbol{F}}^{2\,n}_{i,j}}{\Delta\theta}\right) + \alpha^{n}_{i,j}\hat{\boldsymbol{Q}}^{n}_{i,j}\right),\\
\overset{(2)}{\boldsymbol{F}}{}^{0\,n+1}_{i,j} &= \frac{1}{4}\left[3\boldsymbol{F}^{0\,n}_{i,j} + \overset{(1)}{\boldsymbol{F}}{}^{0\,n+1}_{i,j} + \Delta t^{n}\left(-\frac{1}{(\phi^{n}_{i,j})^{4} r_i^{2}\sin\theta_j}\left(\frac{\Delta\overset{(1)}{\hat{\boldsymbol{F}}}{}^{1\,n+1}_{i,j}}{\Delta r_i} - \frac{\Delta\overset{(1)}{\hat{\boldsymbol{F}}}{}^{2\,n+1}_{i,j}}{\Delta\theta}\right) + \alpha^{n}_{i,j}\overset{(1)}{\hat{\boldsymbol{Q}}}{}^{n+1}_{i,j}\right)\right],\\
\boldsymbol{F}^{0\,n+1}_{i,j} &= \frac{1}{3}\left[\boldsymbol{F}^{0\,n}_{i,j} + 2\overset{(2)}{\boldsymbol{F}}{}^{0\,n+1}_{i,j} + 2\Delta t^{n}\left(-\frac{1}{(\phi^{n}_{i,j})^{4} r_i^{2}\sin\theta_j}\left(\frac{\Delta\overset{(2)}{\hat{\boldsymbol{F}}}{}^{1\,n+1}_{i,j}}{\Delta r_i} - \frac{\Delta\overset{(2)}{\hat{\boldsymbol{F}}}{}^{2\,n+1}_{i,j}}{\Delta\theta}\right) + \alpha^{n}_{i,j}\overset{(2)}{\hat{\boldsymbol{Q}}}{}^{n+1}_{i,j}\right)\right].
\end{aligned}
\quad (5.50)
$$

The superscripts (1) and (2) over the flux difference and source terms mean that these quantities have to be taken at the first and second intermediate Runge–Kutta step, respectively, as functions of the respective intermediate state vector quantities $\overset{(1)}{\boldsymbol{F}}{}^{0\,n+1}_{i,j}$ and $\overset{(2)}{\boldsymbol{F}}{}^{0\,n+1}_{i,j}$. The time integration equations for the expression (5.30) have a similar form.

In this time integration from a particular time slice Σ_{t^n}, on which the metric is given, no explicit time derivatives of the metric occur in the flux part of Equation (5.29). Thus for this part of the conservation equations the data given on Σ_{t^n} are sufficient. However, time derivatives of all metric quantities ϕ, α, and β^i show up in the Christoffel symbols (see Appendix B.2), and thus in the source term $\boldsymbol{Q}$. As the equations for the metric in the CFC approximation do not provide us with explicit expressions for the time derivatives of all of these quantities, we have to approximate them numerically by the following discretized derivatives using values from the two time slices Σ_{t^n} and $\Sigma_{t^{n-1}}$, on which the metric has already been calculated:

$$\left(\frac{\partial\phi}{\partial t}\right)^n_{i,j} = \frac{\phi^n_{i,j} - \phi^{n-1}_{i,j}}{\Delta t^{n-1}}, \qquad \left(\frac{\partial\alpha}{\partial t}\right)^n_{i,j} = \frac{\alpha^n_{i,j} - \alpha^{n-1}_{i,j}}{\Delta t^{n-1}}, \qquad \left(\frac{\partial\beta^i}{\partial t}\right)^n_{i,j} = \frac{\beta^{i\,n}_{i,j} - \beta^{i\,n-1}_{i,j}}{\Delta t^{n-1}}. \tag{5.51}$$

For $\partial_t\phi$ we can also use the analytically equivalent version from Equation (3.34):

$$\left(\frac{\partial\phi}{\partial t}\right)^n_{i,j} = \frac{1}{(\phi^n_{i,j})^6}\left[\left(\frac{\partial\beta^1}{\partial r}\right)^n_{i,j} + \left(\frac{\partial\beta^2}{\partial\theta}\right)^n_{i,j} + \frac{\beta^{1\,n}_{i,j}}{r_i} + \cot\theta_j\beta^{2\,n}_{i,j} + \frac{6\beta^{1\,n}_{i,j}}{\phi^n_{i,j}}\left(\frac{\partial\phi}{\partial\theta}\right)^n_{i,j} + \frac{6\beta^{1\,n}_{i,j}}{\phi^n_{i,j}}\left(\frac{\partial\phi}{\partial\theta}\right)^n_{i,j}\right], \tag{5.52}$$

where we have used the following abbreviation for the radial and angular derivative of a metric quantity q:

$$\left(\frac{\partial q}{\partial r}\right)^n_{i,j} = \frac{q^n_{i+\frac{1}{2},j} - q^n_{i-\frac{1}{2},j}}{\Delta r_i}, \qquad \left(\frac{\partial q}{\partial\theta}\right)^n_{i,j} = \frac{q^n_{i,j+\frac{1}{2}} - q^n_{i,j-\frac{1}{2}}}{\Delta\theta}, \tag{5.53}$$

The numerical deviation between expressions (5.51) and (5.52) for $\partial_t\phi$ during the evolution is a good measure for the accuracy of the numerical scheme and for the quality of the metric extrapolation, if the metric system is not solved at every time step (see also Section 5.6.4 and Section 6.6).

If the conservation equations are written in the form (5.30) rather than in the form (5.31), additional terms appear, which effectively act as sources in addition to the ones originating from curved spacetime ("gravity") and non-Cartesian coordinates ("ficticious forces"). Although formulations (5.30) and (5.31) are equivalent, there is a profound numerical difference between them. For illustrative purposes, we now consider the Newtonian case. Here in axisymmetry with polar coordinates used, the equations for the rest mass ρ, the angular momentum $S_3 = \rho v_3 = \rho r\sin\theta v_\varphi$ and the total energy $E = \rho\epsilon + \frac{1}{2}\rho v^2$ are true conservation equations without source terms. For a closed system, the sum of the fluxes through all interfaces is zero, and if a flux-conservative scheme is used, the conserved quantities are constant throughout the evolution up to machine precision.

This "exact" numerical conservation stems from the fact that for each conserved quantity there exists a corresponding flux divergence, and no source terms are present. This does not hold for Equation (5.31), where the fluxes differ from the ones in Equation (5.30) by the volume element $\sqrt{\gamma}$ (which is $r^2\sin\theta$ in the Newtonian case). Therefore in this formulation we introduce a source terms which numerically "drives" mass, angular momentum and energy creation/destruction, respectively. So the system of the form (5.30) is more in the spirit of the conservative character of the hydrodynamic equations, which is reflected in its superiority as far as numerical conservation of certain quantities is concerned.

However, in the general relativistic conservation equations, only the rest mass D is analytically conserved (which manifests itself in the vanishing first component of $\boldsymbol{Q}$ in Equations (2.28)). Both angular momentum and total energy are not conserved (at least for a system with boundaries not at infinity), as there is angular momentum and energy transport for example by gravitational waves. So the corresponding source term components are not zero, unlike in the Newtonian case. Thus in GR the motivation for writing the equations in the exact numerical conservation form is not as high as in Newtonian hydrodynamics, as in general the strict conservation will be violated anyway for S_3 and τ[k]. In some collapse situations the less conservative form may even be favorable, as the effective viscosity along the rotation axis is apparently higher, and therefore numerical noise at this problematic part of the grid, where some metric components become zero or singular, is reduced.

Another part of the hydrodynamic conservation equations, where analytically equivalent formulations can lead to quite remarkable numerical differences, is the radial and angular flux derivative: We can rewrite the derivatives in the flux divergence terms of Equation (5.31) as follows:

$$\frac{1}{\phi^4 r^2 \sin\theta}\left(\frac{\partial}{\partial r}(\phi^4 r^2 \sin\theta \boldsymbol{F}^1) + \frac{\partial}{\partial\theta}(\phi^4 r^2 \sin\theta \boldsymbol{F}^2)\right) = \frac{3}{\phi^4}\frac{\partial}{\partial r^3}(\phi^4 \boldsymbol{F}^1) - \frac{1}{\phi^4}\frac{\partial}{\partial\cos\theta}(\phi^4 \boldsymbol{F}^2). \quad (5.54)$$

We again point out that analytically both forms are equivalent. However, in the discretized form the r.h.s. form has the advantage of a better effective numerical resolution close to the center and the polar axis, as in the l.h.s. form the factor in front of the derivative becomes analytically singular (and therefore numerically very large in the center of the first radial or angular cells, respectively).

A discretization of the l.h.s. of Equation (5.54) is given by

$$\begin{aligned}\frac{1}{(\phi^n_{i,j})^4 r_i^2 \sin\theta_j}\Bigg(&\frac{(\phi^n_{i+\frac{1}{2},j})^4 r^2_{i+\frac{1}{2}} \sin\theta_j \boldsymbol{F}^{1\,n}_{i+\frac{1}{2},j} - (\phi^n_{i-\frac{1}{2},j})^4 r^2_{i-\frac{1}{2}} \sin\theta_j \boldsymbol{F}^{1\,n}_{i-\frac{1}{2},j}}{\Delta r_i} + \\ &\frac{(\phi^n_{i,j+\frac{1}{2}})^4 r_i^2 \sin\theta_{j+\frac{1}{2}} \boldsymbol{F}^{2\,n}_{i,j+\frac{1}{2}} - (\phi^n_{i,j-\frac{1}{2}})^4 r_i^2 \sin\theta_{j-\frac{1}{2}} \boldsymbol{F}^{2\,n}_{i,j-\frac{1}{2}}}{\Delta\theta}\Bigg),\end{aligned} \quad (5.55)$$

whereas the r.h.s. is discretized as follows:

$$\frac{1}{(\phi^n_{i,j})^4}\left(3\frac{(\phi^n_{i+\frac{1}{2},j})^4 \boldsymbol{F}^{1\,n}_{i+\frac{1}{2},j} - (\phi^n_{i-\frac{1}{2},j})^4 \boldsymbol{F}^{1\,n}_{i-\frac{1}{2},j}}{\Delta r_i^3} - \frac{(\phi^n_{i,j+\frac{1}{2}})^4 \boldsymbol{F}^{2\,n}_{i,j+\frac{1}{2}} - (\phi^n_{i,j-\frac{1}{2}})^4 \boldsymbol{F}^{2\,n}_{i,j-\frac{1}{2}}}{\Delta\cos\theta_j}\right), \quad (5.56)$$

with $\Delta r_i^3 = r^3_{i+\frac{1}{2}} - r^3_{i-\frac{1}{2}}$ and $\Delta\cos\theta_j = \cos\theta_{j+\frac{1}{2}} - \cos\theta_{j-\frac{1}{2}}$.

In our core collapse simulations it has turned out to be favorable to use form (5.55) for the radial derivative, and form (5.56) for the angular derivative to minimize unwanted numerical artifacts at the center and the rotation axis.

---

[k] If a source of gravitational waves is axisymmetric, the gravitational radiation does *not* carry away angular momentum (see exercise 16.3 in [109]). Furthermore, if a system does not emit gravitational waves, and is isolated in other respects as well, angular momentum is also conserved, and the source term for the S_3 evolution equation vanishes. However, approximating the spacetime by a CFC metric destroys this exact analytic conservation by introducing a nonzero source term. In this case it is irrelevant that there is no gravitational radiation in a CFC spacetime, as this is an artificial restriction due to this specific approximation.

5.5.2 Recovery of the Primitive Quantities

While the conversion between the primitive quantities (ρ, v_i, ϵ) and conserved quantities (D, S_i, τ) is trivial in Newtonian hydrodynamics, this is different in the relativistic case: As there are no closed form relations for the dependence of the primitive variables on the conserved quantities, ρ, v_i and ϵ cannot be explicitely calculated from D, S_i and τ. We therefore have to resort to iterative methods to extract the new primitives from the updated conserved quantities.

For an ideal gas EoS this method has been introduced by Martí et al. for their calculations in [75], and has been described analytically in [77]. We have extended this method to be suitable for our hybrid EoS (4.9).

We calculate a function $f(P^*) \equiv P(\rho^*, \epsilon^*) - P^*$, where $\rho*$ and ϵ^* depend on the conserved quantities and P^* only (in all relations involving the pressure we replace P by P^*):

$$\begin{aligned} f(P^*) = & K\left(D\sqrt{X}\right)^{\gamma}\left(1-\frac{\gamma_{\mathrm{th}}-1}{\gamma-1}\right)+(\gamma_{\mathrm{th}}-1)X\left[\tau+D\left(1-\frac{1}{\sqrt{X}}\right)+P^*\left(1-\frac{1}{X}\right)\right]- \\ & -\frac{(\gamma_{\mathrm{th}}-1)(\gamma-\gamma_1)}{\gamma_1-1)(\gamma_2-1)}K\rho_{\mathrm{nuc}}^{\gamma_1-1}D\sqrt{X}-P^*, \end{aligned} \tag{5.57}$$

where we use the auxiliary quantity $X \equiv 1 - S^2/(\tau + D + P^*)^2$, and $S = S_i S^i$. The new pressure is iteratively computed using the Newton–Raphson method:

$$P^{*\,\mathrm{new}} = P^* - f(P\,*^{)}\left(\frac{df(P^*)}{dP^*}\right)^{-1}, \tag{5.58}$$

where the derivative of $f(P^*)$ is given by

$$\begin{aligned} \frac{df(P^*)}{dP^*} = & \frac{K\left(D\sqrt{X}\right)^{\gamma}S^2\left(1-\frac{\gamma_{\mathrm{th}}-1}{\gamma-1}\right)}{X(\tau+D+P^*)^3}+\frac{2(\gamma_{\mathrm{th}}-1)S^2\left[\tau+D\left(1-\frac{1}{\sqrt{X}}\right)+P^*\left(1-\frac{1}{X}\right)\right]}{(\tau+D+P^*)^3}+ \\ & +(\gamma_{\mathrm{th}}-1)X\left[\frac{DS^2}{X^{3/2}(\tau+D+P^*)^3}+1-\frac{1}{X}+\frac{2P^*S^2}{X^2(\tau+D+P^*)^3}\right]- \\ & -\frac{(\gamma_{\mathrm{th}}-1)(\gamma-\gamma_1)K\rho_{\mathrm{nuc}}^{\gamma_1-1}DS}{(\gamma_1-1)(\gamma_2-1)\sqrt{X}(\tau+D+P^*)^3}-1. \end{aligned} \tag{5.59}$$

The primitive quantities and the Lorentz factor are updated using the following relations:

$$v_i^* = \frac{S_i}{\tau+D+P^*}, \quad W^* = \frac{1}{\sqrt{1-v_i^* v^{i*}}}, \quad \rho^* = \frac{D}{W^*}, \quad \epsilon^* = \frac{\tau+D(1-W^*)+P^*(1-W^{*2})}{DW^*}. \tag{5.60}$$

When convergence is achieved, the temporary variables ρ^*, v_i^*, and ϵ^* have assumed the desired values of the primitive variables ρ, v_i, and ϵ. They obey the relation between the primitive quantities (2.26) and the conserved quantities (2.22–2.24). This recovery procedure has to be done at each time step, after the conserved quantities D, S_i, and τ have been updated, i.e. after each step of the Runge–Kutta integration of the conservation equation described in Section 5.5.1.

5.6 Numerical Solution of the Elliptic Metric System

Finding a numerical stable and efficient method for solving the system of metric equations (3.52, 3.53, 3.54) is in no way trivial. The metric equations are governed by a system with the following properties, which make a numerical implementation rather cumbersome: The equations are (i) elliptic, (ii) coupled, and (iii) nonlinear. Their numerical solution is therefore much harder and more time consuming than the solution of their Newtonian counterpart, Poisson's equation $\Delta\Phi = 4\pi\rho$ for the gravitational potential Φ.

In general, the numerical solution of an elliptic problem is more difficult than the solution of a hyperbolic problem. A common numerical approach for solving hyperbolic equations is based on finite difference or finite volume discretization, and forward time integration which represents the Cauchy problem. If one uses an explicit integration scheme to propagate forward quantities at a specific grid point on the basis of a hyperbolic equation, only knowledge of the values of the quantities at the nearest grid points (i.e. on grid points which comprise the numerical discretization stencil, which rarely involves more than e.g. 5 or 9 points) is needed. However, in elliptic equations the solution for a single grid point involves and influences all other points on the discrete grid.

So while hyperbolic equations can numerically be regarded as a nearest neighbor interaction problem (like point particles which are influenced only by very few other ones, if the forces between them fall off rapidly enough), elliptic problems are more like a system of point particles where the forces between all particles have to be taken into account due to their long effective range.

5.6.1 Finite Differencing – Newton–Raphson Iteration

If we have to solve a linear system like Poisson's equation on a numerical grid, one of the standard methods is to discretize the equation. Let the vector of unknowns be $\boldsymbol{u} = (u_{i,j})$, and the vector of sources be $\boldsymbol{f} = (f_{i,j})$, where (i, j) labels the position (r_i, θ_j) on the grid. For computational purposes, the entries are usually ordered in a single vector array according to $k = (i-1)n_\theta + j$. This discretization then leads to solving a linear matrix equation with the right hand side being the source vector of the original equation:

$$\boldsymbol{A}\boldsymbol{u} = \boldsymbol{f}. \tag{5.61}$$

Depending on the size of the discretization stencil and the extension of the grid, the matrix $\boldsymbol{A}$ of dimension $n_r \times n_\theta$ is more or less densely filled. In general, however, the matrix is sparse, i.e. the number of nonzero elements is much smaller than the total number of elements. For solving sparse linear systems of equations, there exist a variety of efficient numerical methods and software packages for various computer architectures.

Although the CFC metric equations do not form a linear system like Poisson's equation, we can still try to reduce them to a linear system, to which we could then apply a standard linear solver. Therefore our strategy for solving the system of elliptic metric equations (3.52, 3.53, 3.54) is as follows:

We first define a vector of unknowns, whose components are the five metric quantities:

$$\boldsymbol{u} = (u^k) = \begin{pmatrix} \phi \\ \alpha\phi \\ \beta^1 \\ \beta^2 \\ \beta^3 \end{pmatrix}. \tag{5.62}$$

Then the metric equations read (with $u_{,f} = \partial_f u$, $u_{,fg} = \partial_f \partial_g u$):

$$\begin{aligned}
0 = f^1(u^k) = {} & u^1_{,rr} + \frac{2u^1_{,r}}{r} + \frac{u^1_{,\theta\theta}}{r^2} + \frac{\cot\theta}{r^2} u^1_{,\theta} + 2\pi (u^1)^5 (\rho h W^2 - P) + \\
& + \frac{(u^1)^7}{48(u^2)^2} \Big[3r^2 \sin^2\theta (u^5_{,r})^2 + \frac{3(u^3_{,\theta})^2}{r^2} + \frac{4(u^3)^2}{r^2} + 4(u^3_{,r})^2 + 3r^2 (u^4_{,r})^2 + 3\sin^2\theta (u^5_{,\theta})^2 - \frac{8u^3 u^3_{,r}}{r} + \\
& \quad + 6u^3_{,\theta} u^4_{,r} + \frac{4u^3 u^4_{,\theta}}{r} - 4u^3_{,r} u^4_{,\theta} + 4(u^4_{,\theta})^2 + \frac{4\cot\theta u^3 u^4}{r} - 4\cot\theta u^4 u^3_{,r} - 4\cot\theta u^4 u^4_{,\theta} + \\
& \quad + 4\cot^2\theta (u^4)^2 \Big],
\end{aligned} \tag{5.63}$$

$$\begin{aligned}
0 = f^2(u^k) = {} & u^2_{,rr} + \frac{2u^2_{,r}}{r} + \frac{u^2_{,\theta\theta}}{r^2} + \frac{\cot\theta}{r^2} u^2_{,\theta} - 2\pi (u^1)^4 u^2 (\rho h (3W^2 - 2) + 5P) - \\
& - \frac{7(u^1)^7}{48(u^2)^2} \Big[3r^2 \sin^2\theta (u^5_{,r})^2 + \frac{3(u^3_{,\theta})^2}{r^2} + \frac{4(u^3)^2}{r^2} + 4(u^3_{,r})^2 + 3r^2 (u^4_{,r})^2 + 3\sin^2\theta (u^5_{,\theta})^2 - \frac{8u^3 u^3_{,r}}{r} + \\
& \quad + 6u^3_{,\theta} u^4_{,r} + \frac{4u^3 u^4_{,\theta}}{r} - 4u^3_{,r} u^4_{,\theta} + 4(u^4_{,\theta})^2 + \frac{4\cot\theta u^3 u^4}{r} - 4\cot\theta u^4 u^3_{,r} - 4\cot\theta u^4 u^4_{,\theta} + \\
& \quad + 4\cot^2\theta (u^4)^2 \Big],
\end{aligned} \tag{5.64}$$

$$\begin{aligned}
0 = f^3(u^k) = {} & u^3_{,rr} + \frac{2u^3_{,r}}{r} + \frac{u^3_{,\theta\theta}}{r^2} + \frac{\cot\theta}{r^2} u^3_{,\theta} - \frac{2u^3}{r^2} - \frac{2\cot\theta u^4}{r} - \frac{2u^4_{,\theta}}{r} - \frac{16\pi u^2 S_1}{u^1} - \\
& - \frac{1}{u^2} \left[\frac{2}{3} \left(u^2_{,r} - \frac{7u^2 u^1_{,r}}{u^1} \right) \left(2u^3_{,r} - u^4_{,\theta} - \frac{2u^3}{r} - \cot\theta u^4 \right) + \left(u^2_{,\theta} - \frac{7u^2 u^1_{,\theta}}{u^1} \right) \left(u^4_{,r} + \frac{u^3_{,\theta}}{r^2} \right) \right] + \\
& + \frac{1}{3} \left(u^3_{,rr} + u^4_{,r\theta} + \frac{2u^3_{,r}}{r} - \frac{2u^3}{r^2} + \cot\theta u^4_{,r} \right),
\end{aligned} \tag{5.65}$$

$$\begin{aligned}
0 = f^4(u^k) = {} & u^4_{,rr} + \frac{4u^4_{,r}}{r} + \frac{u^4_{,\theta\theta}}{r^2} + \frac{\cot\theta}{r^2} u^4_{,\theta} + \frac{2u^3_{,\theta}}{r^3} + \frac{(1 - \cot\theta) u^4}{r^2} - \frac{16\pi u^2 S_2}{r^2 u^1} - \\
& - \frac{1}{u^2} \left[\left(u^2_{,r} - \frac{7u^2 u^1_{,r}}{u^1} \right) \left(u^4_{,r} + \frac{u^1_{,\theta}}{r^2} \right) + \frac{2}{3r^2} \left(u^2_{,\theta} - \frac{7u^2 u^1_{,\theta}}{u^1} \right) \left(-u^3_{,r} + 2u^4_{,\theta} + \frac{u^3}{r} - \cot\theta u^4 \right) \right] + \\
& + \frac{1}{3r^2} \left(u^3_{,r\theta} + u^4_{,\theta\theta} + \frac{2u^3_{,\theta}}{r} - \frac{u^4}{\sin^2\theta} \right),
\end{aligned} \tag{5.66}$$

$$\begin{aligned}
0 = f^5(u^k) = {} & u^5_{,rr} + \frac{4u^5_{,r}}{r} + \frac{u^5_{,\theta\theta}}{r^2} + \frac{3\cot\theta}{r^2} u^5_{,\theta} - \frac{16\pi u^2 S_3}{r^2 \sin^2\theta u^1} - \\
& - \frac{1}{u^2} \left[\left(u^2_{,r} - \frac{7u^2 u^1_{,r}}{u^1} \right) u^5_{,r} + \frac{1}{r^2} \left(u^2_{,\theta} - \frac{7u^2 u^1_{,\theta}}{u^1} \right) u^5_{,\theta} \right].
\end{aligned} \tag{5.67}$$

Now we discretize these equations on the (r,θ)-grid, denoting the components u^k $(k = 1,\dots,5)$ at the position (r_i,θ_j) by $u^k_{i,j}$. The metric quantities are defined on cell centers:

$$u^k(r_i,\theta_j) = u^k_{i,j}. \tag{5.68}$$

Their values at zone interfaces (needed for the hydrodynamic solver like in the flux difference equations (5.40, 5.41)), are obtained by interpolation. The radial and angular derivatives are approximated by linear finite differences. On a grid which is non-equidistant in radial, and equidistant in angular direction, they are given by

$$\begin{aligned}
\left.\frac{\partial u^k}{\partial r}\right|_{i,j} &= \frac{u^k_{i+1,j} + (a_i^2-1)u^k_{i,j} - a_i^2 u^k_{i-1,j}}{\Delta r_{i-\frac{1}{2}} a_i(a_i+1)} + O(\Delta r^2_{i-\frac{1}{2}}),\\
\left.\frac{\partial u^k}{\partial \theta}\right|_{i,j} &= \frac{u^k_{i,j+1} - u^k_{i,j-1}}{2\Delta\theta} + O(\Delta\theta^2),\\
\left.\frac{\partial^2 u^k}{\partial r^2}\right|_{i,j} &= 2\frac{u^k_{i+1,j} - (a_i+1)u^k_{i,j} + a_i u^k_{i-1,j}}{\Delta r^2_{i-\frac{1}{2}} a_i(a_i+1)} + O(\Delta r^2_{i-\frac{1}{2}}),\\
\left.\frac{\partial^2 u^k}{\partial \theta^2}\right|_{i,j} &= \frac{u^k_{i,j+1} - 2u^k_{i,j} + u^k_{i,j-1}}{\Delta\theta^2} + O(\Delta\theta^2),\\
\left.\frac{\partial^2 u^k}{\partial r\theta}\right|_{i,j} &= \frac{u^k_{i+1,j+1} - u_{i+1,j-1} - u^k_{i-1,j+1} + u^k_{i-1,j-1}}{2\Delta r_{i-\frac{1}{2}}\Delta\theta(a_i+1)} + O(\Delta r_{i-\frac{1}{2}}\Delta\theta).
\end{aligned} \tag{5.69}$$

We therefore need a 9-point stencil to represent the discretized equations:

$$\begin{array}{ccccc}
{\scriptstyle i-1,j-1} & & {\scriptstyle i-1,j} & & {\scriptstyle i-1,j+1}\\
 & \bullet & \bullet & \bullet & \\
{\scriptstyle i,j-1} & \bullet & \bullet & \bullet & {\scriptstyle i,j+1}\\
 & \bullet & \bullet & \bullet & \\
{\scriptstyle i+1,j-1} & & {\scriptstyle i+1,j} & & {\scriptstyle i+1,j+1}
\end{array} \tag{5.70}$$

Hence, the system of metric equations, when discretized, gives rise to a nonlinear system of dimension $5 \times n_r \times n_\theta$,

$$f^k_{i,j}(u^n_{i-1,j-1}, u^n_{i-1,j}, u^n_{i-1,j+1}, u^n_{i,j-1}, u^n_{i,j}, u^n_{i,j+1}, u^n_{i+1,j-1}, u^n_{i+1,j}, u^n_{i+1,j+1}) = 0, \tag{5.71}$$

or

$$\boldsymbol{f}(\boldsymbol{u}) = 0, \tag{5.72}$$

for which we have to find the roots $u^n_{i,j}$.

The standard numerical method to find the roots of such a system of equations is to apply a Newton–Raphson iteration. This means that the nonlinear problem of dimension $5 \times n_r \times n_\theta$ is reduced to a linear one of the same dimension, but at the cost of having to solve the linear system several times until the desired accuracy is reached.

We illustrate this method first for the root of an equation for a single unknown,

$$\tilde{f}(\tilde{u}) = 0. \tag{5.73}$$

Then the Newton–Raphson method to find the unknown $\tilde{u}_0$, which solves Equation (5.73), yields an iterative procedure involving the derivative of the function $\tilde{f}$ with respect to $\tilde{u}$ (the Jacobian $\tilde{J}$ of $\tilde{f}$),

$$\tilde{u}^{s+1} = \tilde{u}^s + \Delta\tilde{u}^s = \tilde{u}^s - \frac{\tilde{f}(\tilde{u}^s)}{\tilde{J}(\tilde{u}^s)} = \tilde{u}^s - \left(\frac{\partial \tilde{f}(\tilde{u}^s)}{\partial \tilde{u}^s}\right)^{-1} \tilde{f}(\tilde{u}^s), \tag{5.74}$$

Where s is the iteration step. In general, this is a very easy, robust and fast numerical method for finding the root of a function $\tilde{f}$.

In multi-dimensions, i.e. if the function $\hat{\boldsymbol{f}}$ is a function vector of an unknown vector $\boldsymbol{u}$, the Newton–Raphson equation (5.74) is generalized in vector form to

$$\hat{\boldsymbol{u}}^{s+1} = \hat{\boldsymbol{u}}^s + \Delta\hat{\boldsymbol{u}}^s = \hat{\boldsymbol{u}}^s - \left(\hat{\boldsymbol{J}}(\hat{\boldsymbol{u}}^s)\right)^{-1} \hat{\boldsymbol{f}}(\hat{\boldsymbol{u}}^s) = \hat{\boldsymbol{u}}^s - \left(\frac{\partial \hat{\boldsymbol{f}}(\hat{\boldsymbol{u}}^s)}{\partial \hat{\boldsymbol{u}}^s}\right)^{-1} \hat{\boldsymbol{f}}^s(\hat{\boldsymbol{u}}^s), \tag{5.75}$$

or for the single components to

$$\hat{u}^{s+1}_{\hat{\imath}} = \hat{u}^s_{\hat{\imath}} + \Delta\hat{u}^s_{\hat{\imath}} = \hat{u}^s_{\hat{\imath}} - \left(\hat{J}^s_{\hat{\imath},\hat{\jmath}}(\hat{u}^s_{\hat{k}})\right)^{-1} \hat{f}_{\hat{\jmath}}(\hat{u}^s_{\hat{k}}) = \left(\frac{\partial \hat{f}_{\hat{\imath}}(\hat{u}^s_{\hat{k}})}{\partial \hat{u}^s_{\hat{\jmath}}}\right)^{-1} \hat{f}_{\hat{\jmath}}(\hat{u}^s_{\hat{k}}). \tag{5.76}$$

It immediately becomes clear from Equation (5.76) that the Newton–Raphson method involves the solution of the following linear problem with a dimension of the maximum of the index $\hat{\imath}$ during every iteration:

$$\hat{J}^s_{\hat{\imath},\hat{\jmath}} \Delta\hat{u}^s_{\hat{\imath}} = -\hat{f}^s_{\hat{\jmath}}, \qquad \text{or in vector form: } \hat{\boldsymbol{J}}^s \Delta\hat{\boldsymbol{u}}^s = -\hat{\boldsymbol{f}}^s. \tag{5.77}$$

However, the Jacobi matrix $\hat{\boldsymbol{J}} = (\hat{J}_{\hat{\imath},\hat{\jmath}})$ of the nonlinear system is in general both sparse and diagonally dominant, which reduces the complexity of the linear problem significantly.

5.6.2 The Linear Problem

Now we want to apply the Newton–Raphson iteration scheme for multi-dimensions (5.76), to the system of discretized metric equations, which emerge from plugging Equations (5.68) and (5.69) into the analytic metric equations (5.63–5.67).

The Jacobi matrix of this system is defined as

$$\hat{\boldsymbol{J}} = (\hat{J}_{\hat{\imath},\hat{\jmath}}) = \left(\frac{\partial \hat{f}_{\hat{\imath}}}{\partial \hat{u}_{\hat{\jmath}}}\right) = \left(\frac{\partial f^k_{i,j}}{\partial u^n_{l,m}}\right). \tag{5.78}$$

As indicated by the last transformation in Equation (5.78), the discretized five functions $f^k_{i,j}$ and five unknowns $u^n_{l,m}$, which each depend on three indices, can be represented by a single vector of functions $\hat{f}_{\hat{\imath}}$ and a single vector of unknowns $\hat{u}_{\hat{\jmath}}$. The relation between the vector index and the three indices of the original quantities is given by

$$\left.\begin{array}{l} \hat{\imath} = (i-1) \times n_\theta \times 5 + (j-1) \times 5 + k, \\ \hat{\jmath} = (l-1) \times n_\theta \times 5 + (m-1) \times 5 + n, \end{array}\right\} \quad \text{with } \hat{\imath}, \hat{\jmath} = 1, \ldots, n_r \times n_\theta \times 5. \tag{5.79}$$

We use this transformation to express more clearly the fact that for numerical purposes the functions and unknowns are one-dimensional vectors rather than multi-dimensional constructs.

As the five functions $f^k_{i,j}$ at a zone (i, j) in the system of equations (5.71) depend only on the five metric unknowns u^q at the neighboring points within the 9 point stencil, the Jacobi matrix will be a sparse matrix consisting of nine bands composed of blocks of size 5×5 with the following structure:

$$\hat{\boldsymbol{J}} = \underbrace{\left(\begin{array}{c|c|c|c|c}
\overbrace{\begin{array}{cccc} \boxed{5} & \boxed{6} & & \\ \boxed{4} & \boxed{5} & \boxed{6} & \\ & \boxed{4} & \boxed{5} & \boxed{6} \\ & & \boxed{4} & \boxed{5} \end{array}}^{5 \times n_\theta} &
\begin{array}{cccc} \boxed{8} & \boxed{9} & & \\ \boxed{7} & \boxed{8} & \boxed{9} & \\ & \boxed{7} & \boxed{8} & \boxed{9} \\ & & \boxed{7} & \boxed{8} \end{array} & & & \\ \hline
\begin{array}{cccc} \boxed{2} & \boxed{3} & & \\ \boxed{1} & \boxed{2} & \boxed{3} & \\ & \boxed{1} & \boxed{2} & \boxed{3} \\ & & \boxed{1} & \boxed{2} \end{array} &
\begin{array}{cccc} \boxed{5} & \boxed{6} & & \\ \boxed{4} & \boxed{5} & \boxed{6} & \\ & \boxed{4} & \boxed{5} & \boxed{6} \\ & & \boxed{4} & \boxed{5} \end{array} &
\begin{array}{cccc} \boxed{8} & \boxed{9} & & \\ \boxed{7} & \boxed{8} & \boxed{9} & \\ & \boxed{7} & \boxed{8} & \boxed{9} \\ & & \boxed{7} & \boxed{8} \end{array} & & \\ \hline
& \ddots & \ddots & \ddots & \\ \hline
& & \begin{array}{cccc} \boxed{2} & \boxed{3} & & \\ \boxed{1} & \boxed{2} & \boxed{3} & \\ & \boxed{1} & \boxed{2} & \boxed{3} \\ & & \boxed{1} & \boxed{2} \end{array} &
\begin{array}{cccc} \boxed{5} & \boxed{6} & & \\ \boxed{4} & \boxed{5} & \boxed{6} & \\ & \boxed{4} & \boxed{5} & \boxed{6} \\ & & \boxed{4} & \boxed{5} \end{array} &
\begin{array}{cccc} \boxed{8} & \boxed{9} & & \\ \boxed{7} & \boxed{8} & \boxed{9} & \\ & \boxed{7} & \boxed{8} & \boxed{9} \\ & & \boxed{7} & \boxed{8} \end{array} \\ \hline
& & & \begin{array}{cccc} \boxed{2} & \boxed{3} & & \\ \boxed{1} & \boxed{2} & \boxed{3} & \\ & \boxed{1} & \boxed{2} & \boxed{3} \\ & & \boxed{1} & \boxed{2} \end{array} &
\begin{array}{cccc} \boxed{5} & \boxed{6} & & \\ \boxed{4} & \boxed{5} & \boxed{6} & \\ & \boxed{4} & \boxed{5} & \boxed{6} \\ & & \boxed{4} & \boxed{5} \end{array}
\end{array}\right)}_{5 \times n_\theta \times n_r}, \tag{5.80}$$

where the single blocks of the sparse Jacobi matrix bands are given by

$$\begin{array}{lll}
\boxed{1} = \dfrac{\partial f^k_{i,j}}{\partial u^l_{i-1,j-1}}, & \boxed{2} = \dfrac{\partial f^k_{i,j}}{\partial u^l_{i-1,j}}, & \boxed{3} = \dfrac{\partial f^k_{i,j}}{\partial u^l_{i-1,j+1}}, \\
\boxed{4} = \dfrac{\partial f^k_{i,j}}{\partial u^l_{i,j-1}}, & \boxed{5} = \dfrac{\partial f^k_{i,j}}{\partial u^l_{i,j}}, & \boxed{6} = \dfrac{\partial f^k_{i,j}}{\partial u^l_{i,j+1}}, \\
\boxed{7} = \dfrac{\partial f^k_{i,j}}{\partial u^l_{i+1,j-1}}, & \boxed{8} = \dfrac{\partial f^k_{i,j}}{\partial u^l_{i+1,j}}, & \boxed{9} = \dfrac{\partial f^k_{i,j}}{\partial u^l_{i+1,j+1}}.
\end{array} \tag{5.81}$$

Note that the indices k and l label the position of the entry in the vertical and horizontal direction of the block, respectively. This corresponds to the following positions in the discretization stencil:

$$\begin{array}{ccccc} {\scriptstyle i-1,j-1} & & {\scriptstyle i-1,j} & & {\scriptstyle i-1,j+1} \\ & \boxed{1} & \boxed{2} & \boxed{3} & \\ {\scriptstyle i,j-1} & \boxed{4} & \boxed{5} & \boxed{6} & {\scriptstyle i,j+1} \\ & \boxed{7} & \boxed{8} & \boxed{9} & \\ {\scriptstyle i+1,j-1} & & {\scriptstyle i+1,j} & & {\scriptstyle i+1,j+1} \end{array} . \tag{5.82}$$

In order to determine the filling factor of $\hat{\boldsymbol{J}}$, i.e. the ratio of nonzero entries to the number of elements, we first look at the number of blocks $\boxed{i}$:

$$\begin{array}{lll} \boxed{1}: (n_r-1)\times(n_\theta-1), & \boxed{2}: (n_r-1)\times n_\theta, & \boxed{3}: (n_r-1)\times(n_\theta-1), \\ \boxed{4}: n_r\times(n_\theta-1), & \boxed{5}: n_r\times n_\theta, & \boxed{6}: n_r\times(n_\theta-1), \\ \boxed{7}: (n_r-1)\times(n_\theta-1), & \boxed{8}: (n_r-1)\times n_\theta, & \boxed{9}: (n_r-1)\times(n_\theta-1). \end{array} \tag{5.83}$$

As the total number of blocks of linear size 5 in the matrix is $(n_r \times n_\theta)^2$, we get for the block filling factor:

$$f_{\text{block fill}} = \frac{9\times n_r\times n_\theta - 6n_r - 6n_\theta + 4}{(n_r\times n_\theta)^2}. \tag{5.84}$$

Here the numerator is the sum of the number of blocks $\boxed{i}$ from Equation (5.83).

Concerning the derivatives (5.69), some are zero for certain indices k, and the filling of the blocks is

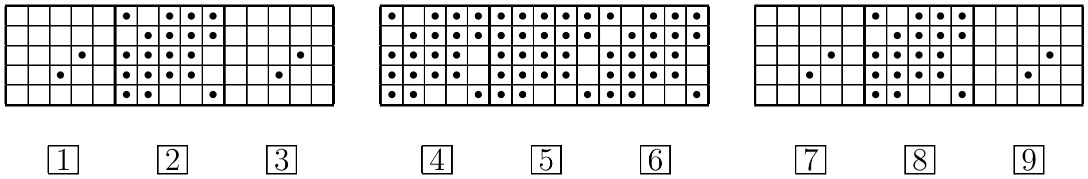

,

i.e. the numbers of elements per block $\boxed{i}$ is

$$\begin{array}{lll} \boxed{1}: 2, & \boxed{2}: 19, & \boxed{3}: 2, \\ \boxed{4}: 19, & \boxed{5}: 21, & \boxed{6}: 19, \\ \boxed{7}: 2, & \boxed{8}: 19, & \boxed{9}: 2. \end{array} \tag{5.85}$$

Combining the number of blocks (5.83) with the number of elements per block (5.85) yields the maximum element filling factor (some entries can still be zero for specific matter distributions and symmetries):

$$f_{\text{element fill}} = \frac{105\times n_r\times n_\theta - 46n_r - 46n_\theta + 8}{(5\times n_r\times n_\theta)^2}. \tag{5.86}$$

Table 5.2 shows some values of the block and element filling factors for sample grid resolutions.

n_r	n_θ	$f_{\text{block fill}}$	$f_{\text{element fill}}$
10	10	7.84×10^{-2}	3.83×10^{-2}
100	100	8.88×10^{-4}	4.16×10^{-4}
200	50	8.85×10^{-4}	4.15×10^{-4}
50	200	8.85×10^{-4}	4.15×10^{-4}
200	200	2.23×10^{-4}	1.04×10^{-4}

Table 5.2: *Block and element filling factors of the Jacobi matrix for sample grid resolutions; note that the filling factor is symmetric with respect to the number of radial and angular grid points* n_r *and* n_θ*. For increasing grid size, the filling factors decrease and the matrices become more sparse.*

However, setting up the Jacobi matrix $\hat{\boldsymbol{J}}$ is not yet the end of the story. It becomes clear from Equation (5.71) that at the grid boundaries, i.e. for indices

$$\begin{array}{lll} i = 1, & i = n_r, & \forall\, j, \\ j = 1, & j = n_\theta, & \forall\, i, \end{array} \tag{5.87}$$

due to the form of discretization of derivatives (5.69), the functions $f^k_{i,j}$ depend on metric quantities $u^n_{l,m}$ which lie on ghost zones outside the numerical grid. This also holds for the Jacobi matrix via Equations (5.81). What still needs to be done is to specify the symmetry and boundary conditions at the grid boundaries, i.e. for the indices given in (5.87). For the metric the general symmetry conditions have been derived in Section 5.1.2, and the boundary conditions are stated in Section 5.1.3. When applied to the discretized equations, we get the following conditions for the unknowns $u^k_{i,j}$ at the boundaries:

$$\begin{array}{|r|r|} \hline \text{center} & u^k_{0,j} = \pm^k_{\text{c}} u^k_{1,j} \\ \hline \text{equator} & u^k_{i,n_\theta+1} = \pm^k_{\text{e}} u^k_{i,n_\theta} \\ & u^k_{n_r+1,n_\theta+1} = \pm^k_{\text{e}} u^k_{n_r+1,n_\theta} \\ \hline \text{polar axis} & u^k_{i,0} = \pm^k_{\text{p}} u^k_{i,1} \\ & u^k_{n_r+1,0} = \pm^k_{\text{e}} u^k_{n_r+1,1} \\ \hline \text{mixed} & u^k_{0,0} = \pm^k_{\text{c}} \pm^k_{\text{p}} u^k_{1,1} \\ & u^k_{0,n_\theta+1} = \pm^k_{\text{c}} \pm^k_{\text{e}} u^k_{1,n_\theta} \\ \hline \end{array} . \tag{5.88}$$

Here $\pm^k_{\text{c}}$, $\pm^k_{\text{e}}$, and $\pm^k_{\text{p}}$ denote the (symmetric or antisymmetric) boundary condition for the unknown quantities u^k at the center, pole, and equator, respectively, as derived in Section 5.1.2.

For the corresponding locations in the Jacobi matrix this implies:

$i=1$ (center)	$i-1,j-1$	$\frac{\partial f^k_{1,j}}{\partial u^l_{0,j-1}} = \pm^l_{\mathrm{c}} \cdot \frac{\partial f^k_{1,j}}{\partial u^l_{1,j-1}}$	ⓐ	$\boxed{1}$
		$\frac{\partial f^k_{1,1}}{\partial u^l_{0,0}} = \pm^l_{\mathrm{c}} \cdot \pm^l_{\mathrm{p}} \cdot \frac{\partial f^k_{1,1}}{\partial u^l_{1,1}}$	ⓑ	
	$i-1,j$	$\frac{\partial f^k_{1,j}}{\partial u^l_{0,j}} = \pm^l_{\mathrm{c}} \cdot \frac{\partial f^k_{1,1}}{\partial u^l_{1,j}}$	ⓒ	$\boxed{2}$
	$i-1,j+1$	$\frac{\partial f^k_{1,j}}{\partial u^l_{0,j+1}} = \pm^l_{\mathrm{c}} \cdot \frac{\partial f^k_{1,j}}{\partial u^l_{1,j+1}}$	ⓓ	$\boxed{3}$
		$\frac{\partial f^k_{1,n_\theta}}{\partial u^l_{0,n_\theta+1}} = \pm^l_{\mathrm{c}} \cdot \pm^l_{\mathrm{e}} \cdot \frac{\partial f^k_{1,n_\theta}}{\partial u^l_{1,n_\theta}}$	ⓔ	
$j=1$ (polar axis)	$i-1,j-1$	$\frac{\partial f^k_{i,1}}{\partial u^l_{i-1,0}} = \pm^l_{\mathrm{p}} \cdot \frac{\partial f^k_{i,1}}{\partial u^l_{i-1,1}}$	ⓕ	$\boxed{1}$
		$\frac{\partial f^k_{1,1}}{\partial u^l_{0,0}} = \pm^l_{\mathrm{p}} \cdot \pm^l_{\mathrm{c}} \cdot \frac{\partial f^k_{1,1}}{\partial u^l_{1,1}}$	ⓖ	
	$i,j-1$	$\frac{\partial f^k_{i,1}}{\partial u^l_{i,0}} = \pm^l_{\mathrm{p}} \cdot \frac{\partial f^k_{i,1}}{\partial u^l_{i,1}}$	ⓗ	$\boxed{4}$
	$i+1,j-1$	$\frac{\partial f^k_{i,1}}{\partial u^l_{i+1,0}} = \pm^l_{\mathrm{p}} \cdot \frac{\partial f^k_{i,1}}{\partial u^l_{i+1,1}}$	ⓘ	$\boxed{7}$
		$\frac{\partial f^k_{n_r,1}}{\partial u^l_{n_r+1,0}} = 0$	ⓙ	
$j=n$ (equator)	$i-1,j+1$	$\frac{\partial f^k_{i,n_\theta}}{\partial u^l_{i-1,n_\theta+1}} = \pm^l_{\mathrm{e}} \cdot \frac{\partial f^k_{i,n_\theta}}{\partial u^l_{i-1,n_\theta}}$	ⓚ	$\boxed{3}$
		$\frac{\partial f^k_{1,n_\theta}}{\partial u^l_{0,n_\theta+1}} = \pm^l_{\mathrm{e}} \cdot \pm^l_{\mathrm{c}} \cdot \frac{\partial f^k_{1,n_\theta}}{\partial u^l_{1,n_\theta}}$	ⓛ	
	$i,j+1$	$\frac{\partial f^k_{i,n_\theta}}{\partial u^l_{i,n_\theta+1}} = \pm^l_{\mathrm{e}} \cdot \frac{\partial f^k_{i,n_\theta}}{\partial u^l_{i,n_\theta}}$	ⓜ	$\boxed{6}$
	$i+1,j+1$	$\frac{\partial f^k_{i,n_\theta}}{\partial u^l_{i+1,n_\theta+1}} = \pm^l_{\mathrm{e}} \cdot \frac{\partial f^k_{i,n_\theta}}{\partial u^l_{i+1,n_\theta}}$	ⓝ	$\boxed{9}$
		$\frac{\partial f^k_{n_r,n_\theta}}{\partial u^l_{n_r+1,n_\theta+1}} = 0$	ⓞ	

. (5.89)

With ⓘ we have labeled the different symmetry conditions, and the $\boxed{i}$ refer to the derivatives given in Equation (5.81). Note that the following symmetry conditions are identical: ⓑ = ⓖ, ⓔ = ⓛ.

Assuming the metric quantities to be constant at the outer radial boundary, as specified in Section 5.1.3, the outer boundary of the grid at $i = m+1$ has no effect on the Jacobi matrix structure, as the corresponding derivatives vanish to 2nd order (elements ⓙ and ⓞ).

Taking these symmetry conditions into account, the Jacobi matrix has to be extended by additional entries. In practice this is done by adding to the Jacobi matrix $\hat{\boldsymbol{J}}$ a symmetry matrix $\hat{\boldsymbol{J}}_{\mathrm{symm}}$:

$$\hat{\boldsymbol{J}}_{\mathrm{tot}} = \hat{\boldsymbol{J}} + \hat{\boldsymbol{J}}_{\mathrm{symm}}. \tag{5.90}$$

The locations of the blocks $\textcircled{\textit{i}}$ in the symmetry matrix are:

$$\hat{\boldsymbol{J}}_{\text{symm}} = \left(\begin{array}{c|c|c|c|c}
\begin{matrix} \textcircled{x} & \textcircled{d} & & \\ \textcircled{a} & \textcircled{c} & \textcircled{d} & \\ & \textcircled{a} & \textcircled{c} & \textcircled{d} \\ & & \textcircled{a} & \textcircled{y} \end{matrix} & \begin{matrix} \textcircled{i} & \\ & \\ & \\ & \textcircled{n} \end{matrix} & & & \\
\hline
\begin{matrix} \textcircled{f} & \\ & \\ & \textcircled{k} \end{matrix} & \begin{matrix} \textcircled{h} & \\ & \\ & \textcircled{m} \end{matrix} & \begin{matrix} \textcircled{i} & \\ & \\ & \textcircled{n} \end{matrix} & & \\
\hline
 & \ddots & \ddots & \ddots & \\
\hline
 & & \begin{matrix} \textcircled{f} & \\ & \\ & \textcircled{k} \end{matrix} & \begin{matrix} \textcircled{h} & \\ & \\ & \textcircled{m} \end{matrix} & \begin{matrix} \textcircled{i} & \\ & \\ & \textcircled{n} \end{matrix} \\
\hline
 & & & \begin{matrix} \textcircled{f} & \\ & \\ & \textcircled{k} \end{matrix} & \begin{matrix} \textcircled{h} & \\ & \\ & \textcircled{m} \end{matrix}
\end{array}\right), \qquad (5.91)$$

$$\text{with} \begin{cases} \textcircled{x} = \textcircled{c} + \textcircled{g} + \textcircled{h}, \\ \textcircled{y} = \textcircled{c} + \textcircled{l} + \textcircled{m}. \end{cases}$$

Each 5×5 block $\textcircled{\textit{i}}$ is identical to the corresponding block $\boxed{j}$ in the rightmost column of (5.89), except that it is preceeded by either a plus or minus sign, depending on the appropriate symmetry condition.

By comparing the block filling for the Jacobian matrix and the symmetry matrix, it is obvious that the sparsity pattern of $\hat{\boldsymbol{J}}$ is not changed $\hat{\boldsymbol{J}}_{\text{symm}}$.

The linear problem which has to be solved during each Newton–Raphson iteration is thus defined by

$$\hat{\boldsymbol{J}}^{s}_{\text{tot}} \Delta \hat{\boldsymbol{u}}^{s} = \hat{\boldsymbol{f}}^{s}. \qquad (5.92)$$

5.6.3 Numerical Methods for Solving the Linear Problem

As we will show in Section 5.6.4, the performance of the evolution problem is dominated by the computation time spent in the metric solver, and thus by the computational efficiency of the linear solver. Therefore we have to make sure that we solve the linear problem as efficiently as possible. This boils down to the requirement of finding a fast numerical method for solving the sparse linear matrix problem (5.92). As our collapse simulations have been performed on a NEC SX-5 vector supercomputer, the method of choice should also exploit the specific advantages of this computer architecture.

The simplest solver for a linear problem one could think of, is the direct (exact) inversion of a matrix, with the use of e.g. Gauss–Jordan elimination, or exact LU decomposition [100]. On the other hand, matrix inversion can also be accomplished by approximation and iteration methods like incomplete LU factorization. As these methods converge to the correct solution with some specified accuracy, they are for numerical purposes practically as good as exact solvers. Still these methods make no assumption about the structure of the linear problem, and thus do not utilize the sparsity of the matrix to reduce the complexity of the algorithm.

However, there are linear solvers especially designed for sparse linear problems, which are, if applied to the appropriate problem, much faster than general linear solvers. Furthermore, as the solution of large sparse linear problems is routinely encountered in numerical codes, there are a number of widespread and tested standard methods for solving these. Among those methods are successive over-relaxation (SSOR), conjugate gradient (CG) methods, etc. [105].

Nevertheless, despite of the existence of rather specialized and highly efficient sparse linear solvers, we have found that for our particular linear problem (5.92) our own implementation of an especially tailored solver method shows the best computational performance. To demonstrate that, we compare the ability of the following methods to deal with the linear problem resulting from the Newton–Raphson iteration of the discretized metric equations:

Gauss–Jordan elimination:

This is a direct method to invert the matrix $\hat{\boldsymbol{J}}^s$ in order to find the solution vector $\Delta\hat{\boldsymbol{u}}^s$. It assumes nothing about the filling pattern or sparsity of the matrix. We have implemented a standard Gauss–Jordan elimination scheme with full pivoting [100]. This simple method is extremely slow for all but small grid sizes, as it is an $(n_r \times n_\theta)^3$ process. Therefore it is of very limited practical use, and usually cannot be the basis of a linear solver for numerical simulations. On the other hand, the advantage of any direct method is that the number of arithmetic operations for the solution is entirely determined by the number of unknowns, and therefore known a priori.

Conjugate gradient methods for sparse matrices:

As an iterative method, the conjugate gradient (CG) method approaches the solution of the linear problem through a sequence of approximations, until some specified level of accuracy r_{tol} with respect to the exact solution is reached:

$$\max\left(\hat{\boldsymbol{J}}^s_{\mathrm{tot}}\Delta\hat{\boldsymbol{u}}^s - \hat{\boldsymbol{f}}^s\right) \le r_{\mathrm{tol}}. \tag{5.93}$$

For iterative methods it is often crucial for the speedup of convergence to apply a preconditioner to the linear problem. A preconditioner maps the original linear system

$$\hat{\boldsymbol{J}}^s_{\mathrm{tot}}\Delta\hat{\boldsymbol{u}}^s = \hat{\boldsymbol{f}}^s \tag{5.94}$$

onto a system

$$\bar{\boldsymbol{J}}^s_{\mathrm{tot}}\Delta\bar{\boldsymbol{u}}^s = \bar{\boldsymbol{f}}^s, \tag{5.95}$$

such that

$$\bar{\boldsymbol{J}}^s_{\mathrm{tot}} = \boldsymbol{P}_{\mathrm{l}}^{-1}\hat{\boldsymbol{J}}^s_{\mathrm{tot}} \simeq \boldsymbol{I} \tag{5.96}$$

for a left preconditioner $\boldsymbol{P}_{\text{l}}$, or

$$\bar{\boldsymbol{J}}^{s}_{\text{tot}} = \hat{\boldsymbol{J}}^{s}_{\text{tot}} \boldsymbol{P}_{\text{r}}^{-1} \simeq \boldsymbol{I} \tag{5.97}$$

for a right preconditioner $\boldsymbol{P}_{\text{r}}$ (here $\boldsymbol{I}$ is the diagonal unity matrix). For a good choice of the preconditioner matrix $\boldsymbol{P}$ the new linear system exhibits better convergence characteristics. In order to achieve this, the matrix $\boldsymbol{P}$ should be as close to the original matrix $\hat{\boldsymbol{J}}^{s}_{\text{tot}}$ as possible, as well as invertible in a simple and fast way. Thus, in preconditioning one has to balance the reduction in the number of iterations against additional computational costs for the calculation and inversion of the preconditioner matrix.

For testing our code we have implemented a bi-conjugate gradient stabilized (BiCGStab) method, which can make use of several preconditioning methods like inversion of the diagonal 5×5 blocks of the Jacobi matrix (which exploits the diagonal dominance of $\hat{\boldsymbol{J}}^{s}_{\text{tot}}$), or incomplete *LU* decomposition (where the *LU* factorization of the Jacobi matrix is used): $\boldsymbol{P} = \boldsymbol{LDU}$ with $\boldsymbol{L}$ ($\boldsymbol{U}$) being the lower (upper) triangular matrix with unit diagonal elements, and $\boldsymbol{D}$ being the diagonal matrix.

If the preconditioning does not outweigh the solution of the linear problem, this is a $(n_r \times n_\theta)^2$ process. However, for large matrices, the preconditioning is generally slow and does not vectorize well, and convergence problems with the BiCGStab solver are often encountered.

Block tridiagonal sweeping method:

This method is especially designed for block tridiagonal matrices, i.e. matrices $\boldsymbol{A}$ which consist of a sequence of blocks $\boldsymbol{D}_i$ along the diagonal, and of blocks $\boldsymbol{L}_i$ and $\boldsymbol{R}_i$ directly left and right of these (here for $i = 1, \ldots, 5$):

$$\boldsymbol{A} = \left(\begin{array}{c|c|c|c|c} \boldsymbol{D}_1 & \boldsymbol{R}_1 & & & \\ \hline \boldsymbol{L}_2 & \boldsymbol{D}_2 & \boldsymbol{R}_2 & & \\ \hline & \boldsymbol{L}_3 & \boldsymbol{D}_3 & \boldsymbol{R}_3 & \\ \hline & & \boldsymbol{L}_4 & \boldsymbol{D}_4 & \boldsymbol{R}_4 \\ \hline & & & \boldsymbol{L}_5 & \boldsymbol{D}_5 \end{array}\right) . \tag{5.98}$$

All other elements of $\boldsymbol{A}$ must vanish. A solution of the linear problem defined by $\boldsymbol{A}$ is then obtained by sweeping down along the diagonal from the upper left corner to the lower right corner. During this downward sweep the submatrices $\boldsymbol{L}_i$, $\boldsymbol{D}_i$, and $\boldsymbol{R}_i$ have to be inverted. In an upward sweep the solution vector is recursively extracted from the inverted submatrices:

down-sweep: 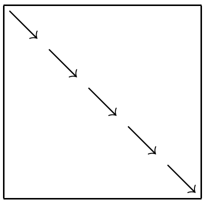 , up-sweep: 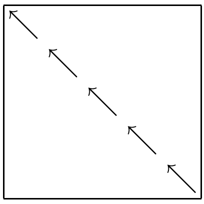 .

As this is the method of choice in our solver for the metric equations, we explain the sweeping method in more detail in the following.

For the sweeping method to be applicable, the matrix $\boldsymbol{A}$ must be of the form (5.98). However, the combined Jacobi and symmetry matrix, which defines the linear problem we have to solve during each Newton–Raphson iteration, has nine bands of blocks rather than three. The bands $\boxed{1}$, $\boxed{2}$, $\boxed{3}$, and $\boxed{7}$, $\boxed{8}$, $\boxed{9}$ are furthermore separated from the diagonal bands $\boxed{4}$, $\boxed{5}$, $\boxed{6}$. Nevertheless we can combine the left three, the middle three, and the right three bands, and collect them in the left, diagonal, and right band of submatrices $\boldsymbol{L}_i$, $\boldsymbol{D}_i$, and $\boldsymbol{R}_i$, respectively. Then the matrix $\hat{\boldsymbol{J}}$ has the required structure of $\boldsymbol{A}$ in Equation (5.98). The tradeoff of this collecting is that the sweeping method only makes the assumption of zero elements outside the blocks $\boldsymbol{L}_i$, $\boldsymbol{D}_i$, and $\boldsymbol{R}_i$, whereas most of the block elements of the submatrices in the tridiagonal form of $\hat{\boldsymbol{J}}$ will be empty. Thus we cannot exploit the sparsity to the full extent when we use the sweeping method.

The iterative scheme for this method then goes as follows: First, as already mentioned, we combine the nonzero entries of $\hat{\boldsymbol{J}}_{\mathrm{tot}}$ into blocks $\boldsymbol{L}_i$, $\boldsymbol{D}_i$ and $\boldsymbol{R}_i$ of size $5 \times n_\theta$ $(i = 1, \ldots, n_r)$, such that we get a tridiagonal band matrix with three bands of these larger blocks. We also divide the vector of unknowns $\Delta\hat{\boldsymbol{u}}$ and the function vector $\hat{\boldsymbol{f}}$ into n_r chunks $\Delta\hat{\boldsymbol{u}}_i$ and $\hat{\boldsymbol{f}}_i$ of size $5 \times n_\theta$:

$$\hat{\boldsymbol{J}}_{\mathrm{tot}} = \left(\begin{array}{c|c|c|c|c} \boldsymbol{D}_1 & \boldsymbol{R}_1 & & & \\ \hline \boldsymbol{L}_2 & \boldsymbol{D}_2 & \boldsymbol{R}_2 & & \\ \hline & \ddots & \ddots & \ddots & \\ \hline & & \ddots & \ddots & \ddots \\ \hline & & & \boldsymbol{L}_{n_r} & \boldsymbol{D}_{n_r} \end{array}\right), \quad \Delta\hat{\boldsymbol{u}} = \left(\begin{array}{c} \Delta\hat{\boldsymbol{u}}_1 \\ \hline \Delta\hat{\boldsymbol{u}}_2 \\ \hline \vdots \\ \hline \vdots \\ \hline \Delta\hat{\boldsymbol{u}}_{n_r} \end{array}\right), \quad \hat{\boldsymbol{f}} = \left(\begin{array}{c} \hat{\boldsymbol{f}}_1 \\ \hline \hat{\boldsymbol{f}}_2 \\ \hline \vdots \\ \hline \vdots \\ \hline \hat{\boldsymbol{f}}_{n_r} \end{array}\right). \tag{5.99}$$

Then the linear problem can be written as

$$\boldsymbol{L_i}\Delta\hat{\boldsymbol{u}}_{i-1} + \boldsymbol{D_i}\Delta\hat{\boldsymbol{u}}_i + \boldsymbol{R_i}\Delta\hat{\boldsymbol{u}}_{i+1} = \hat{\boldsymbol{f}}_i. \tag{5.100}$$

Introducing the two definitions

$$\hat{\boldsymbol{r}}_i = \Delta\hat{\boldsymbol{u}}_i - \boldsymbol{Y}_i\Delta\hat{\boldsymbol{u}}_{i+1}, \qquad \text{and} \quad \boldsymbol{M}_i = \boldsymbol{L}_i\boldsymbol{Y}_{i-1} + \boldsymbol{D}_i, \tag{5.101}$$

we get the following relation:

$$\boldsymbol{M}_i\hat{\boldsymbol{r}}_i + \boldsymbol{M}_i\boldsymbol{Y}_i\Delta\hat{\boldsymbol{u}}_{i+1} = \hat{\boldsymbol{f}}_i - \boldsymbol{L}_i\hat{\boldsymbol{r}}_{i-1} - \boldsymbol{R}_i\Delta\hat{\boldsymbol{u}}_{i+1}. \tag{5.102}$$

A comparison of coefficients in this equation yields recursive equations for $\hat{\boldsymbol{r}}_i$ and $\boldsymbol{Y}_i$:

$$\boldsymbol{M}_i\hat{\boldsymbol{r}}_i = \hat{\boldsymbol{f}}_i - \boldsymbol{L}_i\hat{\boldsymbol{r}}_{i-1}, \tag{5.103}$$

$$\boldsymbol{M}_i\boldsymbol{Y}_i = -\boldsymbol{R}_i. \tag{5.104}$$

So in the end we have a recursive scheme for solving the linear problem: We start with setting $\hat{\boldsymbol{r}}_0 = 0$ and $\boldsymbol{Y}_0 = 0$ as initial values for calculating the next values in the downward sweep:

$$\hat{\boldsymbol{r}}_i = \boldsymbol{M}_i^{-1}(\hat{\boldsymbol{f}}_i - \boldsymbol{L}_i\hat{\boldsymbol{r}}_{i-1}), \qquad \boldsymbol{Y}_i = -\boldsymbol{M}_i^{-1}\boldsymbol{R}_i. \tag{5.105}$$

This involves the inversion of the dense submatrix $\boldsymbol{M}_i$ (or more generally, the solution of the linear problem defined by $\boldsymbol{M}_i$), which has the size $5 \times n_\theta$. (Note that even if the initial submatrices $\boldsymbol{L}_i$, $\boldsymbol{D}_i$, and $\boldsymbol{R}_i$ were sparse, the matrices $\boldsymbol{M}_i$ will in general be dense.) For solving the recursive submatrix equation (5.105), we use a standard *LU* decomposition scheme for dense matrices, as e.g. implemented in the LAPACK numerical library.

When all the $\hat{\boldsymbol{r}}_i$ and $\boldsymbol{Y}_i$ are calculated, we can extract the solution vector in a downward sweep from Equation (5.101), where we use $\Delta\hat{\boldsymbol{u}}_{n_r+1}$ as starting value.

As the sweeping method is a recursive scheme, we can vectorize only over the inner submatrix inversion part. However, even for moderately large n_θ we are able to get into vector register saturation on the computers we use. In total the sweeping method exhibits an $n_r \times n_\theta^2$ behavior, and is thus in performance superior to both the Gauss–Jordan and the BiCGStab methods, particularly as it does not to suffer from convergence problems due to the direct solver nature of the iterative sweeping part of the algorithm.

5.6.4 Computational Performance of the Metric Solver – Metric Extrapolation

In order to estimate the accuracy of the numerical solution of the metric equations, we have to address two distinct questions: Firstly, how well is the analytic solution of the equations approximated by the numerical solution obtained by solving the discretized equations. And secondly, to what degree of numerical precision are the discretized metric equations solved by the Newton–Raphson scheme, which is obviously an iterative and thus an approximate solver.

The relation between the discretized equations and the analytic formulation is straightforward. As the derivatives showing up in Equation (5.69) are second order accurate in both Δr_i and $\Delta\theta$, we can infer that the discretization method is second order accurate. Therefore, the difference between the analytic solution and the exact solution of the discretized equations will vanish with the inverse square of the grid resolution. This second order accurate behavior of the discretization scheme, and its implementation in our code, will be demonstrated in Section 6.7.

However, we still have to ensure that the discretized equations are solved accurately enough. In Section 5.6.2 we have shown how the nonlinear problem can be solved by an iteration involving the subsequent solution of linear problems. We can assume that the linear solvers introduced in Section 5.6.3 yield a solution of the linear problems which is accurate up to machine precision (at least for the sweeping method, which is the one we use for our simulations). Therefore, if we get convergence of the Newton–Raphson iteration with some specified tolerance limit, we can be sure that the numerical nonlinear problem is solved to the desired level of accuracy.

There are two tolerance measures we utilize to control convergence of the Newton–Raphson method to the actual solution. One is the maximum increment of the solution vector over the grid:

$$\Delta\hat{u}^s_{\max} = \max\left(\Delta\hat{\boldsymbol{u}}^s\right) = \max\left(\Delta\hat{u}^s_{\hat{\imath}}\right). \tag{5.106}$$

The max function involved here is simply the maximum of the absolute value of the vector elements.

As the machine precision of floating point arithmetics on the computers we have run our simulations on is somewhat better than 10^{-15}, the tolerance level $\Delta\hat{u}^s_{\max} \leq 10^{-15}$, which we have set, is a good convergence criterion. We were able to meet this convergence criterion in all our computations.

The other accuracy criterion which is implemented in our code is based on the maximum residual of the function vector on the grid:

$$\hat{f}^s_{\max} = \max\left(\hat{\boldsymbol{f}}(\hat{\boldsymbol{u}}^s)\right) = \max\left(\hat{f}_{\hat{\imath}}(\hat{u}^s_{\hat{\jmath}})\right). \tag{5.107}$$

If $\hat{\boldsymbol{u}}^s$ is the exact solution of the discretized equations $\hat{\boldsymbol{f}}(\hat{\boldsymbol{u}}^s) = 0$, then $\hat{f}^s_{\max} = 0$. Thus the deviation of $\hat{f}^s_{\max}$ from zero in combination with the convergence criterion is an excellent measure of the performance of the Newton–Raphson solver. In practical applications of the nonlinear solver, we use a threshold for the function residual of $\hat{f}^s_{\max} \leq 10^{-18}$.

A combination of the two criteria (5.106) and (5.107) gives us confidence that the Newton–Raphson solver converges to the correct solution with the desired accuracy. In Figure 5.4 we show how $\Delta\hat{u}^s_{\max}$ and $\hat{f}^s_{\max}$ decrease with the number of iterations s in the metric computation of a typical core collapse model around the time of maximum density. Both of these measures exhibit an inverse exponential behavior until saturation is reached when the increment $\hat{\boldsymbol{u}}^s$ comes into the vicinity of machine precision.

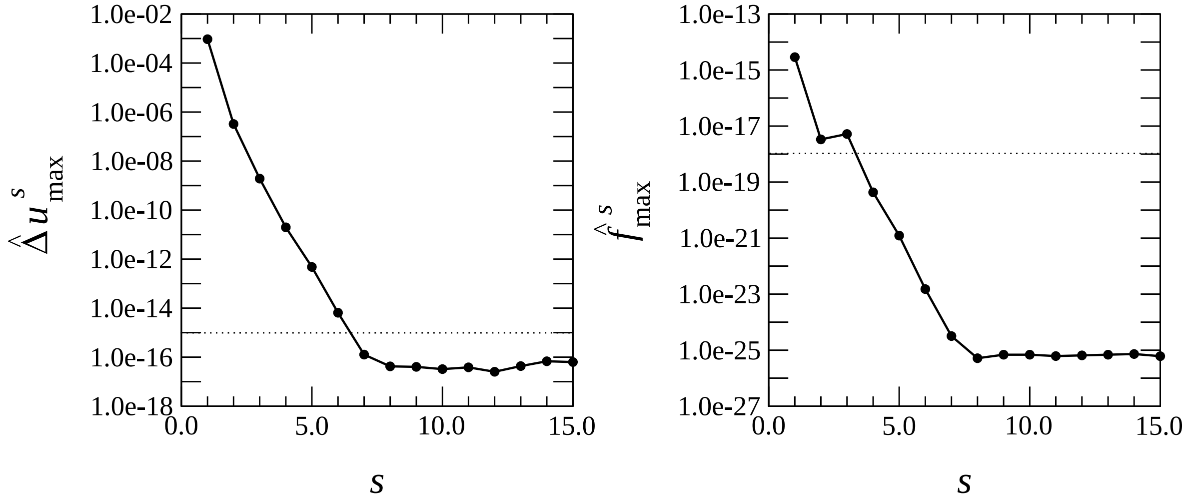

Figure 5.4: *Decrease of the maximum increment of the unknown vector* $\Delta\hat{u}^s_{\max}$ *(left panel) and of the function residual* $\hat{f}^s_{\max}$ *(right panel) with the number of Newton–Raphson iterations* s *for a typical metric computation: Until* $\Delta\hat{u}^s_{\max}$ *reaches the limit set by the machine precision of the computer at* $s \approx 8$*, both tolerance measures decrease exponentially. After that they saturate well below the precision thresholds used in the code, which are marked by the horizontal dotted lines. The threshold imposed on the function residual is used only to detect total failures of the Newton–Raphson method.*

In Section 5.6.2 we have seen that the iterative solution of the linear problem in the metric solver is a computationally very expensive procedure. We have performed comparisons between the execution time for one metric solution (for different linear solver methods) and one hydrodynamic time step; these demonstrate that, particularly for grid sizes appropriate for our collapse simulations, the computation is by far dominated by the metric solver. It is therefore essential to have a linear solution method at hand which is most efficient. In our case this is the up/down sweeping method introduced in Section 5.6.2. Still one metric computation can be as time-consuming as about 100 hydrodynamic time steps!

On the other hand there is a complementary approach to reduce the overall computational time for the evolution: As long as the metric quantities do not change too rapidly with time, it is a fair approximation not to solve for the metric at every time step. Therefore, one can introduce a sequence of "metric" time slices $\Sigma_{t^{\hat{n}}}$, which are a subset of the "hydrodynamic" time slices Σ_{t^n}, on which the hydrodynamic quantities are evolved:

$$\{\Sigma_{t^{\hat{n}}}\} \subset \{\Sigma_{t^n}\}. \tag{5.108}$$

In practice this means that the metric is calculated only on some of the "hydrodynamic" time slices, viz. on the "metric" time slices. We introduce the metric resolution parameter $\Delta n_{\mathrm{metric}}$, such that $\mathrm{mod}\,(n, \Delta n_{\mathrm{metric}}) = 0$. Then $\Delta n_{\mathrm{metric}}$ expresses the difference in time steps between two "hydrodynamic" time slices on which the metric is calculated. The time difference between two metric calculations is $\Delta t^{\hat{n}}$. If the interval $\Delta t^{\hat{n}}$ between metric calculations can be chosen to be large compared to Δt^n without sacrificing numerical accuracy of the evolution, the resulting payoff in saving of computer time can be enormous.

During the simulation, the metric resolution parameters should vary with time in a way which adapts to the specific phase of the collapse scenario. During the infall phase, it can be chosen to be comparatively large, whereas around bounce time, where the highest densities, the largest variations of the hydrodynamic and metric quantities, and the most significant deviations from spherical symmetry are encountered, it must be reset to smaller values. After the ring-down phase, when the proto-neutron star has essentially settled down to a quasi-equilibrium state, with the shock wave traveling through the outer layers of the iron core, it can be increased once more. The case of distinct "multiple bounces" deserves special attention: Here the metric resolution has to be refined during each of the multiple bounces, where the highest densities are being encountered.

We have chosen to split the core collapse scenario into three different phases: The pre-bounce phase lasts from the start of the evolution until the maximum density on the grid ρ_{max} reaches a threshold density, which is a specified fraction of the nuclear density: $\rho_{\mathrm{thr}} \equiv f_{\mathrm{refine}}\rho_{\mathrm{nuc}}$. During that phase the metric is calculated every $n^{(1)}_{\mathrm{metric}}$ "hydrodynamic" time steps. The following bounce phase then lasts for a certain time $\Delta t_{\mathrm{refine}}$, and the metric is solved on every $n^{(2)}_{\mathrm{metric}}$th time slice. After this time interval, in the post-bounce phase, the metric resolution parameters is set to $n^{(3)}_{\mathrm{metric}}$.

In multiple bounce scenarios, i.e. for a collapse where the maximum density has multiple distinct peaks in time, often separated by several 10 ms, the evolution time is split into a series of consecutive bounce phases interspersed with phases, where the density is below the threshold marked by ρ_{thr}. During the bounce phases, the metric resolution is given by $n^{(2)}_{\mathrm{metric}}$, and before the first bounce and in between the bounces by $n^{(1)}_{\mathrm{metric}}$.

The collapse phases introduced above are sketched in Figure 5.5, while the actual values for

f_{refine} and $\Delta t_{\mathrm{refine}}$ used in our simulation are summarized for the two different collapse types in Table 5.3.

Collapse type	f_{refine}	ρ_{thr} [10^{14} g cm^{-3}]	$\Delta t_{\mathrm{refine}}$ [ms]	$n_{\mathrm{metric}}^{(1)}$	$n_{\mathrm{metric}}^{(2)}$	$n_{\mathrm{metric}}^{(3)}$
Regular collapse	0.1	0.2	5.0	100 pre-bounce phase	10 bounce phase	50 post-bounce phase
Multiple bounce collapse	0.02	0.04	—	100 inter-bounce phase	10 bounce phase	—

Table 5.3: *Values for the metric refinement parameters* f_{refine}*,* ρ_{thr}*,* $\Delta t_{\mathrm{refine}}$*, and* n_{metric} *for regular collapse models and for multiple bounce scenarios, as used in our simulations.*

Obviously, in reality the metric quantities ϕ, α, and β^i are not constant between the metric computations done on the "metric" time slices $\Sigma_{t^{\hat{n}}}$. In order to approximate the actual evolution of the metric on the "hydrodynamic" time slices (when it is not calculated), the state of the metric at old "metric" time slices can be used to extrapolate the metric quantities forward in time. If the metric is kept constant between computations, we only have to keep its state from the last "metric" time slice. For linear (parabolic) extrapolation, the metric from the last two (three) "metric" time slices has to be retained in memory. Figure 5.6 schematically shows the approximation of the actual metric calculated at every time slice by a metric which is calculated at every 10th time step, and is kept constant or is linearly or parabolically extrapolated in between.

Tests of collapse models with different intervals of metric calculation will be shown in Section 6.7.2. They demonstrate clearly that our choice of values for the metric resolution parameters, which is given in Table 5.3, is appropriate to obtain the desired accuracy. Due to the superior accuracy of the 3rd order parabolic metric extrapolation scheme, as demonstrated in Figure 5.6, we use this method in all our simulations.

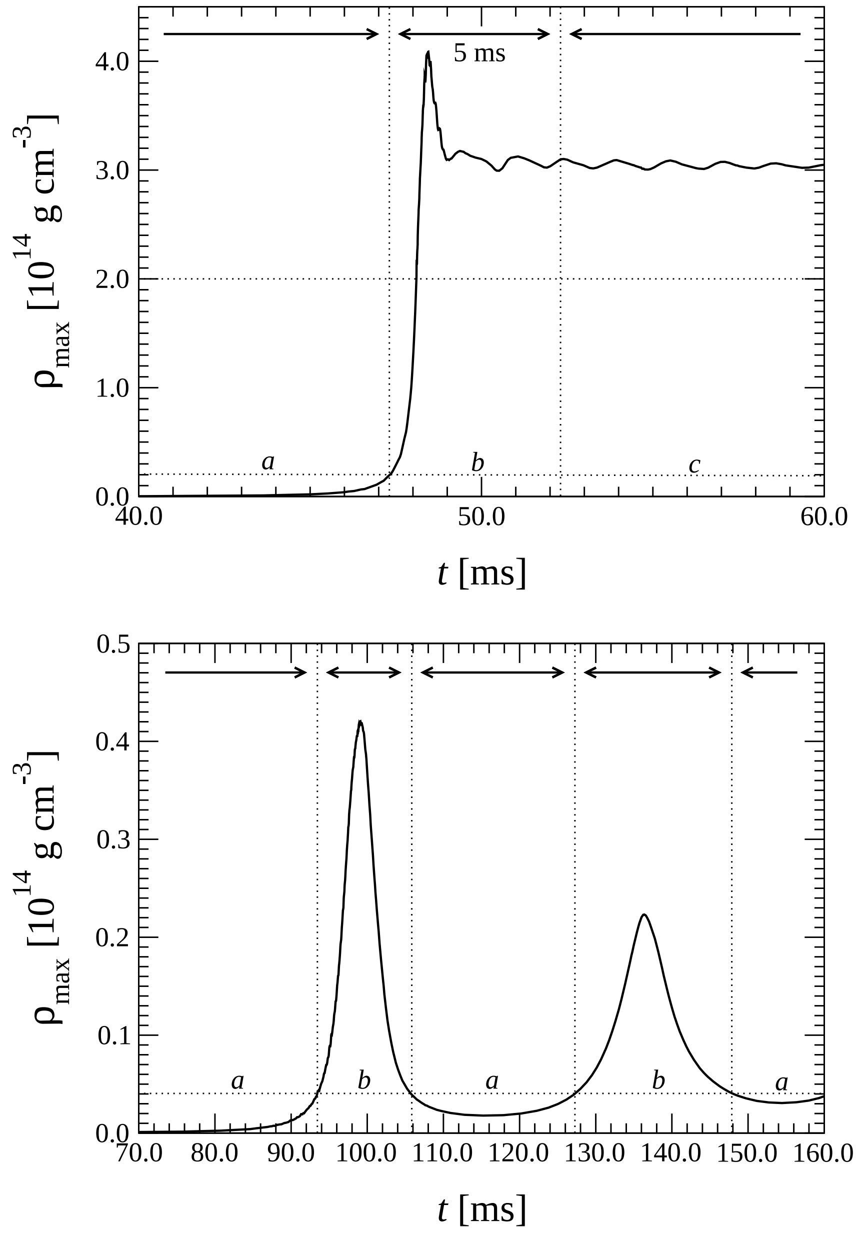

Figure 5.5: *The collapse phases used for specifying the metric resolution for regular collapse models (upper panel) and multiple bounce collapse models (lower panel): In a regular collapse, the metric is calculated every on* $n^{(1)}_{\mathrm{metric}}$*th time step in the pre-bounce phase (a). In the bounce phase (b), which starts when the maximum density* ρ_{max} *is higher than* $0.1\rho_{\mathrm{nuc}}$*, the metric is calculated every* $n^{(2)}_{\mathrm{metric}}$*th time step. After* 5 ms*, the post-bounce phase begins (c), with the metric being calculated every* $n^{(3)}_{\mathrm{metric}}$*th time step. In a multiple bounce model, the inter-bounce phases (a), during which the metric is calculated on every* $n^{(1)}_{\mathrm{metric}}$*th time step, are interspersed with the bounce phases (b), where the metric is calculated every* $n^{(2)}_{\mathrm{metric}}$*th time step. Due to the lower average maximum densities, in these models the density threshold is specified by* $\rho_{\mathrm{max}} \geq 0.02\rho_{\mathrm{nuc}}$.

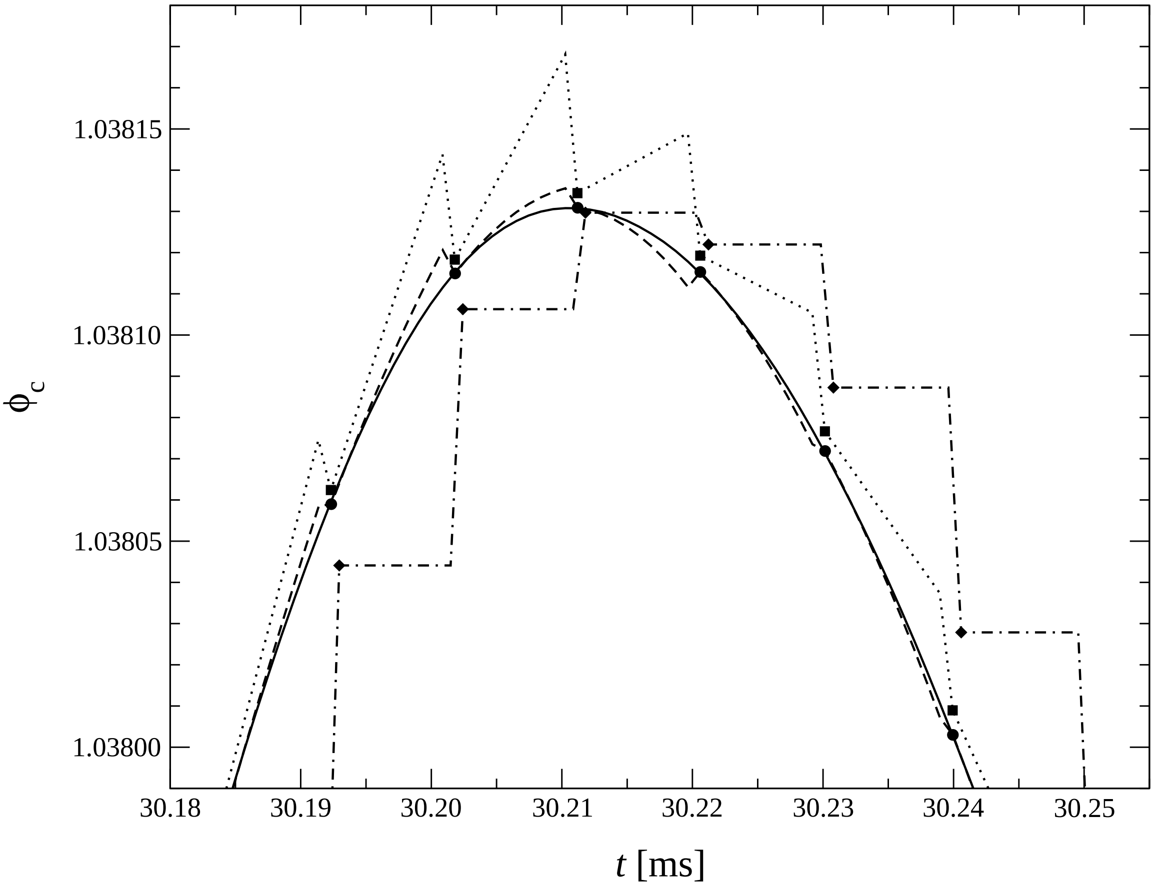

Figure 5.6: *Approximation of the metric evolution by extrapolation: The evolution of the central value of the conformal factor quantity* ϕ_{c} *during core bounce, which is calculated at every time step (solid line), is very well approximated by a parabolic extrapolation of the metric which is calculated at every 10th time step (dashed line, circles). If the extrapolation scheme is linear (dotted line, squares) or constant (dashed-dotted lines, diamonds), the approximation is less accurate. The symbols mark the instants when the metric is actually calculated. The model used for this plot is* A1B3G5 *in low grid resolution; for the usual resolution of* 200×30 *grid points (see Section 6.7.2), deviations between the different metric extrapolation schemes are hardly visible.*

Chapter 6

Tests

As our numerical code combines many different numerical techniques, and has been written from scratch, in this section we present a series of tests which have been performed to check whether the code e.g. can maintain long-term stability, yields the correct numerical evolution behavior for analytically known problems, produces appropriate results for test problems when compared to other relativistic hydrodynamic codes, and has sufficient accuracy.

6.1 Relativistic Shock Tube Tests

Shock tube tests can efficiently test the ability of a code to handle shock fronts. This is a severe and mandatory test to validate a code which is based on high-resolution shock-capturing methods for the hydrodynamic evolution. Normally, for smooth matter distributions without the presence of discontinuities, HRSC codes solve many “microscopic” Riemann problems at the level of grid cells by representing the smooth data by a discontinuous distribution. In a shock tube test, a “macroscopic” Riemann problem has to be solved. Initial data are given for a fluid system which has two states of constant pressure, density and velocity, initially separated by a boundary. When these data are evolved in time, one gets a combination of constant states separated by shocks, contact discontinuities, and rarefaction waves. The Riemann problem can be calculated analytically even in relativity [77], and thus we can compare the numerical results against the analytic solution in a straightforward way.

As sample shock tube tests we have performed simulations of the two relativistic shock tube problems analyzed by Martí and Müller [77]. The initially constant states on the left and right side of the discontinuity are given in Table 6.1. Both cases are computed in a flat one-dimensional Minkowski spacetime using Cartesian coordinates in an interval $x \in [0, 1]$. The EoS is assumed to be polytropic with an adiabatic index $\gamma = 5/3$, and the initial discontinuity is placed at $x = 0.5$. Following [77], we also set $P_\mathrm{r} = 0.66 \times 10^{-6}$ in problem 2, since, as any other hydrodynamics code, our code cannot handle zero pressure regions. The grid used in the simulations consists of 500 equidistant zones. The results for the mildly relativistic problem 1 are shown in Figure 6.1, and for the more difficult relativistic blast wave problem 1 in Figure 6.2, both after an evolution time of $t_{\text{final}} = 0.25$. In both cases the profiles of the density ρ, the pressure P, and the velocity v_x reproduce the analytic solution very well. The typical nonlinear features of a Riemann problem solution like rarefaction wave, contact discontinuity, or shock front are resolved properly. In those runs we have used PPM reconstruction.

	Problem 1		Problem 2	
	left state	right state	left state	right state
ρ	10.0	1.0	1.0	1.0
P	13.3	0.0	10^3	10^{-2}
v_x	0.0	0.0	0.0	0.0

Table 6.1: *Density ρ, pressure P, and velocity v_x initial values for the left and right states of the relativistic shock tube problems 1 and 2 of Martí and Müller [77].*

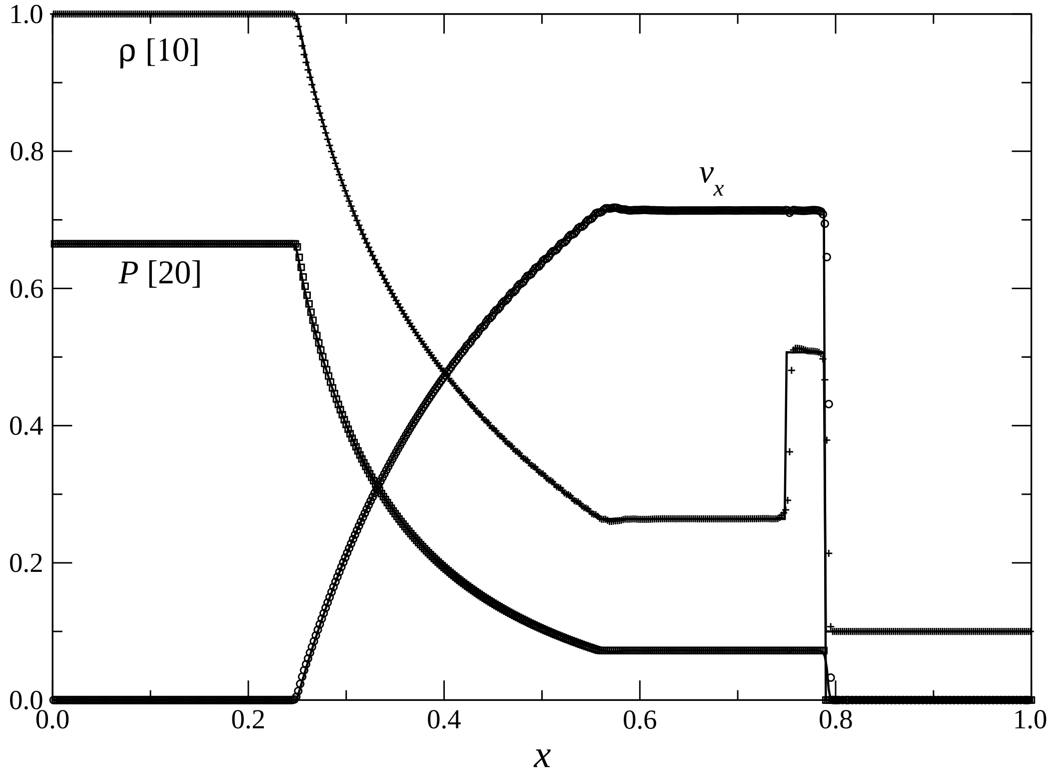

Figure 6.1: *Numerical (symbols) and analytic (solid line) profiles of the (rescaled) density ρ, pressure P, and velocity v_x for the shock tube problem 1 from Table 6.1. See text for simulation details.*

As we have built different reconstruction methods into the code, shocks tube tests also help to show the superiority of high order reconstruction compared to e.g. constant Gudunov reconstruction. In Figure 6.3 we compare numerical results for the density profile after $t_{\text{final}} = 0.35$ for the two shock tube problems from Table 6.1 for a first order (Godunov) and a third order (PPM) reconstruction scheme. As expected, PPM reconstruction not only resolves the shock front much better (i.e. with a spread of less grid points), but also has less numerical

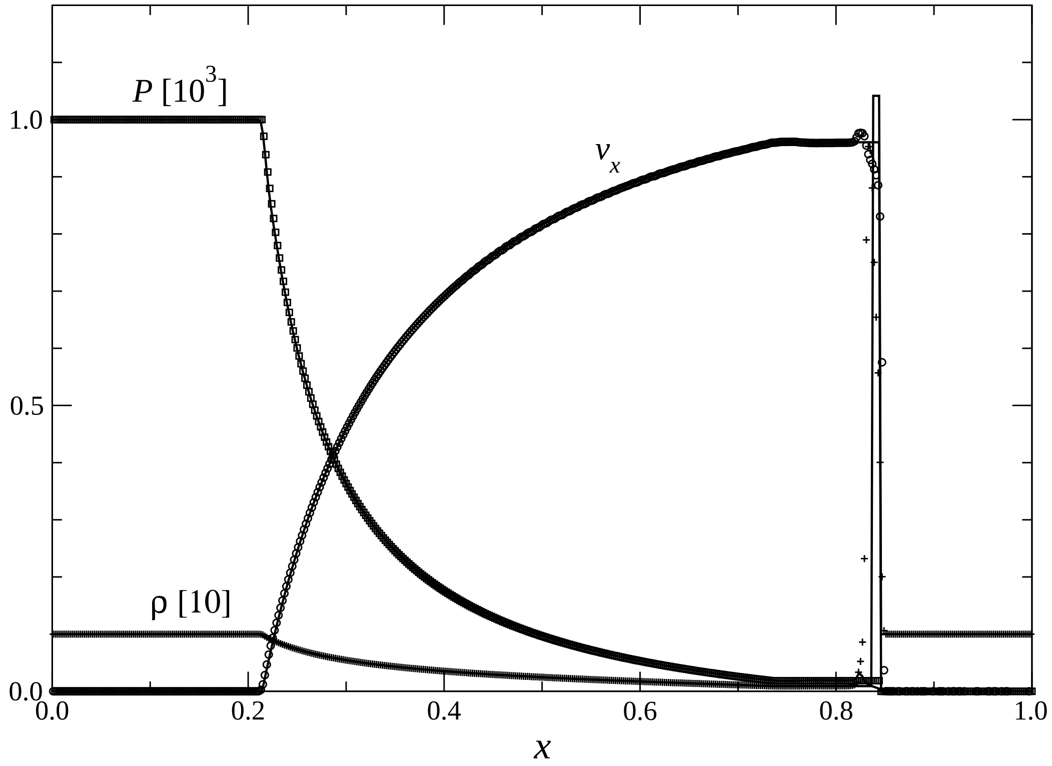

Figure 6.2: *Numerical (symbols) and analytic (solid line) profiles of the (rescaled) density* ρ*, pressure* P*, and velocity* v_x *for the shock tube problem 2 from Table 6.1. See text for simulation details.*

dissipation (particularly visible in problem 2). It is also assuring that high order reconstruction does not introduce unwanted high frequency oscillations behind the shock. Such spurious numerical oscillations can be observed in non-HRSC codes, like the one used for comparison in Section 6.3.

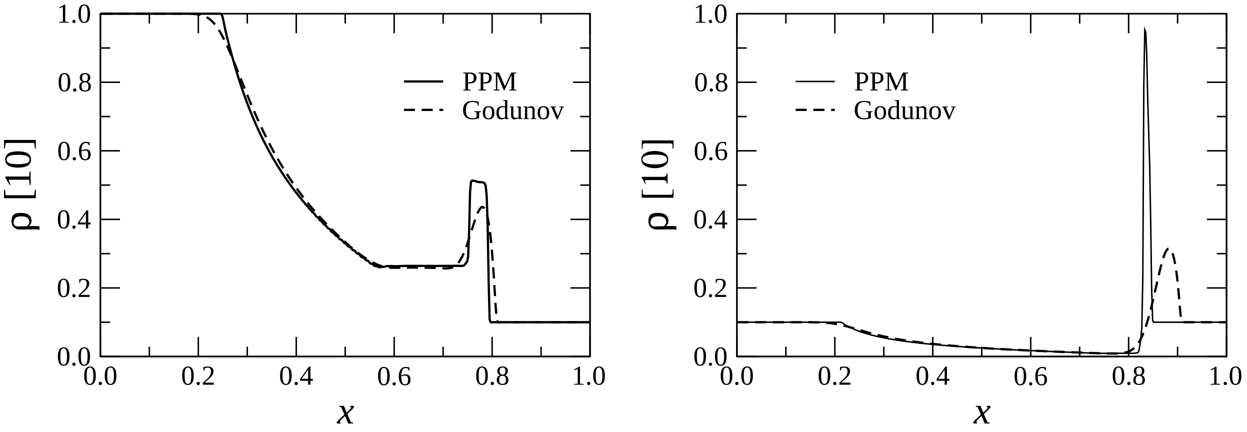

Figure 6.3: *Comparison of first order Godunov (dashed line) and third order PPM (solid line) reconstruction for shock tube problems 1 (left panel) and 2 (right panel) from Table 6.1. The snapshots show the density* ρ *at* $t_{\mathrm{final}} = 0.35$.

We have also performed additional simulations of these two shock tube problems using radial and non-equidistant Cartesian grids. We have further tested second order (MUSCL) reconstruction schemes with minmod and MC slope limiters [69]. For all our core collapse simulations, however, we have used PPM reconstruction, which provides the best numerical accuracy.

6.2 Rotating Neutron Stars

A severe test for both the evolution code and the initial data solver is to construct either a spherically symmetric or a rotating stellar model in stable equilibrium, and to evolve it without changing the EoS. If the initial model is accurate, and if the evolution scheme is implemented properly, then the matter and metric profiles of the model should oscillate only slightly around their initial equilibrium states. For a rotating model, particularly the rotation profile should be preserved for several rotation periods.

In order to enhance relativistic effects, we have used a rapidly and uniformly rotating neutron star model with a polytropic matter distribution (see Table 6.2) rather than an iron core model, which is not very relativistic prior to collapse. One nice feature of these tests is that they allow for a rather independent check of the metric and the hydrodynamics part of the code: If desired, the code can evolve only the hydrodynamic quantities according to Equation (2.25) while keeping the metric fixed (Cowling approximation), or evolve both the hydrodynamics and the spacetime (fully coupled evolution). In both cases we observe that the neutron star remains in equilibrium to high accuracy for several 10 milliseconds, which corresponds to many dynamic timescales.

ρ_c $[10^{14}$ g cm$^{-3}]$	γ	K (cgs)	$r_\mathrm{e}/r_\mathrm{p}$	M_rest $[M_\odot]$	M_grav $[M_\odot]$	β [%]	Ω/Ω_K [%]	T [ms]
7.905	2.0	1.456×10^5	0.70	1.756	1.627	7.419	76.0	1.0

Table 6.2: *Parameters of the rotating neutron star model used for the stability tests: ρ_c is the central density, γ and K specify the EoS, $r_\mathrm{e}/r_\mathrm{p}$ is the ratio of equatorial to polar radius of the star, $M_\mathrm{rest/grav}$ are the rest/gravitational masses, β is the rotation rate, Ω/Ω_K is the ratio of angular velocity of the star and its Keplerian angular velocity, and T is the rotation period. Note that this model corresponds to the (albeit nonrotating) model II in Font et al. [38].*

In Figure 6.4 we show the time evolution of the density ρ, the lapse α, and the radial velocity $v_r = \sqrt{\gamma^{11}} v_1$ evaluated inside the star in the equatorial plane at a radius of 8.77 km; in this simulation the metric was evolved fully dynamic. All three quantities oscillate around their initial equilibrium value, the oscillations being triggered by numerical discretization errors. The fact that these small amplitude oscillations are hardly damped reflects the very low numerical viscosity of the HRSC scheme. The small secular drift in ρ and α is an artifact of the numerical scheme and has also been observed by Font et al. [38]. Contrary to their tests of a nonrotating neutron star in the Cowling approximation, the oscillations in ρ and v_r in our simulation are of higher amplitude due to the coupling of the hydrodynamics to the metric, and the rapid rotation of the star.

In Figure 6.5 we plot the radial profiles of the density ρ and the rotation velocity $v_\varphi = \sqrt{\gamma^{33}} v_3$ along the equatorial plane for the same neutron star model. Even after 5 rotation periods the rotation profile is rather close to its initial distribution. Only at the stellar surface, the angular velocity slightly deviates from its initial shape during the evolution due to interaction with the atmosphere (see Section 5.3).

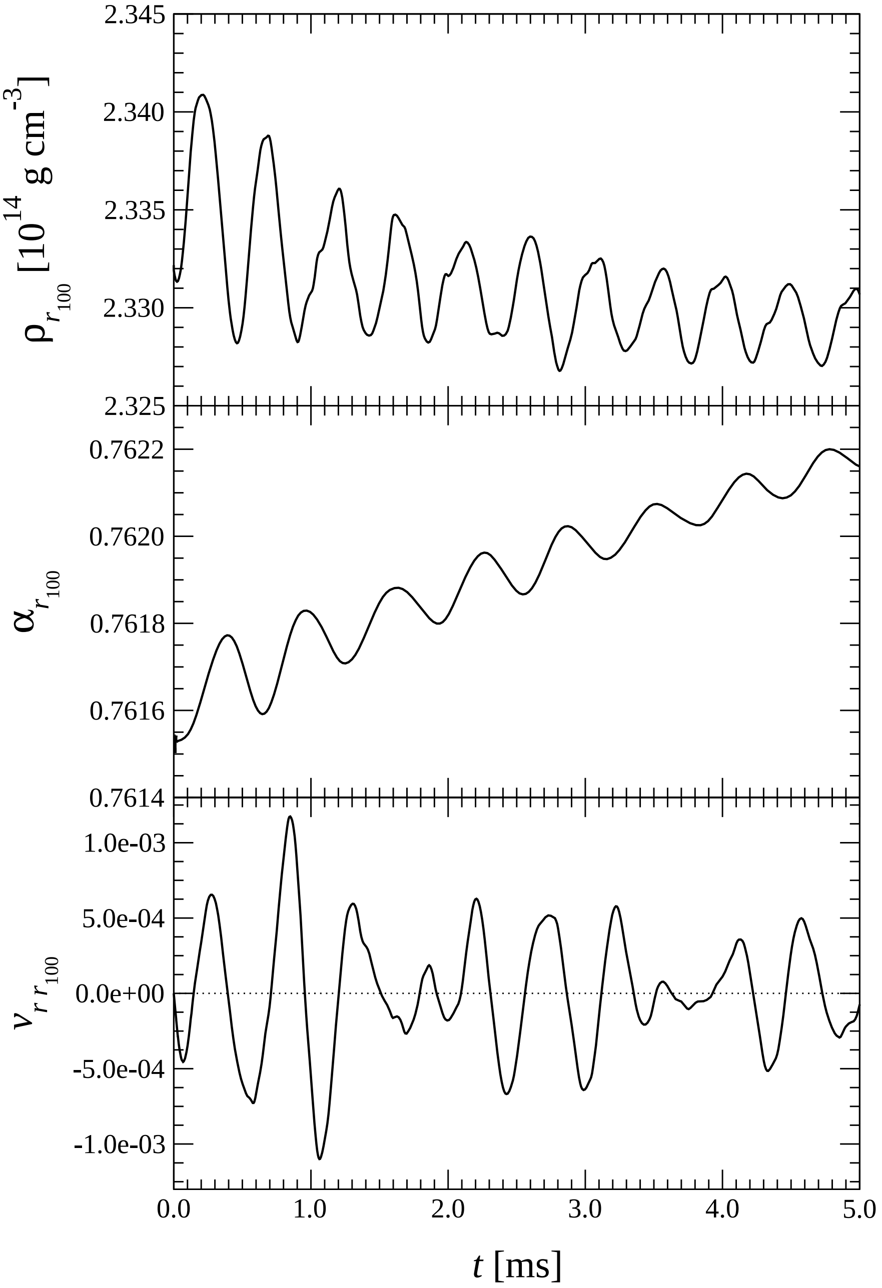

Figure 6.4: *Time evolution of hydrodynamic and metric quantities of a neutron star model which rotates with uniform angular velocity close to its Keplerian limit: The density* ρ *(upper panel), the lapse function* α *(middle panel), and the radial velocity* v_r *(lower panel) are evaluated at a radius* $r_{100} = 8.77$ km *and an angle* $\theta = \pi/2$. *The shape of the oscillations are very close to the results for a spherically symmetric neutron star in the Cowling approximation presented in [38] (see Figure 2 and 4 therein).*

In this test run the metric equations were solved every 200th time step, which corresponds to a time interval between two metric time slices of 0.06 ms[a]. For a fixed metric, i.e. in the Cowling approximation, the code can keep the neutron star in equilibrium for many rotation periods as well.

As the neutron star model specified in Table 6.2 is rapidly rotating and thus deviates strongly from spherical symmetry, the evolution of such a highly relativistic configuration is a convincing test for the ability of the CFC to yield a good approximation of the exact spacetime. The initial model for the neutron star has been calculated in the exact metric (4.12) without assuming conformal flatness. The initial data are then matched to the CFC spacetime according to Equation (5.13). The fact that the evolution code maintains stability for many rotation periods already proves the validity of the CFC in the case of rotating neutron stars, particularly as it is not possible to keep Newtonian initial neutron star models in equilibrium with the CFC evolution code, or vice versa relativistic initial neutron star models with a Newtonian evolution code. This observation is supported by Figure 6.6, which shows how well the conformal factor of the CFC metric ϕ^{CFC} approximates the corresponding metric quantity in the exact metric ϕ^{ex} (left panels). The excellent approximation of the azimuthal component of the exact shift vector $\beta^{3\,\mathrm{ex}}$ by the CFC shift vector component $\beta^{3\,\mathrm{CFC}}$ is shown in the right panels. This very good matching is in agreement with the results for rapidly rotating neutron stars in the CFC spacetime by Cook et al. [22].

The neutron star models used in the above tests were not disturbed from their equilibrium state. However, in order to determine the oscillation normal modes of rotating neutron stars, a standard method in numerical relativity is to add low amplitude perturbations to the initial equilibrium density distribution, which then excite normal modes of specific parities. The frequencies of these normal modes and their first few harmonics can then be extracted by Fourier analysis of quantities like the density or radial velocity read out at a fixed location in the star. This has already been done for spherically symmetric and uniformly rotating relativistic neutron stars [38, 35], however only for a fixed background spacetime. As the tests above indicate, this code can be used to determine normal mode frequencies for rotating relativistic stars with a fully coupled and evolved spacetime. The long-term stability of the code even for rapidly rotating neutron stars allows one to compute the evolution for many rotation periods and to extract the oscillation frequencies very accurately.

---

[a] This time interval is both small compared to the star's rotation period and the frequencies of the strongest radial oscillations.

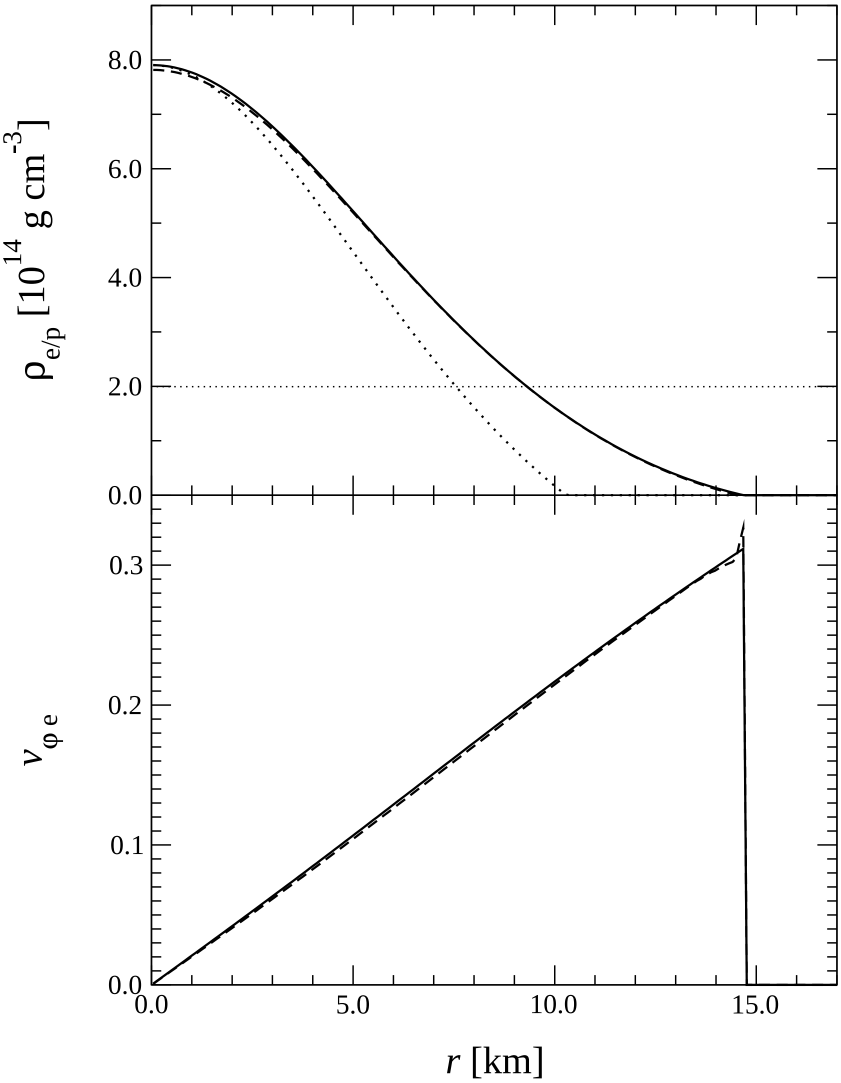

Figure 6.5: *Evolution of the density profile (upper panel) and angular velocity profile (lower panel) in a neutron star model which rotates with uniform angular velocity close to its Keplerian limit: The equatorial density profile* ρ_{e} *at* $t = 5.0$ ms *(dashed line), corresponding to 5 rotation periods, is close to the initial profile at* $t = 0.0$ ms *(solid line). The same holds for the angular velocity profile* $v_{\varphi\mathrm{e}}$*, also plotted at* $t = 5.0$ ms *(dashed line) and* $t = 0.0$ ms *(solid line); this behavior is similar to the results for a rotating neutron star in the Cowling approximation presented in [38] (see Figure 6 therein). The spike in the* $t = 5.0$ ms *profile of* $v_{\varphi\mathrm{e}}$ *close to the neutron star boundary is a numerical artifact due to the artificial atmosphere. The height of the spike oscillates in time with a maximum amplitude as plotted here. Note that the neutron star model rotates with more than 30% of the speed of light at the equator. The dotted profile in the upper panel is the initial density along the polar axis* ρ_{p}*. Due to the rapid rotation, the polar radius of the neutron star is only 70% of its equatorial radius. The horizontal dotted line in the density plot marks nuclear matter density.*

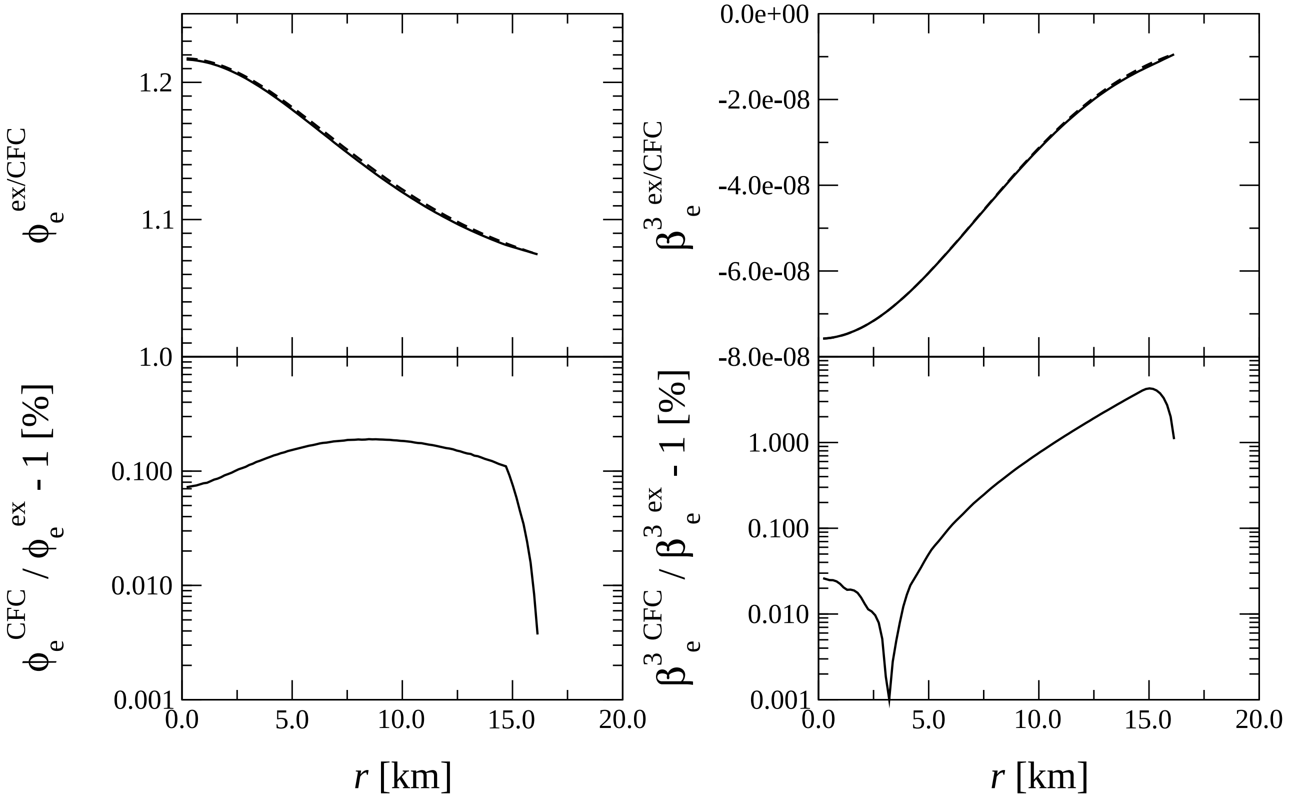

Figure 6.6: *Quality of the CFC approximation for rapidly rotating neutron star initial data: The values for the exact and approximate conformal factor* $\phi_{\text{e}}^{\text{ex}}$ *and* $\phi_{\text{e}}^{\text{CFC}}$ *(upper left panel), and for the exact and approximate shift vector component* $\beta_{\text{e}}^{3\,\text{ex}}$ *and* $\beta_{\text{e}}^{3\,\text{CFC}}$ *(upper right panel), both evaluated along the equatorial plane, agree very well. In the lower panels the corresponding relative deviations are plotted. For the conformal factor the deviations are less than* 0.2%*, while they stay below* 4% *for the shift vector even where it is very close to zero.*

6.3 Spherical Core Collapse

The problem of relativistic core collapse for an ideal fluid in spherical symmetry has been successfully solved in numerical relativity by May and White in 1966 [80]. Their code used a Lagrangian formulation, where the coordinates label mass shells rather than spatial positions, and thus comove with the fluid. To damp out unwanted spurious numerical oscillations behind shock fronts, this code utilized a simple form of artificial viscosity. As we have a May–White type Lagrangian code to our disposal [23], we are able to compare our code, which uses a HRSC method for calculating the hydrodynamics, and is based on Eulerian-type fixed coordinates, against a Lagrangian finite difference code, at least in the case of spherically symmetric core collapse[b].

For this test we set up a nonrotating equilibrium star as initial data on a two-dimensional (r, θ)-grid, with the same EoS and central density as in the (rotating) initial models listed in Section 4.4. During the evolution, we do not use the hybrid EoS (4.9), but a simple ideal fluid EoS,

$$P = (\gamma - 1)\rho\epsilon. \tag{6.1}$$

The effective stiffening of the EoS at supranuclear matter densities is modeled by a variable adiabatic index given by the following relation [104, 131]:

$$\gamma = \begin{cases} \gamma_1 & \text{for } \rho < \rho_{\mathrm{nuc}}, \\ \gamma_1 + \frac{1}{2}\log\dfrac{\rho}{\rho_{\mathrm{nuc}}} & \text{for } \rho \geq \rho_{\mathrm{nuc}}, \end{cases} \tag{6.2}$$

with $\gamma_1 = 1.320$. As initially all derivatives in the angular direction are zero, with this spherical core collapse model we can easily test the ability of the code to maintain spherical symmetry throughout the collapse.

Furthermore, this test is important insofar, as the numerical treatment of the evolution equations, and the coordinate choice of both codes are different. While the May–White code obtains very good radial resolution throughout all phases of the collapse by virtue of its comoving coordinates[c], the Eulerian geometry of the coordinates of our code lack this property, as the resolution is fixed. As most of the matter finally concentrates in the center of the numerical grid in the form of the stable neutron star, whose volume is small compared to the initial extent of the iron code, in Eulerian coordinates we have to select a radial resolution fine enough to resolve the dynamics of collapse over two orders of magnitude in space already from the beginning. Because of the CFL criterion this slows down our code considerably, whereas the May–White code allows for much larger time steps initially, while still having superior resolution during and after the bounce. On the other hand, after the shock forms and the hydrodynamic quantities exhibit discontinuities, the HRSC properties of our scheme are superior to the artificial viscosity approach of the May–White formulation in terms of correct shock propagation speed and good resolution of the discontinuity.

---

[b] Due to the special choice of the radial coordinate, the May–White code cannot be extended to multi-dimensions.

[c] Comoving coordinates are an ideal way to automatically adapt the radial resolution to the flow by following the motion of the mass elements.

The different ability of both codes to handle these two issues of radial resolution and capturing of shocks, can clearly be seen in Figure 6.7: In the upper panel we plot the evolution of the central density around the time of bounce. Even during this evolution stage, where the highest densities are reached[d], the density obtained with our code very accurately follows the density from the May–White code. However, due to its superior effective radial resolution, the May–White code resolves the dip in the central density evolution after the maximum density peak better, and also produces a smoother density curve. Up to the formation of the shock front, both codes yield equally good results for the radial infall velocity profiles. The profiles at $t = 60$ ms (before bounce) and $t = 75$ ms (after bounce) are plotted in the lower panel of Figure 6.7. When the velocity profile becomes discontinuous at the location of the shock front, our code demonstrates the superiority of the HRSC scheme: The shock front is steeper and confined to less grid zones than the one in the May–White code. Additionally, the velocity behind the shock is higher and the shock propagates faster, which is a result of much less numerical dissipation. If the artificial viscosity is reduced in the May–White code to remedy its negative effects, unphysical spurious oscillations grow behind the shock front (see inset in the lower panel).

To simulate the core collapse problem in spherical symmetry, Romero et al. [104] have used a reformulation of the spherically symmetric relativistic hydrodynamic equations as a set of conservation laws. Similar to what is implemented in our code, they also have used modern high-resolution shock-capturing methods to simulate core collapse; thus, their results are ideal for comparison with our code. However, as we could not exactly identify the initial model used for the core collapse runs presented in [104], we have used their results only for a rough comparison with the above spherically symmetric test model. As far as the spread of the shock, the amplitude of oscillations in the stable post-bounce inner core, and the conservation of total rest mass and gravitational mass (see also Section 6.4) are concerned, our code yields equally good results. The dynamic range and the radial resolution of their simulations is approximately the same as in our model. Hence, we are confident of the correct implementation of our numerical schemes.

---

[d] Note that due to the relatively soft supranuclear EoS (6.1, 6.2), the core dives deeply into the potential well and reaches very high densities of more than $5\rho_{\mathrm{nuc}}$.

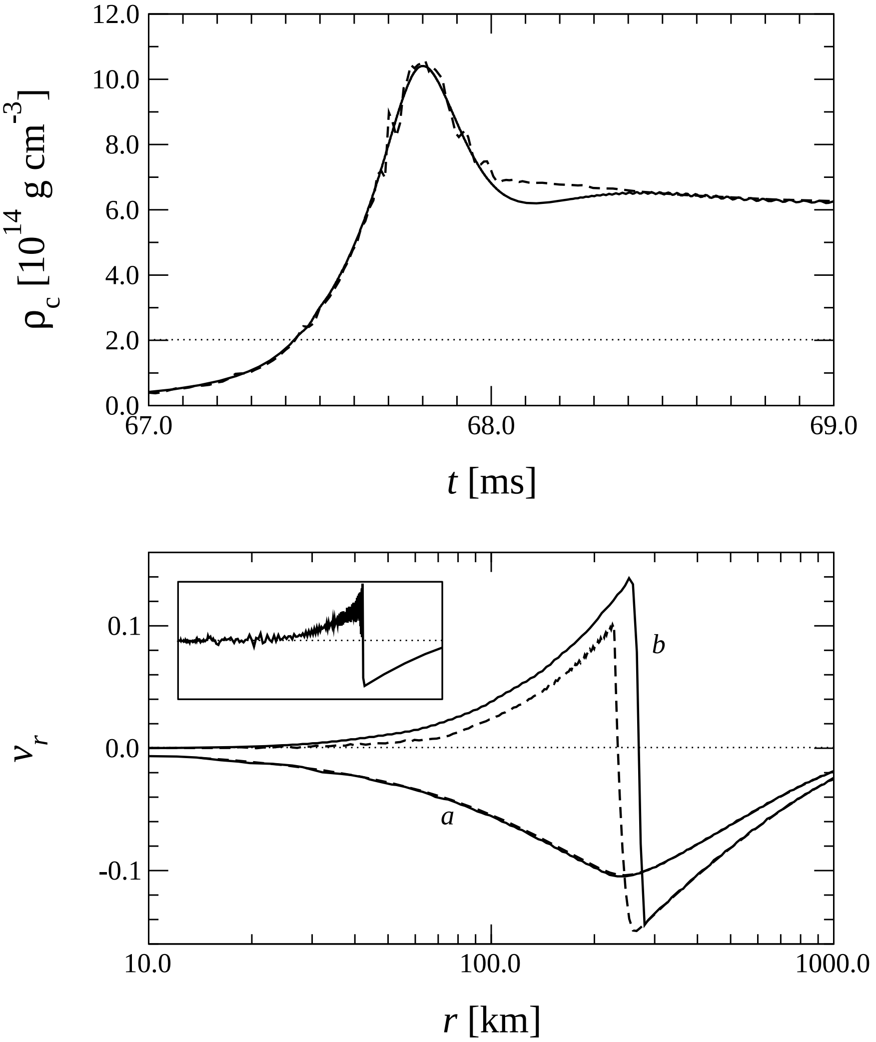

Figure 6.7: *Comparison of results obtained with our Eulerian HRSC code (solid lines) against results from a Lagrangian finite difference code (dashed lines) applied to spherically symmetric core collapse: The time evolution of the central density* ρ_c *(upper panel), here plotted around bounce time, agrees very well during all stages of the collapse. In the lower panel, the radial velocity profiles from both codes are plotted at* $t = 60$ ms *(a) and at* $t = 75$ ms *(b). During the infall phase before core bounce (a), the velocity profiles match very well. When the shock front propagates outward (b), the alignment is less good. In the inset the velocity profile from the finite difference code for very low artificial viscosity is plotted at* $t = 75$ ms*. The vertical dotted line in the density plot marks nuclear matter density.*

6.4 Integral Quantities – Conservation of Rest Mass and Angular Momentum

The hydrodynamics part of our code solves the system of relativistic hydrodynamic equations (2.35–2.37) for the state vector of the conserved quantities D, S_i, and τ (2.22–2.24). These equations derive their conservative character directly from the relativistic equations of motion (2.19), which are conservation equations for the rest mass current and the energy-momentum tensor. Equations (2.35–2.37) are the general relativistic extension of the Newtonian conservation equations (2.29–2.31). Analogous to the conserved quantities related to symmetries in Newtonian gravity, in general relativity one can define integral quantities which are conserved in an isolated system. However, in a curved spacetime, the notion of total mass and total angular momentum is not as clear as in Euclidean space (for a summary on the different regions around an isolated source in spacetime and their relation to total mass and angular momentum, see Box 19.1 in [85]). The way to define the mass M and angular momentum J is to match integral quantities of spacetime to appropriate line element quantities in the weak field limit.

In the $\{3+1\}$ formalism, the general definitions for the (baryon) rest mass M_{rest}, the proper mass M_{proper}, the gravitational mass M_{grav}, the angular momentum J_{rot}, and the rotational mass (energy) M_{rot} are [40]

$$M_{\mathrm{rest}} = -\int dV \rho u_\mu n^\mu, \tag{6.3}$$

$$M_{\mathrm{proper}} = -\int dV \rho (1+\epsilon) u_\mu n^\mu, \tag{6.4}$$

$$M_{\mathrm{grav}} = -\int dV \left(2T_{\mu\nu} - g_{\mu\nu} T\right) t^\mu n^\nu, \tag{6.5}$$

$$J_{\mathrm{rot}} = -\int dV T_{\mu\nu} s^\mu n^\nu, \tag{6.6}$$

$$M_{\mathrm{rot}} = -\int dV T_{\mu\nu} s^\mu n^\nu \frac{s_\lambda u^\lambda}{2 n_\kappa u^\kappa}, \tag{6.7}$$

where u^μ is the four-velocity, n^μ is the unit vector normal to the three-dimensional hypersurface, and t^μ and s^μ are a time-like and a space-like Killing vector, respectively[e]. The rotation axis is perpendicular to s^μ. For the CFC metric (3.12) in axisymmetry, where $s^\mu = \hat{e}^3$ (i.e. the unit vector in φ-direction), the above integral quantities assume the following form:

$$M_{\mathrm{rest}} = -2\pi \int dr d\theta r^2 \sin\theta \phi^6 \rho W, \tag{6.8}$$

$$M_{\mathrm{proper}} = -2\pi \int dr d\theta r^2 \sin\theta \phi^6 \rho (1+\epsilon) W, \tag{6.9}$$

$$M_{\mathrm{grav}} = -2\pi \int dr d\theta r^2 \sin\theta \phi^6 \left(\alpha (2\rho h W^2 + 2P - \rho h) - 2\rho h W^2 v_i \beta^i\right), \tag{6.10}$$

---

[e] Note that the gravitational mass M_{grav} is only defined this way if a time-like Killing vector exists, i.e. if we have a stationary solution. In a dynamic context we can assume that M_{grav} is calculated in a series of (quasi-)equilibrium states of the system. However, strictly speaking M_{grav} is defined only for stationary systems.

$$J_{\rm rot} = -2\pi \int dr d\theta r^2 \sin\theta \phi^6 \rho h W^2 v_3, \tag{6.11}$$

$$M_{\rm rot} = -2\pi \int dr d\theta r^2 \sin\theta \phi^6 \rho h W^2 \frac{v_3(\alpha v^3 - \beta^3)}{2}. \tag{6.12}$$

From these quantities, we get the following relation for the mass $M_{\rm pot}$ associated to the potential binding energy and the rotation rate β:

$$M_{\rm pot} = M_{\rm grav} - M_{\rm proper} - M_{\rm rot}, \qquad \beta = \frac{M_{\rm rot}}{|M_{\rm pot}|} = \frac{M_{\rm rot}}{|M_{\rm grav} - M_{\rm proper} - M_{\rm rot}|}. \tag{6.13}$$

The formulation of integral quantities (6.8–6.12) is an extension of the masses and angular momentum defined in [65] for nonzero radial and angular velocity and shift vector components in a conformally flat metric. It is obvious that the integrand of the rest mass and the angular momentum can be written as $\sqrt{\gamma}D$ and $\sqrt{\gamma}S_3$, respectively, which are the first and fourth component of the state vector in Equation (2.26), corresponding to the continuity equation and the angular momentum conservation equation.

Like in Newtonian gravity, the general relativistic continuity equation (2.35) is also a strict conservation law. For the angular momentum $J_{\rm rot}$, whose evolution is determined by the third component of the momentum equation (2.36), one has to distinguish several cases: In an exact spacetime (described e.g. by an unconstrained ADM metric (2.11)), any rotating matter distribution in equilibrium will exhibit a vanishing source term in the equation for S_3. If gravitational waves are radiated away by the system, e.g. during a core collapse, angular momentum can be carried off from the source by them. However, in axisymmetry, the angular momentum of gravitational radiation is zero, and again $J_{\rm rot}$ is conserved (see Exercise 16.3 in [109]). For an approximate metric like the CFC metric, the situation is not as trivial: Although gravitational waves are not explicitely present in the spacetime, the peculiarity of the CFC metric as an *approximation* of the exact metric will result in a small but nonzero contribution to the source term for the angular momentum conservation equation.

If an appropriate and correctly implemented conservative scheme is used to numerically evolve a physical system governed by conservation laws, the analytic conservation of a certain quantity is reflected in the numerical method by a conservation of the associated numerical quantity up the machine precision. However, in the case of the hydrodynamic conservation laws in Newtonian gravity (2.29–2.31) or in general relativity (2.35–2.37), and their numerical implementation in our code, there are several prerequisites for achieving “exact” numerical conservation of the total rest mass $M_{\rm rest}$ and the total angular momentum $J_{\rm rot}$:

Stationarity of the metric:

Instead of being conservation equations for the quantities D, S_i, and τ, the evolution equations (5.29) are written in the form of conservation equations for the generalized conserved quantities $\sqrt{\gamma}D$, $\sqrt{\gamma}S_i$, and $\sqrt{\gamma}\tau$. The common factor $\sqrt{\gamma}$ contains the term ϕ^6, which obviously varies with time. If the metric components would be determined by evolution equations (like e.g. the ADM metric evolution equations), it would be possible to evolve the volume weighted state vector $\sqrt{\gamma}\boldsymbol{F}^0$ and extract the state vector $\boldsymbol{F}^0$ on the new time slice from $\sqrt{\gamma}\boldsymbol{F}^0$ using the value $\sqrt{\gamma}$ computed from the metric which has been evolved forward in time independently. However, in the CFC approximation the metric is computed not by evolution equations but by constraint equations, and the equations which are actually used for the evolution are of the form (5.31). These exhibit effective source terms which contain the time derivative of $\sqrt{\gamma}$. If the metric is assumed to be stationary (Cowling approximation), these additional source terms are zero, $\hat{\boldsymbol{Q}} = \boldsymbol{Q}$, and the equations (5.31) become genuine conservation equations even for a CFC metric.

Vanishing physical and geometrical source terms:

A quantity, whose evolution in time is determined by a conservation equation, is only conserved if it is not subject to external real forces (i.e. physical, like gravitational forces), or ficticious forces (i.e. geometrical, like Coriolis forces; see Section 5.5.1). Source terms associated to ficticious forces vanish only if the evolution equations are written in the form (5.31) rather than in the (analytically equivalent) form (5.30). The only conservation equation, where the source term due to gravitational forces is zero in all situations, is the one for the rest mass D. As already mentioned, in an axisymmetric situation the source term in the angular momentum conservation equation for S_3 also vanishes, but only for an exact metric, not for a CFC metric.

Influence of the atmosphere:

The last requirement for conservation of a certain quantity is that the sum of the fluxes through the interfaces of all finite volume cells must be zero, i.e. the system must be closed. For the numerical implementation this means that there must not be any artificial atmosphere (such as the one introduced in Section 5.3), as this acts as (an albeit possibly small) source or drain of mass, energy, and momentum. Furthermore, the numerical fluxes through all boundaries have to be exactly zero.

We have performed tests where we have evolved the state vector according to equations (5.31) for a fixed spacetime metric. Additionally, the fluxes at the outer boundary were explicitely set to zero[f], and no artifical atmosphere was used. In this restricted test situation, we could obtain conservation of the rest mass and the angular momentum of

$$dM_{\mathrm{rest}} \equiv \left| \frac{M_{\mathrm{rest}}}{M_{\mathrm{rest}\,0}} - 1 \right| \lesssim 10^{-15}, \qquad dJ_{\mathrm{rot}} \equiv \left| \frac{J_{\mathrm{rot}}}{J_{\mathrm{rot}\,0}} - 1 \right| \lesssim 10^{-15}, \tag{6.14}$$

i.e. up to machine precision; here $M_{\mathrm{rest}\,0}$ and $J_{\mathrm{rot}\,0}$ are the initial total rest mass and angular momentum, respectively. In Newtonian gravity, the same level of conservation could be reached for the total angular momentum J_{rot}.

In a dynamic core collapse simulation, these above restrictions have to be abandoned. Then the nonstationarity of the metric and (in the case of nonsphericity) the artificial atmosphere destroy the exact conservation of the numerical scheme. These violations of exact conservation become apparent in the quantities dM_{rest} and dJ_{rot}. If precautions are taken, these changes in M_{rest} and J_{rest} are small – typically of the order of the discretization errors –, but they are nevertheless orders of magnitude larger than machine precision. By carefully fine-tuning the atmosphere setup as specified in Table 5.1, we could achieve a relative mass conservation dM_{rest} of better than 3% and a relative angular momentum conservation dJ_{rot} of better than 20% in

---

[f] The fluxes across the equatorial plane and along the polar axis are always zero in our code.

all simulations of the collapse models listed in Table 4.2. These values are an upper limit, and for many models the conservation was better by orders of magnitude, especially for rapidly collapsing models and less rapidly rotating models, which allow for a lower density atmosphere.

In Figure 6.8, where we plot the behavior of mass and angular momentum conservation in the rotational core collapse model A3B2G4, one can clearly identify the individual contributions of the three effects to the violation of conservation described in the above list: In Newtonian gravity, the only source for mass and angular momentum accretion is the artificial atmosphere. This becomes visible as a small monotonous increase in M_{rest} and J_{rot}. Until bounce, the mass increase in relativistic gravity exhibits the same behavior. However, due to the nonzero source term in the angular momentum equation in relativity, dJ_{rot} is larger than its Newtonian counterpart already during the infall phase. Around the time of bounce, where the temporal variation of ϕ and thus $\sqrt{\gamma}$ is largest, dM_{rest} and dJ_{rot} vary considerably, too. When the central density has settled down to a constant value, and the core has reached a new equilibrium configuration, the variations of M_{rest} and J_{rot} in the relativistic case again show a similar increase rate like in Newtonian gravity. One important fact to note is that the violation of conservation due to the three effects (variation of $\sqrt{\gamma}$, source term in the angular momentum equation, and atmosphere) is of the same order of magnitude.

The impact of the artificial atmosphere on the conservation of total mass and angular momentum can be seen in Figure 6.9: In the highly nonspherical rotational core collapse model A4B2G2, the shock propagates outward at different speeds in the polar and equatorial direction. When the shock reaches the surface of the star in the polar regions, a considerable amount of mass, but obviously not much angular momentum is lost to the atmosphere. Later the shock also passes the equatorial surface, as it propagates slower in this direction, and as the stellar radius is larger at the equator. Around that time, the curve of mass loss once more steepens, and significantly more angular momentum is lost, as the relative contributions of fluid elements to the total angular momentum is higher in the equatorial regions than in the polar regions. In Figure 6.9 the variation of dM_{rest} and dJ_{rot} due to rapid changes of the volume element $\sqrt{\gamma}$ around peak maximum density can also be observed.

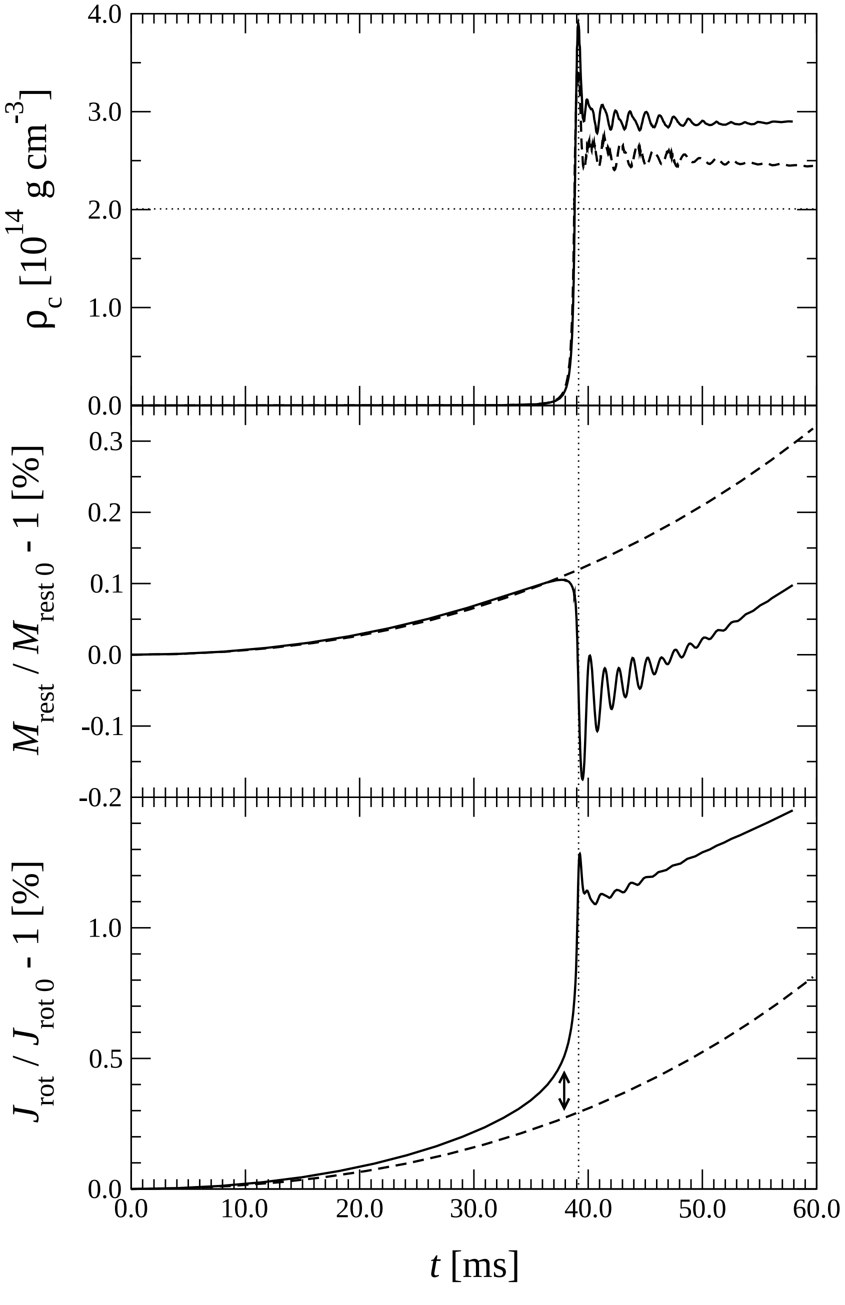

Figure 6.8: *Conservation of total rest mass and angular momentum in the relativistic (solid lines) and Newtonian (dashed lines) simulation of model* A3B2G4*: Until the time of bounce* $t_{\mathrm{b}} \approx 39$ ms *(indicated by the vertical dotted line), the relative changes in the total rest mass* M_{rest} *(middle panel) and angular momentum* J_{rot} *(lower panel) due to interaction of the stellar interior with the artifical atmosphere are small compared to the respective initial values* $M_{\mathrm{rest}\,0}$ *and* $J_{\mathrm{rot}\,0}$*. A nonzero source terms in the evolution equation for* S_3 *additionally drives non-conservation of the angular momentum in relativistic gravity (indicated by the arrow). As the central density* ρ_{c} *(upper panel) and thus the metric volume factor* $\sqrt{\gamma}$ *contained in the conservation equations vary most during the bounce, a strong oscillatory variation of total mass and angular momentum can be observed in this phase. The horizontal dotted line in the density plot marks nuclear matter density.*

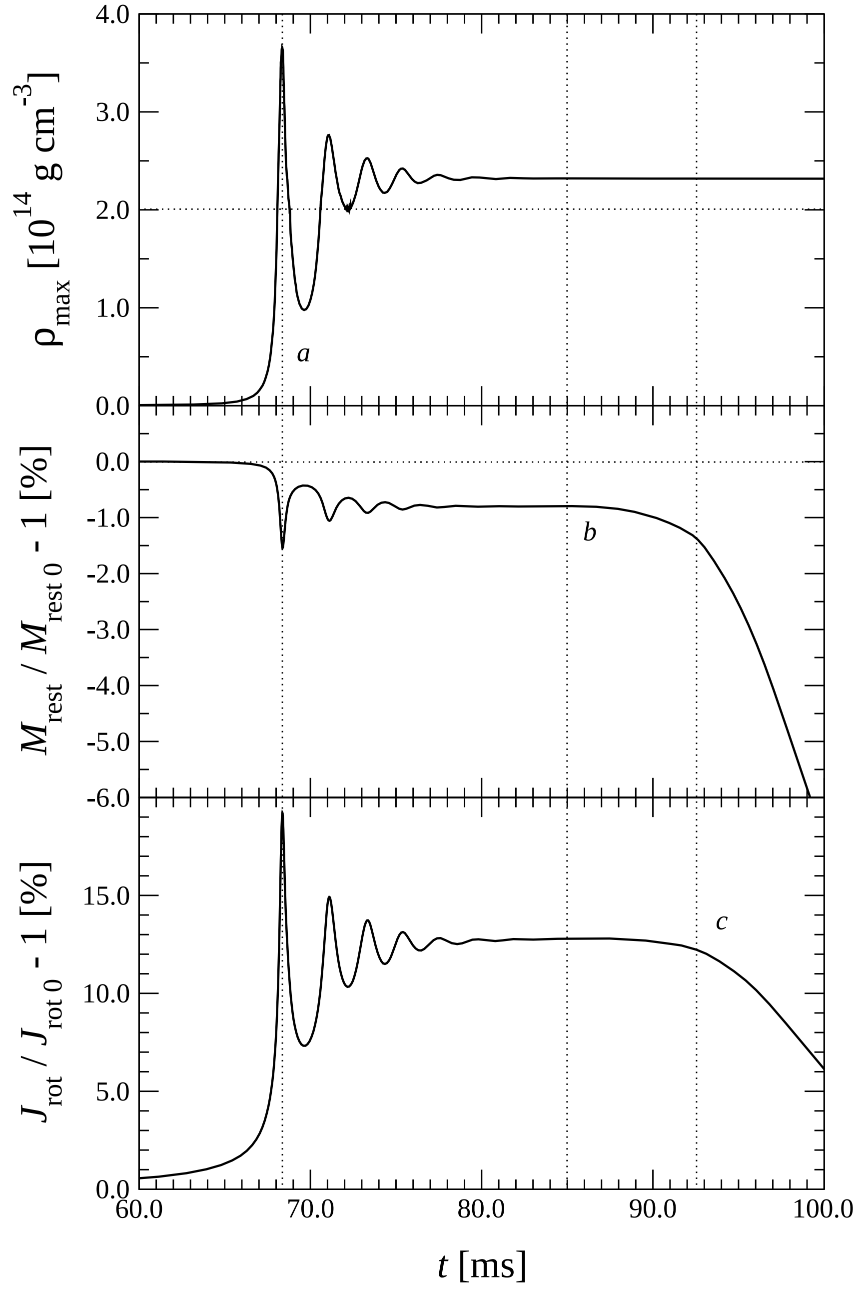

Figure 6.9: *Influence of the artificial atmosphere and of the time dependence of the volume element* $\sqrt{\gamma}$ *on the conservation of total rest mass and angular momentum for model* A4B2G2*: Around the time of bounce* $t_\mathrm{b} \approx 68.5$ ms *(a), the maximum density* ρ_max *(upper panel), which is off-center in this toroidal model, and thus the value of the volume element* $\sqrt{\gamma}$ *oscillate strongly; this oscillatory behavior manifests itself in a relative change of the total rest mass* M_rest *(middle panel) and angular momentum* J_rot *(lower panel) compared to the respective initial values* $M_{\mathrm{rest}\,0}$ *and* $J_{\mathrm{rot}\,0}$*. Before bounce the change of total mass and angular momentum due to interaction of the stellar interior with the atmosphere is small. At* $t \approx 85$ ms *(b), the shock reaches the stellar surface, first at the pole at* $R_\mathrm{b\,p} \approx 1,200$ km*; this leads to mass loss. At* $t \approx 92.5$ ms *(c), the slower shock along the equatorial plane passes the stellar surface, which is located at* $R_\mathrm{b\,e} \approx 1,320\ \mathrm{km} > R_\mathrm{b\,p}$*; this results in loss of total angular momentum, and also increases the mass loss. The horizontal dotted line in the density plot marks nuclear matter density.*

6.5 Excitation of the Thermal Pressure

When introducing the hybrid EoS (4.9) in Section 4.2 as a combination of a polytropic and a thermal contribution to the pressure, we have already mentioned that the thermal part should only play a non-negligible role in the presence of a shock front. During the infall phase of core collapse, i.e. before nuclear matter density is reached and the core bounces, it should make no significant difference whether the EoS is purely polytropic ($P = K\rho^{\gamma_1}$), or given by the hybrid EoS of Equation (4.9). This should also hold for the ideal gas EoS $P = (\gamma_1 - 1)\rho\epsilon$. Thus for all three cases, the respective profiles of hydrodynamic quantities during infall should deviate only slightly from each other.

We have tested the validity of this assumption by collapsing model A3B2G4 to nuclear matter density using the three different EoS, and comparing the time evolution of the density and the internal energy. The left panel of Figure 6.10 shows the evolution of the relative deviations of the density ρ, when comparing the simulation using the hybrid EoS with one using the ideal gas EoS, and with one using the polytropic EoS. The evolution of the relative deviations for the energy density ϵ are plotted in the right panel. For both hydrodynamic quantities, which are being evaluated at a fixed radius $r_{100} = 159$ km, and for both comparisons the relative difference is minute throughout the infall phase, reaching at most 2% just before the central part reaches nuclear matter density. This proves that during the infall phase the collapse proceeds adiabatically, and the polytropic density profile is preserved.

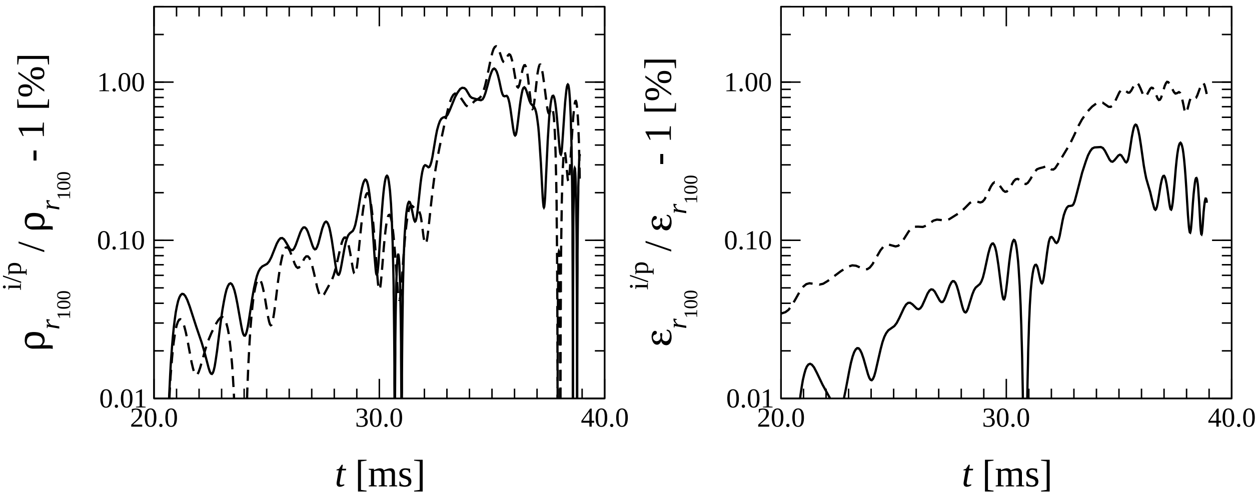

Figure 6.10: *Relative deviation between the evolution of the density ρ (left panel) and the internal energy density ϵ (right panel) for different EoS in model* A3B2G4*: The relative deviations in both the density and energy density between a simulation using the hybrid EoS and one with the ideal gas EoS (solid lines), or one with the polytropic EoS (dashed lines) are less than 2% until the time nuclear matter density is reached at about* 39 ms*. The hydrodynamic quantities are evaluated in the equatorial plane at a radius* $r_{100} = 159$ km.

When continuing the collapse of the above model with the hybrid EoS until the adiabatic exponent in the EoS increases from γ_1 to γ_2 due to nuclear matter effects, the formation and subsequent propagation of the shock front produces a thermal contribution, which will manifest itself in the total pressure. This can be seen in the pressure profiles of Figure 6.11, where we plot

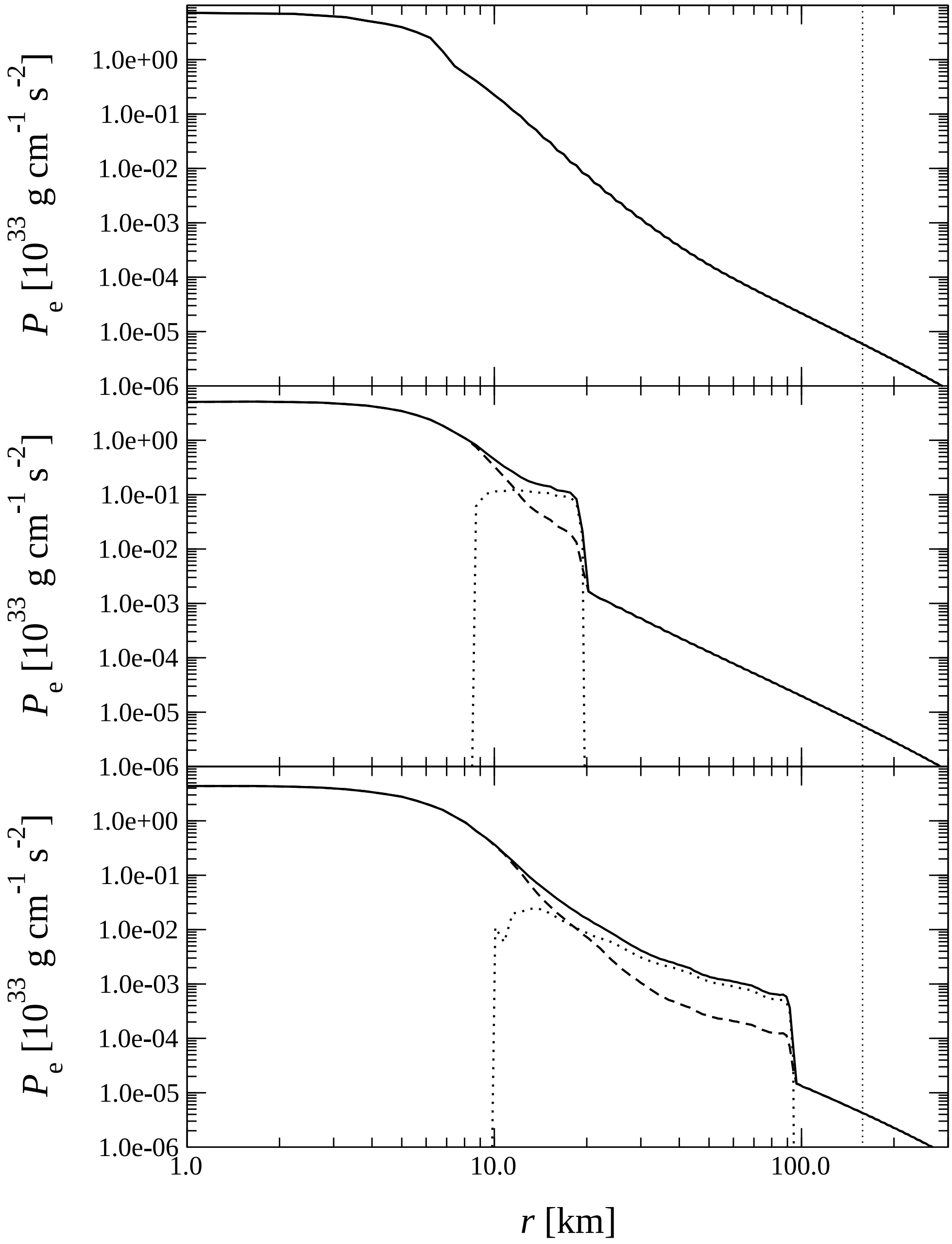

Figure 6.11: *Contribution of the polytropic pressure* P_{p} *(dashed lines) and the thermal pressure* P_{th} *(dotted lines) to the total pressure* P *(solid lines) at different stages of the collapse of model* A3B2G4*, evaluated along the equatorial plane: Before the bounce at* $t = 39$ ms *(upper panel), the contribution of the thermal pressure to the total pressure is insignificant, i.e. the profiles of* P *and* P_{p} *are identical. Right after bounce at* $t = 39.5$ ms *(middle panel), the shock front forms, and the thermal pressure begins to rise. At* $t = 42$ ms *(lower panel), when the shock front propagates through the outer parts of the core, the thermal pressure is and remains dominant in the post-shock region, and drives the shock further outward. Right behind the shock front,* P_{th} *is almost one order of magnitude larger than* P_{p}*. The vertical dotted line marks the radius where the pressure in Figure 6.12 is evaluated.*

the polytropic and thermal contribution of the hybrid EoS to the total pressure. We see that the thermal contribution is negligible before the formation of the shock wave (upper panel), builds up as the shock front forms (middle panel), and acts as a significant source of total pressure right behind the shock front (lower panel). Still, in regions which have not yet been affected by the shock (at larger radii), and inside the unshocked inner core, the thermal contribution is very close to zero. The sudden rise of the thermal pressure behind the shock front is also illustrated in Figure 6.12. We have found that the ratio between thermal and total pressure is typically 80% right behind the shock front in all collapse models. During the further evolution, while the shock front propagates outward, this ratio, and thus the thermal contribution of the heated post-shock matter to the overall pressure, remains approximately constant right behind the shock front. Thus as a rule of thumb we can say that about 80% of the pressure can be attributed to thermal pressure anywhere and anytime behind the shock. Farther behind the shock front, the ratio of thermal to total pressure declines, and the contribution from the polytropic pressure becomes more important again (see Figure 6.11).

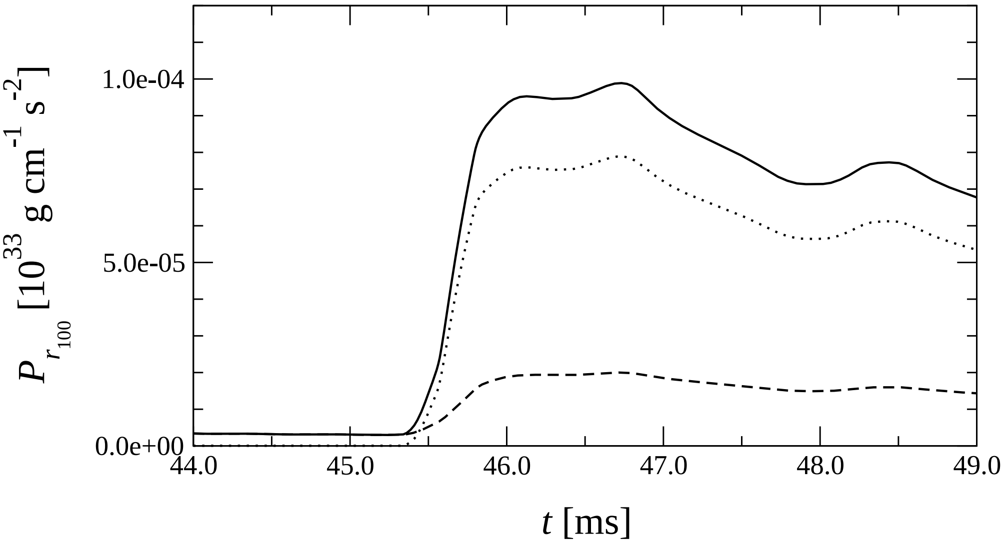

Figure 6.12: *Evolution of the polytropic pressure* P_p *(dashed lines), thermal pressure* P_th *(dotted lines), and total pressure* P *(solid lines) in the equatorial plane at* $r_{100} = 159$ km *for model* A3B2G4*: Before bounce the total pressure is approximately constant over time, with* $P = P_\mathrm{p}$ *and* $P_\mathrm{th} = 0$*. When the shock front passes at* $t \approx 45.5$ ms*, the thermal pressure rises steeply, initially contributing about 80% to the increased total pressure. At later times both the total pressure and the contribution of* P_th *decline.*

6.6 Quality of the CFC Approximation during Rotational Core Collapse

When the conformally flat three-metric was introduced as an approximation of the exact spacetime metric in Section 3.3.1, we have already pointed out the limitations of this approximation. For highly relativistic and nonspherical configurations we expect growing deviations of the CFC metric from the exact solution of the metric equation. We have set up a variety of tests to quantify these deviations and assess the validity of the CFC approximation. The complexity of these tests gradually increases from stationary rotating (and thus distorted) neutron star models to dynamic spherical collapse models, and finally to dynamic nonspherical core collapse models.

In Figure 6.6 in Section 6.2 we have already presented the excellent agreement between components of the exact metric and respective components of the approximate CFC metric for rapidly rotating neutron star initial data. The ability of the evolution core to keep long-term stability when evolving this initial configuration also indicates that the CFC metric is close to the exact metric. However, as the neutron star model is highly relativistic and nonspherical, the CFC metric will solve the exact metric equations not exactly.

There are several ways to quantify the violations of the exact metric equations: Obviously, one can reinsert the CFC metric obtained by solving the CFC metric equations (3.52–3.54) into the Einstein equations (2.2). In numerical relativity similar methods are applied to test the accuracy of numerical solutions of a spacetime metric calculated from the ADM equations [83]. However, the essential drawback of this method is that the constituents of the Einstein equations like the four-Ricci tensor $R_{\mu\nu}$ or the four-energy-momentum tensor $T_{\mu\nu}$ are very complex algebraic constructs and have several thousand terms even in axisymmetry. On the other hand, the ADM metric equations (3.7–3.10) are equivalent to the Einstein equations. As we only use a subset of the full set of ADM equations to calculate the CFC metric, we can use the other equations to test the quality of the CFC approximation. The method of choice is to re-insert the CFC metric components into the individual ADM metric equations, and to compare the left and right hand sides of the respective equations[g]. If the metric, which is inserted, is an exact solution of the Einstein equations, the numerical inequality between the left and right hand sides of the ADM equations converges to zero with increasing resolution. For an approximate metric like the CFC metric, in the equation for a metric quantity q_i there will be a nonzero relative residual

$$r_{q_i} \equiv \left| \frac{\mathrm{lhs}\, q_i}{\mathrm{rhs}\, q_i} - 1 \right| > 0 \tag{6.15}$$

for at least some of the quantities q_i irrespective of numerical resolution[h]. Here $\mathrm{lhs}\, q$ and $\mathrm{rhs}\, q$ stand for the left and right hand side of the equation, respectively. In the following we will test which of the ADM equations will exhibit such a residual due to the CFC approximation, and to what degree they are violated.

---

[g] In the evolution equations for γ_{ij} (3.7) and K_{ij} (3.7), the left hand sides are simply the time derivatives of the respective quantities.

[h] For finite resolution, the residual resulting from numerical truncation errors will add to this residual.

In the derivation of the metric equations for the CFC metric components ϕ and β^i in Section 3.3.3, additionally to the ADM Hamiltonian and momentum constraint equations (3.9, 3.10) only the maximal slicing condition was used. Therefore, the metric equations (3.52–3.54) are analytically equivalent to the ADM constraint equations, and any solution according to CFC metric equations will also be a solution of the ADM constraint equations, at least up to the precision of the numerical scheme.

The evolution equations for the three-metric γ_{ij} (3.7) are also identically fulfilled for the off-diagonal elements of γ_{ij}, as for a CFC metric they transform into the definition of the extrinsic curvature (3.33). As the three-metric γ_{ii} is conformally flat, of the six evolution equations (3.7) there remains only the evolution equation for the conformal factor ϕ, Equation (3.34). We have found that the residual of this equation,

$$r_\phi = \left|\frac{\mathrm{lhs}\,\phi}{\mathrm{rhs}\,\phi} - 1\right| = \left|\frac{\partial_t \phi}{\frac{1}{6}\phi \nabla_k \beta^k} - 1\right|, \tag{6.16}$$

is very close to zero in various test situations, including rotational core collapse. For the test model A3B4G3, the radial profile of r_ϕ is plotted in the right panel of Figure 6.13, shortly before maximum density is reached during bounce. Except where a pole develops due to a zero denominator in Equation (6.16), r_ϕ is everywhere less than 0.2%, particularly in the dense interior. Hence, we infer that the ADM evolution equations for the diagonal elements of γ_{ij} are well solved by the CFC metric, too.

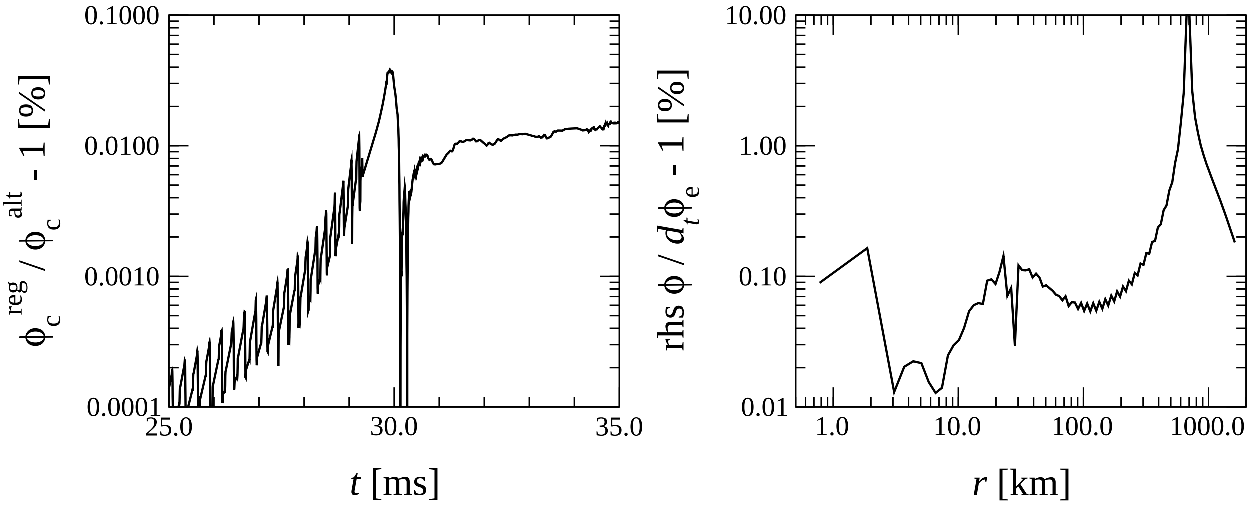

Figure 6.13: *Numerical equivalence of the left hand side (*$\mathrm{lhs}\,\phi = \partial_t\phi$*) and right hand side (*$\mathrm{rhs}\,\phi$*) of the evolution equation for* ϕ*: The relative difference for the evolution of* ϕ_{c} *in model* A1B3G5*, obtained by using the discretization of* $\partial_t\phi$ *according to Equation (5.51) (*reg*) or Equation (5.52) (*alt*) in the numerical source terms, is minute (left panel). In the test model* A3B4G3*, the residual* r_ϕ *of the evolution equation for* ϕ*, plotted along the equatorial radius at* $t \approx 41$ ms *(right panel), is small everywhere. This proves that the ADM equation (3.7) is solved to high accuracy by the CFC metric. Note that the pole at large* r *in the plot of* r_ϕ *is due to a vanishing denominator in Equation (6.16).*

Figure 6.13 proves that the analytic equivalence of the left and right hand side of Equation (3.34) is represented well by the numerical scheme: The results of core collapse simulations using the left or right hand side of Equation (3.34) in the discretized equation for the time derivative of the conformal factor deviate only slightly from each other: In the left panel of Figure 6.13 we show the evolution of the relative difference of the central value of the conformal factor ϕ_c for model A1B3G5, using Equation (5.51) or Equation (5.52) for $\partial_t \phi$ in the source terms. Even at maximum density during core bounce, when the time variation of ϕ is maximal, the values for ϕ_c from both simulations differ only by about 0.03%. Thus any of the discretized expressions for $\partial_t \phi$ as stated in Equations (5.51) or (5.52) can be used in the source terms of the numerical scheme. Neither of the two formulations is preferable by being numerically more accurate or stable.

With the ADM constraint equations being solved identically, and the ADM evolution equation for the three-metric being solved either identically (for the off-diagonal elements) or to a very high degree (for the diagonal elements), this leaves the ADM evolution equation for the extrinsic curvature as another way of checking the accuracy of the CFC approximation: As in the case of the evolution equation for the three-metric, one can compare the left and right hand sides of that equation. We note that such a procedure has also been used by Gourgoulhon et al. [48] in their validation of initial data for binary black holes, yielding satisfactory results for the CFC approximation even in such extremely relativistic (stationary) situations[i].

As a consequence of the maximal slicing condition (3.28), the sum of the left and right hand sides of the equation for the diagonal elements of the extrinsic curvature are identical up to numerical discretization errors at all grid points in any evolution. Furthermore, in spherical symmetry, the left and right hand sides of all six evolution equation for K_{ij} agree, as in this case the CFC metric is an exact solution of the spacetime (see Section 3.3.1). For the evolution equation of K_{11} this is demonstrated in the upper panel of Figure 6.14. In this simulation a nonrotating initial model with the same EoS and central density as in the (rotating) initial models listed in Section 4.4 collapses to supranuclear matter density, with the collapse initiated by reducing the adiabatic index to $\gamma_1 = 1.300$. As the EoS does not change at nuclear matter density, the collapse proceeds until a black hole forms. Both at moderate and at high supranuclear matter densities the left and right hand sides of the equation for K_{11} agree very well[j]. As the CFC metric is an analytically exact metric in spherical symmetry, this test shows that our numerical scheme for solving the metric equations is implemented correctly, and the method of comparing the left and right hand sides of the ADM equations during the evolution, e.g. in Equation (3.8), instead of computing the full Einstein tensor $G_{\mu\nu}$ and checking the equality $G_{\mu\nu} = 8\pi T_{\mu\nu}$, is appropriate.

However, inserting the CFC metric into the same equation for the case of the rapidly rotating (and therefore nonspherical) neutron star model specified in Section 6.2 yields a detectable deviation of the left and right hand side of the evolution equations for the diagonal elements, which cannot be reduced by increasing the numerical resolution[k]. This deviation is entirely

---

[i] Comparisons with Damour's analytic post-Newtonian expansion show satisfactory agreement up to third order in the expansion [47].

[j] However, as both sides are very small with absolute magnitudes of the order of the numerical discretization errors, they will deviate from each other in the center due to numerical inaccuracies.

[k] The left hand sides of the extrinsic curvature evolution equation (3.8), $\partial_t K_{ij}$, are analytically zero for equilibrium models. In a numerical evolution however, they acquire a finite nonzero (but small) value which decreases with increasing resolution.

due to the CFC approximation, as it vanishes for neutron star models in spherical symmetry, where the CFC is exact. The lower panel of Figure 6.14 shows the discrepancy between the left and right hand side of the evolution equation for K_{11}. On the other hand, this pronounced violation of some of the six components of Equation (3.8) does not directly reflect the quality of the CFC approximation in terms of its ability to model the exact spacetime of a given matter distribution accurately. As we have seen in Section 6.2, despite Equation (3.8) not being fulfilled, the equilibrium of the rotating neutron star models can nevertheless be maintained, and the exact metric is well approximated by the CFC metric quantities.

A violation of the evolution equation 3.8 for the diagonal elements of K_{ij} occurs in all highly relativistic pronouncedly nonspherical spacetimes, for example in the core collapse test model A3B4G3: Whereas the agreement between left and right hand sides of the equation is fair for lower densities at the beginning of the infall phase, at the high densities encountered in the center during and after the bounce the misalignment becomes as prominent as for the rotating equilibrium neutron star model (see lower panel of Figure 6.15). On the other hand, for example the evolution equation for K_{13} is solved to high accuracy, which is reflected by the very good alignment of the left and right hand sides of that equation even in the center of the core, as shown in the upper panel of Figure 6.15.

These observations raise the question why the left and right hand sides of some of the evolution equation for the extrinsic curvature disagree so much for nonspherical matter distributions. The reason for this becomes clear by investigating the structure of the ADM evolution equations for K_{ij}:

$$\begin{aligned}\partial_t K_{ij} = {} & \underbrace{-\nabla_i \nabla_j \alpha}_{\textcircled{a}} \underbrace{+\alpha R_{ij}}_{\textcircled{b}} \underbrace{+\alpha K K_{ij}}_{\textcircled{c}} \underbrace{-\alpha 2 K_{ik} K^k_j}_{\textcircled{d}} \underbrace{+\beta^k \nabla_k K_{ij}}_{\textcircled{e}} \underbrace{+K_{ik} \nabla_j \beta^k}_{\textcircled{f}} \underbrace{+K_{jk} \nabla_i \beta^k}_{\textcircled{g}} - \\ & \underbrace{-8\pi\alpha\left(S_{ij} - \tfrac{1}{2}\gamma_{ij}(S - \rho_{\mathrm{H}})\right)}_{\textcircled{h}} . \end{aligned} \tag{6.17}$$

In comprehensive tests of many dynamic collapse models we have found that the terms ⓒ–ⓖ are negligibly small compared to terms ⓐ, ⓑ, and ⓗ everywhere on the grid during all times. The relevant terms ⓐ, ⓑ, and ⓗ depend only on the metric quantities α (which is fixed by a gauge condition) and ϕ, but not on the shift vector components β^i. This points towards the inability of the conformally flat three-metric γ_{ij}, which has only one nonzero quantity ϕ, to exactly represent the physical spacetime. On the other hand, the quality of the shift vector components, which are calculated directly according to the ADM momentum constraint equations (3.10) (which are equivalent to the metric equations (3.54)), is not measured by Equation (3.8).

Therefore, the misalignment of the evolution equation for the extrinsic curvature is not a result of strong deviations of the shift vector components, but due to the restriction imposed onto the three-metric γ_{ij} by the CFC approximation. This conjecture is additionally supported by the following observations: As demonstrated in Figure 6.6 in Section 6.2, even for high density configurations like rapidly rotating neutron stars in equilibrium, the value of the shift vector component β^3 calculated by the CFC equation (3.54) is close to the exact value.

This also explains the very good matching of the left and right hand sides of Equation (3.8) for

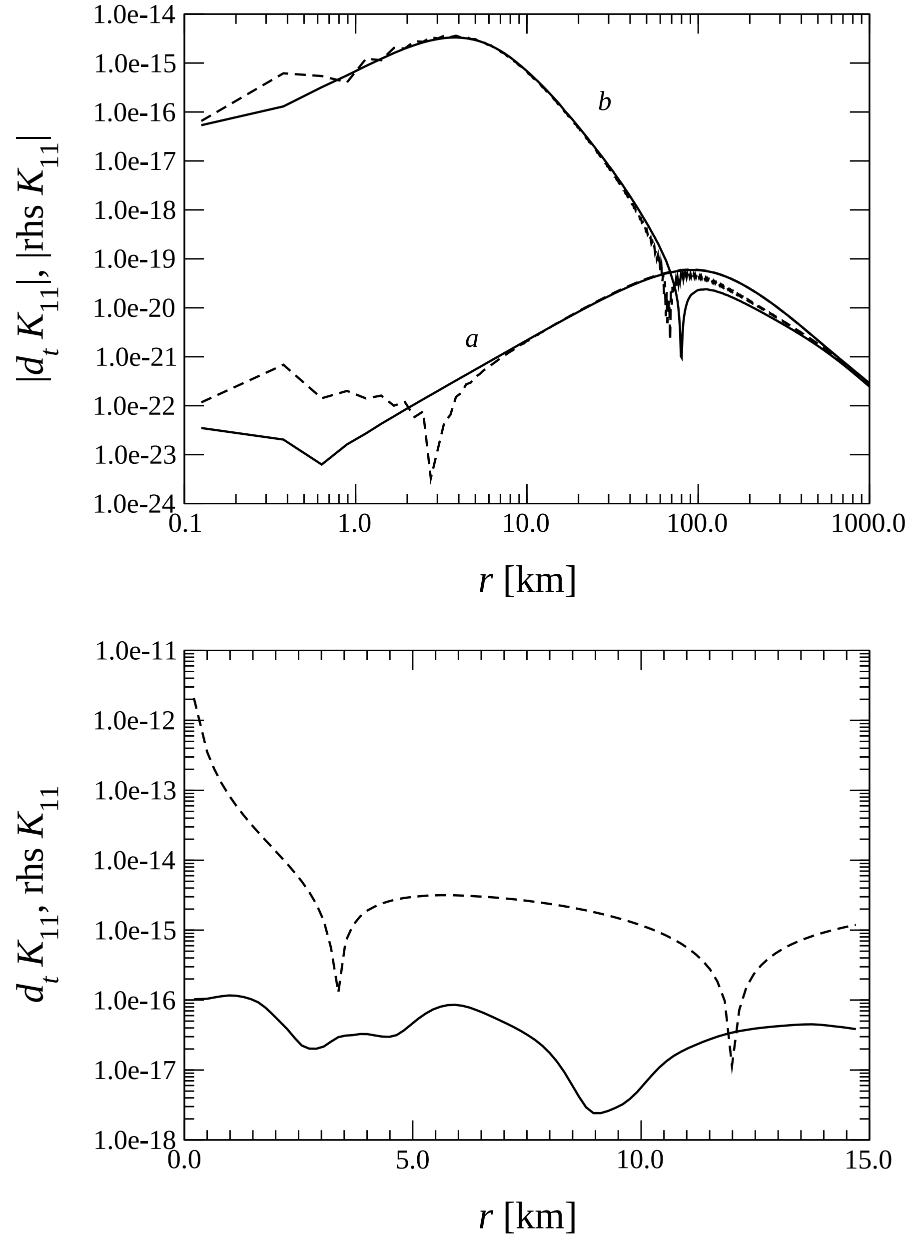

Figure 6.14: *Effect of the CFC approximation on the ADM evolution equation for* K_{11} *in a spherical core collapse model (upper panel) and in the equilibrium rotating neutron star model from Table 6.2 (lower panel): While the equatorial radial profiles of the left hand side (solid lines) and of the right hand side (dashed lines) of the ADM evolution equation coincide closely for the spherically symmetric model, they exhibit significant misalignment in the case of the neutron star model due to the deviation of the CFC metric from the exact spacetime metric. In the upper panel, the profiles are plotted at* $t = 20$ ms, *and at* $t = 38.45$ ms *when the central density reached more than 5 times nuclear matter density. The mismatch between the curves in the upper panel is caused by numerical discretization errors and converges away with increasing resolution.*

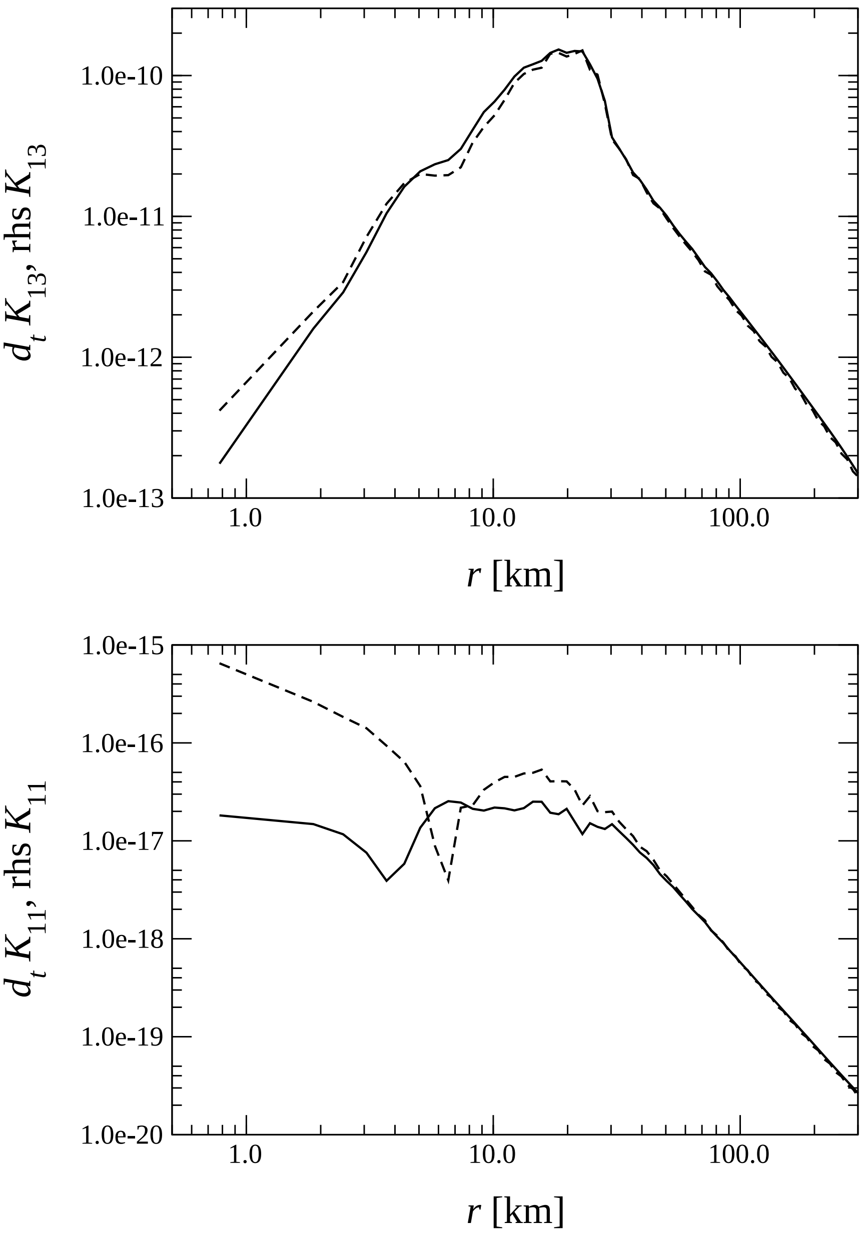

Figure 6.15: *Effect of the CFC approximation on the ADM evolution equation for* K_{13} *(upper panel) and* K_{11} *(lower panel) in the rotational core collapse test model* A3B4G3*: In the case of the evolution equation for* K_{13}*, where the terms* ⓐ *and* ⓑ *in Equation (6.17) vanish, the equatorial radial profiles of the left hand side (solid lines) and of the right hand side (dashed lines) of the ADM evolution equation coincide closely down to small radii, where the relativistic effects are most significant. These terms are nonzero in the evolution equation for* K_{11}*, which causes the non-negligible misalignment of the left and right hand side of that equation (as seen in the lower panel). The equations are evaluated at* $t = 41$ ms*, which is about* 1 ms *before bounce.*

K_{13} even for rapidly rotating and collapsing models: For this component the problematic terms ⓐ and ⓑ in Equation (6.17) vanish. (For K_{12} and K_{23} the deviations are more pronounced, since the polar velocity v_2 is very close to zero in our collapse models, and therefore the left and right hand sides of these evolution equations are dominated by truncation errors.)

The above considerations about the quality of the conformal flatness condition and the relations between the (exact) ADM metric equations and the (approximate) CFC metric equations can be summarized as follows: The ADM constraint equations are solved identically and yield expressions for the conformal factor ϕ and the shift vector β^i. The lapse function α is determined by the maximal slicing condition together with the trace of Equation (3.8). Equation (3.34), which stems from the ADM evolution equation for γ_{ij}, is solved to high accuracy even for strongly relativistic situations.

For some components of K_{ij}, the ADM extrinsic curvature evolution equations are not well solved for relativistic nonspherical matter distributions, both in equilibrium and dynamic situations, as the three-metric is constrained by the CFC. In both stationary and highly dynamic evolutions, the violations of this equation are of comparable strength. Obviously, the extrinsic curvature very sensitively reflects the inability of the CFC metric to *exactly* represent the actual spacetime. However, these violations affect neither the stability of the evolution nor the good quality of the CFC approximation compared to the exact metric even for highly relativistic configurations, like e.g. rapidly rotating neutron stars. Apart from this, these equations are never used in our approach to determine any of the metric quantities. Therefore, in our code the K_{ij} which are particular combinations of the metric components ϕ, α, and β^i, only act as auxiliary quantities with no direct physical interpretation.

6.7 Convergence and Accuracy Tests

6.7.1 Order of Numerical Convergence

We still have to address the issue of convergence and accuracy of the code. One central statement of numerics is the one of accuracy up to a certain order, in our case up to second order. When a system of equations is solved numerically, a simulation with a higher grid resolution yields a solution with higher accuracy. More precisely, for a system which is second order convergent, an increase in the number of grid points by a factor m_i in the coordinate direction i results in a decrease of the deviation between the numerical solution and the analytic solution by a factor m_i^2.

The numerical methods we have chosen to discretize the analytic equations are in general second order accurate in space and time. This translates into an approximation of the analytic solution by its numerical counterpart in the following way (here we confine ourselves to the spatial representation, although these considerations are also valid for accuracy in time):

$$f_{\text{num}}(x_i, x_j) = f_{\text{ana}} + O(\Delta x_i^2, \Delta x_i \Delta x_j, \Delta x_j^2), \tag{6.18}$$

or, on a polar grid (r_i, θ):

$$f_{\text{num}}(r, \theta) = f_{\text{ana}} + O(\Delta r_i^2, \Delta r_i \Delta\theta, \Delta\theta^2), \tag{6.19}$$

where f_{ana} and f_{num} are the analytic and numerical solution of some equation on a 2-dimensional grid, respectively.

Usually the analytic solution f_{num} of the system of equations is not known. However, if the system of equations is indeed second order convergent, one can check for convergence without prior knowledge of the analytic solution: By solving the numerical system for three different resolutions, where the number of grid points are e.g. n_{i1}, $2n_{i2}$, and $4n_{i3}$, respectively, the analytic solution can be canceled out:

$$\begin{aligned}
f_{\text{num}}^{n_i}(x_i, x_j) &= f_{\text{ana}}(x_i, x_j) + O(\Delta x_i^2, \Delta x_i x_j, \Delta x_j^2), \\
f_{\text{num}}^{2n_i}(x_i, x_j) &= f_{\text{ana}}(x_i, x_j) + \frac{1}{4} O(\Delta x_i^2, \Delta x_i x_j, \Delta x_j^2), \\
f_{\text{num}}^{4n_i}(x_i, x_j) &= f_{\text{ana}}(x_i, x_j) + \frac{1}{16} O(\Delta x_i^2, \Delta x_i x_j, \Delta x_j^2).
\end{aligned}$$

From this we can then infer a condition for second order convergence of a particular discretization scheme:

$$r_{\text{conv}} = \left| \frac{f_{\text{num}}^{2n_i} - f_{\text{num}}^{4n_i}}{f_{\text{num}}^{n_i} - f_{\text{num}}^{2n_i}} \right| = \frac{1}{4}. \tag{6.20}$$

Note that the solutions f_{num} for the different spatial resolutions have to be evaluated at the same evolution time. The condition for second order convergence (6.20) can be tested for various hydrodynamic and metric quantities.

In general, the order of convergence f_{conv} of a system of discretized equations can be determined according to

$$f_{\text{conv}} = \frac{\ln r_{\text{conv}}}{\ln 2}. \tag{6.21}$$

We have successfully tested second order convergence of the code in various situations, including simulations of spherically symmetric core collapse, evolution of the hydrodynamics in a stationary spacetime (Cowling approximation), and evolution of rotational core collapse models. In Figure 6.16 we show results for the quantities ρ and ϕ for a fully dynamic evolution of a rapidly rotating core collapse model. We have increased the spatial resolution in both the radial and angular direction and find second order convergence everywhere on the grid, except close to the outer boundary, where boundary effects lower the order of convergence. This demonstrates that the hydrodynamic evolution scheme and the metric solver are accurate up to second order.

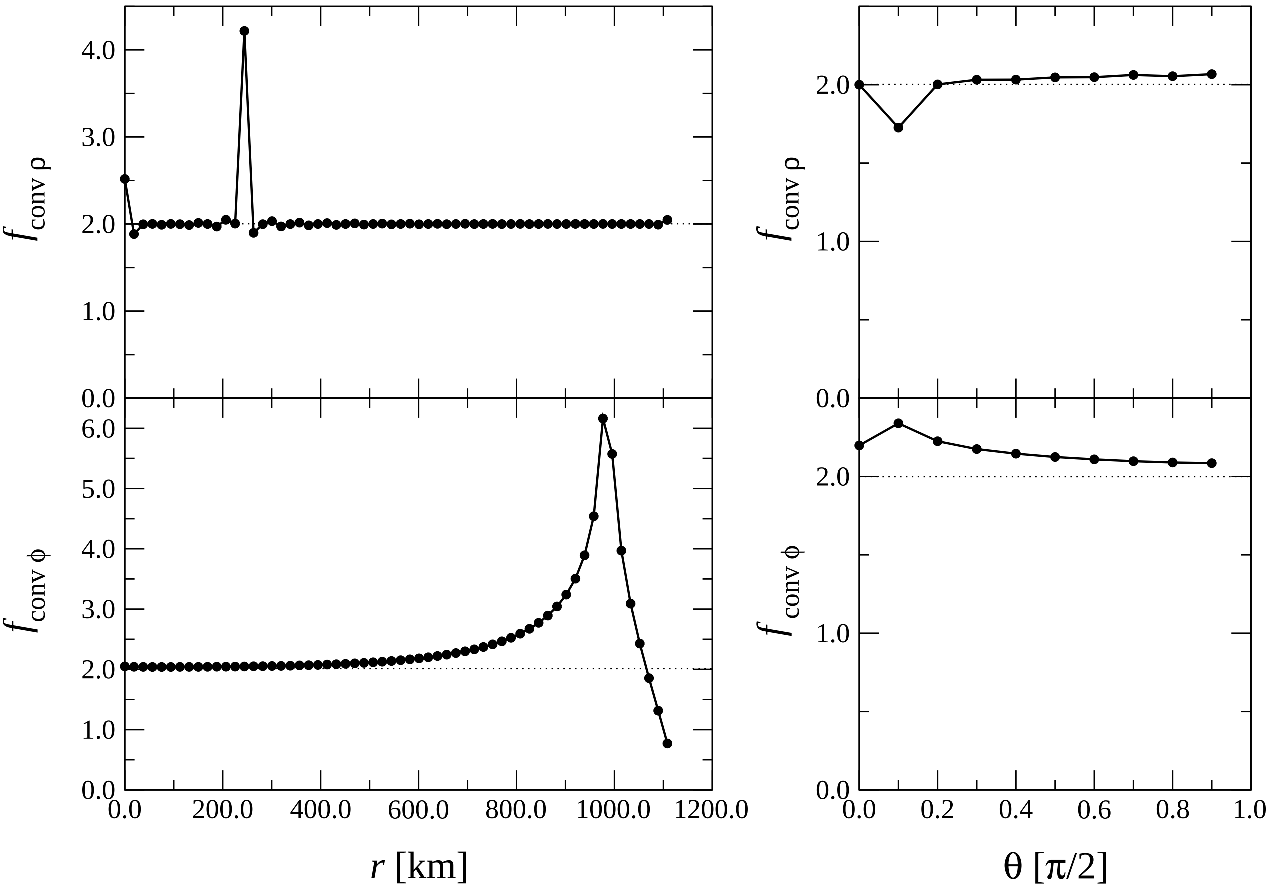

Figure 6.16: *Order of convergence in the evolution of a rapidly rotating core collapse model: Both in the radial direction (left panels) and angular direction (right panels), the density* ρ *(upper panels) and the conformal factor* ϕ *(lower panels) exhibit second order convergence. The order of convergence* $f_{\mathrm{conv}\,\rho}$ *and* $f_{\mathrm{conv}\,\phi}$ *in* r*- and* θ*-direction are determined by evaluating* ρ *and* ϕ *along constant angles* $\theta_{n_\theta/2}$ *and constant radii* $r_{n_r/2}$*, respectively. Note that the order of convergence for* ϕ *in the radial direction decreases to less than 1 at the outer boundary; this is caused by boundary effects. The horizontal dotted lines mark the value of* f_{conv} *for second order convergence. The single point spikes are a result of inaccuracies due to numerical truncation errors.*

6.7.2 Grid and Metric Resolution Tests – Metric Extrapolation Tests

When analyzing the order of convergence as in Section 6.7.1, there arises a practical problem: One can only make definite statements about second order convergence if the grid is uniform and the time step is fixed. It also fails if shocks are present, which is the case after bounce; in a shock the second order hydrodynamics scheme is reduced to first order accuracy. This means that we can prove second order convergence of the code only in a narrow regime of space and time during the evolution. Because of its limitations, with this method we cannot check whether the resolution in space and time we have chosen is good enough to resolve the physical features of a particular model. As we compute the metric not on every time slice but only on multiples of them, we also have to demonstrate that this reduced calculation of the metric in time is good enough for all practical purposes.

In order to be able to answer these questions, we have performed several resolution tests with four collapse models, representing multiple bounce collapse (A2B4G1), regular collapse (A3B2G4), and collapse of a rapidly and differentially rotating core (A4B4G4); for a definition of collapse types, we refer to Section 7.1. We have simulated these models using the regular resolution of the grid and the metric computation as specified in Sections 5.1.1 and 5.6.4, using double resolution in the radial and angular direction, and using double resolution of the metric computation. In Figure 6.17 we show a comparison between the results for hydrodynamic, metric, and derived quantities obtained from the resolution tests of models A2B4G1 and A3B2G4[l]. As the gravitational wave signal amplitude A_{20}^{E2} (upper panels) is determined by the quadrupole moment, i.e. a volume integral over the entire core, it is comparatively insensitive to local deviations between simulations using different resolutions. Thus we expect a good agreement for the evolution of A_{20}^{E2} in all four resolution tests of the two models; this is confirmed by the plots in Figure 6.17. The evolution of the conformal factor at the center ϕ_{c} is more sensitive to local deviations, as here the metric quantity ϕ is evaluated at a single grid point, and ϕ has its maximum at the center. Nevertheless, as the metric is determined by an elliptic system of equations, its components are influenced by the global state of the system; additionally this quantity does not exhibit shocks. As a result of these properties of metric quantities, the values for the evolution of ϕ_{c} (middle panels) also coincide very well in the test models for all investigated resolutions. A very strong test for the quality of the chosen standard resolution is to probe for possible deviations in the shape of e.g. a radial profile of a hydrodynamic quantity, particularly if a strong shock is present in the profile. The radial profile along the equatorial plane for the radial velocity $v_r = \sqrt{v_1 v^1}$ shortly after core bounce, obtained by simulations of the two test models with standard resolution, double radial resolution and double resolution for the metric computation[m], exhibits excellent agreement even in the region of the shock. Obviously, a better radial resolution (green lines) results in a steeper shock. Nevertheless, all features of the profile of v_r both in the region of the shock itself and in the smooth regions before and behind the shock, as well as the position and height of the shock, are well captured in all resolution tests.

The results presented in Figure 6.17 demonstrate impressively, that our standard resolution

---

[l] The results from the resolution tests of A4B4G4 are qualitatively similar.

[m] As $v_{r\,\mathrm{e}}$ is evaluated at the center of the cells (r_i, θ_{n_θ}), a grid with a different angular resolution has different values of θ_{n_θ}; thus, we cannot unambiguously compare quantities evaluated at these grid points for different n_θ.

of the grid and the metric computation is fine enough for investigating rotational core collapse; any increase in resolution does not change the dynamics of metric or hydrodynamic quantities significantly, even in the center during core bounce, where the highest densities and largest time derivatives are encountered.

The test methods discussed above only prove that the numerics converge with second order to the solution of the discretized equations, and that the resolution suffices to be in the zone of convergence. They do not allow for checking whether the equations in the code are the correct discretized equations of the analytic equations. This is not a mathematical, but rather a computational problem, as we have to make sure that we code up the equations not only in second order accurate form, but also in a correct way. One can always think of a second order convergent code, which yields the incorrect physics due to programming errors. Thus, in order to minimize the risk of such errors in our code, we have performed the tests stated in Sections 6.1 to 6.5, which compare solutions obtained with our code against known analytic solutions, or against solutions from independent codes; they also scrutinize different parts of the code, and check long-term stability of stationary solutions. Together with the convergence and resolution tests presented in this section, this gives us strong confidence that the code is both second order convergent and yields the correct physics, and that the chosen resolution is appropriate to resolve the core collapse problem.

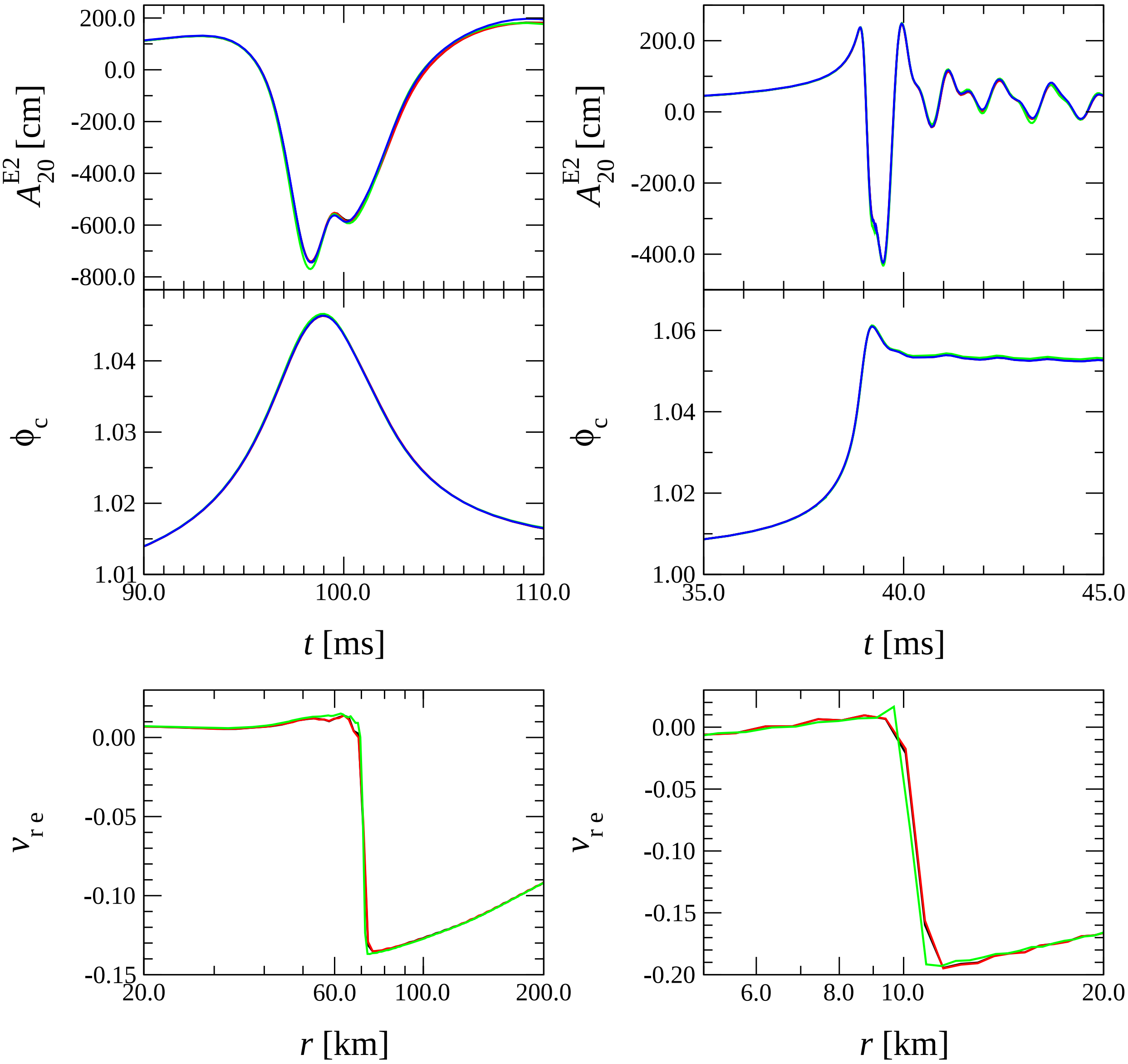

Figure 6.17: *Tests of the resolution of the grid and metric computation for the rotational core collapse models* A2B4G1 *(left panels) and* A3B2G4 *(right panels): The evolution of the gravitational wave signal amplitude* A_{20}^{E2} *(upper panels) and the evolution of the conformal factor at the center* ϕ_{c} *(middle panel) coincide very well for regular resolution (black lines), double radial resolution (red lines), double angular resolution (green lines), and double resolution of metric computation (blue lines). The agreement of radial profiles along the equatorial plane for* v_r *(lower panels), here plotted for regular resolution and double resolution in radial direction and metric computation, is also excellent. The profiles of* $v_{r\,\mathrm{e}}$ *are evaluated shortly after core bounce at* $t = 99.0$ ms *(model* A2B4G1*) and* $t = 39.25$ ms *(model* A3B2G4*), when the shock forms.*

Chapter 7

Results and Discussion

In the following, we present the results from simulating all 26 models as defined in Section 4.4. In order to be able to clearly identify the impact of relativistic gravity on the collapse dynamics, we have simulated those models in both Newtonian and relativistic gravity. If not stated explicitely otherwise, the results presented refer to the relativistic simulation of a particular model.

7.1 Collapse and Waveform Types

Before we turn to elaborate on the differences between general relativistic and Newtonian simulations of rotational core collapse, we want to present three typical collapse models. These are representative to three classes, into which the set of models splits. Following Zwerger [146], who has first identified these three classes, we call them type I, II, and III[a]. In the following three parts of this sections, we will demonstrate their peculiarities, and explain the physical effects which lead to the different collapse types.

The evolution of any core collapse can be divided up into three phases:

Infall phase:

This phase is initiated by the instability when the EoS of the initial model, which is in equilibrium, changes. The entire core contracts, with the inner part collapsing homologously ($v_1 \propto r$), and the outer part falling supersonically. Depending on the collapse parameters, in our models the infall phase lasts between about 30 ms and 100 ms.

Bounce phase:

When the EoS stiffens due to nuclear forces, or when centrifugal forces due to rotational spin-up become dominant, the inner core decelerates, and the contraction of the inner core is abruptly stopped on a timescale of about 1 ms. Because of inertia, the inner core

---

[a] Zwerger's classification is based on the form of the gravitational wave signal. As the gravitational radiation waveform is closely linked to the collapse dynamics, it also mirrors the collapse behavior, and the signal types can in general be used to classify the collapse type.

shoots over its equilibrium configuration, and therefore rebounces. Depending on the rotation strength and the EoS during the collapse, the bounce can occur at subnuclear or supranuclear densities. During that phase, the amplitude of the gravitational wave signal is highest.

Ring-down phase, or re-expansion phase:

If the infall has been happening moderately fast, and the centrifugal forces do not dominate the dynamics, the inner core settles down to a new equilibrium state. While the shock wave, which forms at the boundary between the inner and the outer core, propagates outwards, the inner core oscillates over a time of typically several 10 ms with a superposition of several more or less damped eigenmodes which have frequencies of about 10^3 Hz (ring-down). This collapse type is called regular collapse.

If the core collapses very rapidly (i.e. on a timescale of about 30 ms), the core plunges deeply into the gravitational potential well. Thus the central density reaches significantly higher values, and the signal waveform changes qualitatively compared to collapse models with a slower infall. Such models belong to the rapid collapse type.

On the other hand, if the core is predominantly stopped by centrifugal forces, the core as a whole expands again and recollapses. It experiences several distinct sequences of infall, bounce, and re-expansion separated by up to 50 ms, generating an outward shock at each bounce. Finally it settles down in an equilibrium state. The behavior of such a type is dubbed multiple bounce collapse.

If the maximum central density is close to or above nuclear matter density, and if the core rotates differentially and rapidly, a combination of regular and multiple collapse is possible. Then the core re-expands less than in a genuine multiple bounce, but still bounces and re-expands coherently.

In Figure 7.1, snapshots of radial profiles of the equatorial density and radial velocity at different evolution times are plotted. In this typical regular collapse model A3B2G4, the three phases of infall (profiles *a, b, c*), bounce (profiles *d, e*), and ring-down and shock propagation (profiles *f, g*) can be identified. As the shock front passes by, the density rises by almost one order of magnitude[b].

7.1.1 Type I Collapse Model – Regular Collapse

As in the work by Zwerger [146], we choose model A1B3G3 as a representative model for a regular collapse. In Figure 7.2 the time evolution of the central density ρ_{c} and the gravitational wave signal amplitude A_{20}^{E2} are plotted. (For a definition of the gravitational wave amplitude A_{20}^{E2} and the numerical wave extraction techniques, we refer to Appendix C.) The three phases

---

[b] For a strong shock, the ratio between the density in front of the shock ρ_1 and the density behind the shock ρ_2 is given by

$$\frac{\rho_2}{\rho_1} \approx \frac{\gamma+1}{\gamma-1}. \tag{7.1}$$

For an adiabatic index of 1.30, the pressure thus rises by a factor of about 8 across the shock discontinuity.

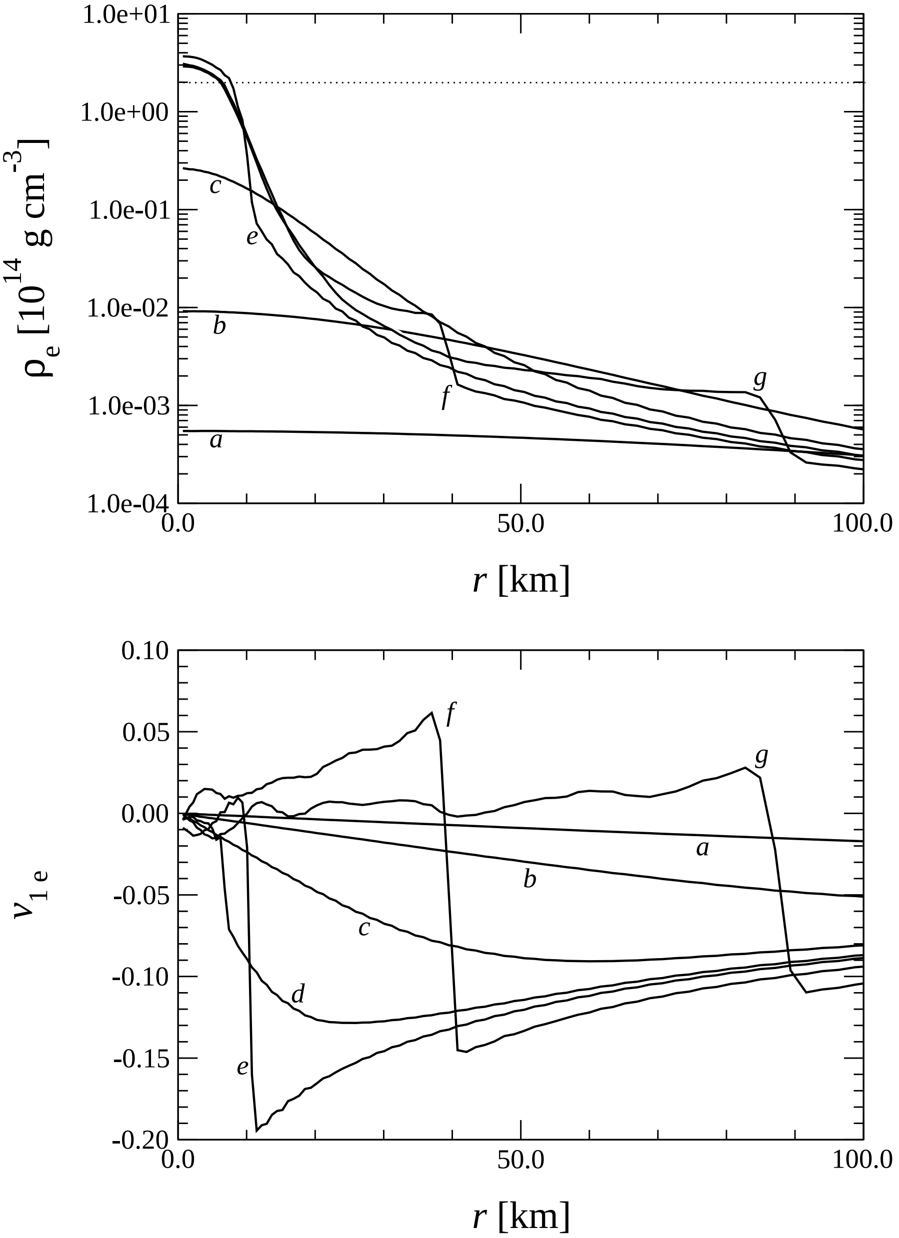

Figure 7.1: *Snapshots of radial profiles of the equatorial density* ρ_{e} *(upper panel) and radial velocity* $v_{r\,\mathrm{e}}$ *(lower panel) for model* A3B2G4*. The labels refer to* $t_a = 25.0$ ms*,* $t_b = 35.0$ ms*,* $t_c = 38.25$ ms*,* $t_d = 39.0$ ms*,* $t_e = 39.25$ ms*,* $t_f = 40.0$ ms*, and* $t_g = 41.75$ ms*, respectively. For clarity, profile d is not plotted in the upper panel. The dotted line specifies nuclear matter density.*

of the collapse are clearly identifiable in both quantities: The infall lasts until about 48 ms. In the subsequent bounce phase nuclear matter density is exceeded at 48.10 ms, and maximum density is reached with $\rho_{\mathrm{c\,b}} = 4.09 \times 10^{14}$ g cm^{-3} $\approx 2\rho_{\mathrm{nuc}}$ at $t_{\mathrm{b}} = 48.45$ ms. After that the core rebounces and rings down to its equilibrium state with a final central density of $\rho_{\mathrm{c\,f}} \approx 3.0 \times 10^{14}$ g cm^{-3} $\approx 1.5\rho_{\mathrm{nuc}}$.

The corresponding gravitational wave signal amplitude first rises during the infall phase, and turns negative shortly before bounce. It has a negative peak with $|A^{\mathrm{E2}}_{20}|_{\mathrm{max}} = 483.86$ cm at $t_{\mathrm{gw}} = 48.88$ ms. In all regular collapse models the maximum signal amplitude is negative. As $t_{\mathrm{b}} < t_{\mathrm{gw}}$, the negative flank of the wave signal exhibits a small local minimum at the time of bounce, a feature which was identified and discussed in Zwerger's work[c]. The ring-down phase of the inner core is directly reflected in the wave signal, which oscillates accordingly. As in the Newtonian runs by Zwerger, the maxima of A^{E2}_{20} in the ring-down phase are less damped than the minima due to the stronger accelerations encountered at the high density extrema of the core. Clearly this relativistic model is of type I like its Newtonian counterpart, and the wave signal belongs to the standard signal class in [146].

7.1.2 Type II Collapse Model – Multiple Bounce Collapse

For an adiabatic index γ_1 close to its initial value of 4/3, and for rapid and highly differential rotation, centrifugal forces can not only influence the core collapse dynamics, but even halt the collapse at densities lower than nuclear matter density, and thus cause a subnuclear bounce. This can indeed be observed in some of our collapse models. To demonstrate this, we choose model A2B4G1[d]. Figure 7.3 again shows the time evolution of the quantities ρ_{c} and A^{E2}_{20}.

In both the central density and the wave signal, distinct extrema are discernable. Again, like in the regular collapse case, the (negative) maximum of the signal waveform $|A^{\mathrm{E2}}_{20}|_{\mathrm{max}} =$ 744.61 cm is reached at a time $t_{\mathrm{gw}} = 98.38$ ms which is shortly before the time $t_{\mathrm{b}} = 99.09$ ms of the first maximum of the central density $\rho_{\mathrm{c\,b}} = 0.42 \times 10^{14}$ g cm^{-3} $\approx 0.2\rho_{\mathrm{nuc}}$. This is also true for the following signal peaks, where the waveform develops a local peak in the negative flank of the second signal peak, which for the third peak produces a double maximum.

7.1.3 Type III Collapse Model – Rapid Regular Collapse

If the infall of the core proceeds rapidly (i.e. almost with free fall velocity) because the value of γ_1 is much smaller than 4/3, the corresponding behavior of the density is hardly affected compared to a regular collapse of type I. As in a regular bounce model, ρ_{c} becomes and stays higher than nuclear matter density. Due to the rapid contraction of the core, the average densities are very high, and the inner core oscillates only slightly after the bounce. In model A1B3G5, which is

---

[c] The occurrence of this small intermediate spike in a regular collapse is model dependent, as pointed out in [146].

[d] Model A1B3G1, which is the representative multiple bounce models in the Newtonian simulations in [146] exhibits no multiple bounce behavior in our relativistic simulations. This discrepancy between collapse types in relativistic and Newtonian models will be discussed in Section 7.5.

a typical rapid bounce model, the values for the maximum and the final central density are $\rho_{\mathrm{c\,b}} = 4.49 \times 10^{14}$ g cm$^{-3} \approx 2.5\rho_{\mathrm{nuc}}$ at $t_{\mathrm{b}} = 30.10$ ms, and $\rho_{\mathrm{c\,f}} \approx 3.5 \times 10^{14}$ g cm$^{-3} \approx 1.75\rho_{\mathrm{nuc}}$.

However, the gravitational wave signal amplitude changes its shape qualitatively compared to type I models, which can be seen in Figure 7.4 where the evolution of ρ_{c} and A^{E2}_{20} are plotted. Obviously, $|A^{\mathrm{E2}}_{20}|_{\mathrm{max}} = 106.21$ cm at $t_{\mathrm{gw}} = 29.91$ ms is now assigned to the first positive peak of the signal, contrary to the signal waveform of the regular collapse models, where the maximum is at the first negative peak.

In rapid collapse models, the negative peak, which dominates the waveform of the collapse models I and II is almost entirely suppressed, and the overall amplitude of the signal is significantly smaller. There is no clear feature in the waveform which identifies the time of bounce t_{b}, which falls into the time interval in which the waveform exhibits the declining flank of the signal maximum peak.

For a given initial model, the transition between type I and III collapses occurs gradually with decreasing γ_1 values. In the gravitational wave signal this can be seen by a decrease of the negative main peak and a stronger emphasis of the first positive peak.

The above investigation of the three different collapse types has shown that relativistic simulations of rotational core collapse exhibit the same qualitative collapse dynamics and allow for the same classification as Newtonian simulations. However, there are important and non-negligible differences arising from relativistic effects in other aspects. In the following we will work out these differences.

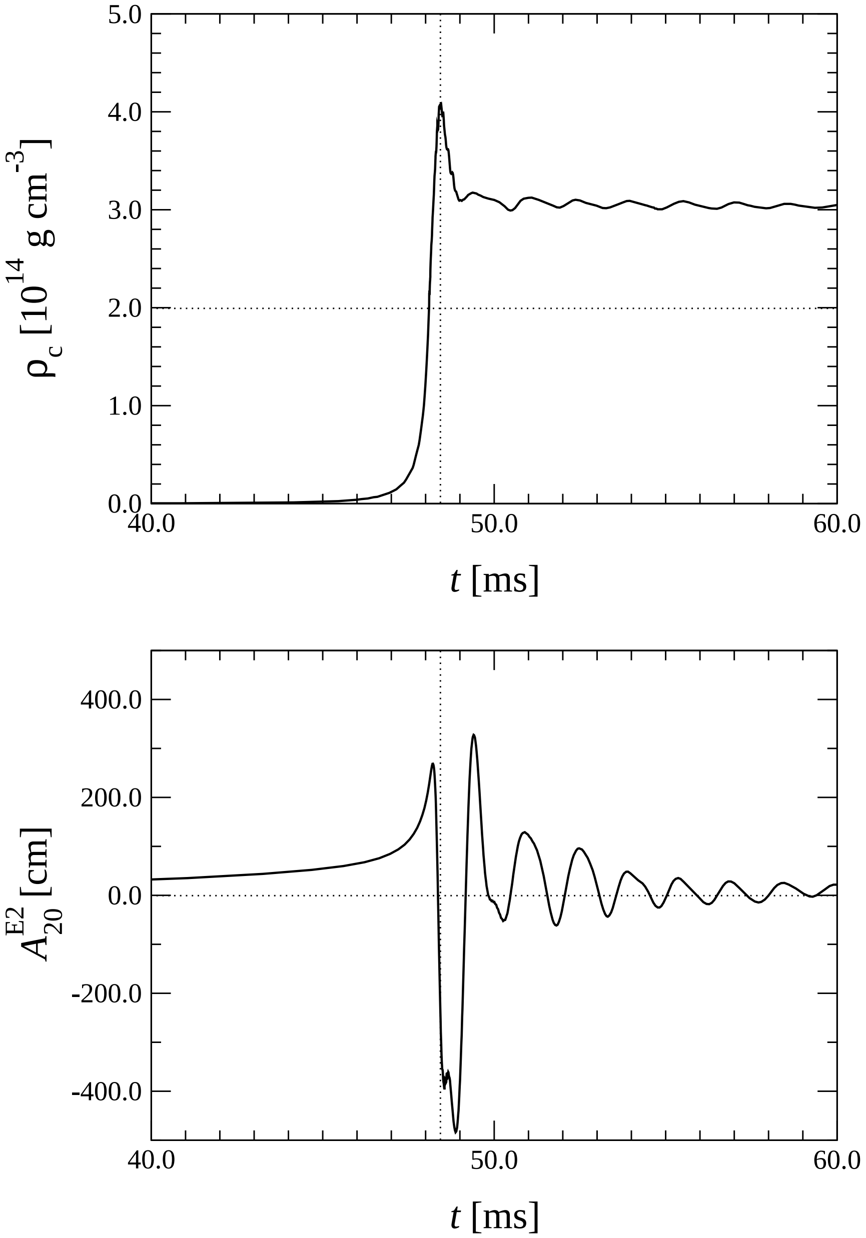

Figure 7.2: *Time evolution of the central density* $\rho_{\rm c}$ *(upper panel) and the gravitational wave signal amplitude* $A^{\rm E2}_{20}$ *(lower panel) for the regular collapse model* A1B3G3*. The horizontal dotted line in the upper panel marks nuclear matter density* $\rho_{\rm nuc}$*, and the vertical dotted line the time of maximum central density* $t_{\rm b}$*.*

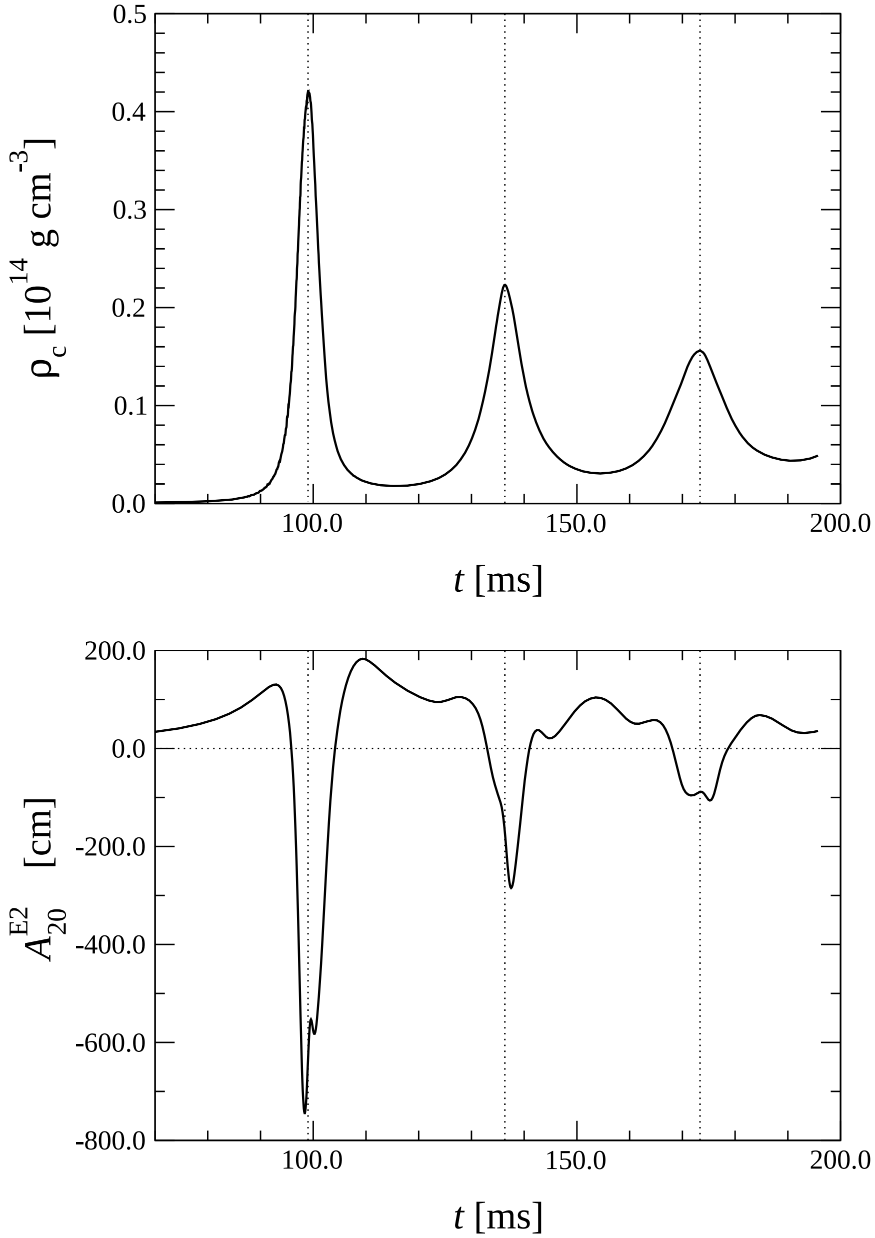

Figure 7.3: *Time evolution of the central density* ρ_c *(upper panel) and the gravitational wave signal amplitude* A^E2_{20} *(lower panel) for the multiple bounce collapse model* A2B4G1*. The vertical dotted lines mark the times of maximum central density* t_b *in each bounce.*

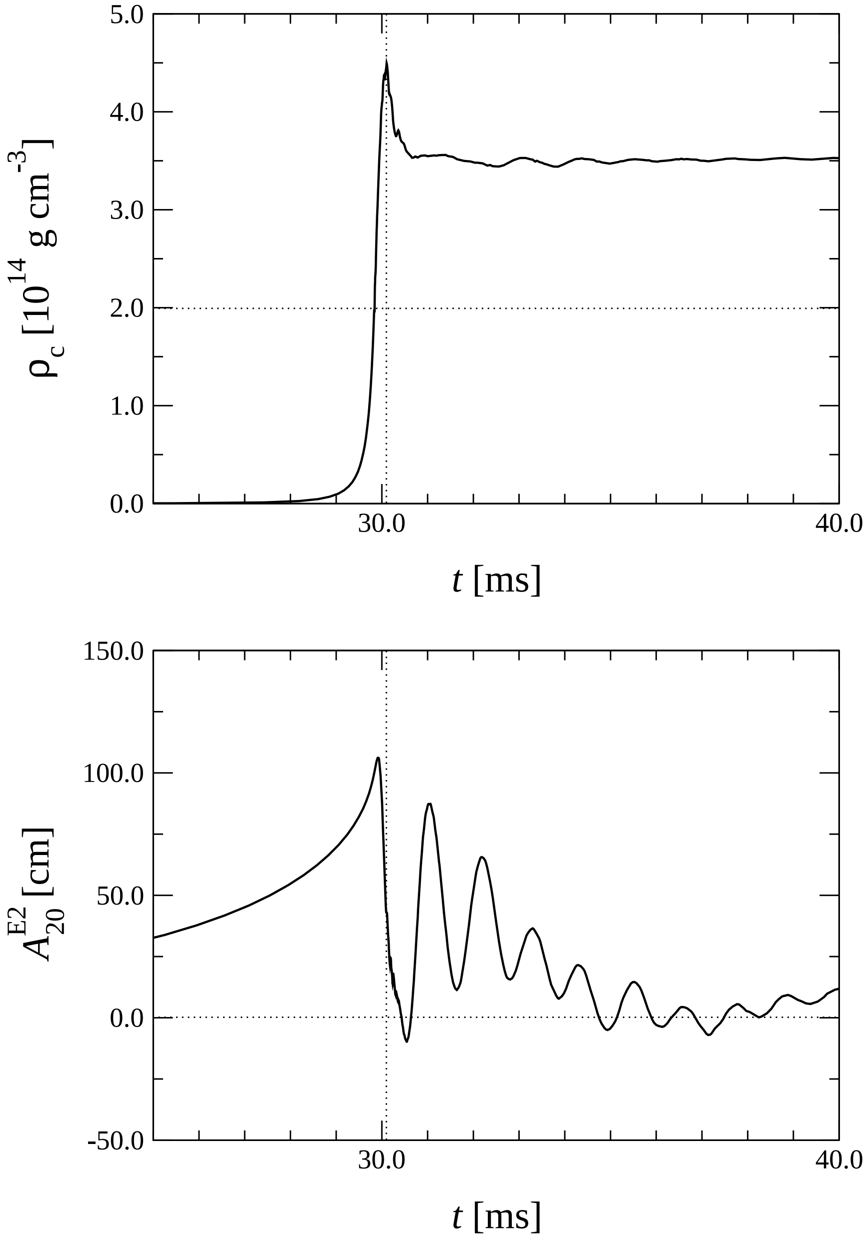

Figure 7.4: *Time evolution of the central density* ρ_c *(upper panel) and the gravitational wave signal amplitude* A_{20}^{E2} *(lower panel) for the rapid collapse model* A1B3G5*. The horizontal dotted line in the upper panel marks nuclear matter density* ρ_nuc*, and the vertical dotted line the time of maximum central density* t_b*.*

7.2 Homology of the Infall

When investigating the quality of homology of the inner core during the collapse, one can already determine differences between relativistic and Newtonian simulations: Homologous infall is defined by the (negative) radial infall velocity v_r being proportional to the radius, with the proportionality constant (i.e. the slope of $v_r(r)$) growing with time according to the self-similar solution of Goldreich and Weber [46]. If centrifugal forces can be neglected, in Newtonian core collapse homologous behavior can be observed in the regions of the inner core, which is the part of the core where the mass shells stay in sonic contact. Therefore the inner core is bounded by the sonic sphere, i.e. the sphere defined by the sonic point. It is this inner core which comes to a sudden halt within a fraction of a millisecond during the bounce, and forms the proto-neutron star. The ratio between the masses of the inner and the outer core crucially influences the dynamics of the prompt shock, and thus also specifies the location of the heating region behind the stalled shock in the delayed explosion scenario.

The analytic Goldreich–Weber solution for a homologously collapsing core is only valid in spherical symmetry for a Newtonian $1/r$ potential. Therefore we expect both rotation and relativistic effects to have effects on the quality of homology, and the radial extent and mass of the inner core. Figure 7.5 shows the radial profile of the infall velocity at the equator $v_{r\,\mathrm{e}}$ in the rather rapidly collapsing model A3B2G4, just before the EoS changes when nuclear matter density is reached. It is obvious that the radius of the homological region, i.e. the maximum radius for which there is a linear relation between v_r and r, which also corresponds to the size of the inner core, is significantly smaller in the relativistic case. This is mainly due to the higher infall velocities encountered in the relativistic simulation due to the deeper gravitational potential, which shifts the sonic sphere to smaller radii. Also within the inner core, the deviations from an exact $v_r \propto r$ profile are more pronounced in the relativistic simulation compared to the Newtonian one, which can be clearly seen in the more rounded profile of the velocity in the left panel of the figure, and especially in the right panel of the figure, where the velocity profile is tilted such that its slope is zero close to the center. This behavior can be explained by the fact that if relativistic gravity is approximated by a potential, this potential has a radial dependency close to, but not exactly, $1/r$. From Figure 7.5 one can estimate the radius of the homologous region at the equator to be $r_{\mathrm{hom}}^{\mathrm{R}} \approx 12$ km for the relativistic case, and $r_{\mathrm{hom}}^{\mathrm{N}} \approx 20$ km for the Newtonian case, respectively. The difference in radius between both cases of about 8 km is much more than the difference in the radii of equal masses, which in this region is about 1.5 km. This means that not only the radial extent of the homologously infalling inner core is smaller in a relativistic gravitational potential, but that also the mass contained in this region and thus the mass of the inner core is significantly smaller[e]. However, although parts of the relativistic inner core do not contract exactly homologously, sonic contact will still be maintained throughout the inner core. As a result, contrary to Newtonian gravity, the quality of homology during the infall phase is not a good measure for determining the extent and mass of the inner core which finally constitutes the proto-neutron star.

While the collapse dynamics in model A3B2G4, which collapses to supranuclear densities, are not strongly influenced by rotation, the effects of rotation on the homology become visible

---

[e] One can show that in Lagrangian mass coordinates the boundary of the inner core is at smaller masses in a relativistic simulation. Thus the fraction of total mass contained in the inner core is smaller.

in model A2B4G1, whose radial profile of the infall velocity at the equator $v_{r\,\mathrm{e}}$ just before the centrifugal bounce at subnuclear densities is plotted in Figure 7.6. Again, as in the denser and thus more relativistic model A3B2G4, the sonic sphere of the relativistic simulation is smaller than in the Newtonian case. Furthermore, however, except close to the center the homology is destroyed due to the rapid spinup of the inner core and the strong centrifugal forces, which make the core bounce before it reaches supranuclear densities. This breaking of the collapse decelerates the infall and thus reduces the slope of the velocity profile near the center. Note that this deceleration does not result from any changes in the EoS or occurrence of shocks. As the central parts of the inner core effectively fall with lower velocities, the radius of the sonic sphere and thus the mass of the inner core will increase, because more mass shells out to a larger radius can stay in sonic contact.

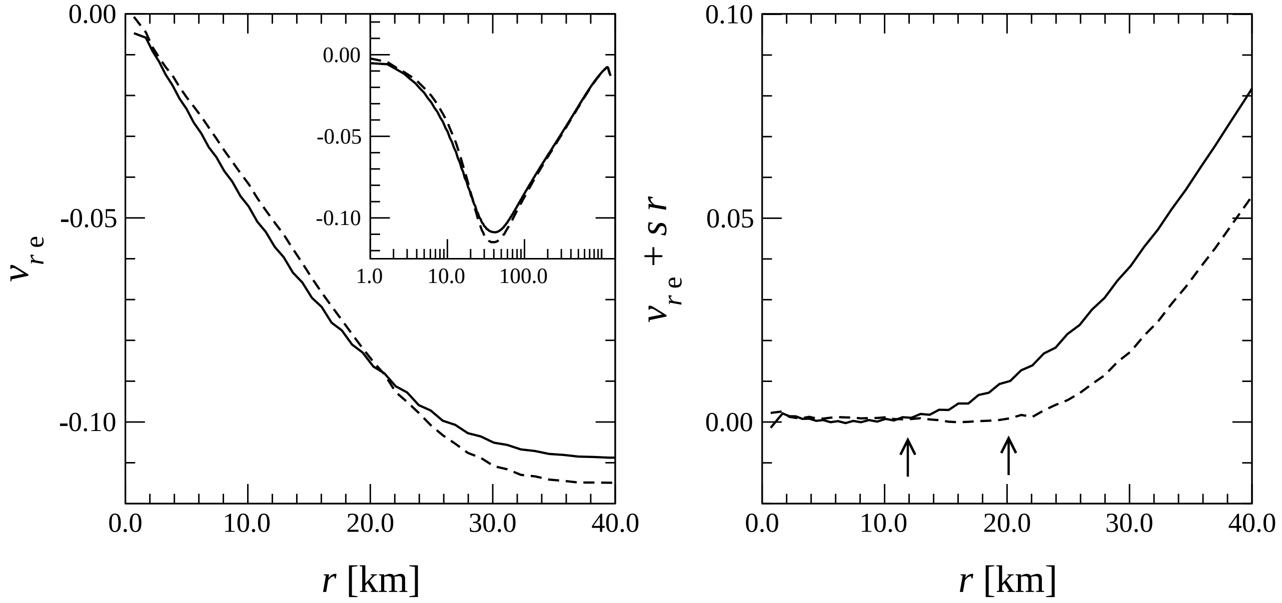

Figure 7.5: *Homology of the infall for the rapid collapse model* A3B2G4*: Both in relativistic (solid lines) and Newtonian (dashed lines) gravity, the profiles of the radial velocity along the equatorial plane* $v_{r\,\mathrm{e}}$*, which are plotted shortly before bounce at* $t = 38.75$ ms*, exhibit homologous behavior near the center of the star (left panel). The size of the inner core is larger for the Newtonian model. This becomes clear when* $v_{1\,\mathrm{e}} = v_{1\,\mathrm{e}} - s \cdot r$*, where* s *is the slope for small* r*, is plotted (right panel). The arrows indicate the radii where the homology fails. The inset in the left panel shows the velocity profile up to the outer core radius in a logarithmic plot.*

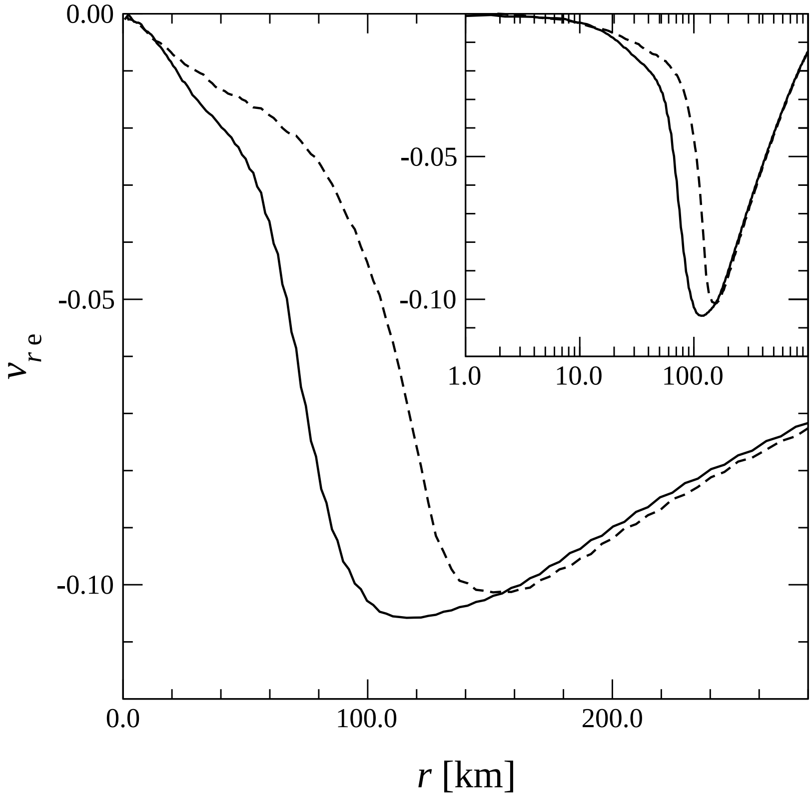

Figure 7.6: *Homology of the infall for the slow collapse model* A2B4G1*: Both in relativistic (solid line) and the Newtonian (dashed line) gravity, the profiles of the radial velocity along the equatorial plane* $v_{r\,\mathrm{e}}$*, which are plotted shortly before bounce at* $t = 98.0$ ms*, exhibit homologous behavior only in a small region in the central part of the inner core. Farther outside, the homology is severely spoilt by the breaking action of centrifugal forces due to rotation. These forces determine the dynamics of this model and stop the collapse at subnuclear densities. The inset shows the velocity profile up to the outer core radius in a logarithmic plot.*

7.3 Central Densities and Time of Bounce

An obvious set of quantities to use for investigating differences between models evolving in Newtonian and relativistic gravity are the maximum central density reached during the evolution $\rho_{\mathrm{c\,b}}$, and the corresponding time of bounce t_{b}, which are defined as

$$\rho_{\mathrm{c\,b}} \equiv \max\, \rho_{\mathrm{c}}(t), \qquad t_{\mathrm{b}} = t(\rho_{\mathrm{c}} = \rho_{\mathrm{c\,b}}). \tag{7.2}$$

Another important criterion is the central density at the end of the simulation $\rho_{\mathrm{c\,f}}$. The time t_{f} when a particular simulation was terminated, was specified such that in a regular type I or rapid type III collapse the ring-down oscillations have sufficiently been damped, and the central density has settled down to an approximately constant value. For multiple bounce type II collapse simulations at least two subsequent bounces were covered, often three (see the plots showing the evolution of the central density in Appendix D). The quantities introduced in Equation (7.2) are listed for all 26 models in Table 7.1 (A1 and A2 models), Table 7.2 (A3 models), and Table 7.3 (A4 models). If the final central density $\rho_{\mathrm{c\,f}}$ is above ρ_{nuc} for a particular model, a multiple bounce collapse can be excluded. Note that some models cross the nuclear matter density threshold at several distinct times $t_{\rho_{\mathrm{c}}=\rho_{\mathrm{nuc}}}$. Such models usually exhibit a type I/II transition behavior. After the first bounce their core oscillates coherently with large amplitude, however without the large time intervals between subsequent bounces which are characteristic for a type II multiple bounce collapse. For genuine multiple bounce models the final central density $\rho_{\mathrm{c\,f}}$ is not specified as their inner core does not reach a new stable equilibrium configuration during the simulated evolution time.

From the information contained in Tables 7.1–7.3, two important conclusions can be derived: With the exception of run A4B4G4[f], the maximum central densities reached during the main bounce are on average significantly higher in the relativistic simulations than in simulations with a Newtonian gravitational potential. In some cases, which all show a type II multiple bounce collapse, $\rho_{\mathrm{c\,b}}$ increases by more than a factor of 2 due to relativistic effects; in model A3B3G1 the maximum central density increases by almost a factor 5. This behavior is a direct consequence of the deeper potential in relativistic gravity, which leads to higher infall velocities and denser and more compact inner cores. Note that the density listed for the relativistic simulations in Tables 7.1–7.3 is the primitive quantity ρ, i.e. the rest mass. Both the corresponding generalized relativistic conserved density $D = \rho W$ in the state vector (2.26) and the effective density $\rho(1+\epsilon)$ used in the integral of the gravitational mass in Equation (6.10) are even larger than ρ. The influence of relativistic effects on $\rho_{\mathrm{c\,b}}$ becomes particularly evident in the regular collapse model A3B2G4, which we have evolved with a soft supranuclear EoS ($\gamma_2 = 2.0$, model A3B2G4$_{\mathrm{soft}}$) and the regular EoS ($\gamma_2 = 2.5$; model A3B2G4). Until nuclear matter density is reached at $t_{\rho_{\mathrm{c}}=\rho_{\mathrm{nuc}}} = 38.83$ ms, the evolution of the collapse proceeds identically in both models. At this point the cores in both models have the same linear momentum S_1 corresponding to the radial infall of the mass shells. However, in the subsequent bounce, where the increasing pressure forces due to the jump in the adiabatic index γ act against the momentum of the contracting core and lead to a reversal of the velocity, a softer EoS results in higher average densities in the central regions and thus an ever deeper relativistic gravitational potential well. This is

---

[f] In the rapidly and highly differential models A4B4 and A4B5 which develop toroidal density structures (see Section 7.7), the central density is of less importance as it is not identical to the maximum density in the core.

reflected by a more than proportional relativistic density increase $\rho^{\mathrm{R}}_{\mathrm{c\,b}}/\rho^{\mathrm{N}}_{\mathrm{c\,b}} - 1 = 27\%$ in model A3B2G4$_{\mathrm{soft}}$ compared to $\rho^{\mathrm{R}}_{\mathrm{c\,b}}/\rho^{\mathrm{N}}_{\mathrm{c\,b}} - 1 = 14\%$ in model A3B2G4.

The shorter infall times and the resulting higher average radial infall velocities in the relativistic simulations of most models can also be attributed to the deeper gravitational potential. In relativistic gravity, the core of model A3B2G1 collapses through to very high supranuclear central densities and bounces at $t_{\mathrm{b}} = 92.42$ ms, whereas in the Newtonian run the core is stopped by centrifugal forces at around nuclear matter density at $t_{\mathrm{b}} = 94.32$ ms, leading to a significant difference in the times of bounce $\Delta t_{\mathrm{b}} \equiv t^{\mathrm{R}}_{\mathrm{b}} - t^{\mathrm{N}}_{\mathrm{b}} = 1.9$ ms. On the other hand, some relativistic models seem to collapse slower than their Newtonian counterparts, particularly models with high rotation rate and very differential rotation profile. However, as already mentioned, the inner cores of these models develop a torus-like structure and thus the central density is no good criterion for indicating the time of bounce anymore. Furthermore, in such rapidly rotating cores the bounce occurs at subnuclear densities due to centrifugal forces. A detailed discussion of this scenario, where the relativistic effects are hard to disentangle and interpret, follows in Section 7.7.

Model	$\rho_{\mathrm{c\,b}}$ $[10^{14}\ \mathrm{g\ cm^{-3}}]$	t_{b} [ms]	$\rho_{\mathrm{c\,f}}$ $[10^{14}\ \mathrm{g\ cm^{-3}}]$	$t_{\rho_{\mathrm{c}}=\rho_{\mathrm{nuc}}}$ [ms]	$\Delta t_{\rho_{\mathrm{c}}>\rho_{\mathrm{nuc}}}$ [ms]	$\rho^{\mathrm{R}}_{\mathrm{c\,b}}/\rho^{\mathrm{N}}_{\mathrm{c\,b}} - 1$ [%]
A1B1G1$^{\mathrm{R}}$	4.57	90.87	3.3	90.48	17.71+	+42
A1B1G1$^{\mathrm{N}}$	3.22	92.23	2.4	91.76	1.31	
				95.05	13.64+	
A1B2G1$^{\mathrm{R}}$	4.17	91.56	3.1	91.17	22.27+	+45
A1B2G1$^{\mathrm{N}}$	2.89	93.10	—	92.61	1.22	
				101.30	1.69	
				108.64	1.81	
A1B3G1$^{\mathrm{R}}$	3.63	92.85	2.8	92.43	41.53+	+67
A1B3G1$^{\mathrm{N}}$	2.17	94.70	—	94.58	0.51	
A1B3G2$^{\mathrm{R}}$	3.86	69.10	2.9	68.74	45.78+	+37
A1B3G2$^{\mathrm{N}}$	2.83	69.87	—	69.47	1.24	
				76.39	1.42	
				83.16	1.11	
A1B3G3$^{\mathrm{R}}$	4.09	48.45	3.1	48.10	21.00+	+21
A1B3G3$^{\mathrm{N}}$	3.38	48.57	2.5	48.22	21.17+	
A1B3G5$^{\mathrm{R}}$	4.49	30.10	3.5	29.84	29.29+	+6
A1B3G5$^{\mathrm{N}}$	4.26	29.98	3.0	29.70	28.99+	
A2B4G1$^{\mathrm{R}}$	0.42	99.09	—			+268
A2B4G1$^{\mathrm{N}}$	0.11	99.71	—			

Table 7.1: *Summary of the bounce density for relativistic (R) and Newtonian (N)* A1 *and* A2 *models:* $\rho_{\mathrm{c\,b}}$ *is the central density at bounce,* t_{b} *is the time of bounce,* $\rho_{\mathrm{c\,f}}$ *is the central density at the time when the simulation was stopped,* $t_{\rho>\rho_{\mathrm{nuc}}}$ *is the time when the density rises above nuclear matter density,* $\Delta t_{\rho>\rho_{\mathrm{nuc}}}$ *is the time interval during which the central density exceeds nuclear matter density, and* $\rho^{\mathrm{R}}_{\mathrm{c\,b}}/\rho^{\mathrm{N}}_{\mathrm{c\,b}} - 1$ *is the relative increase (+) or decrease (−) of* $\rho^{\mathrm{R}}_{\mathrm{c\,b}}$ *compared to* $\rho^{\mathrm{N}}_{\mathrm{c\,b}}$*. A + sign behind the value for* $\Delta t_{\rho>\rho_{\mathrm{nuc}}}$ *indicates that the central density was still higher than nuclear matter density when the simulation was stopped at* t_{f}*.* $\rho_{\mathrm{c\,f}}$ *is not given for multiple bounce models; a + sign behind its value means that* ρ_{c} *is still rising at* t_{f}*, as the neutron star is accreting mass.*

Model	$\rho_{\mathrm{c\,b}}$ $[10^{14}\ \mathrm{g\ cm}^{-3}]$	t_{b} [ms]	$\rho_{\mathrm{c\,f}}$ $[10^{14}\ \mathrm{g\ cm}^{-3}]$	$t_{\rho_{\mathrm{c}}=\rho_{\mathrm{nuc}}}$ [ms]	$\Delta t_{\rho_{\mathrm{c}}>\rho_{\mathrm{nuc}}}$ [ms]	$\rho^{\mathrm{R}}_{\mathrm{c\,b}}/\rho^{\mathrm{N}}_{\mathrm{c\,b}} - 1$ [%]
A3B1G1$^{\mathrm{R}}$	4.15	91.27	3.1	90.91	22.74+	+38
A3B1G1$^{\mathrm{N}}$	3.00	92.72	—	92.26	1.29	
				92.32	1.05	
				100.25	1.40	
				106.60	1.64	
				112.67	1.48+	
A3B2G1$^{\mathrm{R}}$	3.45	92.42	2.6	92.05	40.64+	+52
A3B2G1$^{\mathrm{N}}$	2.28	94.32	—	93.88	0.86	
A3B2G2$^{\mathrm{R}}$	3.58	69.15	2.7	68.81	28.88+	+34
A3B2G2$^{\mathrm{N}}$	2.68	69.98	—	69.56	1.11	
				77.79	1.20	
				86.45	0.35	
A3B2G4$^{\mathrm{R}}_{\mathrm{soft}}$	5.64	39.18	3.4	38.83	18.57+	+27
A3B2G4$^{\mathrm{N}}_{\mathrm{soft}}$	4.45	39.14	2.7	38.78	20.85+	
A3B2G4$^{\mathrm{R}}$	3.90	39.14	2.9	38.83	19.09+	+14
A3B2G4$^{\mathrm{N}}$	3.41	39.07	2.5	38.78	20.90+	
A3B3G1$^{\mathrm{R}}$	2.36	95.26	—	94.84	0.97	+400
A3B3G1$^{\mathrm{N}}$	0.47	96.57	—			
A3B3G2$^{\mathrm{R}}$	2.56	70.96	—	70.37	1.33	+133
				78.19	1.13	
				85.95	0.38	
A3B3G2$^{\mathrm{N}}$	1.10	71.77	—			
A3B3G3$^{\mathrm{R}}$	2.91	49.42	—	49.12	1.60	+23
				52.01	27.32+	
A3B3G3$^{\mathrm{N}}$	2.36	49.64	—	49.30	1.08	
A3B3G5$^{\mathrm{R}}$	3.64	30.53	2.8	30.26	26.42+	+6
A3B3G5$^{\mathrm{N}}$	3.44	30.36	2.3	30.11	26.96+	
A3B4G2$^{\mathrm{R}}$	0.38	74.51	—			+145
A3B4G2$^{\mathrm{N}}$	0.16	73.99	—			
A3B5G4$^{\mathrm{R}}$	0.18	44.31	—			+17
A3B5G4$^{\mathrm{N}}$	0.15	44.31	—			

Table 7.2: *Summary of the bounce density for relativistic (R) and Newtonian (N)* A3 *models: Quantities like in Table 7.1.*

Model	$\rho_{\mathrm{c\,b}}$ [10^{14} g cm^{-3}]	t_{b} [ms]	$\rho_{\mathrm{c\,f}}$ [10^{14} g cm^{-3}]	$t_{\rho_{\mathrm{c}}=\rho_{\mathrm{nuc}}}$ [ms]	$\Delta t_{\rho_{\mathrm{c}}>\rho_{\mathrm{nuc}}}$ [ms]	$\rho^{\mathrm{R}}_{\mathrm{c\,b}}/\rho^{\mathrm{N}}_{\mathrm{c\,b}} - 1$ [%]
A4B1G1$^{\mathrm{R}}$	3.71	90.45	2.4+	90.19	28.85+	+50
A4B1G1$^{\mathrm{N}}$	2.47	91.77	—	91.53	0.56	
				101.89	0.58	
				110.33	0.53	
				118.09	0.32	
A4B1G2$^{\mathrm{R}}$	3.59	68.07	2.4+	67.85	22.14+	+42
A4B1G2$^{\mathrm{N}}$	2.53	68.69	—	68.47	0.50	
				73.59	0.65	
				78.12	0.50	
A4B2G2$^{\mathrm{R}}$	2.68	68.34	1.6	68.18	0.32	
				70.90	0.27	+25
A4B2G2$^{\mathrm{N}}$	2.14	69.02	—	69.00	0.08	
A4B2G3$^{\mathrm{R}}$	2.42	48.69	—	48.53	0.29	+12
A4B2G3$^{\mathrm{N}}$	2.15	48.74	—	48.74	0.16	
A4B4G4$^{\mathrm{R}}$	0.25	39.85	—			+2
A4B4G4$^{\mathrm{N}}$	0.25	39.66	—			
A4B4G5$^{\mathrm{R}}$	0.17	32.24	—			−60
A4B4G5$^{\mathrm{N}}$	0.42	31.91	—			
A4B5G4$^{\mathrm{R}}$	0.05	37.58	—			+0
A4B5G4$^{\mathrm{N}}$	0.05	37.29	—			
A4B5G5$^{\mathrm{R}}$	0.09	30.68	—			+20
A4B5G5$^{\mathrm{N}}$	0.07	30.82	—			

Table 7.3: *Summary of the bounce density for relativistic (R) and Newtonian (N)* A4 *models: Quantities like in Table 7.1.*

7.4 Gravitational Wave Amplitudes

It can be expected that the differences in maximum central density between a relativistic and a Newtonian simulation of a particular model, listed and discussed in Section 7.3, are also reflected in the gravitational wave signal. Before elaborating on the qualitative changes in the collapse type and thus the signal form due to relativistic effects in Sections 7.5 and 7.6, we want to summarize for all models some essential quantities derived from the gravitational wave signal. The obvious quantities to investigate are the maximum positive signal amplitude $A^{\rm E2}_{20+\,\rm max}$, the maximum negative signal amplitude $A^{\rm E2}_{20-\,\rm max}$, the maximum absolute signal amplitude $|A^{\rm E2}_{20}|_{\rm max}$, and the time of the maximum absolute signal amplitude $t_{\rm gw}$, which are defined as follows:

$$\begin{aligned} A^{\rm E2}_{20+\,\rm max} &= \max\,(A^{\rm E2}_{20}), && (7.3)\\ A^{\rm E2}_{20-\,\rm max} &= -\max\,(-A^{\rm E2}_{20}), && (7.4)\\ |A^{\rm E2}_{20}|_{\rm max} &= \max\,(|A^{\rm E2}_{20}|), && (7.5)\\ t_{\rm gw} &= t(A^{\rm E2}_{20} = |A^{\rm E2}_{20}|_{\rm max}). && (7.6) \end{aligned}$$

The values of these quantities and some other quantities derived from them are listed in Tables 7.4–7.6 for all 26 models in both relativistic and Newtonian gravity. As in the Newtonian simulations of Zwerger [146], the time of maximum signal amplitude is always later than the time of maximum central density, $t_{\rm gw} > t_{\rm b}$, except in the rapidly collapsing models A1B3G5 and A3B3G5. However, these are the only models where the maximum signal amplitude is positive. Still maximum negative signal amplitude is reached after bounce also in these models: $t(A^{\rm E2}_{20-\,\rm max}) > t_{\rm b}$. Therefore, it is obviously a common feature of core collapse in both relativistic and Newtonian gravity, that the time of bounce falls into the declining slope of the first negative signal peak. This observation has been discussed in detail by Zwerger.

On average, the relativistic models also share with their Newtonian counterparts the wide spread in the range of observed maximum signal amplitudes: In our sample of 26 models, the Newtonian maximum signal amplitudes range from about 100 cm to over 5000 cm. The relativistic simulations exhibit the same lower limit, whereas the highest maximum signal amplitude reaches only about 3000 cm. The maximum signal amplitudes of core collapse models with moderate rotation strength and differentiality of the rotation law, and with an adiabatic index in the middle of the parameter interval, lie usually between 500 cm and 1000 cm. Both kinds of simulations also show the same tendency in the dependence of $|A^{\rm E2}_{20}|_{\rm max}$ on the collapse parameters: Iron cores which initially rotate almost uniformly and thus slowly, and which collapse slowly due to a high γ_1, collapse to high supranuclear densities and are decelerated strongly in the deep gravitational potential. However, due to the rapid infall, the mass of the inner core in such a collapse model is comparatively small (see Section 7.2), and most of the matter is concentrated at small radii during bounce time. The resulting small quadrupole moment leads to a very small gravitational wave signal. If such initial models collapse more slowly, they can bounce at densities below or around nuclear matter density, which yields a large gravitational wave signal due to coherent deceleration of large parts of a more extended core. If the initial rotation rate is higher, and the rotation profile more differential, the signal strength is also enhanced on average. However, for extremely rapidly and differentially rotating models, a lower γ_1 and thus a faster contraction leads to a larger signal, as otherwise centrifugal forces decelerate the collapse already at lower densities.

On the other hand, the relative deviations of the maximum signal amplitud between the relativistic and the Newtonian simulation of the same model prove that relativistic corrections do indeed play an important role in the collapse dynamics. The gravitational wave amplitude A_{20}^{E2} is a very appropriate tool to measure global changes in the collapse dynamics, as it is determined by the bulk motion of the matter rather than by just local effects. The fact that $|A_{20}^{\mathrm{E2}}|_{\mathrm{max}}$ can increase or decrease for a collapse model by up to 70% as a result of relativistic effects demonstrates that the dynamics of large regions in the core are considerably altered by relativistic corrections during rotational core collapse. In many models the global change of collapse dynamics is also reflected by a change of the collapse type according to the definitions in Section 7.1. Whether the maximum signal amplitude increases or decreases in relativistic gravity is closely linked to whether the collapse type changes between a Newtonian and a relativistic simulation of a particular model. This issue will be addressed in the following sections.

Model	$A_{20\,+\,\mathrm{max}}^{\mathrm{E2}}$ [cm]	$A_{20\,-\,\mathrm{max}}^{\mathrm{E2}}$ [cm]	$\lvert A_{20}^{\mathrm{E2}}\rvert_{\mathrm{max}}$ [cm]	t_{gw} [ms]	$A_{20\,+\,\mathrm{max}}^{\mathrm{E2}} - A_{20\,-\,\mathrm{max}}^{\mathrm{E2}}$ [cm]	Type	$\frac{\lvert A_{20}^{\mathrm{E2}}\rvert_{\mathrm{max}}^{\mathrm{R}}}{\lvert A_{20}^{\mathrm{E2}}\rvert_{\mathrm{max}}^{\mathrm{N}}} - 1$ [%]
A1B1G1$^{\mathrm{R}}$	295.7	-548.8	548.8	90.91	844.2	I	-68
A1B1G1$^{\mathrm{N}}$	651.8	-1698.3	1698.4	92.76	2350.8	I/II	
A1B2G1$^{\mathrm{R}}$	560.2	-1278.3	1278.3	91.97	1838.3	I	-46
A1B2G1$^{\mathrm{N}}$	978.7	-2354.6	2354.6	93.52	3333.9	II	
A1B3G1$^{\mathrm{R}}$	533.4	-2484.7	2484.7	93.18	3018.2	I	$+70$
A1B3G1$^{\mathrm{N}}$	190.8	-1463.4	1463.4	94.99	1654.6	II	
A1B3G2$^{\mathrm{R}}$	536.6	-1445.3	1445.3	69.47	1981.1	I	-31
A1B3G2$^{\mathrm{N}}$	755.1	-2084.4	2084.4	70.29	2839.5	II	
A1B3G3$^{\mathrm{R}}$	327.9	-483.9	483.9	48.88	811.2	I	-50
A1B3G3$^{\mathrm{N}}$	576.5	-975.9	975.9	49.00	1553.0	I	
A1B3G5$^{\mathrm{R}}$	106.2	-36.5	106.2	29.91	142.8	III	-19
A1B3G5$^{\mathrm{N}}$	130.5	-38.0	130.5	29.78	168.6	III	
A2B4G1$^{\mathrm{R}}$	183.1	-744.6	744.6	98.38	927.8	II	$+14$
A2B4G1$^{\mathrm{N}}$	166.9	-651.7	651.7	100.21	818.6	II	

Table 7.4: *Summary of the gravitational wave signal amplitude for relativistic (R) and Newtonian (N)* A1 *and* A2 *models:* $A_{20\,+/-\,\mathrm{max}}^{\mathrm{E2}}$ *is the maximum positive/negative signal amplitude,* $|A_{20}^{\mathrm{E2}}|_{\mathrm{max}}$ *is the maximum absolute signal amplitude,* t_{gw} *is the time of maximum absolute signal amplitude,* $A_{20\,+\,\mathrm{max}}^{\mathrm{E2}} - A_{20\,-\,\mathrm{max}}^{\mathrm{E2}}$ *is the difference between maximum positive and negative signal amplitude,* Type *is the signal and collapse type as described in Sections 7.1.1–7.1.3, and* $|A_{20}^{\mathrm{E2}}|_{\mathrm{max}}^{\mathrm{R}}/|A_{20}^{\mathrm{E2}}|_{\mathrm{max}}^{\mathrm{N}} - 1$ *is the relative increase (+) or decrease (−) of* $|A_{20}^{\mathrm{E2}}|_{\mathrm{max}}^{\mathrm{R}}$ *compared to* $|A_{20}^{\mathrm{E2}}|_{\mathrm{max}}^{\mathrm{N}}$.

Model	$A^{\mathrm{E2}}_{20+\max}$ [cm]	$A^{\mathrm{E2}}_{20-\max}$ [cm]	$\lvert A^{\mathrm{E2}}_{20}\rvert_{\max}$ [cm]	t_{gw} [ms]	$A^{\mathrm{E2}}_{20\,\max} - A^{\mathrm{E2}}_{20\,\min}$ [cm]	Type	$\frac{\lvert A^{\mathrm{E2}}_{20}\rvert^{\mathrm{R}}_{\max}}{\lvert A^{\mathrm{E2}}_{20}\rvert^{\mathrm{N}}_{\max}} - 1$ [%]
A3B1G1$^{\mathrm{R}}$	689.7	-1325.2	1325.2	91.57	2014.6	I	-47
A3B1G1$^{\mathrm{N}}$	863.4	-2509.9	2509.9	93.04	3373.0	II	
A3B2G1$^{\mathrm{R}}$	648.0	-2709.5	2709.5	92.67	3357.8	I	$+58$
A3B2G1$^{\mathrm{N}}$	174.9	-1711.0	1711.0	94.36	1885.7	II	
A3B2G2$^{\mathrm{R}}$	647.6	-1972.6	1972.6	69.43	2620.1	I	-18
A3B2G2$^{\mathrm{N}}$	639.2	-2407.0	2407.0	70.24	3046.6	II	
A3B2G4$^{\mathrm{R}}_{\mathrm{soft}}$	280.9	-527.9	527.9	39.44	808.8	I	-32
A3B2G4$^{\mathrm{N}}_{\mathrm{soft}}$	422.2	-781.1	781.1	39.43	1203.3	I	
A3B2G4$^{\mathrm{R}}$	246.6	-426.3	426.3	39.49	673.0	I	-39
A3B2G4$^{\mathrm{N}}$	386.3	-703.2	703.2	39.45	1089.4	I	
A3B3G1$^{\mathrm{R}}$	238.2	-1713.4	1713.4	95.20	1951.2	II	$+58$
A3B3G1$^{\mathrm{N}}$	153.3	-1087.3	1087.3	96.63	1240.0	II	
A3B3G2$^{\mathrm{R}}$	319.8	-1953.6	1953.6	70.93	2273.3	I/II	$+38$
A3B3G2$^{\mathrm{N}}$	233.0	-1419.5	1419.5	71.65	1652.2	II	
A3B3G3$^{\mathrm{R}}$	309.6	-1542.7	1542.7	49.65	1852.5	I/II	$+4$
A3B3G3$^{\mathrm{N}}$	327.4	-1480.1	1480.1	49.83	1807.9	I/II	
A3B3G5$^{\mathrm{R}}$	239.9	-96.9	239.9	30.32	336.8	III	-9
A3B3G5$^{\mathrm{N}}$	263.4	-163.7	263.4	30.16	427.2	III	
A3B4G2$^{\mathrm{R}}$	291.8	-862.4	862.4	73.61	1154.8	II	-4
A3B4G2$^{\mathrm{N}}$	244.6	-893.9	893.9	74.53	1138.9	II	
A3B5G4$^{\mathrm{R}}$	481.0	-421.5	481.0	38.97	902.0	III	-9
A3B5G4$^{\mathrm{N}}$	527.9	-466.6	527.9	38.84	994.2	III	

Table 7.5: *Summary of the gravitational wave signal amplitude for relativistic (R) and Newtonian (N)* A3 *models: Quantities like in Table 7.4.*

Model	$A^{\mathrm{E2}}_{20\,+\,\max}$ [cm]	$A^{\mathrm{E2}}_{20\,-\,\max}$ [cm]	$\lvert A^{\mathrm{E2}}_{20}\rvert_{\max}$ [cm]	t_{gw} [ms]	$A^{\mathrm{E2}}_{20\,+\,\max} - A^{\mathrm{E2}}_{20\,-\,\max}$ [cm]	Type	$\frac{\lvert A^{\mathrm{E2}}_{20}\rvert^{\mathrm{R}}_{\max}}{\lvert A^{\mathrm{E2}}_{20}\rvert^{\mathrm{N}}_{\max}} - 1$ [%]
A4B1G1$^{\mathrm{R}}$	1121.5	-1766.0	1766.0	90.53	2887.6	I	-11
A4B1G1$^{\mathrm{N}}$	304.1	-1991.5	1991.5	91.95	2295.9	II	
A4B1G2$^{\mathrm{R}}$	867.9	-1713.0	1713.0	68.18	2580.2	I	-16
A4B1G2$^{\mathrm{N}}$	399.0	-2033.8	2033.8	68.88	2432.8	II	
A4B2G2$^{\mathrm{R}}$	1041.9	-2287.6	2287.6	68.37	3329.7	I/II	$+7$
A4B2G2$^{\mathrm{N}}$	380.2	-2131.5	2131.5	69.13	2511.5	II	
A4B2G3$^{\mathrm{R}}$	734.6	-1900.0	1900.0	48.75	2634.7	I/II	-14
A4B2G3$^{\mathrm{N}}$	635.2	-2217.4	2217.4	48.89	2852.9	I/II	
A4B4G4$^{\mathrm{R}}$	868.0	-1346.6	1346.6	39.78	2214.4	–	-23
A4B4G4$^{\mathrm{N}}$	738.8	-1748.3	1748.3	39.74	2487.4	–	
A4B4G5$^{\mathrm{R}}$	625.7	-1566.9	1566.9	31.83	2192.5	–	-27
A4B4G5$^{\mathrm{N}}$	879.6	-2149.1	2149.1	31.76	3028.6	–	
A4B5G4$^{\mathrm{R}}$	974.7	-2342.9	2342.9	37.19	3317.6	–	-21
A4B5G4$^{\mathrm{N}}$	1143.3	-2965.2	2965.2	37.27	4108.2	–	
A4B5G5$^{\mathrm{R}}$	1190.6	-3143.5	3143.5	30.43	4334.7	–	-42
A4B5G5$^{\mathrm{N}}$	3114.9	-5443.9	5443.9	30.97	8558.4	–	

Table 7.6: *Summary of the gravitational wave signal amplitude for relativistic (R) and Newtonian (N)* A4 *models: Quantities like in Table 7.4. The extremely rapidly and strongly differentially rotating models* A4B4, A4B5, A5B4, *and* A5B5 *develop a toroidal density structure; thus, we do not assign a specific collapse type to them.*

7.5 Multiple Bounces

In the parameter study of Newtonian rotational core collapse simulations undertaken by Zwerger [146], models with multiple bounces were observed quite often. Relativistic effects should have a noticeable impact on these collapse models, particularly if the average central density of such a model is high. If the density increase is sufficiently large due to relativistic corrections, nuclear matter density can be exceeded in parts of the core, i.e. the EoS changes qualitatively, and a collapse which leads to a multiple bounce in a Newtonian simulation might become a regular, single bounce.

Before investigating the change of the collapse type, we first want to quantify the effects of relativity on collapse models exhibiting multiple bounce behavior also in GR. Only three of the models we have simulated (models A2B4G1, A3B3G1, and A3B4G2) maintain an unambiguous multiple bounce collapse in a relativistic run. Another one, model A3B3G2, is a transition type model which has both features of a regular and a multiple bounce model. The evolution of the central density of the models A2B4G1, A3B3G1, and A3B3G2 is plotted in Figure 7.7. In model A2B4G1 (upper panel), the central density in both the relativistic and the Newtonian run stays well below nuclear matter density at all evolution times. On the other hand, in the relativistic simulation of model A3B3G1 (middle panel), nuclear matter density is exceeded in the central regions of the core during the first bounce, whereas in the Newtonian simulation the density stays significantly below nuclear matter density in all parts of the core. The case of model A3B3G2 (lower panel) deserves special attention: While the evolution of the central density in the Newtonian run is according to a normal multiple bounce, the model almost behaves like a transition between a multiple bounce collapse and a regular collapse in the relativistic simulation: There are still pronounced and distinct separate peaks of the central density; nevertheless, the values of the local minima of the central density rise noticeable with time and tend towards nuclear matter density. Nevertheless, we add this ambiguous case to the class of multiple bounce collapse models also in relativistic gravity.

There are some features shared by all three models which can be attributed to the influence of relativistic gravity: As summarized in Table 7.7, the peak central densities associated with the individual bounces in the relativistic runs are much higher (by up to an order of magnitude) compared to the ones in the Newtonian runs. As a consequence of the higher central and average densities in the relativistic models, the period of time between subsequent bounces is decreased by a factor of up to 2. This reflects the simple fact that a denser configuration oscillates faster.

The peak densities and thus the influence of relativistic effects on the collapse dynamics increase from model A2B4G1 via model A3B3G1 to model A3B3G2. The sequence of plots in Figure 7.7 clearly shows how relativistic corrections can alter the collapse dynamics for multiple collapse models with a peak density close to or above nuclear matter density. With increasing central densities, the influence of relativity can actually affect the dynamics so much that the collapse type for a particular model becomes different from that of the Newtonian simulation. The models for which this happens, and the respective collapse types in relativistic and Newtonian simulations are listed in Table 7.8. One important observation is that only changes from type II (multiple bounce collapse) in Newtonian gravity to type I (regular collapse)

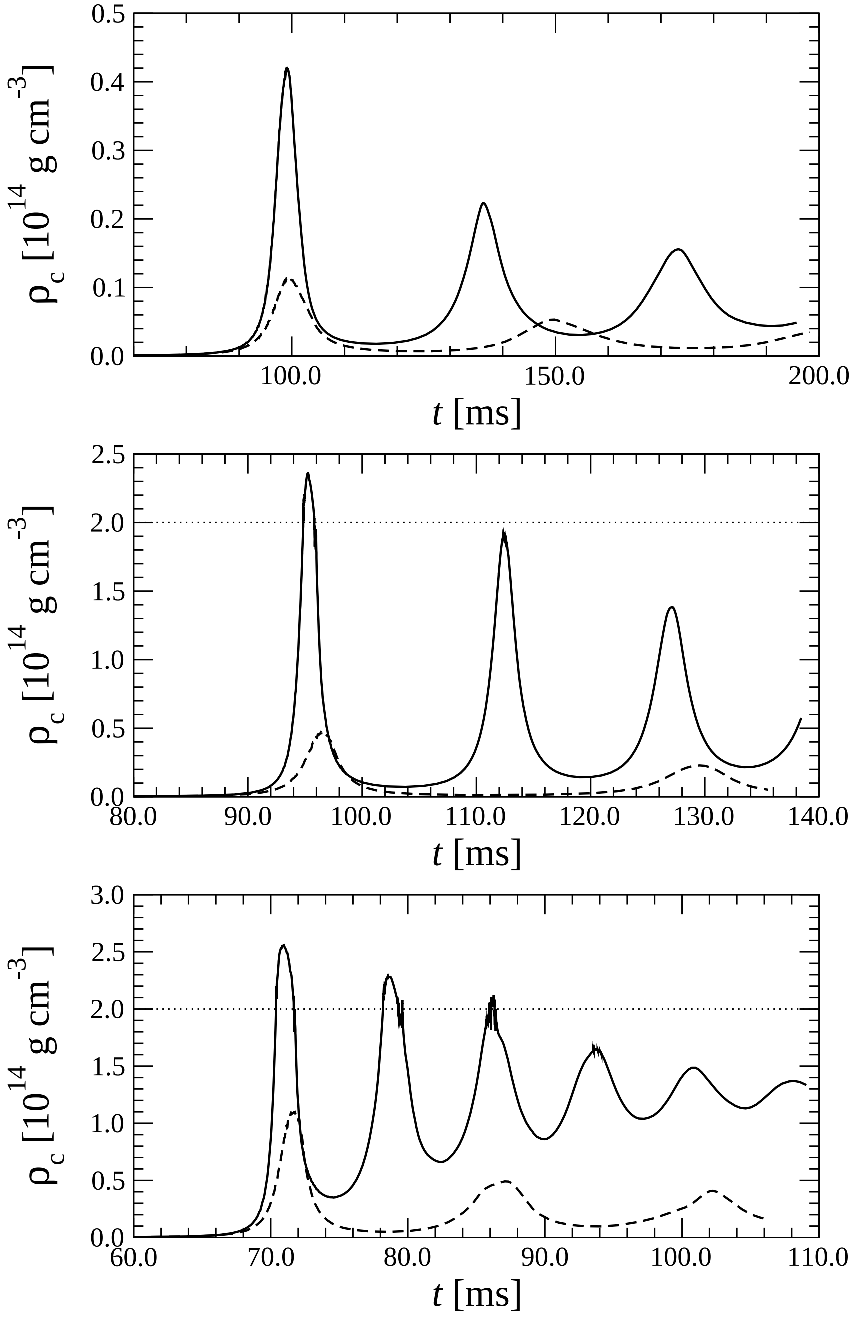

Figure 7.7: *Evolution of the central density in the relativistic (solid lines) and Newtonian (dashed lines) simulation of the multiple bounce collapse models* A2B4G1 *(upper panel),* A3B3G1 *(middle panel), and* A3B3G2 *(lower panel): With increasing peak density and thus large relativistic corrections, the qualitative differences between the evolutions of the central density in the relativistic and the Newtonian configurations become more pronounced. Note the significantly shorter oscillation periods in the relativistic simulations. The relativistic model* A3B3G2 *no longer exhibit unambiguous multiple bounce behavior, but rather tends towards a transition type to a regular bounce. The horizontal dotted lines mark nuclear matter density. If the central density only slightly exceeds nuclear matter density during a bounce, the sudden stiffening of the EoS causes the oscillatory behavior of the density as seen in the relativistic run in the lower panel.*

Model	$\rho_{\mathrm{c\,b_1}}$ $[10^{14}$ g cm$^{-3}]$	$\rho_{\mathrm{c\,b_1}}$	$t_{\mathrm{b_1}}$ [ms]	$t_{\mathrm{b_2}}$ [ms]	Δt_{b} [ms]	$\dfrac{\rho^{\mathrm{R}}_{\mathrm{c\,b_1}}}{\rho^{\mathrm{N}}_{\mathrm{c\,b_1}}} - 1$ [%]	$\dfrac{\rho^{\mathrm{R}}_{\mathrm{c\,b_2}}}{\rho^{\mathrm{N}}_{\mathrm{c\,b_2}}} - 1$ [%]	$\dfrac{\Delta t^{\mathrm{R}}_{\mathrm{b}}}{\Delta t^{\mathrm{N}}_{\mathrm{b}}} - 1$ [%]
A2B4G1$^{\mathrm{R}}$	0.42	0.22	99.09	136.33	37.24	+268	+319	−25
A2B4G1$^{\mathrm{N}}$	0.11	0.05	99.71	149.58	49.87			
A3B3G1$^{\mathrm{R}}$	2.36	1.91	95.26	112.42	17.16	+400	+699	−48
A3B3G1$^{\mathrm{N}}$	0.47	0.24	96.57	129.43	32.86			
A3B3G2$^{\mathrm{R}}$	2.56	2.29	70.96	78.57	7.61	+133	+364	−50
A3B3G2$^{\mathrm{N}}$	1.10	0.49	71.77	87.10	15.33			
A3B4G2$^{\mathrm{R}}$	0.38	0.19	74.51	95.96	21.45	+144	+204	−16
A3B4G2$^{\mathrm{N}}$	0.16	0.06	73.99	99.51	25.52			

Table 7.7: *Summary of the parameters of the first two bounces in the relativistic (R) and Newtonian (N) multiple bounce models* A2B4G1, A3B3G1, A3B3G2, *and* A3B4G2*:* $\rho_{\mathrm{c\,b_{1/2}}}$ *are the peak central densities of the first/second bounce,* $t_{\mathrm{b_{1/2}}}$ *are the times of the first/second bounce,* $\Delta t_{\mathrm{b}} = t_{\mathrm{b_2}} - t_{\mathrm{b_1}}$ *is the period of time between the first and second bounce,* $\rho^{\mathrm{R}}_{\mathrm{c\,b_{1/2}}}/\rho^{\mathrm{N}}_{\mathrm{c\,b_{1/2}}} - 1$ *is the relative increase of* $\rho^{\mathrm{R}}_{\mathrm{c\,b_{1/2}}}$ *compared to* $\rho^{\mathrm{N}}_{\mathrm{c\,b_{1/2}}}$*, and* $\Delta t^{\mathrm{R}}_{\mathrm{b}}/\Delta t^{\mathrm{N}}_{\mathrm{b}} - 1$ *is the relative decrease of* $\Delta t^{\mathrm{R}}_{\mathrm{b}}$ *compared to* $\Delta t^{\mathrm{N}}_{\mathrm{b}}$*.*

Model	Type	$\rho_{\mathrm{c\,b}}$ $[10^{14}$ g cm$^{-3}]$	Model	Type	$\rho_{\mathrm{c\,b}}$ $[10^{14}$ g cm$^{-3}]$
A1B1G1$^{\mathrm{R}}$	I	4.57	A3B2G2$^{\mathrm{R}}$	I	3.58
A1B1G1$^{\mathrm{N}}$	I/II	3.22	A3B2G2$^{\mathrm{N}}$	II	2.68
A1B2G1$^{\mathrm{R}}$	I	4.17	A3B3G3$^{\mathrm{R}}$	I	2.91
A1B2G1$^{\mathrm{N}}$	II	2.89	A3B3G3$^{\mathrm{N}}$	I/II	2.36
A1B3G1$^{\mathrm{R}}$	I	3.63	A4B1G1$^{\mathrm{R}}$	I	3.71
A1B3G1$^{\mathrm{N}}$	II	2.17	A4B1G1$^{\mathrm{N}}$	II	2.47
A1B3G2$^{\mathrm{R}}$	I	3.86	A4B1G2$^{\mathrm{R}}$	I	3.59
A1B3G2$^{\mathrm{N}}$	I/II	2.83	A4B1G2$^{\mathrm{N}}$	II	2.53
A3B1G1$^{\mathrm{R}}$	I	4.15	A4B2G2$^{\mathrm{R}}$	I/II	2.68
A3B1G1$^{\mathrm{N}}$	II	3.00	A4B2G2$^{\mathrm{N}}$	II	2.14
A3B2G1$^{\mathrm{R}}$	I	3.45			
A3B2G1$^{\mathrm{N}}$	II	2.28			

Table 7.8: *Suppression of multiple bounces in relativistic simulations (R) compared to Newtonian simulations (N):* Type *is the collapse type (type I: regular collapse; type II: multiple bounce collapse; type I/II: transition type between regular and multiple bounce collapse) as described in Sections 7.1.1–7.1.3, and* $\rho_{\mathrm{c\,b}}$ *is the central density at the time of bounce. For all models listed here, the collapse proceeds qualitatively different for relativistic gravity, and thus the signal type changes.*

or to the transition type I/II in relativistic gravity seem possible.

According to Table 7.8, the change of type occurring most frequently is from type II in Newtonian gravity to type I in relativistic gravity. For three of these models we plot the evolution of the central density in Figure 7.8, and the gravitational wave signal in Figure 7.9. The reason for the change from a multiple bounce to a regular bounce due to relativistic corrections in the gravitational potential is obvious: Most of the multiple bounce runs in Zwerger's simulations [146] are stopped due to centrifugal forces at densities below ρ_{nuc}. Only a few multiple bounce models collapse through to nuclear matter density, with the maximum central density being $\rho_{\mathrm{c\,b\,max}} = 3.0 \times 10^{14}$ g cm^{-3} in model A3B1G1. Models which reach higher central densities during the bounce are all of regular collapse type. If we apply the following criterion for a multiple bounce collapse,

$$\rho_{\mathrm{c\,b}} \leq \rho_{\mathrm{c\,b\,max}} = 3.0 \times 10^{14} \text{ g cm}^{-3}, \tag{7.7}$$

to our models with relativistic gravity, we find that this criterion is also fulfilled for all the models exhibiting multiple bounces listed in Table 7.7. On the other hand, the collapse models from Table 7.8, which change type from multiple bounce collapse to regular collapse, all have maximum central densities $\rho_{\mathrm{c\,b}} > \rho_{\mathrm{c\,b\,max}}$. The effectively deeper relativistic gravitational potential drives the cores to higher supranuclear densities, and thus the density criterion for a multiple bounce collapse is violated, resulting in a regular collapse where the inner core assumes an equilibrium configuration almost immediately.

The evolution of the central density (plotted in Figure 7.8) clearly shows the influence of relativity on models, which suffer multiple bounces in Newtonian gravity: In model A4B2G2 (lower panel), relativistic effects are not strong enough to drive the core to sufficiently large densities to show a regular bounce behavior. Nevertheless, the inner core reaches an equilibrium configuration with a central density $\rho_{\mathrm{c\,f}} = 1.6 \times 10^{14}$ g cm^{-3} quite quickly, although at subnuclear densities. In models A4B1G2 (middle panel) and A1B3G1 (upper panel), relativistic corrections are strong enough to enable the formation of a core in equilibrium at supranuclear central densities. The change of collapse type is also clearly reflected in the pattern of the gravitational radiation waveform of these models (see Figure 7.9).

The same analysis as above can be applied to models which are of the transition type I/II between a multiple bounce collapse and a regular bounce in Newtonian gravity, and have maximum central densities of around 3×10^{14} g cm^{-3}. In relativistic gravity these models also contract to such high densities that the condition in Equation 7.7 is violated, and the collapse proceeds as a regular type I collapse[g]. The evolution of the central density for the three models from Table 7.8 which show this behavior, are presented in Figure 7.10. However, as these models show a transition type I/II behavior already in Newtonian gravity, and are not clear-cut multiple bounce collapse models, the differences of the waveforms, which are plotted in Figure 7.11, are not as pronounced as those for the models in Figure 7.9. For example, the waveform patterns and amplitudes for model A3B3G3 (lower panel) are almost identical independent of the model being evolved in relativistic or Newtonian gravity. On the other hand,

---

[g] Model A3B3G3 has a maximum central density $\rho_{\mathrm{c\,b}} = 2.91 \times 10^{14}$ g cm^{-3} $< \rho_{\mathrm{c\,b\,max}}$, but it can be regarded as a regular collapse model forming an equilibrium configuration with a central density around ρ_{nuc}. The criterion for a regular collapse in Equation (7.7) obviously allows for exceptions in case of a high rotation rate and strongly differential rotation law.

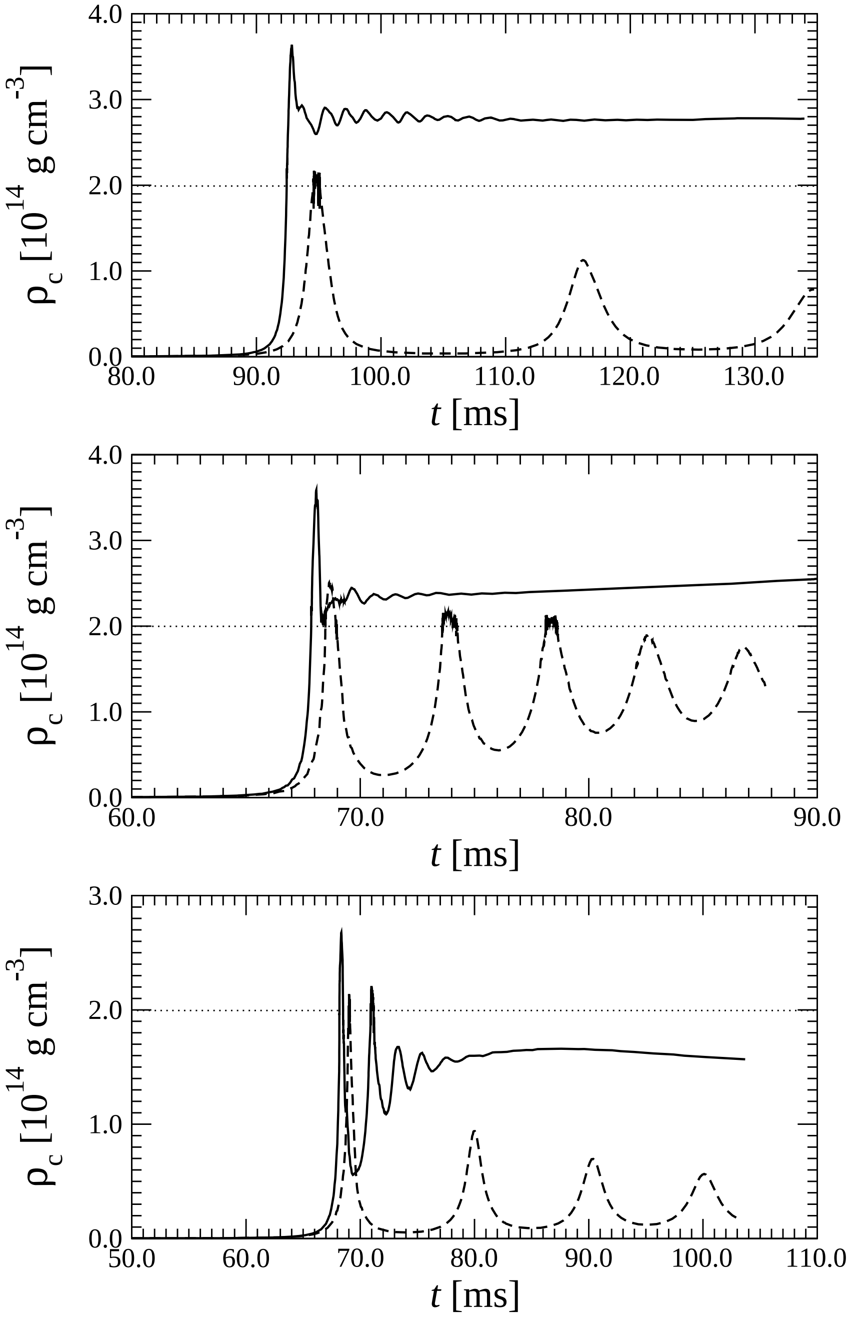

Figure 7.8: *Evolution of the central density* ρ_{c} *in the relativistic (solid lines) and Newtonian (dashed lines) simulation of the models* A1B3G1 *(upper panel),* A4B1G2 *(middle panel), and* A4B2G2 *(lower panel): While the runs with Newtonian gravity are clear multiple bounce collapses, the relativistic runs are of regular bounce type (models* A1B3G1 *and* A4B1G2*), or of transition type between a regular bounce and a multiple bounce (model* A4B2G2*). The horizontal dotted lines mark nuclear matter density.*

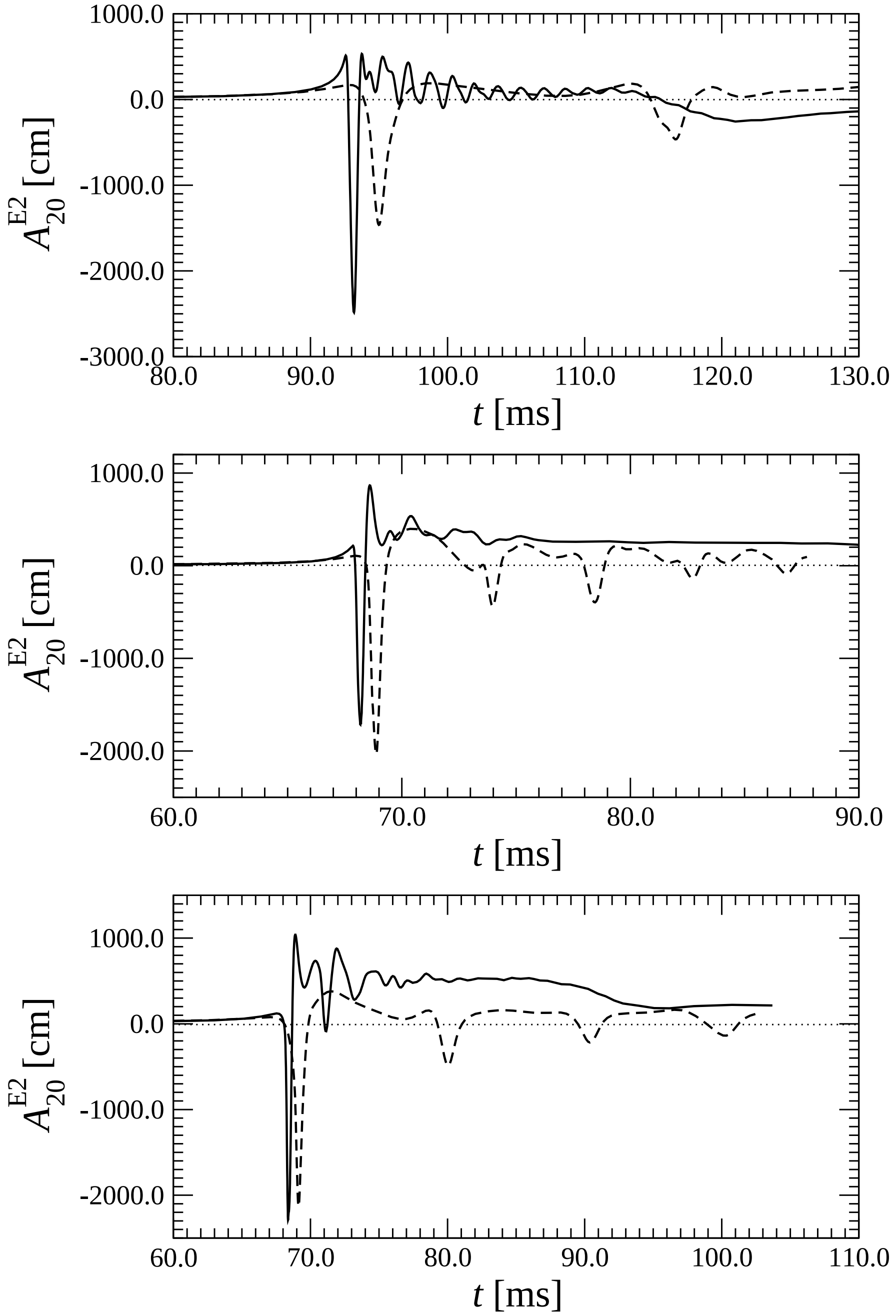

Figure 7.9: *Evolution of the gravitational wave signal amplitude* $A_{20}^{\rm E2}$ *in the relativistic (solid lines) and Newtonian (dashed lines) simulation of the models* A1B3G1 *(upper panel),* A4B1G2 *(middle panel), and* A4B2G2 *(lower panel): The qualitative differences in the waveforms obtained from simulations with relativistic gravity and Newtonian gravity are obvious.*

in model A1B3G2 the typical wave amplitude peaks associated to the distinct multiple bounces can still be seen for the first two bounces in the waveform of the Newtonian run, whereas the signal of the relativistic simulation shows the ring-down characteristic for a regular bounce. The most striking difference between the waveforms in model A1B1G1 (upper panel) is the much lower average amplitude in the relativistic run, which is a consequence of the suppressed coherent motions of the inner core in a regular bounce (see Section 7.6).

The implications of relativistic effects on multiple bounce collapse models can be summarized as follows: Multiple bounce collapse models, which are rather common in Newtonian gravity for low or moderate rotation rates and rotation laws not too far from uniformity, are strongly suppressed in relativistic simulations. In most collapse models, the core contracts to such high central densities, that it cannot be stopped by centrifugal forces and re-expand subsequently. It rather immediately forms a stable configuration which is mainly supported by the stiff supranuclear EoS. This suppression of multiple bounces results in a very strong reduction of the region of parameter space where multiple bounce models are possible, as shown in Figure 7.12. As in the case of Newtonian gravity, only for values of the adiabatic index in the range $\gamma = \{1.320, 1.325\}$, which are very close to the initial $\gamma = 4/3$, multiple bounces occur at all. But whereas the values for the rotation parameter A (differentiality of the rotation law) and the rotation rate β (relative amount of rotational energy) are rather wide for multiple bounce models in Newtonian gravity, relativistic effects narrow the range of possible values for A and β drastically, with only rapidly rotating models with a moderate differential rotation law remaining. (It is probable that the initial models A2B5 and A3B5 would also exhibit multiple bounce behavior in a relativistic simulation given a γ_1 close to 4/3, but as such high rotation rates are astrophysically hard to motivate we have not investigated these models.)

The effects of relativistic gravity in cases of rapid and highly differential rotation, where the core collapse is also stopped by centrifugal forces and re-expands but does not bounce for a second time, are described in Section 7.7.

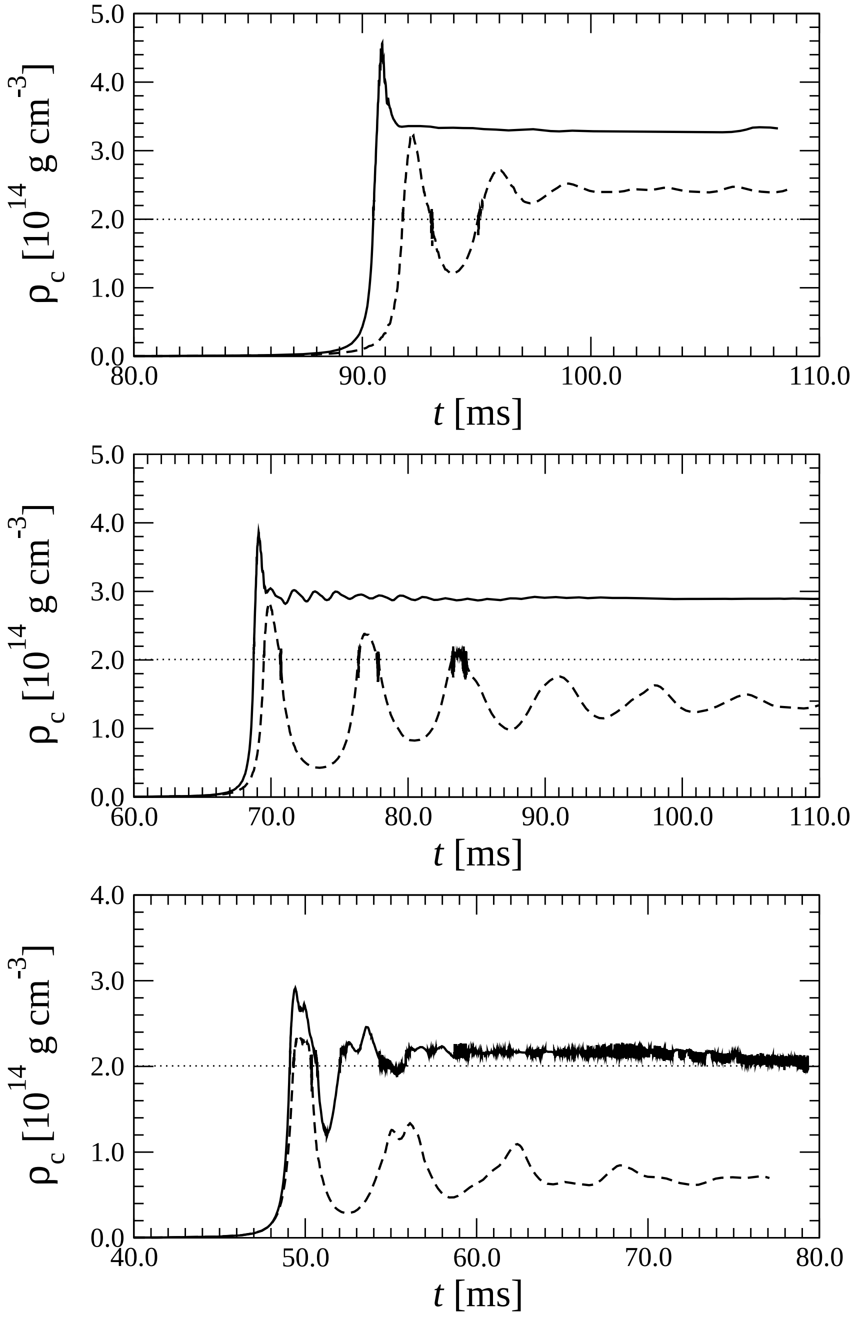

Figure 7.10: *Evolution of the central density* ρ_{c} *in the relativistic (solid lines) and Newtonian (dashed lines) simulation of the models* A1B1G1 *(upper panel),* A1B3G2 *(middle panel), and* A3B3G3 *(lower panel): While the runs with Newtonian gravity are of transition type between regular collapse and multiple bounce collapse, the relativistic runs are regular collapses with* $\rho_{\mathrm{c\,f}} > \rho_{\mathrm{nuc}}$*. The horizontal dotted lines mark nuclear matter density.*

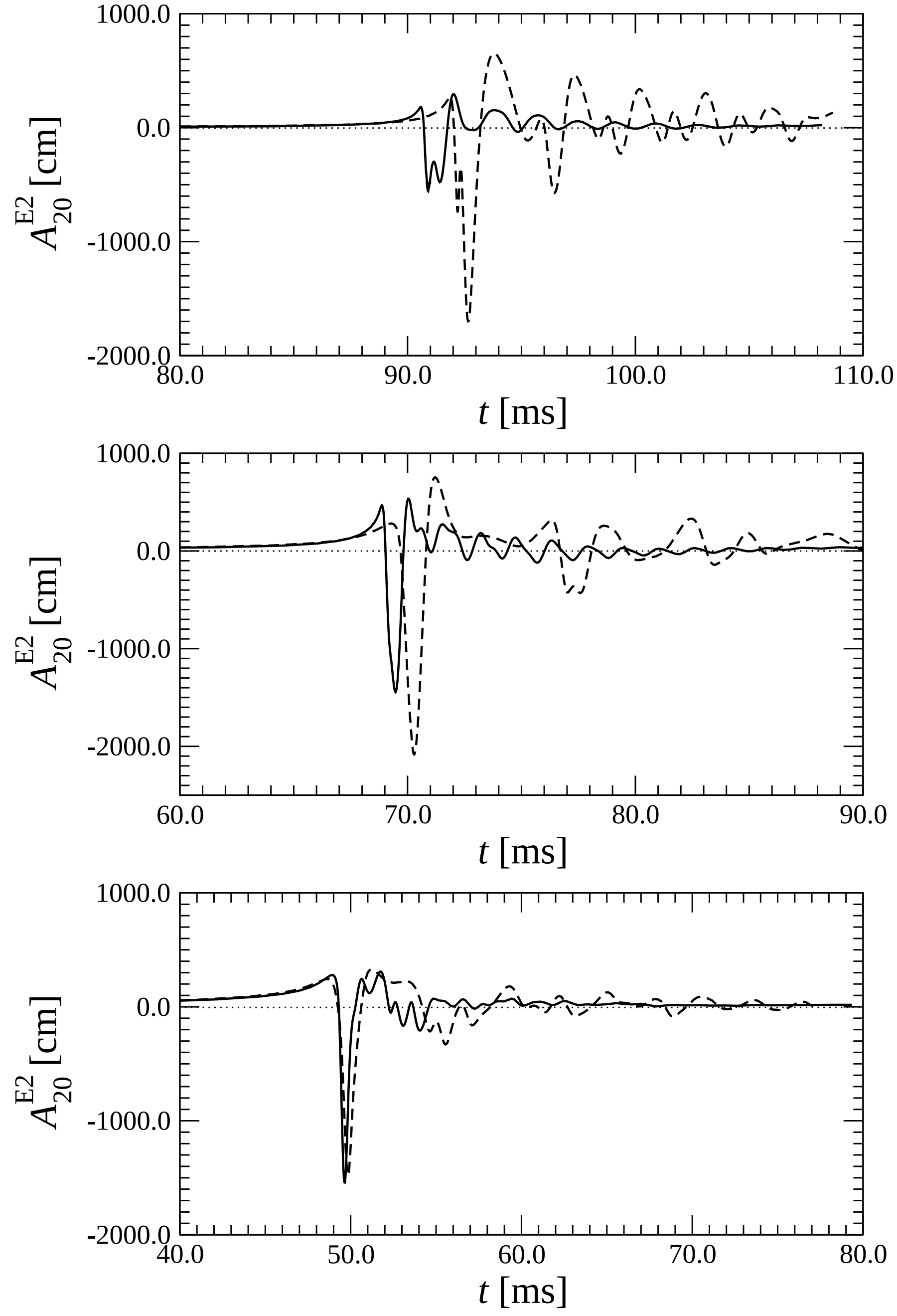

Figure 7.11: *Evolution of the gravitational wave signal amplitude* A_{20}^{E2} *in the relativistic (solid lines) and Newtonian (dashed lines) simulation of the models* A1B1G1 *(upper panel),* A1B3G2 *(middle panel), and* A3B3G3 *(lower panel): While the waveforms obtained from simulations with relativistic gravity show a pronounced ring-down feature, the waveforms from Newtonian simulations exhibit a form which is attributable to the coherent bounce of a transition type I/II collapse.*

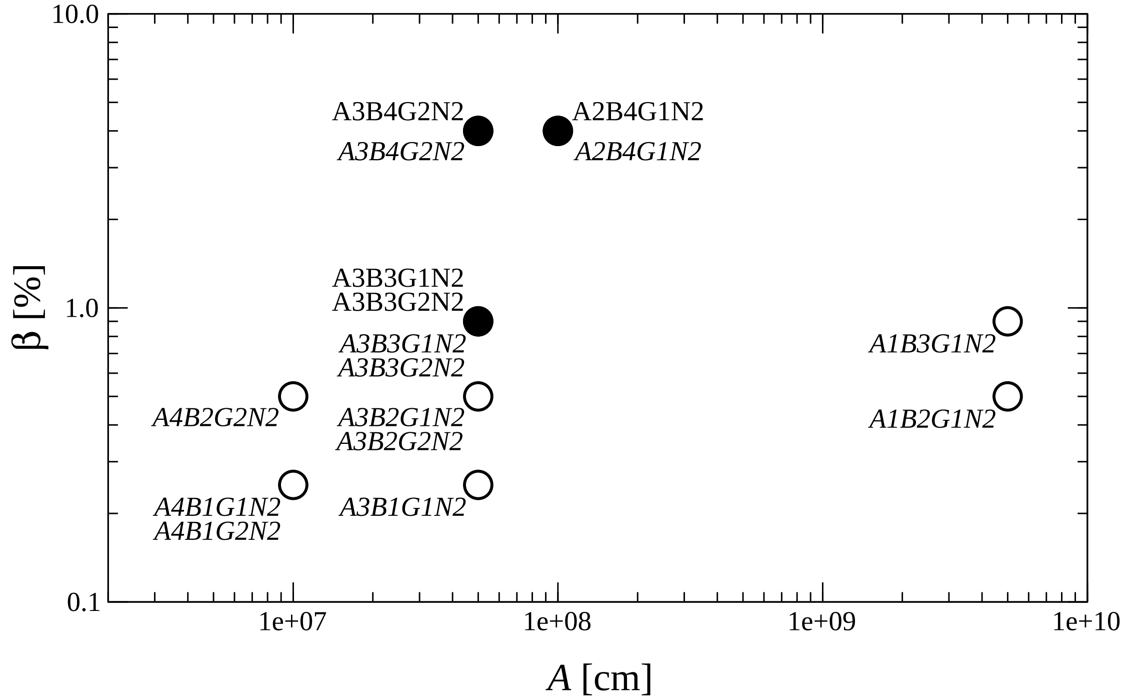

Figure 7.12: *Parameter space spanned by the rotation parameter* A *and the rotation rate* β *for multiple bounce collapse models in relativistic (italic font) and Newtonian (normal font) simulations: The combinations of* A *and* β *for which multiple bounce collapses occur are marked by a circle. If the circle is filled, there is a multiple bounce collapse model in relativistic gravity for the corresponding parameter combination. The other free parameter* γ_1 *is specified by the name of the models.*

7.6 Compactness of the Proto-Neutron Star Core

We now discuss the effects of relativity for models, where the collapse type and thus the signal type are the same for the relativistic and Newtonian simulation. These models are presented in Table 7.9. Although all relativistic simulations reach higher central densities[h] and on average larger infall and rotation velocities, only the three models A2B4G1, A3B3G1, and A3B3G2 have higher maximum (and average) signal amplitudes than their Newtonian counterparts. This fact is surprising, as one would naively expect larger gravitational signals for the denser and more rapidly moving relativistic models.

However, by closely looking at any of the (analytically identical) formulations (C.9, C.10, C.11) used to calculate the gravitational wave signal, it becomes clear that the signal amplitude is determined by the *bulk* motion of the core rather than by the motion of just the innermost mass shells. It is therefore conceivable that a matter configuration with very dense mass shells in the interior, gives rise to a *smaller* gravitational wave signal compared to a configuration, which has a lower central density, but is denser and more rapidly moving in its outer parts. The importance of the bulk motion is emphasized by the weight factor r^2 in the volume integrand

$$\rho r^2 \left(\frac{3}{2} \cos^2 \theta - \frac{1}{2} \right) r^2 \sin \theta dr d\theta = \rho r^2 \left(\frac{3}{2} \cos^2 \theta - \frac{1}{2} \right) dV \tag{7.8}$$

of the standard quadrupole formula (C.9), which allows the matter distribution at large r to contribute significantly to the signal amplitude. This may also explain the behavior of the models in Table 7.9, whose maximum signal amplitudes are smaller in the relativistic case. These models may be more compact near the center but less dense farther out. We will test this "compactness conjecture" in the following.

We first assume that the regions outside the inner core, through which the shock wave propagates, play no important role for the gravitational wave signal, as there both the density and the motions are too small to contribute significantly to the quadrupole moment. Hence, any deviations in density or velocity profiles between the relativistic and Newtonian simulation of a particular model at large radii ($r \gtrsim r_{\text{inner core}}$) will not influence the gravitational wave signal. However, at small radii ($r \lesssim r_{\text{inner core}}$), any differences between matter configurations in relativistic and Newtonian simulations will be important. In Figure 7.13, the equatorial density profiles in the inner core of model A3B2G4$_{\text{soft}}$[i] are plotted for a relativistic and a Newtonian simulation at the time of bounce and after ring-down. As expected, and as confirmed by Table 7.2, a relativistic enhancement of the post-bounce central density of 25% can be observed.

On the other hand, at radii $r \gtrsim 6$ km, the density in the Newtonian models exceeds that of the relativistic one. This first occurs at the time of bounce in the entire post-shock region (upper panel in Figure 7.13), and later after ring-down up to the edge of the inner core (lower panel). This "density crossing" takes place at different radii in the core for different angles θ, but otherwise is a universal feature which can be observed in the inner core at all times $t > t_{\text{b}}$ and for all angular directions. The constancy of this effect over time can be seen in Figure 7.14,

---

[h] Model A4B4G5 is an exception to this general rule.

[i] We have chosen this model, as relativistic effects are very pronounced due to its soft EoS and high central density.

Model	Type	$\rho_{\mathrm{c\,b}}$ $[10^{14}\ \mathrm{g\ cm^{-3}}]$	$\rho_{\mathrm{c\,f}}$ $[10^{14}\ \mathrm{g\ cm^{-3}}]$	$\lvert A_{20}^{\mathrm{E2}}\rvert_{\mathrm{max}}$ [cm]	$\lvert A_{20}^{\mathrm{E2\ R}}\rvert_{\mathrm{max}} \lesseqgtr \lvert A_{20}^{\mathrm{E2\ N}}\rvert_{\mathrm{max}}$
A1B3G3$^{\mathrm{R}}$	I	4.09	3.1	483.9	$<$
A1B3G3$^{\mathrm{N}}$		3.38	2.5	975.9	
A1B3G5$^{\mathrm{R}}$	III	4.49	3.5	106.2	$<$
A1B3G5$^{\mathrm{N}}$		4.26	3.0	130.5	
A2B4G1$^{\mathrm{R}}$	II	0.42	—	744.6	$>$
A2B4G1$^{\mathrm{N}}$		0.11	—	651.7	
A3B2G4$^{\mathrm{R}}_{\mathrm{soft}}$	I	5.64	3.4	527.9	$<$
A3B2G4$^{\mathrm{N}}_{\mathrm{soft}}$		4.45	2.7	781.1	
A3B2G4$^{\mathrm{R}}$	I	3.90	2.9	426.3	$<$
A3B2G4$^{\mathrm{N}}$		3.41	2.5	703.2	
A3B3G1$^{\mathrm{R}}$	II	2.36	—	1713.4	$>$
A3B3G1$^{\mathrm{N}}$		0.47	—	1087.3	
A3B3G2$^{\mathrm{R}}$	II	2.56	—	1953.6	$>$
A3B3G2$^{\mathrm{N}}$		1.10	—	1419.5	
A3B3G5$^{\mathrm{R}}$	III	3.64	2.8	239.9	$<$
A3B3G5$^{\mathrm{N}}$		3.44	2.3	263.4	
A3B4G2$^{\mathrm{R}}$	II	0.38	—	862.4	$<$
A3B4G2$^{\mathrm{N}}$		0.16	—	893.9	
A3B5G4$^{\mathrm{R}}$	III	0.18	—	481.0	$<$
A3B5G4$^{\mathrm{N}}$		0.15	—	527.9	
A4B2G3$^{\mathrm{R}}$	I/II	2.42	—	1900.0	$<$
A4B2G3$^{\mathrm{N}}$		2.15	—	2217.4	
A4B4G4$^{\mathrm{R}}$	II	0.25	—	1346.6	$<$
A4B4G4$^{\mathrm{N}}$		0.25	—	1748.3	
A4B4G5$^{\mathrm{R}}$	II	0.17	—	1566.9	$<$
A4B4G5$^{\mathrm{N}}$		0.42	—	2149.1	
A4B5G4$^{\mathrm{R}}$	II	0.05	—	2342.9	$<$
A4B5G4$^{\mathrm{N}}$		0.05	—	2965.2	
A4B5G5$^{\mathrm{R}}$	II	0.09	—	3143.5	$<$
A4B5G5$^{\mathrm{N}}$		0.07	—	5443.9	

Table 7.9: *Summary of the density at bounce and the gravitational wave signal amplitude for models of the same collapse type in both relativistic (R) and Newtonian (N) simulations:* Type *specifies the signal and collapse type as described in Sections 7.1.1–7.1.3,* $\rho_{\mathrm{c\,b}}$ *is the central density at bounce,* $\rho_{\mathrm{c\,f}}$ *is the central density at the time when the simulation was stopped,* $\lvert A_{20}^{\mathrm{E2}}\rvert_{\mathrm{max}}$ *is the maximum signal amplitude, and* $\lvert A_{20}^{\mathrm{E2\ R}}\rvert_{\mathrm{max}} \lesseqgtr \lvert A_{20}^{\mathrm{E2\ N}}\rvert_{\mathrm{max}}$ *indicates whether the relativistic or Newtonian maximum absolute signal amplitude is higher. Note that only for models* A2B4G1*,* A3B3G1*, and* A3B3G2 *the maximum absolute signal amplitude is larger in the relativistic case.*

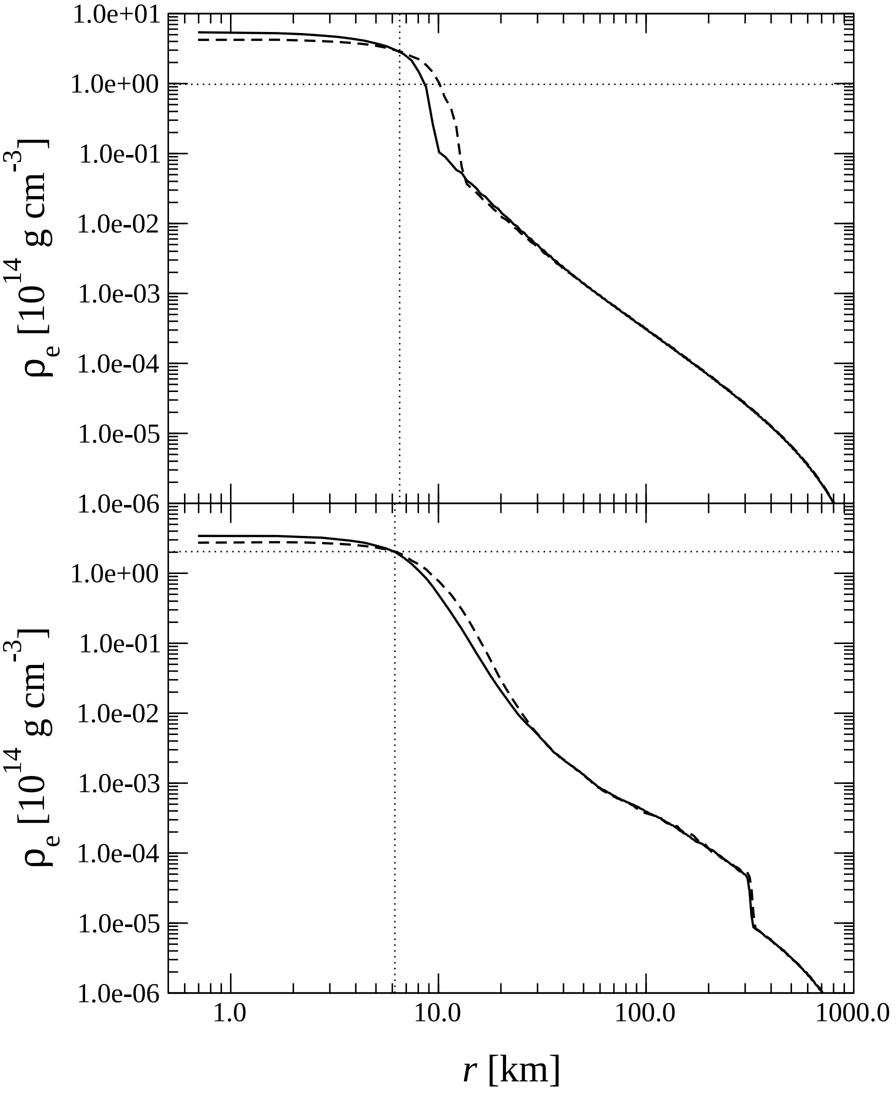

Figure 7.13: *Radial density profiles* ρ_e *at the equator for model* A3B2G4$_\mathrm{soft}$*: Both during the bounce at* $t = 39.25$ ms *(upper panel) and after the core has rung down at* $t = 55.0$ ms *(lower panel), the density of the relativistic simulation (solid line) is higher than the density of the Newtonian simulation (dashed line) in the central region. At* $r \approx 6.5$ km *(upper panel) and* $r \approx 6.2$ km *(lower panel) the density of the relativistic model drops below that of the Newtonian one; the radius of density crossing is indicated by the vertical dotted lines. For large radii the density profiles coincide closely. The position of the shock front is clearly visible in the lower panel and is located at* $r \approx 320$ km.

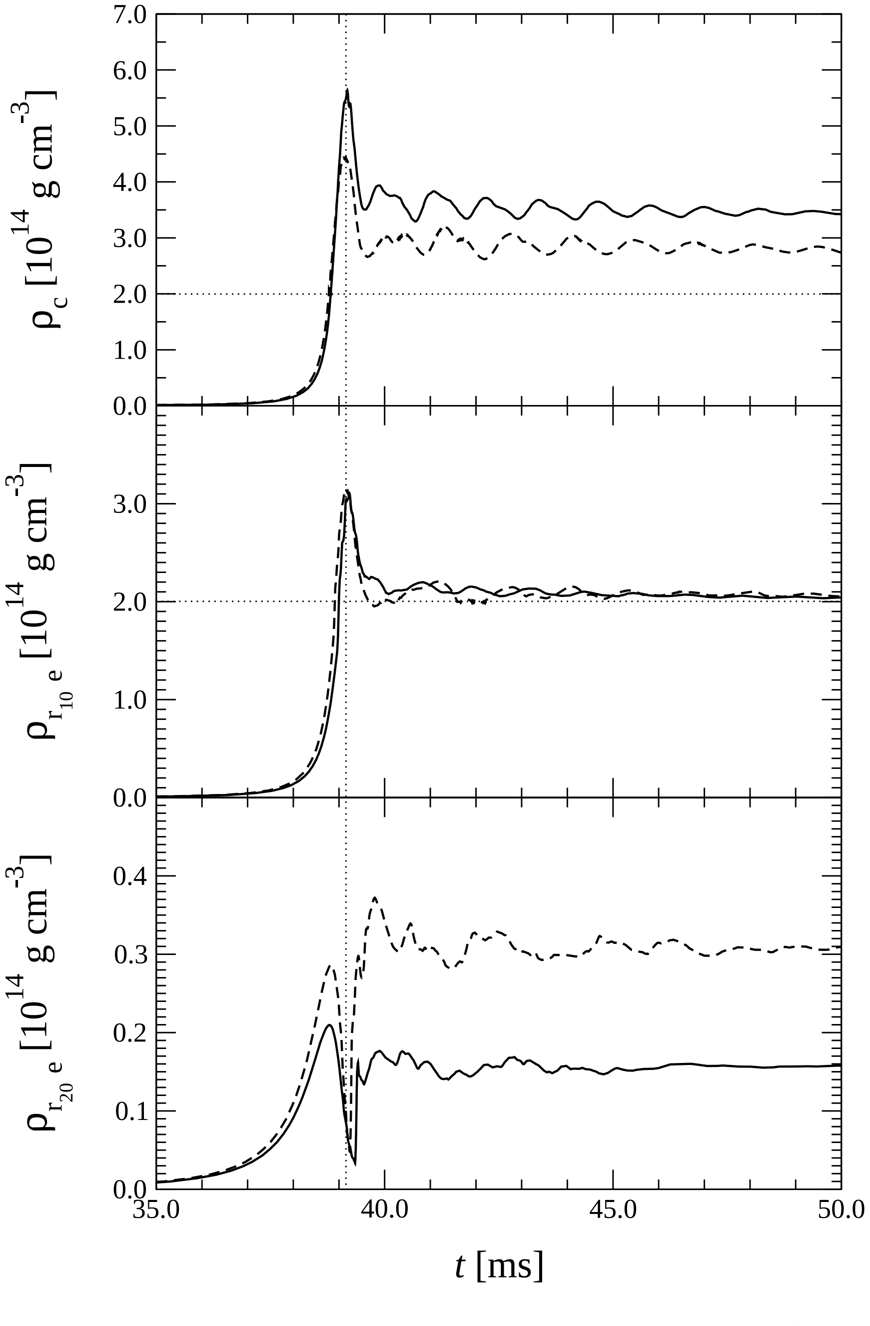

Figure 7.14: *Evolution of the density at different radii in the relativistic (solid lines) and Newtonian (dashed lines) simulation of model* A3B2G4$_{\text{soft}}$*: In the upper panel the central density is plotted; in the middle and lower panel the equatorial density is shown at a radius* $r_{10} = 6.2$ km *and* $r_{20} = 12.9$ km*, respectively. With increasing radius, the density in the Newtonian model exceeds the one in the relativistic model, which indicates that the core in the relativistic model is more compact in the inner regions, and less dense in the outer parts. The vertical dotted line indicates the time of maximum central density* t_{b}*, the horizontal dotted lines specify nuclear matter density* ρ_{nuc}*. Note the different vertical scale of the plots.*

where the evolution of the equatorial density is plotted at different radial locations in the inner core. After the bounce, the central density of the relativistic configuration is always higher than the corresponding Newtonian one (upper panel). However, close to the radius of density crossing, the density difference between both simulations is minute (middle panel). At an even larger radius, but still inside the inner core, the relativistic configuration exhibits a relative density reduction $\rho^{\mathrm{N}}/\rho^{\mathrm{R}} - 1$ of up to -50%.

Repeating the above analysis with the multiple bounce model A2B4G1, whose relativistic simulation yields a larger signal amplitude than the Newtonian one, at first sight shows a situation which is similar to the one of model A3B2G4$_{\mathrm{soft}}$: The central density at the time of bounce is almost 4 times higher in the relativistic run compared to the Newtonian run. The density profiles at the equator shortly after maximum density, which are plotted in Figure 7.15, show the typical density crossing. However, in this case the density crossing occurs at a much larger radius ($r \approx 40$ km). Inside this radius, the cores of both the relativistic and the Newtonian simulation oscillate coherently. The density of the relativistic run is significantly higher throughout the evolution (see Figure 7.16). Furthermore, compared to model A3B2G4$_{\mathrm{soft}}$, where the accelerations of the central parts of the inner core are of comparable strength irrespective of whether the core is evolved in relativistic or Newtonian gravity, in model A2B4G1 the center of the inner core is subject to much higher accelerations in the relativistic run, which is reflected by the shorter width of the density peaks in time, and the shorter intervals between two consecutive bounces.

The impact of the relativistic density reduction in the outer regions of the inner core on the gravitational wave signal can be estimated from Figure 7.17, where the equatorial density profile, weighted with a factor r^2 as in the integrand of the quadrupole formula (7.8), is plotted. In the multiple bounce model A2B4G1, the inner core shows a large relativistic density enhancement in the inner part, and a small density reduction in the outer part; thus the dominance of the Newtonian profile of ρr^2 in the outer region is more than compensated for by the dominance of the relativistic profile in the central region (upper panel). As the central parts of the core are being accelerated strongest during the bounce, it is the inner region which will contribute most to the gravitational wave signal. Therefore the signal amplitude is larger in the relativistic simulation.

The situation is quite different in the regular collapse model A3B2G4$_{\mathrm{soft}}$: Here the dominance of the relativistic weighted density profile is much weaker in the central regions of the core for $r \lesssim 6$ km. Contrary to the small relativistic density enhancement in the central parts, the dominance of the Newtonian weighted density profile in the outer parts is overwhelming (lower panel). Thus even if the mass shells at $r \gtrsim 6$ km are not accelerated so much, the higher weighted density there in the Newtonian configuration will still cause a gravitational wave signal contribution which is much larger than the one in the relativistic case. Therefore, it can be expected that the total signal amplitude is larger in the Newtonian configuration.

To prove the above predictions for the gravitational wave signal amplitudes for the two test models, we have artificially split the quadrupole moment into two parts: For part one, we evaluate the integral in the quadrupole formula (7.8) between the center $r = 0$ and $r = r_{\mathrm{split}}$, and for part two between $r = r_{\mathrm{split}}$ and the outer boundary of the computational domain. We choose the radius r_{split} to be the point of density crossing at the equator during bounce. As

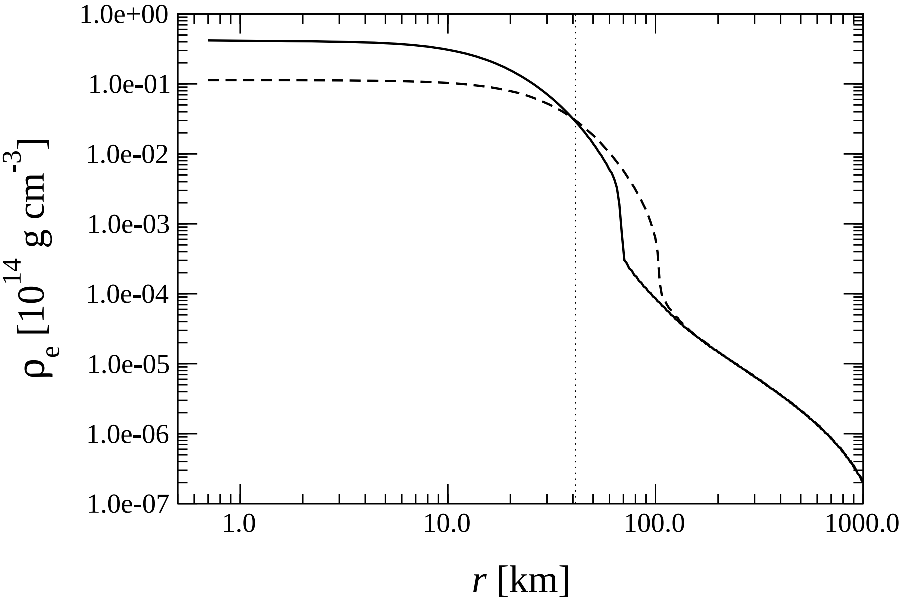

Figure 7.15: *Radial density profiles* ρ_e *at the equator for model* A2B4G1*: During the bounce at* $t = 99.25$ ms*, the density of the relativistic simulation (solid line) is higher than the density of the Newtonian simulation (dashed line) in the central region. At* $r \approx 40.0$ km *the density crossing occurs (which is indicated by the vertical dotted line), i.e. the density of the Newtonian model higher than the one of the relativistic model in the outer regions of the neutron star. For large radii the density profiles coincide. Compared to the regular bounce model of Figure 7.13, the densities of the relativistic and Newtonian simulations cross at a much larger radius in this multiple bounce model, and the inner region, where the relativistic model is more dense, is significantly more extended.*

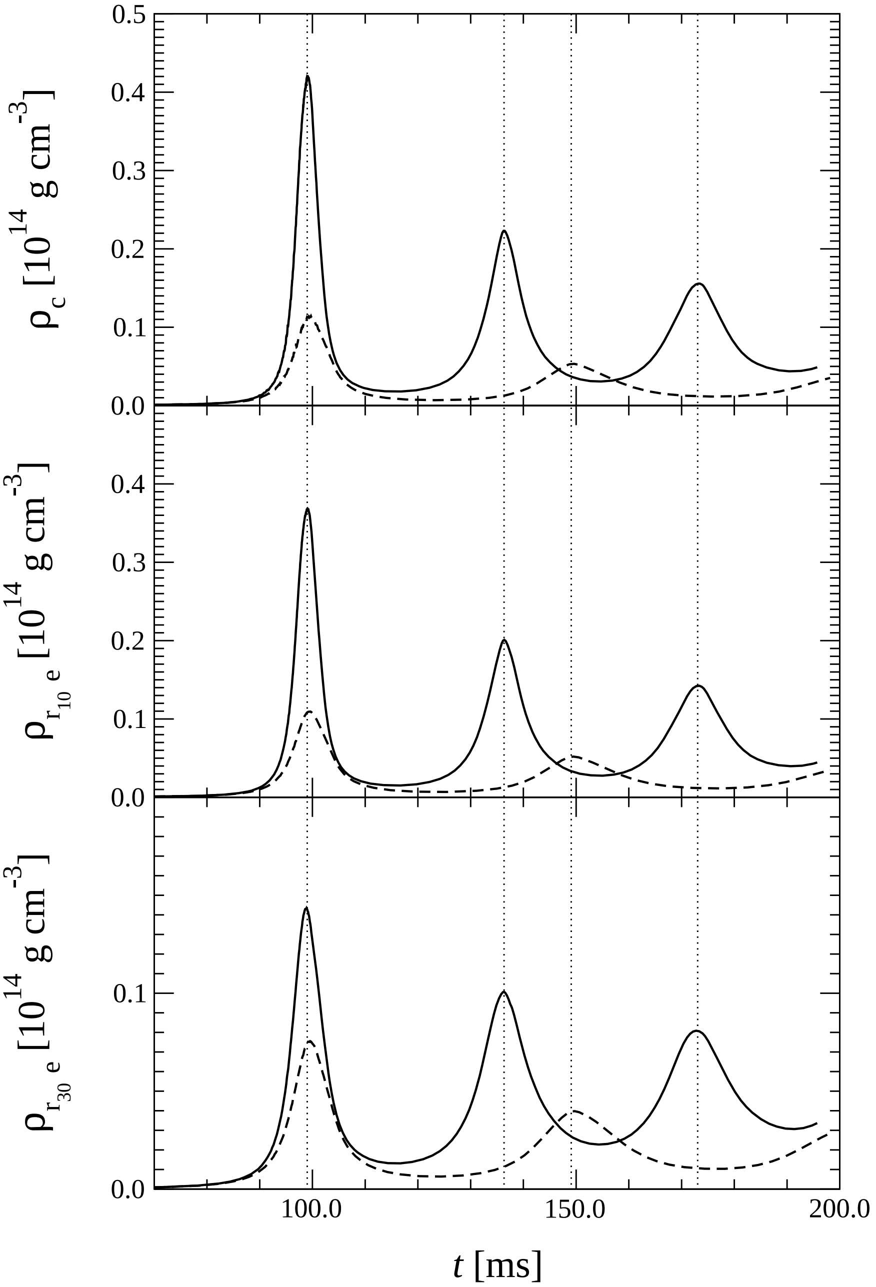

Figure 7.16: *Evolution of the density at different radii in the relativistic (solid lines) and Newtonian (dashed lines) simulation of model* A2B4G1*: In the upper panel the central density is plotted; in the middle and lower panel the equatorial density is shown at a radius* $r_{10} = 6.2$ km *and* $r_{30} = 21.4$ km*, respectively. With increasing radius, the density in the Newtonian model gets closer to the one in the relativistic model, which indicates that the core in the relativistic model is more compact in the inner regions, and less dense in the outer parts. The vertical dotted line indicates the time of maximum central density* t_b*, the horizontal dotted lines specify nuclear matter density* ρ_{nuc}*. Note the different vertical scale of the plots.*

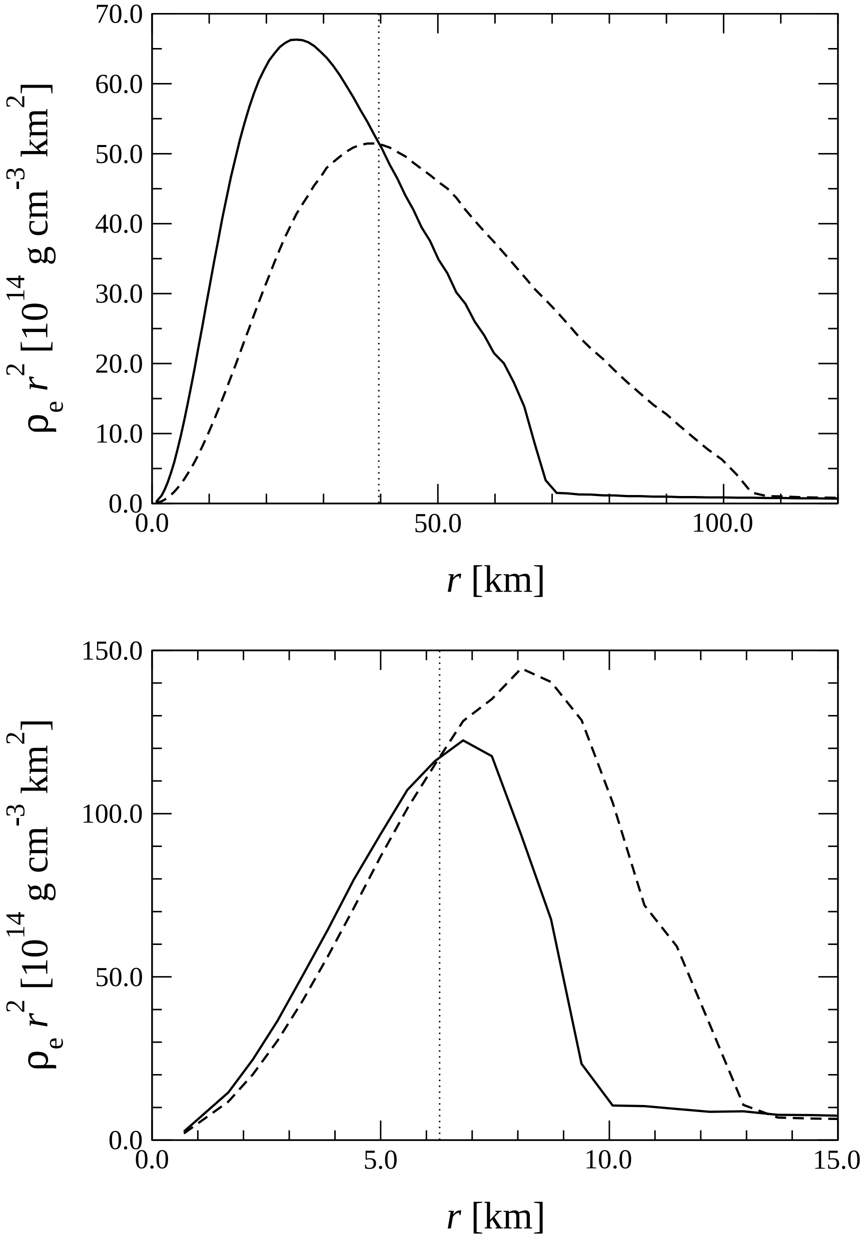

Figure 7.17: *Radial density profile* ρ_{e} *at the equator for models* A2B4G1 *at* $t = 99.25$ ms *(upper panel) and model* A3B2G4$_{\mathrm{soft}}$ *at* $t = 39.55$ ms *(lower panel), weighted with a factor* r^2*: The integrand in the equation for the standard quadrupole formula (C.9) is proportional to* $\rho r^4 \sin\theta dr d\theta = \rho r^2 dV$ *(see Appendix C.2). Therefore, the outer parts of the inner core, where the density of the Newtonian model is higher than the density of the relativistic model, contributes significantly to the quadrupole moment and thus to the signal. The radius of density crossing is indicated by the vertical dotted lines.*

a consequence of this split, we can separate the gravitational wave signal into a contribution from the central regions of the inner core, and a contribution from the rest of the core. The total signal amplitude is simply the sum of both contributions.

The result of this split applied to the models A3B2G4$_{\mathrm{soft}}$ and A2B4G1 can be seen in Figure 7.18 and Figure 7.19, respectively. As already suggested, in the regular bounce model (Figure 7.18) the outer parts of the inner core contribute over-proportionally to the total signal amplitude. This contribution has a much larger signal in the Newtonian case (lower panel), and the pronounced first negative peak of the Newtonian run is entirely missing in the relativistic run. Such a feature in the signal can be attributed to a coherent acceleration of the core, which is obviously suppressed in the outer parts of the core in the relativistic configuration. The signals in the contribution of the central region are of similar amplitude in both the relativistic and the Newtonian run with a moderate dominance of the signal in the relativistic run (middle panel). Consequently, the combined total signal amplitude of the Newtonian simulation is larger than the one of the relativistic simulation (upper panel).

In the Newtonian simulation of model A3B2G4$_{\mathrm{soft}}$, the negative first peaks in the signal of both contributions add up due to the coherent motion of the central and outer parts of the inner core. Contrary to that, in the multiple bounce model A2B4G1 the signal contribution from the inner part (middle panel) is entirely negative, and the one from the outer part (lower panel) is entirely positive in both the relativistic and the Newtonian simulation, as the inner part ($r < r_{\mathrm{split}}$) encompasses almost all of the coherently moving inner core. The total (negative) signal amplitude is constituted by what is left over when the (positive) signal contribution from the outer part is added to the (negative) contribution from the inner part. In both parts of the inner core the signal is higher in relativistic gravity due to the higher densities and accelerations involved. After adding up the two contributions (upper panel), the wave amplitude of the relativistic simulation is higher in all the peaks of the waveform associated to the bounces of the core.

The above analysis also helps to explain the weaker maximum and average gravitational wave signal amplitudes in model A1B1G1 when evolved in relativistic gravity (see Figure 7.20). In general relativity, the central parts of the inner core collapse to almost $2.5\rho_{\mathrm{nuc}}$, and after a single bounce rapidly settle down to an equilibrium state with constant density (middle panel). Due to the compactness of the inner core, the density is rather small in the outer parts of the core (lower panel). The motion of the fluid in the outer regions of the core is not coherent with the motion of the fluid in the inner regions. The parts of the core at radii $r \gtrsim r_{20} = 13.0$ km are already in the region where the shock forms[j]. If the collapse proceeds in a Newtonian gravitational potential, the inner core is much less compact and has a lower central density, but a much higher density at $r_{20} = 13.0$ km. The entire inner core oscillates coherently with large amplitude motions, which results in a huge time variation of the quadrupole moment and thus a large gravitational wave signal. Although the accelerations during the bounces are less violent than in the single bounce of the relativistic simulation, the corresponding gravitational wave signal is significantly larger, the maximum signal amplitude being three times higher than the corresponding one in relativistic gravity.

Summarizing this discussion, we want to point out that a density crossing occurs in all the

---

[j] The influence of the shock is visible as a negative spike in the density plot in the lower panel of Figure 7.20.

models we have investigated. Such a behavior is not only confined to models of the same qualitative collapse type in the relativistic and Newtonian run of a particular model. The density crossing is a manifestation of the increased compactness of the inner core due to relativistic effects. The compactness in the central regions, which is closely linked with a reduced density in the outer regions of the inner core, is responsible for the smaller total signal amplitudes observed in most of the models listed in Table 7.9. The cases, where the signal amplitude of the relativistic simulation is larger than the Newtonian one, are characterized by a multiple bounce collapse, where the maximum central density is close to or above nuclear matter density in the relativistic configuration, and thus much higher than the maximum central density in the Newtonian configuration. Plots of the signal amplitudes for all these models are given in the gravitational wave signal catalogue in Appendix D.

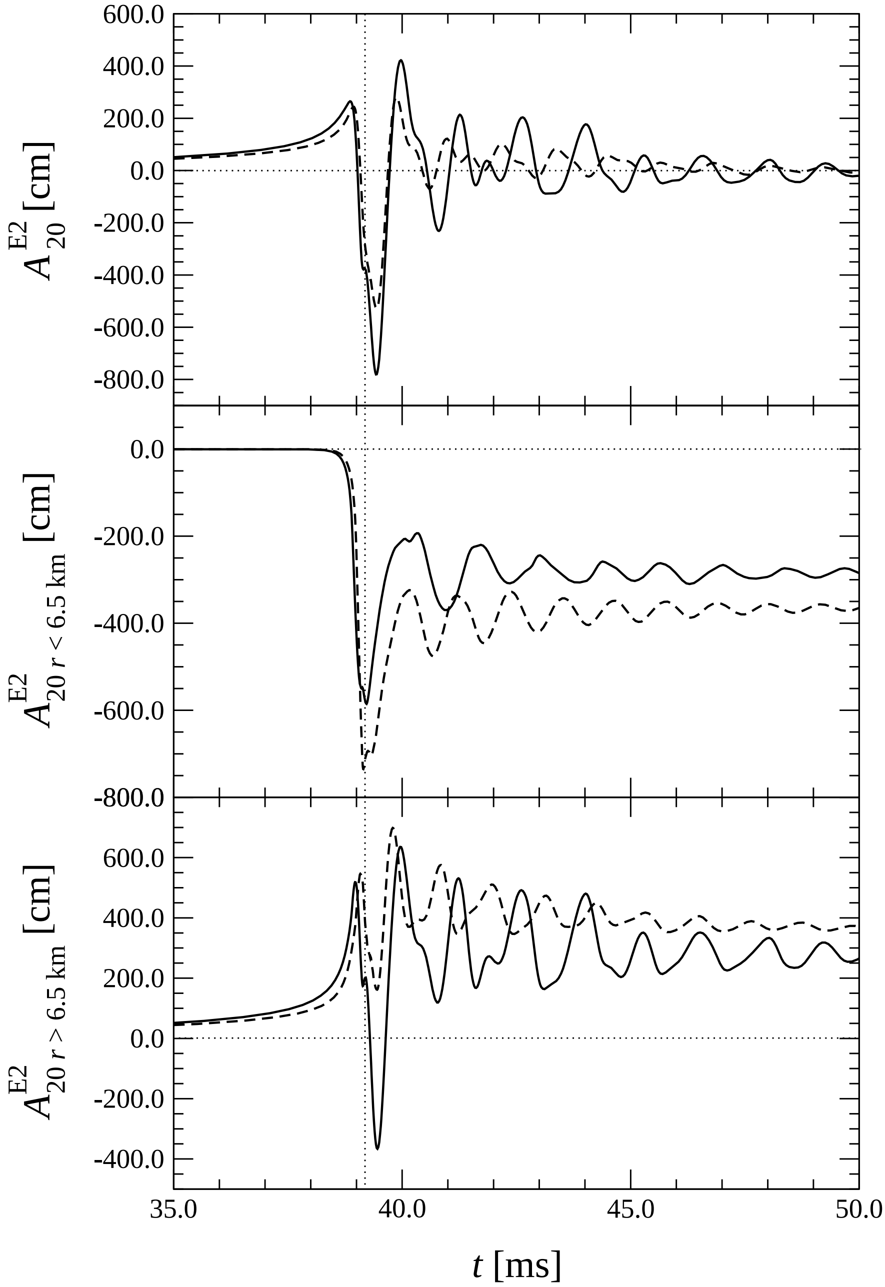

Figure 7.18: *Contribution of the inner and outer part of the computational domain to the gravitational wave signal amplitude in the relativistic (solid lines) and Newtonian (dashed lines) simulation of model* A3B2G4$_{\mathrm{soft}}$*: In the upper panel the total quadrupole signal amplitude* A^{E2}_{20} *is plotted. The middle and the lower panel show the contributions of the mass shells lying inside and outside a sphere of radius* $r = 6.5$ km*. Although the signal amplitude from the inner region is large in the relativistic case, the Newtonian signal amplitude is larger both in the outer parts of the core, and for the entire core. The vertical dotted line indicates the time of maximum central density* t_{b}*.*

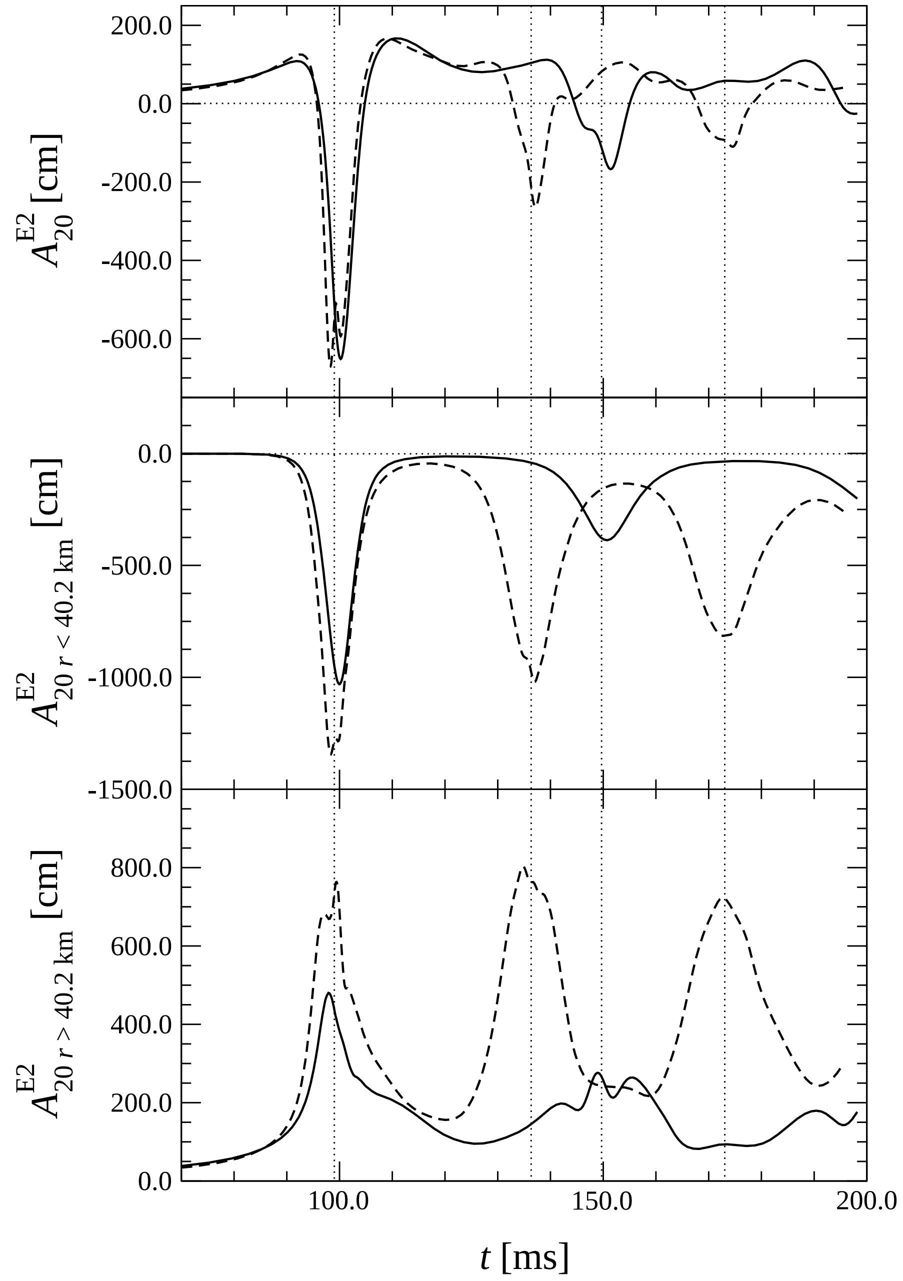

Figure 7.19: *Contribution of the inner and outer part of the computational domain to the gravitational wave signal amplitude in the relativistic (solid lines) and Newtonian (dashed lines) simulation of model* A2B4G1*: In the upper panel the total quadrupole signal amplitude* A_{20}^{E2} *is plotted. The middle and the lower panel show the contributions of the mass shells lying inside and outside a sphere of radius* $r = 40.2$ km*. Contrary to model* A3B2G4$_{\mathrm{soft}}$ *(Figure 7.18), the larger signal amplitude from the inner core in the relativistic case more than compensates for the larger Newtonian signal amplitude from the outer parts of the core; thus the total signal amplitude is larger in the relativistic simulation. The vertical dotted lines indicate the time of maximum central density* t_{b}*.*

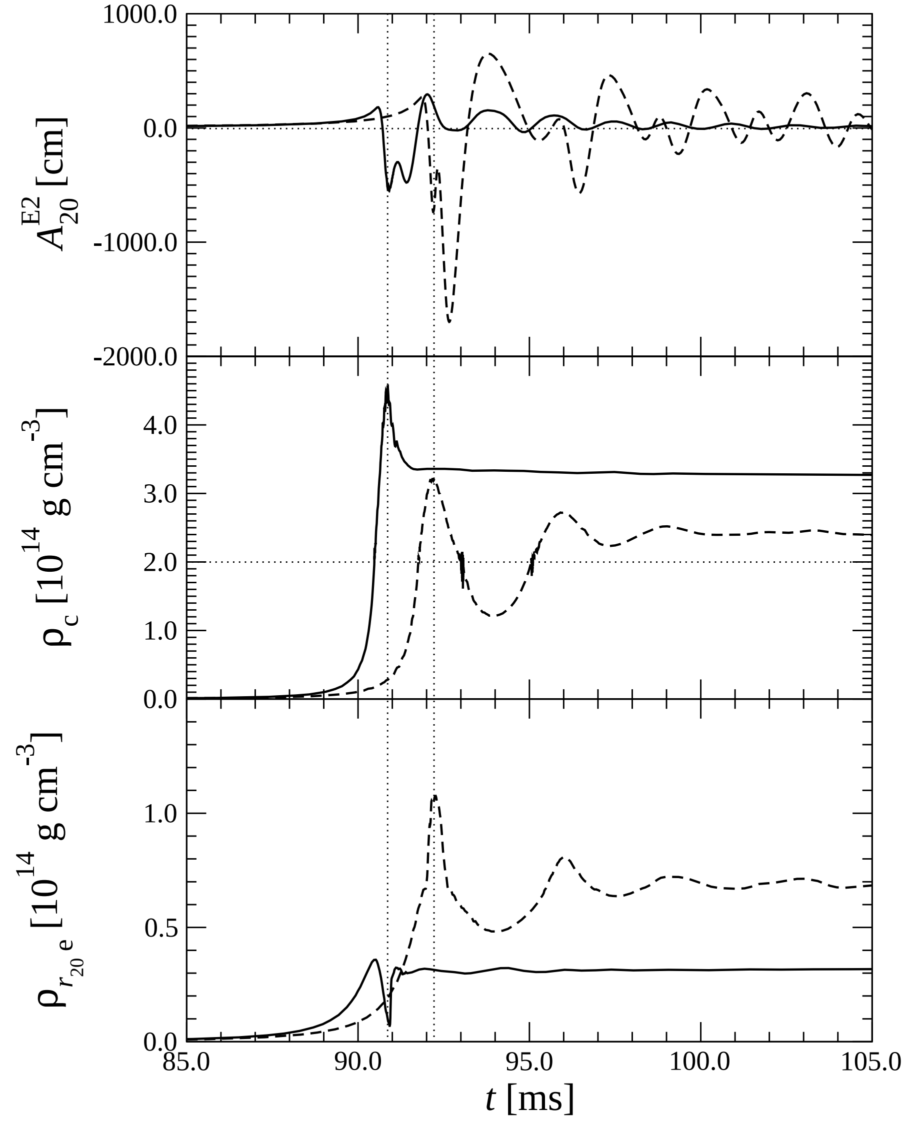

Figure 7.20: *Effects of a coherent motion of the inner core on the gravitational wave signal in the relativistic (solid lines) and Newtonian (dashed lines) simulation of model* A1B1G1*: In the upper panel the evolution of the gravitational wave amplitude* A_{20}^{E2} *is plotted. The middle and lower panel show the evolution of the central density* ρ_{c} *and the equatorial density* $\rho_{r_{20}\,\mathrm{e}}$ *evaluated at a radius* $r_{20} = 13.0$ km*. Contrary to the simulation with relativistic gravity, the inner core oscillates coherently with a large amplitude in Newtonian gravity, which causes a much larger gravitational wave signal. The vertical dotted lines indicate the time of bounce, and the horizontal dotted line in the density plot marks nuclear matter density.*

7.7 Rapidly and Highly Differentially Rotating Models

If initial models which have high rotational energy (i.e. large β), and whose rotation law is very differential (i.e. small A), collapse on a short timescale due to a low adiabatic exponent γ_1, the inner region of the core spins up considerably due to angular momentum conservation. The increasing centrifugal forces usually stop the collapse before nuclear matter density is reached (or at low supranuclear densities), as in ordinary type II multiple bounce models. However, contrary to these models, which have been discussed in Section 7.5, the central density exhibits only a single bounce. After this bounce, the core settles down to a new equilibrium state, often at very low subnuclear central density. However, an investigation of the time evolution of the maximum density in the core ρ_{max} reveals an interesting phenomenon which characterizes these collapse models: The maximum density does not coincide with the central density anymore but instead may exceed the latter by up to 2 orders of magnitude, as shown for the extremely rapidly and highly differentially rotating model A4B5G5 in Figure 7.21[k].

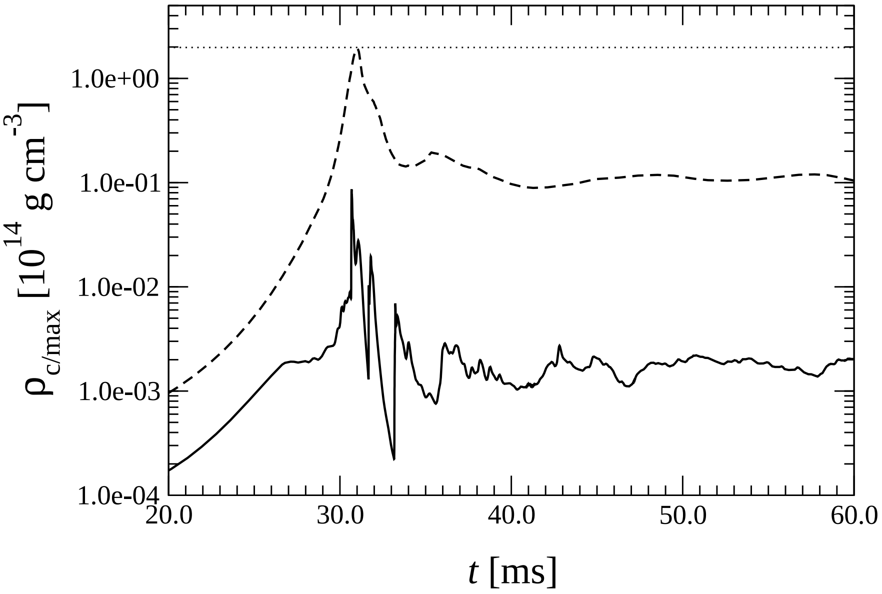

Figure 7.21: *Evolution of the central density (solid line) and the maximum density (dashed line) for the extremely rapidly and highly differentially rotating model* A4B5G5*: The central density* ρ_{c} *is much lower than the (off-center) maximum density* ρ_{max} *at all times (after the bounce by almost 2 orders of magnitude). The horizontal dotted line marks nuclear matter density, which is almost reached but never exceeded by* ρ_{max}.

This means that the maximum density is reached off-center, and (due to symmetry conditions) the shape of the density distribution in the core is torus-like. Some initial models (e.g. models A4B4 and A4B5) already have a torus-like structure. When these models collapse, the torus shape of their density distribution, which can be measured by the ratio $a_{\mathrm{torus}} = \rho_{\mathrm{max}}/\rho_{\mathrm{c}} > 1$, will be significantly enhanced during the evolution. Other rapidly and

---

[k] Similar to the behavior of the central density, the maximum density also exhibits one bounce and then levels off to a constant value after some ring-down phase. In other models, several subsequent oscillation peaks with decreasing amplitude can be observed in the maximum density, like for the central density of a transition type I/II model.

highly differentially rotating initial models like A3B5, A4B1 and A4B2 have a regular oblate structure with $\rho_{\mathrm{max}}/\rho_{\mathrm{c}} = 1$. For particular values of the parameter γ_1, they will develop a toroidal density shape during the infall phase. The density profiles along the equator and the pole for such a model (A4B2G3) are plotted in Figure 7.22. As the core contracts (upper panel), the equatorial density profile starts to become non-monotonous, while the polar profile remains monotonous. At the time of bounce (middle panel), a_{torus} is already significantly larger than 1, and at late evolution times (lower panel) the maximum density is about twice the central density. If the model initially rotates extremely rapidly and highly differentially, the torus structure can be very pronounced, and a_{torus} can assume high values during the collapse. In model A4B5G5 (see Figure 7.23) most of the core's mass is concentrated off-center, where the density is almost 2 orders of magnitude higher than the central density during bounce (middle panel) and after bounce (lower panel), as the already initially toroidal shape gets strongly enhanced during the infall phase (upper panel). The influence of the rotation rate and profile on the development of a torus-like density structure is summarized in the sequence of two-dimensional density plots in Figure 7.24.

For a rapidly and highly differentially rotating core it can be misleading to infer the importance of relativistic effects from the central density alone. For example, in model A4B5G5 the central density is always less than 5% of nuclear matter density, whereas the maximum density is close to nuclear matter density, which results in non-negligible relativistic corrections. The effects of relativistic gravity on the density distribution of the core are demonstrated in Figure 7.25. About 3 ms before bounce, the central parts of the core have a significantly higher average density in relativistic gravity (upper panel). Again, as the relativistic density configuration is more compact, the Newtonian model has a higher density in the outer regions of the core. After bounce and the subsequent ring-down phase, the maximum density in the simulation with relativistic gravity actually falls below the maximum density in the Newtonian simulation. The relativistic gravitational potential concentrates more mass in the central parts of the core, and thereby depletes the torus of mass, which results in a lower average a_{torus}. The Newtonian configuration possesses a lower central density, but a higher maximum density. This effect only occurs in rapidly and highly differentially rotating models. In all other models the maximum density (which in these cases is identical with the central density) is higher in relativistic gravity at all times (see Section 7.3). However, the effect that more mass is concentrated near the center by the deeper relativistic gravitational potential, can also be observed in many models with less rapid and less differential rotation. An example is the regular collapse model A3B3G5, whose core develops a torus-like density structure in Newtonian gravity, but has a regular spheroidal oblate density structure in relativistic gravity (see Figure 7.26).

The implications of these effects of relativistic gravity on the gravitational wave signal are obvious. Above all, both relativistic and Newtonian simulations of rapidly and highly differentially rotating models will have signals with a very high amplitude, as the quadrupole moment of a toroidal density structure is large compared to an oblate density shape. This is confirmed by the high maximum amplitudes of such models as listed in Tables 7.4–7.6. However, due to the lower average and maximum density in the torus, the relativistic models are characterized by gravitational wave signal amplitudes that are lower than the corresponding Newtonian ones. As an example, the signal amplitude for model A4B5G5 is plotted in the upper panel Figure 7.27. In Newtonian gravity the torus has a higher bounce density and rings down to its new equilibrium state with large amplitude oscillations after the bounce (see the evolution plot

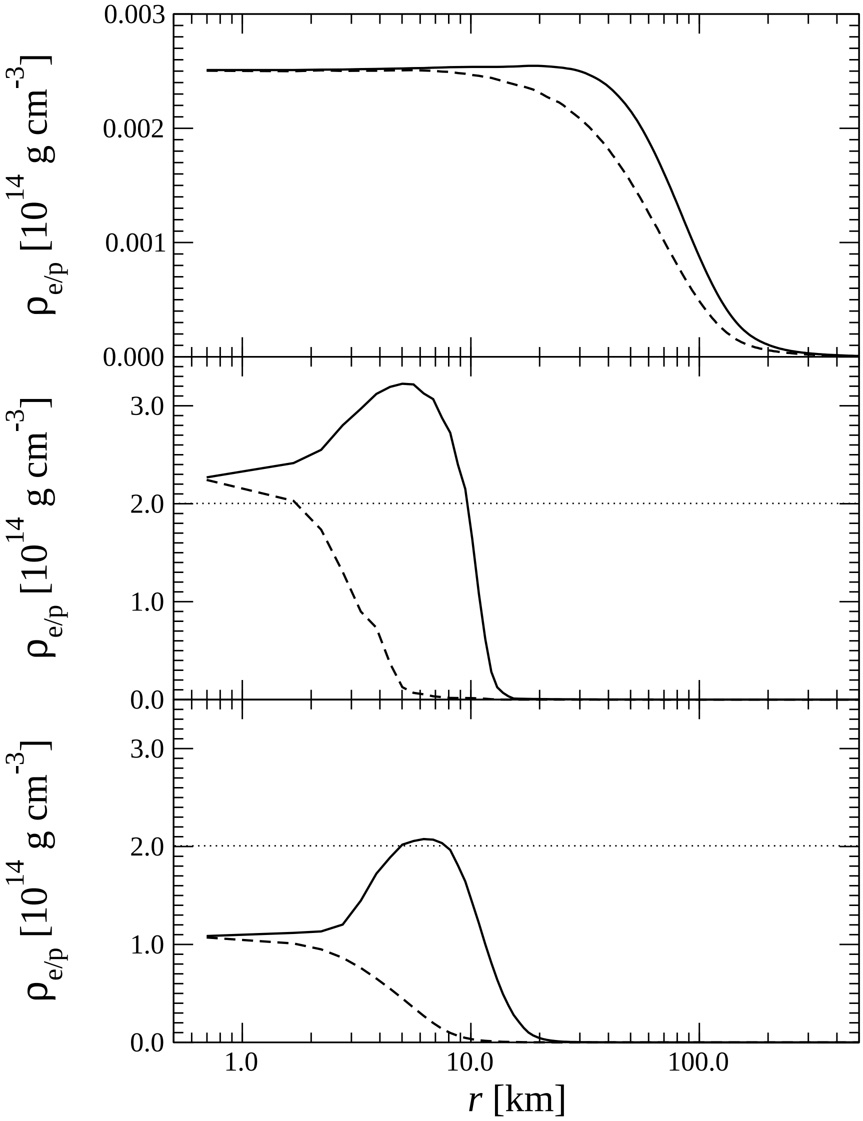

Figure 7.22: *Evolution of the equatorial (solid lines) and polar (dashed lines) density profiles for the rapidly and highly differentially rotating model* A4B2G3*: The equatorial and polar density profiles* ρ_e *and* ρ_p *are plotted before bounce at* $t = 40.0$ ms *(upper panel), during bounce at* $t = 48.75$ ms *(middle panel), and after the ring-down of the inner core at* $t = 80.0$ ms *(lower panel). The initial model already has a toroidal configuration with an off-center maximum density* $\rho_{\mathrm{e\,max}} > \rho_\mathrm{c}$*; this torus-like shape becomes more pronounced during the collapse. The horizontal dotted line marks nuclear matter density.*

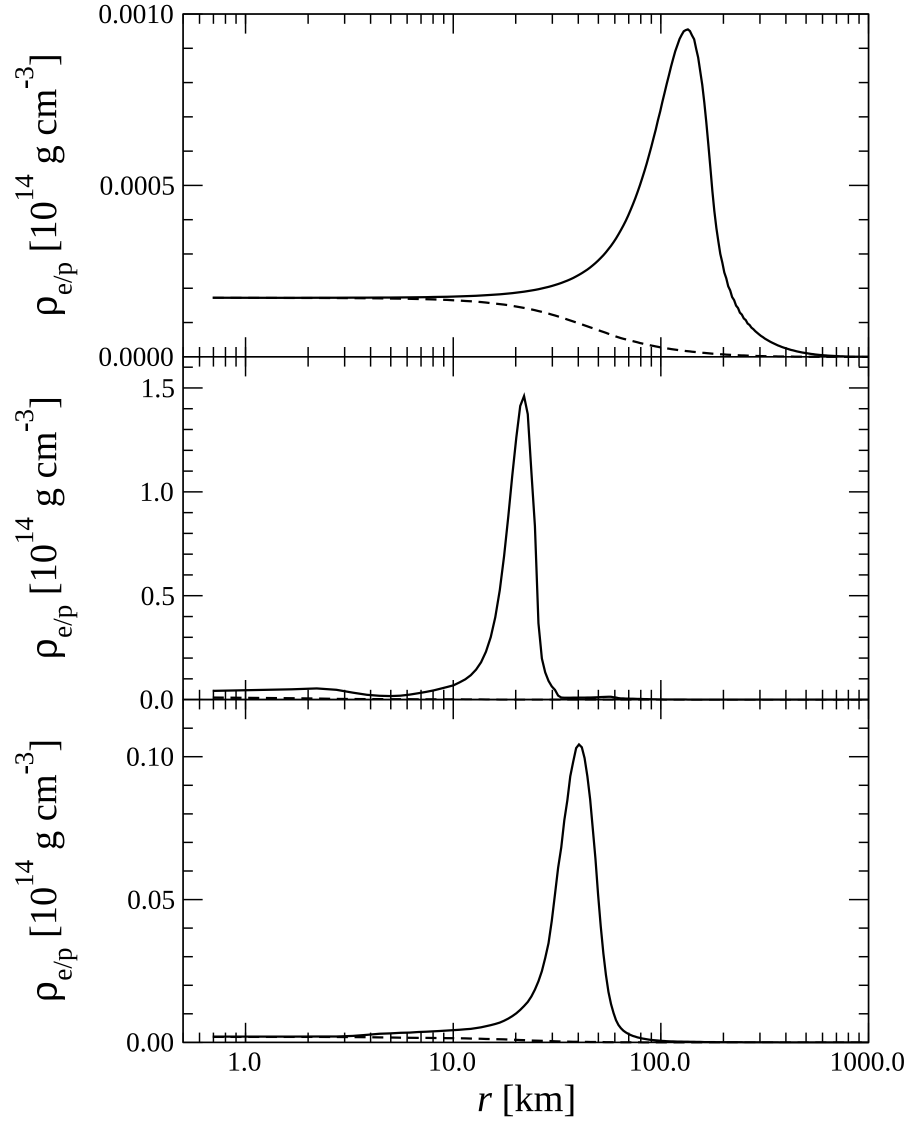

Figure 7.23: *Evolution of the equatorial (solid lines) and polar (dashed lines) density profiles for the extremely rapidly and highly differentially rotating model* A4B5G5*: The equatorial and polar density profiles* ρ_e *and* ρ_p *are plotted before bounce at* $t = 20.0$ ms *(upper panel), during bounce at* $t = 30.75$ ms *(middle panel), and after the ring-down of the inner core at* $t = 60.0$ ms *(lower panel). Already the initial model has a strongly toroidal configuration with an off-center maximum density* $\rho_{\mathrm{e\,max}} \gg \rho_\mathrm{c}$*; this torus-like shape becomes very pronounced during the collapse. The density in all parts of the core is below nuclear matter density throughout the evolution.*

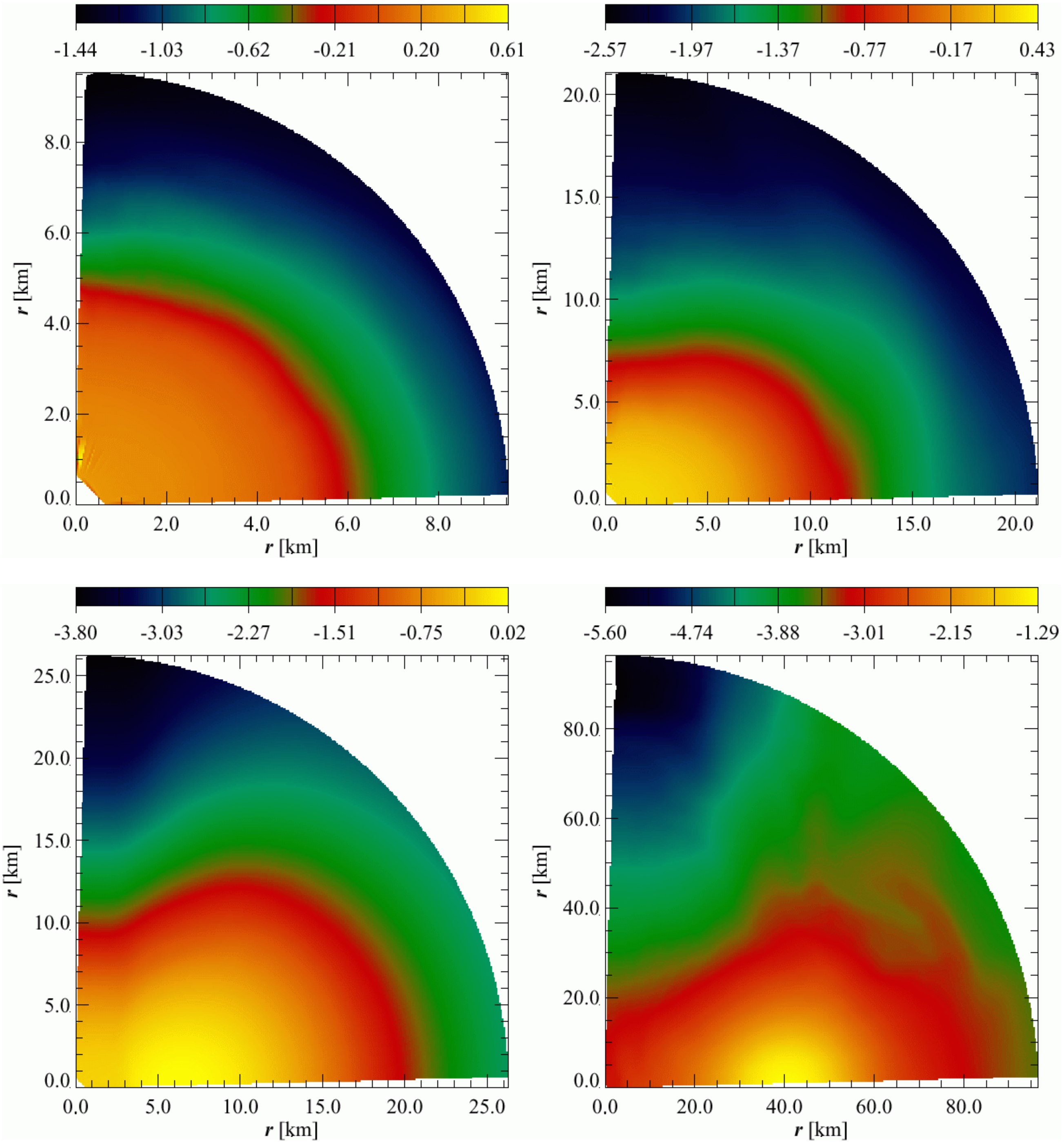

Figure 7.24: *Development of a toroidal density structure with increasing rate and differentiality of rotation: Model* A1B3G5 *(upper left panel) rotates slowly and retains an almost spherical structure; the more rapidly rotating models* A3B2G4$_{\mathrm{soft}}$ *(upper right panel) and* A4B2G3N3 *(lower left panel) develop a visible toroidal density distribution; this influence of centrifugal forces is enhanced by the slower contraction of the core due to the slightly higher* γ_1. *Model* A4B5G5 *(lower right panel) rotates extremely rapidly and differentially and exhibits a remarkable toroidal density structure with a clearly off-center maximum density. The color coding of the plots shows* $\log(\rho\,[10^{14}\ \mathrm{g\ cm^{-3}}])$, *evaluated after the ring-down phase. Note that the radius of the plotted region and the density color coding have different scales in the various plots.*

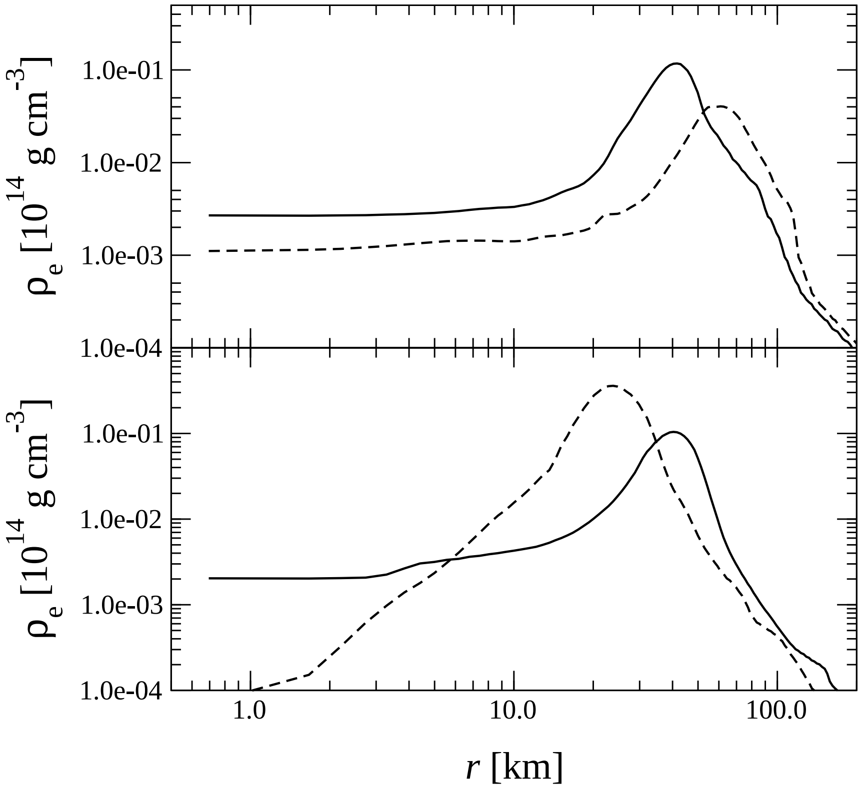

Figure 7.25: *Evolution of the equatorial density profiles in the relativistic (solid lines) and Newtonian (dashed lines) simulation of the extremely rapidly and highly differentially rotating model* A4B5G5*: The equatorial density profile* ρ_e *is plotted shortly before bounce at* $t = 28.0$ ms *(upper panel), and after the ring-down of the inner core at* $t = 60.0$ ms *(lower panel). At both times (and during the entire collapse) the central density is significantly higher in the simulation with relativistic gravity. At larger radii, the Newtonian configuration has a higher density, and even has a higher maximum density at late times (see lower panel). In both the relativistic and Newtonian simulation the density distribution has the shape of a torus.*

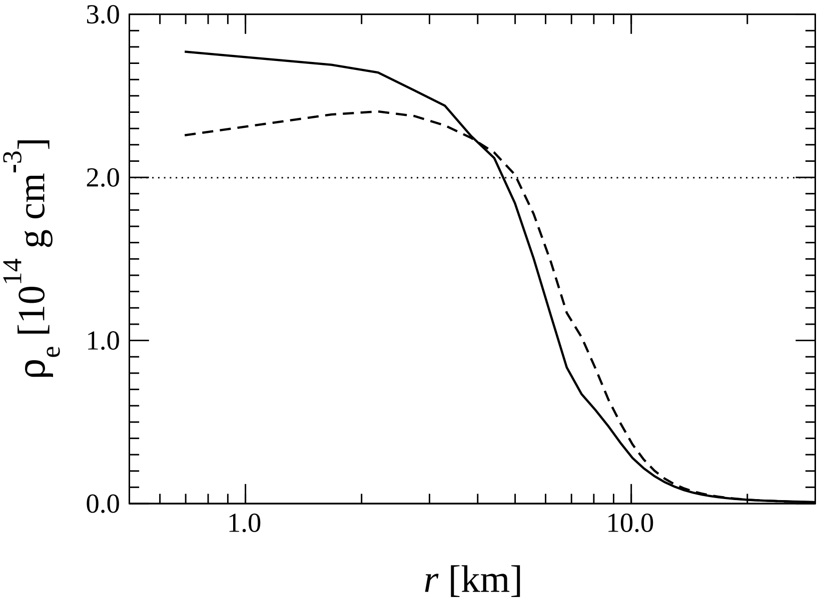

Figure 7.26: *Equatorial density profiles in the relativistic (solid lines) and Newtonian (dashed lines) simulation of the moderately rapidly rotating model* A3B3G5*: While for relativistic gravity the core has a regular oblate density structure, the less deep Newtonian gravitational potential leads to the development of a toroidal density configuration. The horizontal dotted line marks nuclear matter density.*

of the maximum density in the lower panel of Figure 7.27). Thus, the wave signal has a higher (negative) first peak which is followed by the typical ring-down signal. The relativistic configuration has a lower maximum density in the torus and does not oscillate strongly after bounce, which results in a smaller wave signal with hardly any trace of a ring-down. The behavior of the mass shells in the very center is completely irrelevant to the wave signal, as the density there is extremely low compared to the maximum density (middle panel). As demonstrated here for model A4B5G5, in rapidly and highly differentially rotating core collapse relativistic effects again lead to important differences both in the structure of the core and in the gravitational wave signal.

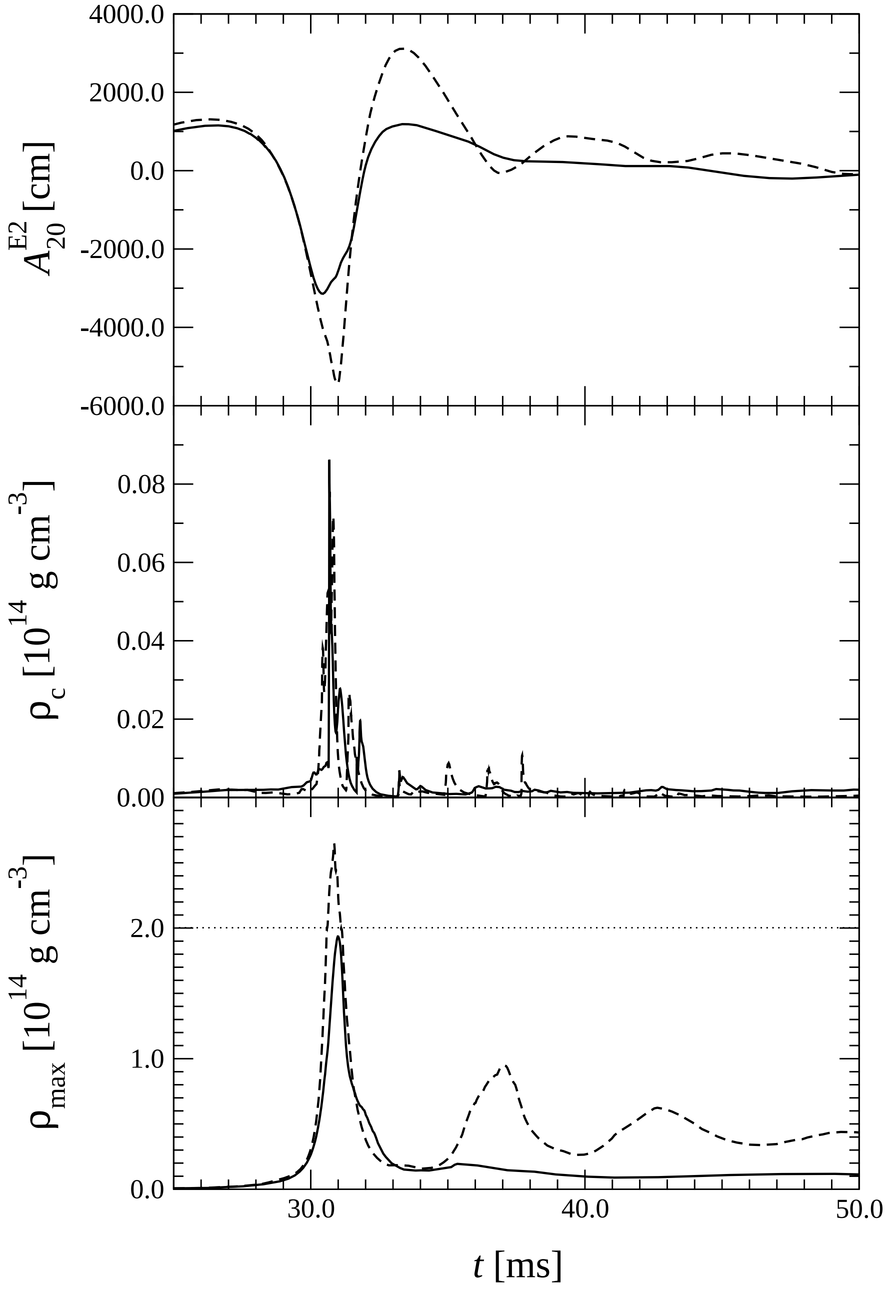

Figure 7.27: *Evolution of the gravitational wave signal amplitude and the maximum density in the relativistic (solid lines) and Newtonian (dashed lines) simulation of the extremely rapidly and highly differentially rotating model* A4B5G5*: The signal amplitude* A^{E2}_{20} *(upper panel) is larger in the Newtonian case, although the central densities (middle panel) are comparable throughout the evolution. However, the (off-center) maximum density* ρ_{max} *(lower panel) of the relativistic and Newtonian model is more than 20 times higher than the central density during bounce. Except at the beginning of the infall phase, and right after the first bounce, the maximum density* ρ_{max} *is lower in the relativistic simulation than the one in the Newtonian simulation, leading to a larger wave signal. The relativistic density enhancement can also be recognized in Figure 7.25. At late evolution times, the Newtonian density is higher by a factor 5. Note that* ρ_{max} *reaches supranuclear densities in the Newtonian case which leads to multiple bounces not present in the relativistic case. The horizontal line marks nuclear matter density.*

7.8 Gravitational Wave Energy Emission and Spectra

While the core collapse dynamics in the center of a supernova is not directly observable, gravitational waves, if detected by e.g. a gravitational wave interferometer, provide an observational means to obtain information about the collapse type. As the gravitational wave signal strengths of even galactic supernova events just fall into the sensitivity range of the detectors currently under construction, and as the sensitivity curve is strongly frequency dependent, it is essential to have detailed knowledge about the expected signal frequencies from rotational core collapse simulations. Even if the signal frequencies are in the frequency range of the detector, powerful filtering techniques have be to applied in the data analysis of the detector output to obtain a reasonable signal-to-noise ratio [99]. Thus, another important goal of numerical simulations of supernova core collapse is to provide observers with templates of the signal waveform from typical collapse events. The filters employed in data analysis strongly depend on the frequency spectrum of these wave templates. Contrary to gravitational waves emitted e.g. by the inspiral of binary black holes or neutron stars, signals from a core collapse supernova are not as “clean”, i.e. monochromatic in frequency. These signals depend on a broad variety of parameters like the rotation rate and profile of the initial model, the EoS during the collapse, and as seen in the previous sections, on general relativistic corrections. Whereas relativistic effects may not play a crucial role in the supernova explosion mechanism, they nevertheless influence the gravitational radiation waveform.

A detailed discussion of the spectra of gravitational waves emitted during rotational core collapse, and their dependence on the collapse type and dynamics can be found in the work of Zwerger [146]. We briefly recapitulate the important quantities, and otherwise refer to this work. The differential energy radiated away by gravitational waves during the collapse is given by

$$\frac{E_{\mathrm{rad}}}{dt} = \frac{1}{32\pi} \left| \frac{dA_{20}^{\mathrm{E2}}}{dt} \right|^2 , \tag{7.9}$$

and the total radiated energy in a collapse event is

$$E_{\mathrm{rad\,tot}} = \frac{1}{32\pi} \int_{-\infty}^{\infty} \left| \frac{dA_{20}^{\mathrm{E2}}}{dt} \right|^2 dt. \tag{7.10}$$

By replacing the gravitational wave amplitude in the time domain $A_{20}^{\mathrm{E2}}(t)$ by its Fourier transform in the frequency domain $\hat{A}_{20}^{\mathrm{E2}}(\nu)$, the total radiated energy $E_{\mathrm{rad\,tot}}$ can be expressed as a frequency integral (here limited to positive frequencies):

$$E_{\mathrm{rad\,tot}} = \frac{1}{16\pi} \int_{0}^{\infty} \nu^2 \left| \hat{A}_{20}^{\mathrm{E2}} \right|^2 d\nu. \tag{7.11}$$

The spectral energy distribution, i.e. the differential energy in the frequency domain, is then

$$\frac{dE_{\mathrm{rad}}}{d\nu} = \frac{1}{16\pi} \nu^2 \left| \hat{A}_{20}^{\mathrm{E2}} \right|^2 . \tag{7.12}$$

The squared absolute value of the Fourier transform of the signal amplitude is called power spectrum:

$$\mathcal{P} = \left| \hat{A}_{20}^{\mathrm{E2}} \right|^2 . \tag{7.13}$$

A good measure for the dominant frequency in the wave signal is the frequency ν_{max}, where the energy spectrum $dE_{\mathrm{rad}}/d\nu$ has its maximum[l].

In Table 7.10 we summarize the results for the radiated energy and the predominant frequency in a comparison between the relativistic and the Newtonian simulations for all 26 collapse models. As discussed in Section 7.3 the average and maximum central densities are higher in relativistic gravity compared to Newtonian simulations. This increases the oscillations frequencies of the inner core during the ring-down phase in a regular collapse situation, and also decreases the time interval between consecutive bounces in multiple bounce models. Therefore, the most obvious effect of general relativity is a significant shift of the gravitational wave frequency spectrum to higher frequencies. Only four models have a higher frequency in Newtonian gravity, and these exceptions can be attributed to a broad global maximum of the energy spectrum with many local peaks; an approximation of the global maximum by a smooth function again yields higher average frequencies for relativistic runs. In the other models, the frequency shift can be as large as a factor 3. These are obviously the models where the deeper relativistic gravitational potential changes a multiple bounce collapse to a regular collapse. The energy spectrum for such a model is plotted in the lower panel of Figure 7.28[m]. While the shapes of the energy spectra are similar for both the relativistic and the Newtonian simulation in cases where the collapse type does not change due to relativistic effects (upper and middle panel), model A3B3G1 clearly has an energy spectrum associated to a multiple bounce in Newtonian gravity, and one typical for a regular collapse in relativistic gravity.

By integrating the spectral energy distribution (7.12) over all frequencies, one can calculate the total energy radiated by the system in form of gravitational waves, as given in Equation (7.11). In a numerical code, however, this method is unfavorable, as high frequency noise contributes significantly to $E_{\mathrm{rad\,tot}}$. It is usually not possible to unambiguously define a cutoff frequency, as E_{rad} does not decline sharply at some specific frequency. Applying a filter (like the Welch filter used for the plots in Figure 7.28) is no remedy either, as it attenuates the energy spectrum and therefore (in some cases grossly) underestimates $E_{\mathrm{rad\,tot}}$. Owing to these problems, in Table 7.10 we use formulation (7.10) to calculate the total radiated energy. Due to the second time derivative in the integrand, and the resulting sensitivity to numerical resolution, however, this method can also only be regarded as an estimate for the actual gravitational wave energy emitted during the core collapse. We therefore refrain from a detailed discussion on this quantity and just comment briefly on the influences on relativistic dynamics on $E_{\mathrm{rad\,tot}}$: In cases, where a multiple bounce collapse exhibits the same behavior in general relativity, the associated gravitational wave energy emission increases due to higher average frequencies and signal amplitudes in the waveform. If a Newtonian multiple bounce model collapses regularly in relativistic gravity, $E_{\mathrm{rad\,tot}}$ also increases in most cases. However, in models which are of regular type I in both Newtonian and relativistic simulations, the on average lower signal amplitudes due to relativistic effects result in a decreased radiated energy, in spite of the higher frequencies of the gravitational waves in relativity. For a more elaborate discussion on the dependence of

---

[l] Note that the energy spectrum may exhibit two maxima of comparable height in distinct frequency regions.

[m] The spectra in this figure have been obtained by performing a fast-Fourier transformation (FFT) on the original gravitational signal which has been resampled to $2^{15} = 32768$ equidistant points. For smoothing out unphysical high frequency noise contributions in the spectrum, we have applied a Welch filter in the FFT. To compensate for the power losses due to the filtering, the energy spectrum has been rescaled by demanding that the total energies in the time domain and frequency domain are the same: $E^{t}_{\mathrm{rad\,tot}} = E^{\nu}_{\mathrm{rad\,tot}}$.

Model	$E_{\mathrm{rad\,tot}}$ $[M_\odot c^2]$	$\nu_{\max}$ [Hz]	$\dfrac{\nu^{\mathrm{R}}_{\max}}{\nu^{\mathrm{N}}_{\max}} - 1$ [%]	Model	$E_{\mathrm{rad\,tot}}$ $[M_\odot c^2]$	$\nu_{\max}$ [Hz]	$\dfrac{\nu^{\mathrm{R}}_{\max}}{\nu^{\mathrm{N}}_{\max}} - 1$ [%]
A1B1G1$^{\mathrm{R}}$	2.69×10^{-8}	564	+10	A3B3G2$^{\mathrm{R}}$	1.07×10^{-7}	385	+41
A1B1G1$^{\mathrm{N}}$	5.85×10^{-8}	515		A3B3G2$^{\mathrm{N}}$	9.25×10^{-9}	274	
A1B2G1$^{\mathrm{R}}$	6.90×10^{-8}	591	+33	A3B3G3$^{\mathrm{R}}$	5.42×10^{-8}	668	+84
A1B2G1$^{\mathrm{N}}$	6.44×10^{-8}	446		A3B3G3$^{\mathrm{N}}$	2.08×10^{-8}	363	
A1B3G1$^{\mathrm{R}}$	1.27×10^{-7}	612	+217	A3B3G5$^{\mathrm{R}}$	1.70×10^{-9}	1006	+4
A1B3G1$^{\mathrm{N}}$	1.83×10^{-8}	193		A3B3G5$^{\mathrm{N}}$	2.73×10^{-9}	964	
A1B3G2$^{\mathrm{R}}$	6.58×10^{-8}	646	+44	A3B4G2$^{\mathrm{R}}$	4.86×10^{-9}	84	−1
A1B3G2$^{\mathrm{N}}$	5.82×10^{-8}	448		A3B4G2$^{\mathrm{N}}$	1.52×10^{-9}	85	
A1B3G3$^{\mathrm{R}}$	1.43×10^{-8}	666	+16	A3B5G4$^{\mathrm{R}}$	1.54×10^{-9}	91	−19
A1B3G3$^{\mathrm{N}}$	2.54×10^{-8}	576		A3B5G4$^{\mathrm{N}}$	1.14×10^{-9}	113	
A1B3G5$^{\mathrm{R}}$	2.37×10^{-10}	896	+5	A4B1G1$^{\mathrm{R}}$	1.60×10^{-7}	1075	+85
A1B3G5$^{\mathrm{N}}$	3.81×10^{-10}	852		A4B1G1$^{\mathrm{N}}$	6.90×10^{-8}	580	
A2B4G1$^{\mathrm{R}}$	3.15×10^{-9}	82	+34	A4B1G2$^{\mathrm{R}}$	1.20×10^{-7}	1111	+17
A2B4G1$^{\mathrm{N}}$	5.87×10^{-10}	61		A4B1G2$^{\mathrm{N}}$	6.24×10^{-8}	946	
A3B1G1$^{\mathrm{R}}$	8.11×10^{-8}	651	+35	A4B2G2$^{\mathrm{R}}$	3.22×10^{-7}	752	+61
A3B1G1$^{\mathrm{N}}$	8.71×10^{-8}	482		A4B2G2$^{\mathrm{N}}$	4.08×10^{-8}	466	
A3B2G1$^{\mathrm{R}}$	2.03×10^{-7}	693	+52	A4B2G3$^{\mathrm{R}}$	1.53×10^{-7}	709	+92
A3B2G1$^{\mathrm{N}}$	2.28×10^{-8}	456		A4B2G3$^{\mathrm{N}}$	5.15×10^{-8}	370	
A3B2G2$^{\mathrm{R}}$	1.12×10^{-7}	727	+47	A4B4G4$^{\mathrm{R}}$	2.11×10^{-8}	305	+35
A3B2G2$^{\mathrm{N}}$	7.56×10^{-8}	494		A4B4G4$^{\mathrm{N}}$	1.58×10^{-8}	226	
A3B2G4$_{\mathrm{soft}^{\mathrm{R}}}$	1.19×10^{-8}	871	+15	A4B4G5$^{\mathrm{R}}$	2.47×10^{-8}	172	−21
A3B2G4$_{\mathrm{soft}^{\mathrm{N}}}$	1.92×10^{-8}	755		A4B4G5$^{\mathrm{N}}$	3.26×10^{-8}	217	
A3B2G4$^{\mathrm{R}}$	8.23×10^{-9}	812	+10	A4B5G4$^{\mathrm{R}}$	2.64×10^{-8}	79	+4
A3B2G4$^{\mathrm{N}}$	1.54×10^{-8}	737		A4B5G4$^{\mathrm{N}}$	2.75×10^{-8}	76	
A3B3G1$^{\mathrm{R}}$	1.12×10^{-7}	231	+25	A4B5G5$^{\mathrm{R}}$	6.25×10^{-8}	134	+16
A3B3G1$^{\mathrm{N}}$	3.75×10^{-9}	185		A4B5G5$^{\mathrm{N}}$	1.54×10^{-9}	159	

Table 7.10: *Summary of the gravitational wave energy and frequency for relativistic (R) and Newtonian (N) collapse models:* $E_{\mathrm{rad\,tot}}$ *is the total energy radiated in the form of gravitational waves,* $\nu_{\max}$ *is the frequency of maximum spectral energy* $dE_{\mathrm{rad}}/d\nu_{\max}$*, and* $\nu^{\mathrm{R}}_{\max}/\nu^{\mathrm{N}}_{\max} - 1$ *is the relative increase (+) or decrease (−) of* $\nu^{\mathrm{R}}_{\max}$ *compared to* $\nu^{\mathrm{N}}_{\max}$*. Note that in most models the relativistic effects increase the frequency where the spectral energy has its maximum.*

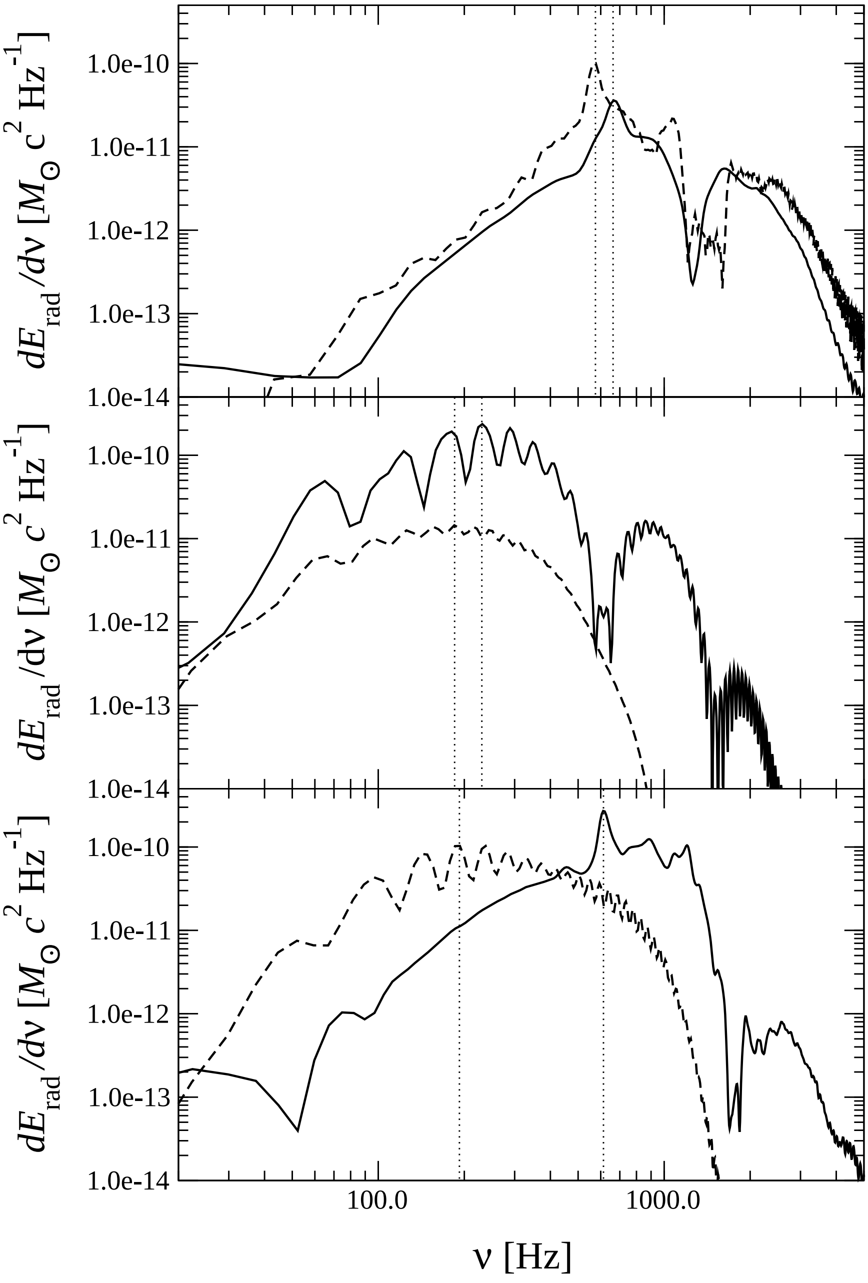

Figure 7.28: *Spectral energy distribution* $dE_{\rm rad}/d\nu$ *of the gravitational wave signal in the relativistic (solid lines) and Newtonian (dashed lines) simulation of model* A1B3G3 *(upper panel),* A3B3G1 *(middle panel), and* A1B3G1 *(lower panel): The energy spectrum of model* A1B3G3 *with a stronger low frequency part and a weaker high frequency part is typical for the signal of a regular collapse. Model* A3B3G1 *is of multiple bounce type in both Newtonian and relativistic gravity; in its energy spectrum a broad low frequency peak dominates. In model* A1B3G1 *relativistic effects change the collapse type from multiple bounce collapse to regular collapse; the shape of the signal waveform, and thus of the energy spectrum reflects this change of collapse type. The left (right) vertical dotted lines mark the maxima of the energy spectrum in Newtonian (relativistic) gravity; due to higher average central densities in relativistic gravity, the maximum of the energy spectrum is shifted to higher frequencies.*

the amount of radiated energy on the collapse parameters, we refer to the corresponding parts in the work of Zwerger [146].

The distribution of the dimensionless signal amplitude at a distance of $r = 10$ kpc from the source, i.e. the gravitational wave strain

$$h^{\rm TT} \equiv h^{\rm TT}_{\theta\theta}(\theta = \pi/2) = \frac{1}{8}\sqrt{\frac{15}{\pi}}\frac{A^{\rm E2}_{20}}{r} = 8.8524 \times 10^{-21} \left(\frac{A^{\rm E2}_{20}}{10^3\ \rm cm}\right)\left(\frac{10\ \rm kpc}{r}\right), \qquad (7.14)$$

is shown in Figure 7.29[n]. A comparison of this figure with Figure 8 in [147] proves that our sub-sample, encompassing 25 of the 78 models in the parameter study of Zwerger and Müller[o], is distributed well across both frequency and signal amplitude space. Within the wide range of the models between 0.4 and 3×10^{-20} in $h^{\rm TT}$ and 60 and 1000 Hz in ν, relativistic effects do not seem to have a significant impact on the shape of the distribution. Only in the high frequency branch, which consists of rapidly collapsing models with waveforms of type I and III, the weaker signal amplitudes (due to the stronger compactness of the inner core in a relativistic gravitational potential) cause a discernible change in the distribution of these models.

The influence of general relativity on the frequency distribution is more clearly identifiable, if only the models are selected which are of multiple bounce type in Newtonian gravity (see Figure 7.30). As explained in Section 7.5, of the 13 models which exhibit this behavior in Newtonian gravity (i.e. half of all models), only 4 models remain of type II in general relativity, namely models A2B4G1, A3B3G1, A3B3G2, and A3B4G2[p]. These models are labeled with *1a*, *1b*, *1c*, and *1d* in Figure 7.30, and their migration in the signal amplitude–frequency diagram is marked by arrows. With the exception of model A3B4G2, which is exceptional due to rapid and strong differential rotation, all models shift towards higher signal amplitudes and frequencies. If the collapse type changes from type II to type I or I/II as a result of relativistic corrections, the signal amplitude can either increase (as in the cases *2a* and *2b*), or decrease (as in the cases *3a* and *3b*). The type and degree of change depends very sensitively on the rotation state of the initial model and the value of γ_1. In these cases the frequency also increases, too. The trend of migration can be summarized by the arithmetic median of all 13 models in Newtonian and relativistic gravity:

$$\left.\begin{array}{l} \nu^{\rm N}_{\rm med} = 394\ \rm Hz \\ \nu^{\rm R}_{\rm med} = 588\ \rm Hz \end{array}\right\} + 49\%, \qquad \left.\begin{array}{l} h^{\rm TT\ N}_{\rm med} = 1.55 \times 10^{-20} \\ h^{\rm TT\ R}_{\rm med} = 1.50 \times 10^{-20} \end{array}\right\} - 3\%. \qquad (7.15)$$

While the increase or decrease of $h^{\rm TT}$ averages out itself, the average frequency is raised by about 50%.

This frequency shift may have important consequences for the prospects of detecting gravitational waves from core collapse supernovae. Again, if all 26 models are considered, the impact of relativistic effects on the distribution of the models relative to the sensitivity curve of the LIGO detector is only small (see upper panel in Figure 7.31). As in the case of Newtonian

---

[n] The error bars mark the frequency range inside which the spectral energy is higher than 50% of its peak value.

[o] We have simulated one additional model with a soft supranuclear EoS (model A3B2G4$_{\rm soft}$).

[p] Of these 4 models, model A3B3G2 is not a clear-cut case and can also be classified as a I/II transition type.

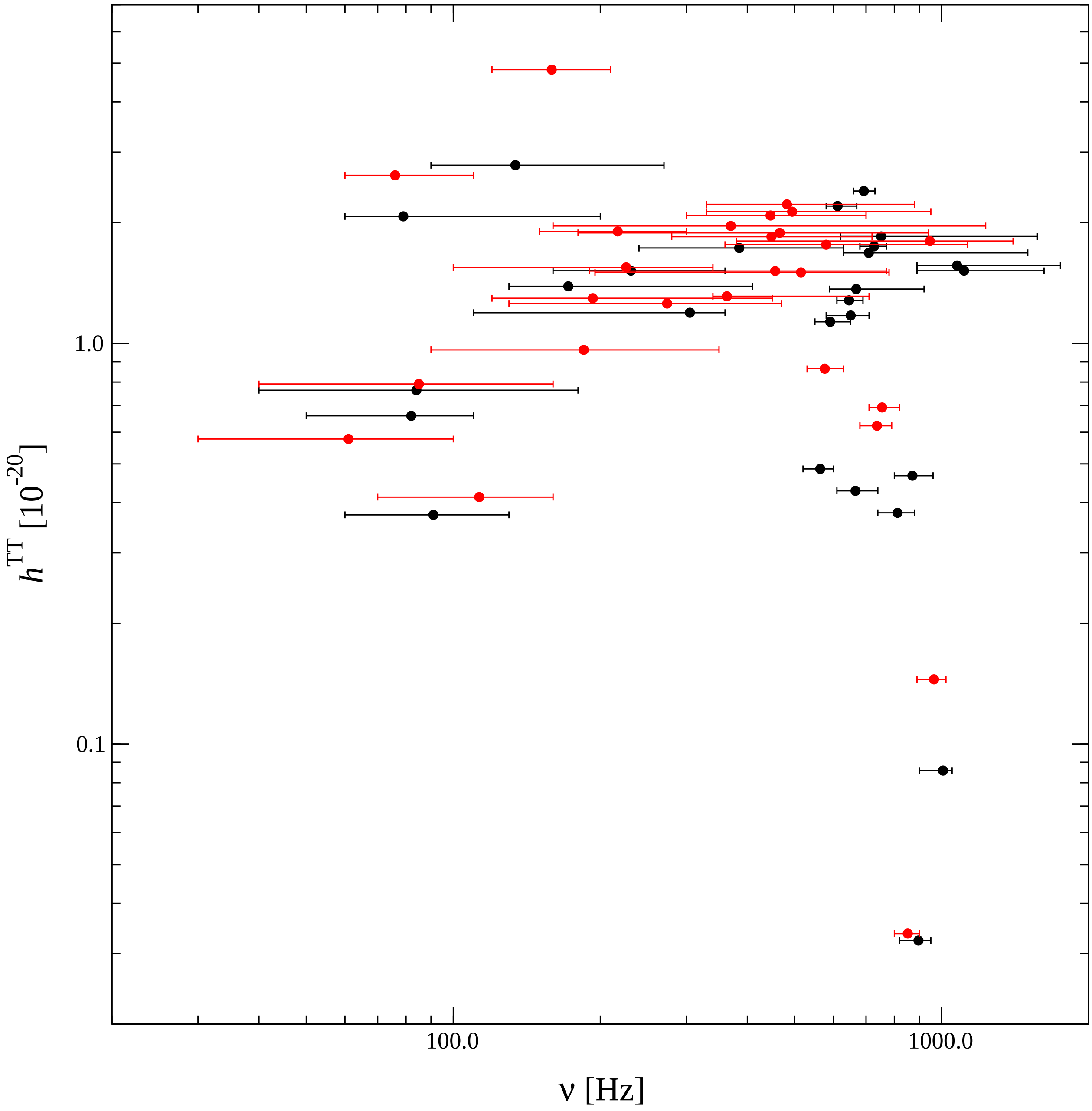

Figure 7.29: *Frequency distribution of the dimensionless signal amplitude* h^{TT} *for a source at* 10 kpc *in the relativistic (black circles) and Newtonian (red circles) simulation of all 26 models: Relativistic effects do not significantly change the global distribution of the signal amplitude in frequency space. The bulk of the models has signals with a strength of about* 0.4 *to* 3×10^{-20} *in a frequency range between* 60 *and* 1000 Hz*, with a high frequency branch of low amplitude signals.*

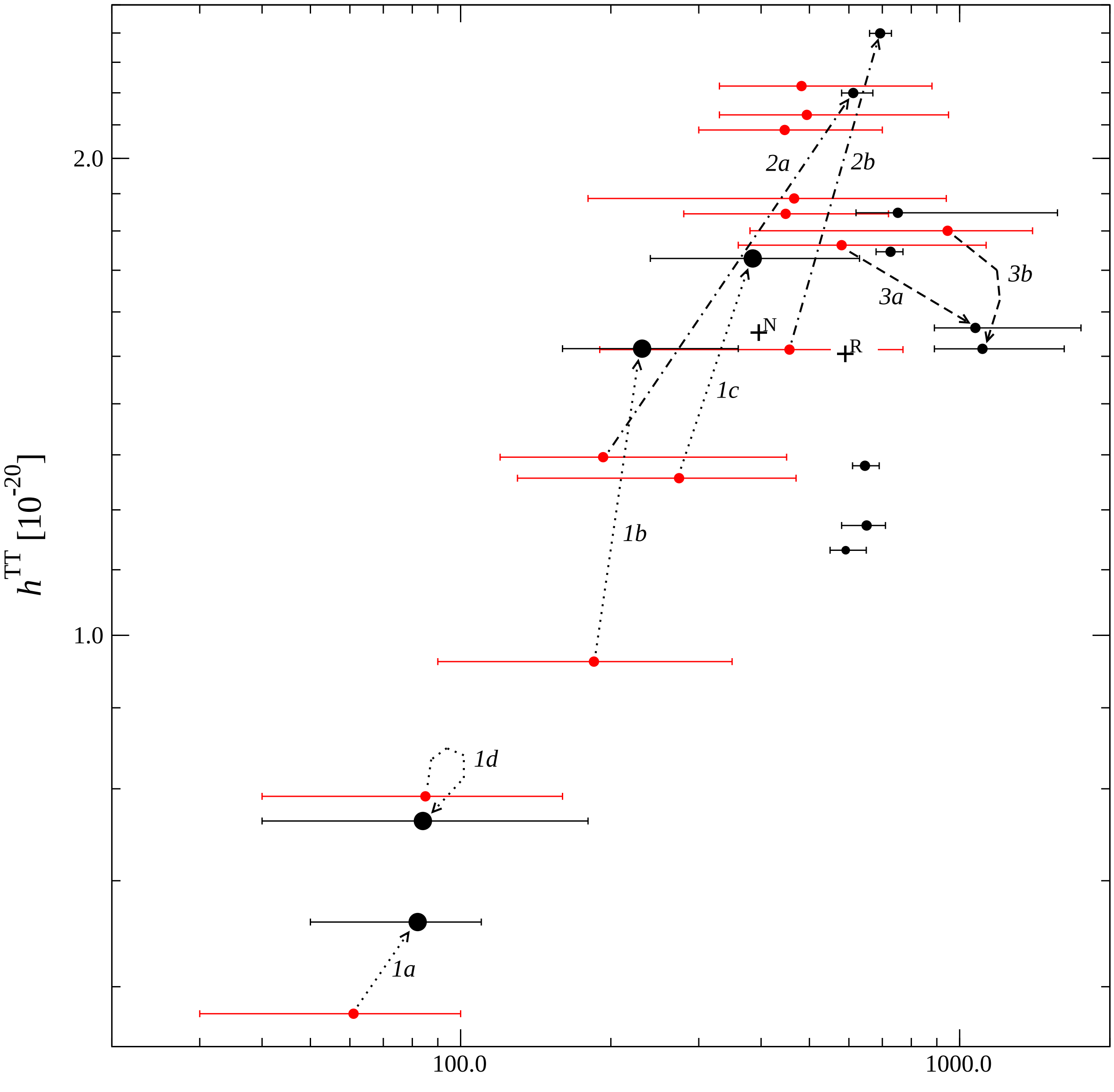

Figure 7.30: *Frequency and signal amplitude shift for the multiple bounce models in Newtonian gravity due to relativistic effects: The models labeled with 1 remain multiple bounce models in relativity; with the exception of model 1d, the amplitude and frequency of their signals increases. Labels 2 and 3 mark examples for models which show regular collapse behavior in relativistic gravity; the frequency of their signals increases, while the signal amplitude can increase (2) or decrease (3). The symbols* $+^{R}$ *and* $+^{N}$ *mark the arithmetic median of the signal amplitudes and frequencies of all models in Newtonian and relativistic gravity, respectively. The dimensionless signal amplitude* h^{TT} *is scaled to a distance of* 10 kpc.

simulations, the prospects to detect gravitational radiation emitted by the models in the high frequency branch are not very encouraging, because above several 100 Hz the sensitivity of the laser interferometer detectors drops rapidly. Still, the bulk of models falls into the range of high sensitivity both for the first and the advanced LIGO detector. A galactic supernova with core collapse dynamics according to one of our models would thus be definitely within the range of detection by first LIGO.

However, if nature should prefer multiple bounce scenarios in core collapse supernovae, the situation would change: Due to the coherent motion of the inner core, these models exhibit particularly strong signals, i.e. they are potentially easy to detect[q]. On the other hand, with increasing signal strength the associated frequencies also rise. Thus, in the signal amplitude–frequency diagram they are aligned parallel to the high frequency slope of the detector sensitivity curve. If the signal of a particular model is close to the detection threshold of a detector, as shown in the lower panel of Figure 7.31 for the 13 Newtonian multiple bounce models scaled to a distance to the source of 100 kpc[r], the influences of relativity can be twofold: In the "best case scenario", the core also bounces multiply in relativistic gravity, and the signal is shifted approximately parallel to the detector sensitivity curve to both higher frequencies and amplitudes (case *a*). However, on average the migration will be only to higher frequencies (along the direction of arrow *b*), according to Equation (7.15). Then in a borderline case the signal may leave the sensitivity window of the detector due to relativistic corrections.

The frequency shift is an effect common to all models, and cannot be compensated for by a possible increase in the signal amplitude. On the contrary, many relativistic models have weaker signal amplitudes due to their higher compactness and suppression of multiple bounces. Therefore, within the limits of our physical model of rotational core collapse, relativistic effects on average tend to decrease the prospects of detectability of gravitational radiation by interferometric detectors[s].

---

[q] Among the Newtonian models which initially have not too extreme rotation rates and profiles (i.e. A1–3, B1–3), the multiple bounce models have the largest average signal amplitudes.

[r] The scaling to a source distance of 100 kpc is arbitrary; it is intended for shifting the high-frequency part of sensitivity curve close to the signal strengths of the models.

[s] In the above discussion, we have restricted ourselves to comment on the detectability of gravitational wave from rotational core collapse by laser interferometer detectors. Resonant bar detectors can have comparable or even better sensitivities than interferometers. However, they are sensitive only in very narrow frequency bands. As the energy spectrum of a gravitational wave signal from a core collapse is comparatively broad (see Figure 7.28), laser interferometers are much better suited for the detection of such a signal.

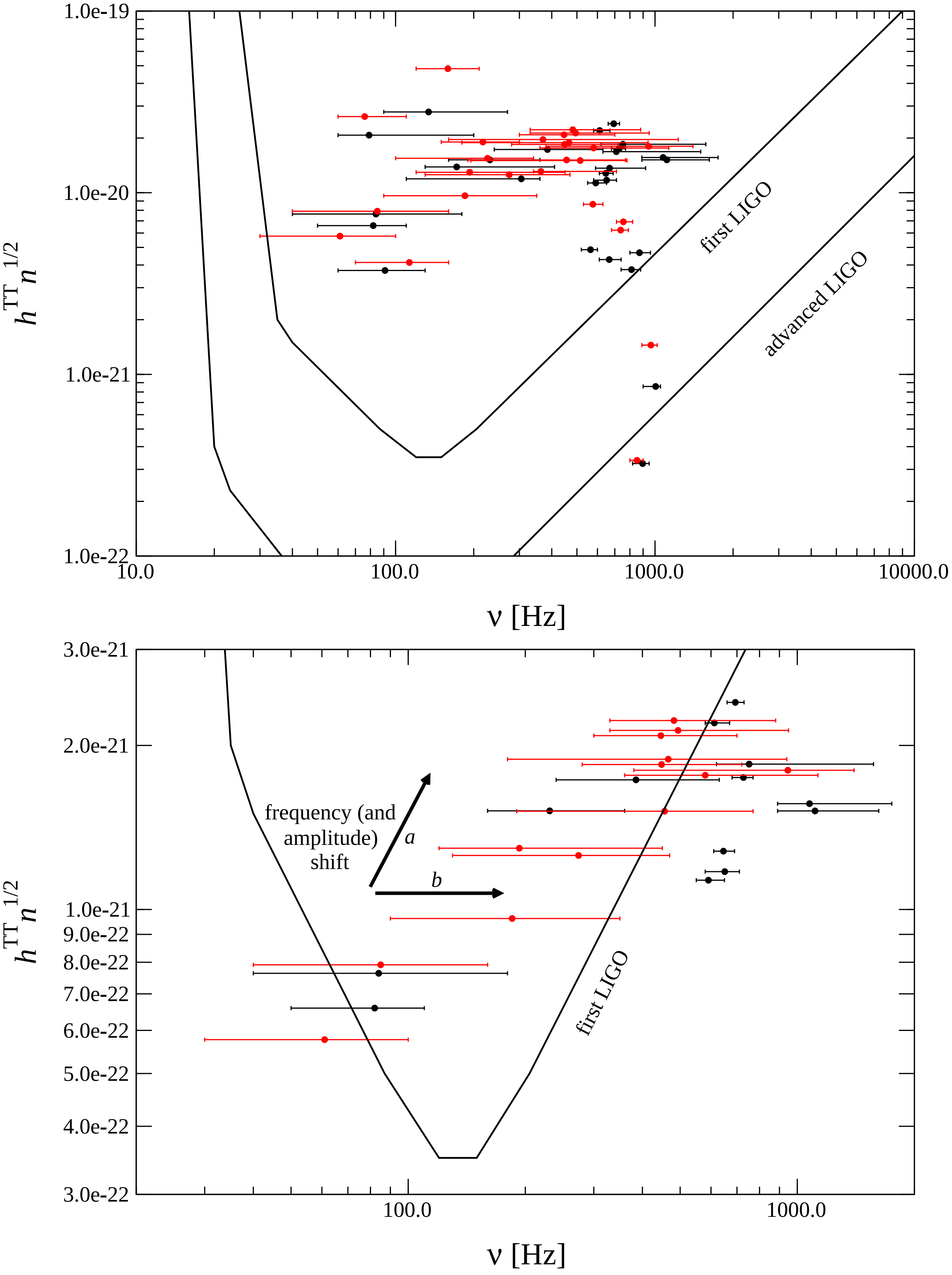

Figure 7.31: *Prospects of detection of the wave signal by LIGO: With the exception of some high frequency models, for a source at a distance of* 10 kpc *the signals of all models are within the sensitivity of the first LIGO detector (upper panel). The frequency (and possibly amplitude) shift in multiple bounce models may shift the signal out of the range of detectability (lower panel). In the lower panel* h^{TT} *is evaluated at* 100 kpc*;* n *is the signal-to-noise ratio.*

7.9 Evolution of the Rotation Rate

As the iron core contracts during the infall phase, angular momentum conservation results in a spinup, i.e. an increase of the average rotation velocity, particularly in the central regions of the inner core. For the rotation rate β, the ratio of rotational energy to potential (binding) energy, this translates into an increase which roughly scales like the inverse of the radius of the inner core [109]:

$$E_{\mathrm{rot}} \sim M \Omega^2 R^2 \sim \frac{J^2}{M R^2}, \qquad |E_{\mathrm{pot}}| \sim \frac{M^2}{R} \qquad \longrightarrow \qquad \beta = \frac{E_{\mathrm{rot}}}{|E_{\mathrm{pot}}|} \sim \frac{J^2}{M^3 R} \propto \frac{1}{R}, \tag{7.16}$$

where M, Ω, R, and J are the typical mass, angular velocity, radius, and angular momentum of the inner core. The exact quantitative behavior of the evolution of β during core collapse is important due to several reasons: Firstly, the rotation state of the inner core after bounce determines the rotation rate and profile of the neutron star which subsequently forms. It is known from observations of pulsars that neutron stars can spin with very high rotation frequencies of the order of milliseconds [73]; however, these millisecond pulsars seem to have gained their high rotation rates via mass transfer from a companion star, and so far there is no clear notion about the initial rotation state of a newborn neutron star.

Secondly, proto-neutron stars with a sufficiently high rotation rate may be subject to the development of triaxial instabilities, driven by various mechanisms [118]. In the case of uniformly rotating, constant density MacLaurin spheroids in Newtonian gravity, the threshold values for the development of instabilities on dynamic and secular timescales are $\beta_{\mathrm{sec}} \approx 13.8\%$ and $\beta_{\mathrm{dyn}} \approx 27.4\%$, respectively, the former one driven by gravitational radiation or viscosity, the latter one by hydrodynamics and gravity[t]. Due to relativistic effects these thresholds are significantly reduced for a variety of polytropic and realistic EoS. Additional to that, the higher average rotation velocities in relativistic simulations of rotational core collapse tend to increase the rotation rate β. Thus, we expect that the criteria for the development of triaxial instabilities during and after core bounce are fulfilled for more models and for longer time intervals compared to Newtonian gravity.

Before turning to the influence of relativistic gravity on the rotation rate, we investigate the qualitative change in the azimuthal velocity $v_\phi = \sqrt{v_3 v^3}$ during core collapse. The radial profiles of v_ϕ at the time of bounce t_{b} for three representative models are plotted in Figure 7.32. As in all other models, the impact of the deeper gravitational potential is obvious: Compared to Newtonian simulations, both the peak and average rotation velocities are higher, and the maximum of v_ϕ is shifted to smaller radii[u]. The differences are most prominent in the case of model A1B3G1 (lower panel), which changes from multiple bounce collapse to regular collapse due to relativistic effects. In relativistic simulations, the core is denser at bounce, and thus it exhibits higher rotation velocities at significantly smaller radii. In model A1B3G5 (upper

---

[t] For a core with an average density of ρ_{nuc} and a radius of about 20 km, the sound travel time through the core and thus the dynamic timescale is roughly 1 ms. As our code is axisymmetric, the growth of such instabilities cannot be simulated; however, the values obtained for β can serve as a criterion to predict the behavior of our models if axisymmetry is relaxed.

[u] Note that the maximum of v_ϕ is at the boundary of the proto-neutron star; the boundary is defined by a drop of the density over several orders of magnitude.

panel), the initially almost uniform rotation profile and the rapid contraction render centrifugal forces almost ineffective, irrespective of Newtonian or relativistic gravity. Therefore, the spinup is weak, and v_ϕ reaches a value of at most 0.08, which is small compared to collapse models with higher initial rotation rates and slower contraction. The highest peak values for v_ϕ were encountered in model A1B3G1, exceeding 0.2 at $r \approx 15$ km during core bounce. This corresponds to a rotation period of $T \approx 1.6$ ms at the boundary of inner core. Two-dimensional plots of the rotation velocity field are presented in Figure 7.33. These plots further illustrate the effects of relativistic gravity. The rotation velocity is on average higher and has its peak value closer to the center not only in the equatorial plane, but for all angular directions. The plots also show that the maximum rotation velocities can occur outside the equatorial plane.

As the rotation energy E_{rot} depends on the square of the rotation velocity (see Equation 6.12), the increase of the average rotation velocities in relativity has important consequences for the evolution of β. This is demonstrated for models A1B3G1, A4B2G3, and A4B5G4 in Figure 7.34: The rotation rate β assumes its maximum values at times of maximum central densities; if the core rebounds in a series of distinct multiple bounces, this is also reflected in multiple peaks of β. As expected, the rotation rate in the relativistic simulations surpasses the rotation rate in the corresponding Newtonian simulations, both in its maximum value and on average. Taking the thresholds β_{sec} and β_{dyn} as a basis for judging whether a model is prone to triaxial instabilities, relativistic effect do not make a difference in model A1B3G1, as $\beta > \beta_{\mathrm{sec}}$ holds only for less than 1 ms. This changes drastically in the already initially rapidly rotating model A4B2G3; here β remains above β_{sec} after core bounce in relativistic gravity and even reaches β_{dyn} for a short time, while in Newtonian gravity it again declines below β_{sec}. Considering the fact that relativistic effects also lower the actual threshold β_{sec}, this is an impressive example how Newtonian simulations yield incorrect predictions about the development of secular instabilities. In the extremely rapidly and differentially rotating model A4B5G4, secular instabilities are likely to develop in both Newtonian and relativistic gravity, but instabilities on a dynamic timescale can only appear in relativistic simulations, where $\beta > \beta_{\mathrm{dyn}}$ holds for almost 5 ms, i.e. several dynamic timescales.

In Tables 7.11–7.13 we list the maximum value for the rotation rate β_{max} and the time intervals where the thresholds for the development of triaxial instabilities are exceeded, for the relativistic and Newtonian simulation of all models. The results listed in these tables confirm the trend from Figure 7.34: Many models which would otherwise stay below β_{sec} fulfill this criterion due to relativistic corrections. In some of the models β stays virtually constant beyond core bounce until the simulation was terminated. A subset of these models even reaches rotation rates exceeding β_{dyn} for several milliseconds in relativistic gravity; the three models in Newtonian gravity for which $\beta > \beta_{\mathrm{dyn}}$ is achieved, stay in this regime at most 1 ms, which is probably too short for a significant growth of triaxial instabilities. In the above discussion, β is the ratio of total rotation mass energy to total potential mass energy, where the corresponding masses encompass the entire core. Strictly speaking, the criteria for instabilities are only valid for the rotation rate of the inner core which will finally form the neutron star. However, E_{rot} and E_{pot} can be only defined globally in an unambiguous way. Furthermore, due to the rapid decrease of density and rotation velocity at the outer boundary of the inner core, the inner core contributes most to the total rotation rate. This has also been observed in the Newtonian core collapse simulations by Zwerger [146]. Thus we can assume that $\beta_{\mathrm{inner\ core}} \approx \beta$.

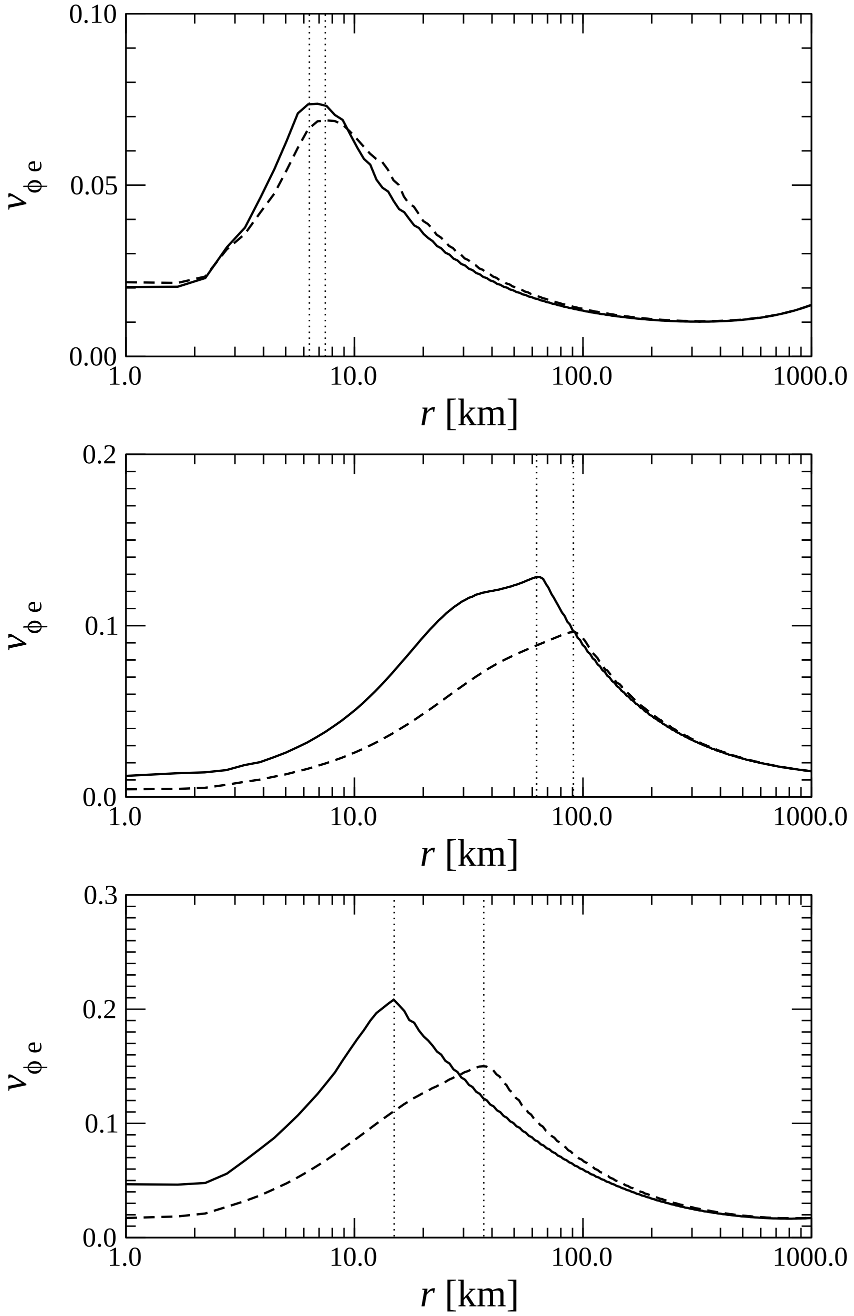

Figure 7.32: *Spinup of the core during the infall phase in the relativistic (solid lines) and Newtonian (dashed lines) simulation of model* A1B3G5 *(upper panel),* A2B4G1 *(middle panel), and* A1B3G1 *(lower panel): Due to angular momentum conservation during contraction, the rotation velocity* v_ϕ *increases considerably in the inner regions of the core. The rotation profiles of* $v_{\phi\,\mathrm{e}}$ *along the equatorial plane, here plotted shortly after* t_b*, exhibit higher maxima in relativistic gravity. The models* A1B3G5 *(rapid collapse) and* A2B4G1 *(multiple bounce) do not change collapse type in the relativistic simulation. The fast contraction in model* A1B3G5 *results in lower average rotation velocities. Relativistic effects cause model* A1B3G1 *to change from multiple bounce to regular collapse. The vertical dotted lines mark the radius of maximum rotation velocity.*

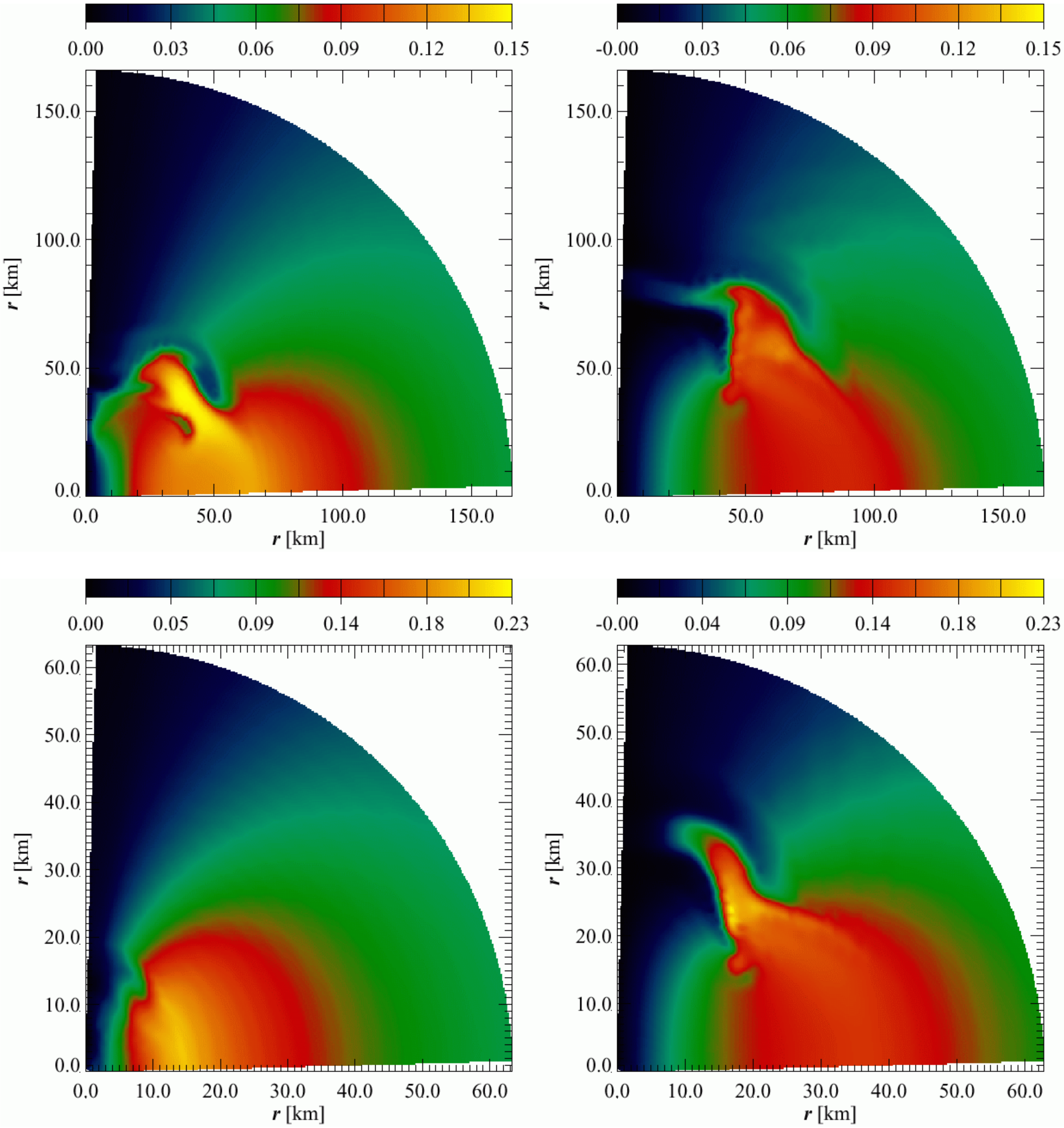

Figure 7.33: *Two-dimensional plots of the rotation velocity of the core at the time of bounce in the relativistic (left panels) and Newtonian (right panels) simulation of model* A2B4G1 *(upper panels) and* A1B3G1 *(lower panels): The increased compactness of the rotation velocity field in relativistic gravity is clearly visible; relativistic effects cause the maxima of the rotation velocity to be higher and significantly closer to the center in both the multiple bounce model* A2B4G1 *and the regular bounce model* A1B3G1*. The color coding of the plots shows the rotation velocity* $v_\phi = \sqrt{v_2 v^2}$*.*

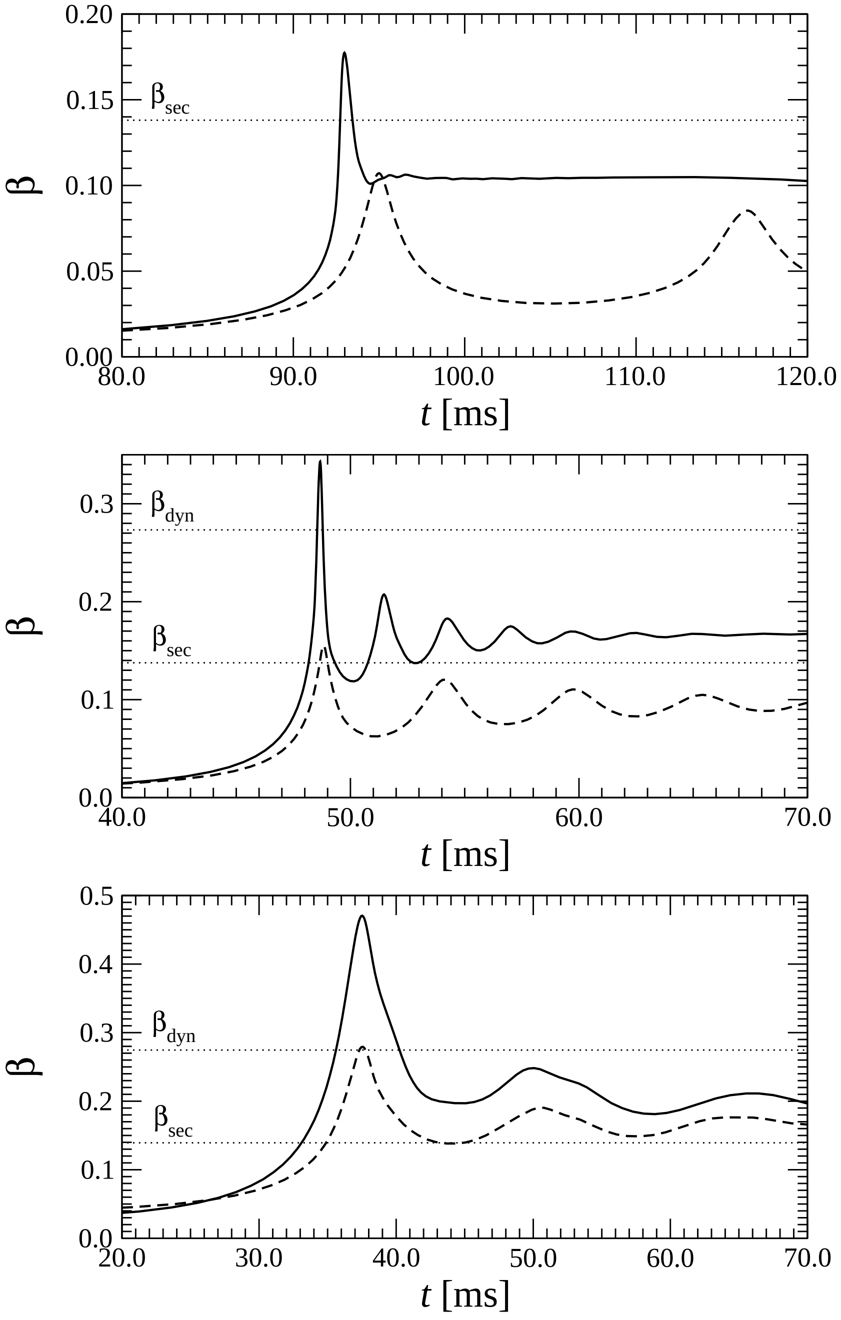

Figure 7.34: *Evolution of the rotation rate β in the relativistic (solid lines) and Newtonian (dashed lines) simulation of model* A1B3G1 *(upper panel),* A4B2G3 *(middle panel), and* A4B5G4 *(lower panel): In model* A1B3G1*, which changes from multiple bounce collapse in Newtonian gravity to regular collapse in relativistic gravity, only the relativistic simulation reaches β_{sec}. The core in the relativistic simulation of the rapidly and moderately differentially rotating model* A4B2G3 *crosses β_{dyn} for a short time, and stays permanently above β_{sec} after ring-down, while its rotation rate is higher than β_{sec} only for a short time in the Newtonian simulation. In the extremely rapidly and differentially rotating model* A4B5G4*, both the Newtonian and the relativistic simulation yield a permanent $\beta > \beta_{\mathrm{sec}}$ after ring-down. Only for relativistic gravity the rotation rate is higher than β_{dyn} for several dynamic time-scales. The horizontal dotted lines labeled β_{sec} and β_{dyn} mark the rotation rate thresholds for the growth of instabilities on secular and dynamic timescales, respectively.*

Model	β_{max} [%]	$t_{\beta_{\mathrm{max}}}$ [ms]	t_{b} [ms]	$t_{\beta>\beta_{\mathrm{sec}}}$ [ms]	$\Delta t_{\beta>\beta_{\mathrm{sec}}}$ [ms]	$t_{\beta>\beta_{\mathrm{dyn}}}$ [ms]	$\Delta t_{\beta>\beta_{\mathrm{dyn}}}$ [ms]	$\beta^{\mathrm{R}}_{\mathrm{max}}/\beta^{\mathrm{N}}_{\mathrm{max}} - 1$ [%]
A1B1G1$^{\mathrm{R}}$	7.7	90.86	90.87					+48
A1B1G1$^{\mathrm{N}}$	5.2	92.26	92.23					
A1B2G1$^{\mathrm{R}}$	12.2	91.60	91.56					+49
A1B2G1$^{\mathrm{N}}$	8.2	93.20	93.10					
A1B3G1$^{\mathrm{R}}$	17.7	92.98	92.85	92.73	0.72			+66
A1B3G1$^{\mathrm{N}}$	10.7	95.00	94.70					
A1B3G2$^{\mathrm{R}}$	15.6	69.20	69.10	69.05	0.38			+47
A1B3G2$^{\mathrm{N}}$	10.6	70.10	69.87					
A1B3G3$^{\mathrm{R}}$	12.7	48.47	48.45					+59
A1B3G3$^{\mathrm{N}}$	08.0	48.66	48.57					
A1B3G5$^{\mathrm{R}}$	05.4	30.14	30.10					+60
A1B3G5$^{\mathrm{N}}$	03.4	30.05	29.98					
A2B4G1$^{\mathrm{R}}$	17.6	98.96	99.09	96.94	4.59			+49
A2B4G1$^{\mathrm{N}}$	11.8	100.12	99.71					

Table 7.11: *Summary of the rotation rate for relativistic (R) and Newtonian (N)* A1 *and* A2 *models:* $\beta_{\mathrm{max}} \equiv \max \beta(t)$ *is the maximum rotation rate,* $t_{\beta_{\mathrm{max}}}$ *is the time of maximum rotation rate,* t_{b} *is the time of bounce,* $t_{\beta>\beta_{\mathrm{sec/dyn}}}$ *is the time when the rotation rate crosses the threshold for secular/dynamic instabilities,* $\Delta t_{\beta>\beta_{\mathrm{sec/dyn}}}$ *is the time interval during which the rotation rate exceeds the threshold for secular/dynamic instabilities, and* $\beta^{\mathrm{R}}_{\mathrm{max}}/\beta^{\mathrm{N}}_{\mathrm{max}} - 1$ *is the relative increase (+) or decrease (−) of* $\beta^{\mathrm{R}}_{\mathrm{max}}$ *compared to* $\beta^{\mathrm{N}}_{\mathrm{max}}$*. A + sign after the value for* $\Delta t_{\beta>\beta_{\mathrm{sec}}}$ *indicates that the rotation rate still exceeds the threshold for secular instabilities when the simulation was stopped.*

Model	β_{max} [%]	$t_{\beta_{\mathrm{max}}}$ [ms]	t_{b} [ms]	$t_{\beta>\beta_{\mathrm{sec}}}$ [ms]	$\Delta t_{\beta>\beta_{\mathrm{sec}}}$ [ms]	$t_{\beta>\beta_{\mathrm{dyn}}}$ [ms]	$\Delta t_{\beta>\beta_{\mathrm{dyn}}}$ [ms]	$\beta^{\mathrm{R}}_{\mathrm{max}}/\beta^{\mathrm{N}}_{\mathrm{max}} - 1$ [%]
A3B1G1$^{\mathrm{R}}$	13.5	91.31	91.27					+81
A3B1G1$^{\mathrm{N}}$	7.5	92.79	92.72					
A3B2G1$^{\mathrm{R}}$	21.4	92.54	92.42	92.26	0.83			+95
A3B2G1$^{\mathrm{N}}$	11.0	94.30	94.32					
A3B2G2$^{\mathrm{R}}$	19.7	69.27	69.15	69.03	0.71			+69
A3B2G2$^{\mathrm{N}}$	11.7	70.13	69.98					
A3B2G4$^{\mathrm{R}}_{\mathrm{soft}}$	16.3	39.20	39.18	39.09	0.32			+72
A3B2G4$^{\mathrm{N}}_{\mathrm{soft}}$	9.5	39.21	39.14					
A3B2G4$^{\mathrm{R}}$	15.1	39.17	39.14	39.08	0.22			+69
A3B2G4$^{\mathrm{N}}$	9.0	39.20	39.07					
A3B3G1$^{\mathrm{R}}$	23.9	95.31	95.26	94.20	2.37			+108
				111.10	2.79			
				125.61	2.92			
A3B3G1$^{\mathrm{N}}$	11.5	96.55	96.57					
A3B3G2$^{\mathrm{R}}$	26.7	70.94	70.96	70.12	2.03			+95
				77.54	2.80			
				84.69	3.48			
				91.69	4.28			
				98.45	10.62+			
A3B3G2$^{\mathrm{N}}$	13.7	71.64	71.77					
A3B3G3$^{\mathrm{R}}$	26.2	49.63	49.42	49.09	1.69			+66
				52.27	2.47			
				55.70	23.64+			
A3B3G3$^{\mathrm{N}}$	15.7	49.84	49.64	49.54	0.63			
A3B3G5$^{\mathrm{R}}$	14.7	30.70	30.53	30.58	0.38			+58
A3B3G5$^{\mathrm{N}}$	9.3	30.65	30.36					
A3B4G2$^{\mathrm{R}}$	21.5	74.03	74.51	71.48	5.51			+46
				93.12	5.52			
				117.71	1.14+			
A3B4G2$^{\mathrm{N}}$	14.7	74.50	73.99	73.48	2.05			
A3B5G4$^{\mathrm{R}}$	30.3	43.92	44.31	40.18	48.14+	42.82	2.92	+47
A3B5G4$^{\mathrm{N}}$	20.7	43.73	44.31	41.18	47.22+			

Table 7.12: *Summary of the rotation rate for relativistic (R) and Newtonian (N)* A3 *models: Quantities like in Table 7.11.*

Model	β_{max} [%]	$t_{\beta_{\mathrm{max}}}$ [ms]	t_{b} [ms]	$t_{\beta>\beta_{\mathrm{sec}}}$ [ms]	$\Delta t_{\beta>\beta_{\mathrm{sec}}}$ [ms]	$t_{\beta>\beta_{\mathrm{dyn}}}$ [ms]	$\Delta t_{\beta>\beta_{\mathrm{dyn}}}$ [ms]	$\beta^{\mathrm{R}}_{\mathrm{max}}/\beta^{\mathrm{N}}_{\mathrm{max}} - 1$ [%]
A4B1G1$^{\mathrm{R}}$	18.8	90.43	90.45	90.31	0.27			+154
A4B1G1$^{\mathrm{N}}$	7.4	91.85	91.77					
A4B1G2$^{\mathrm{R}}$	20.5	68.09	68.07	67.95	0.32			+142
A4B1G2$^{\mathrm{N}}$	8.5	68.77	68.69					
A4B2G2$^{\mathrm{R}}$	31.0	68.34	68.34	67.99	0.81			+147
				70.53	33.17+	68.27	0.17	
A4B2G2$^{\mathrm{N}}$	12.6	69.06	69.02					
A4B2G3$^{\mathrm{R}}$	34.3	48.67	48.69	48.17	1.14			+121
				50.77	1.93			
				53.02	32.97+	48.55	0.24	
A4B2G3$^{\mathrm{N}}$	15.5	48.83	48.74	48.66	0.34			
A4B4G4$^{\mathrm{R}}$	37.4	39.87	39.85	37.46	38.07+	39.05	1.74	+65
A4B4G4$^{\mathrm{N}}$	22.6	39.78	39.66	38.51	2.99			
				46.49	2.81			
A4B4G5$^{\mathrm{R}}$	55.0	32.02	32.24	30.29	39.36+			+79
A4B4G5$^{\mathrm{N}}$	28.0	31.96	31.91	31.04	14.06			
				47.34	3.00	31.16	2.79	
				53.17	11.28+	31.86	0.20	
A4B5G4$^{\mathrm{R}}$	47.1	37.52	37.58	33.06	42.67+	35.61	4.65	+69
A4B5G4$^{\mathrm{N}}$	27.9	37.55	37.29	34.85	44.18+	37.30	0.48	
A4B5G5$^{\mathrm{R}}$	76.8	30.78	30.68	27.78	39.63+	29.14	8.13	+102
A4B5G5$^{\mathrm{N}}$	38.1	30.89	30.82	29.18	39.91+	30.32	1.11	

Table 7.13: *Summary of the rotation rate for relativistic (R) and Newtonian (N)* A4 *models: Quantities like in Table 7.11.*

7.9.1 Problems with the Calculation of the Rotation Rate

As already discussed above, predictions about the actual development of instabilities are hard to make: The thresholds originate from a linear stability analysis with many restrictions. In nature, and in many numerical simulations, the EoS is different, the density is not homogenous, the velocity field is not uniform, etc. What is actually needed in order to prove whether a particular model will eventually develop a triaxial instability is a three-dimensional hydrodynamic simulation of core collapse to a neutron star without any symmetry restrictions. In full general relativity, such a simulation has not been performed yet (for a successful attempt in Newtonian gravity, see [102]).

The issue of the validity of stability analysis is additionally complicated by a specific problem related to the CFC approach for the metric in our code: For high rotation rates, which are encountered at high central densities during and after core bounce, the proto-neutron star is highly distorted. In this regime we expect deviations of the CFC metric from the exact metric in the range of a few percent (see Section 6.2, and [22, 64]). However, in the equation for β (6.13), the potential mass energy M_{pot} is determined by the small difference between the gravitational mass M_{grav} and proper mass M_{proper}. Even for strongly gravitating systems like neutron stars, this difference is only about 10% of the individual terms. Thus, if the values for M_{grav} and M_{proper} are subject to an error of a few percent in the CFC approximation, we expect their difference and, as a consequence, β to deviate by several 10% compared to its value in an exact spacetime. This can indeed be shown by comparing the rotation rate of rapidly rotating neutron star models obtained from the exact initial data solver against the corresponding rotation rate in a CFC spacetime. In such equilibrium situations we could observe deviations between β_{exact} and β_{CFC} of about 15%[v]. However, in all these tests, which included neutron stars with both uniform and strong differential rotation, the approximate value β_{CFC} underestimates the exact value β_{exact}. From these consideration we can infer for rotational core collapse, that the rotation rate computed using the CFC approximation is firstly close to the exact value, and secondly probably an underestimate of the exact value.

Nevertheless, owing to the ambiguities with the definition of the thresholds and the problems with the calculation of the rotation rate in the CFC approximation, we point out that the results of Section 7.9 should be regarded as an estimate rather than a clear prediction about the stability of a particular model.

---

[v] Note that this is only a *relative* deviation between the two values for β.

7.10 Propagation of the Shock Front

After core bounce, the position of the shock can be detected as a strong discontinuity in the profiles of the radial velocity. The radial position of the shock front for a given angle and time depends strongly on the type of collapse, on the density, and on the rotation rate and profile of both the inner core and the outer regions. If the collapse is nearly spherically symmetric, i.e. if the initial rotation rate is small and the contraction proceeds rapidly due to a small adiabatic index, we expect the shock front to be almost isotropic. The formation and propagation of the shock in the regular collapse model A1B3G3 is shown in Figure 7.35. At all times, the velocity field in a meridional plane, $\vec{v}_{\mathrm{mer}} = v_r \hat{e}^1 + v_\theta \hat{e}^2$, is almost radial, i.e. $\vec{v}_{\mathrm{mer}} \approx v_r \hat{e}^1$. Except in the first fractions of a millisecond after bounce, where a small anisotropy can be detected, the shape of the shock front is almost spherical.

This behavior of the shock front propagation changes drastically in the case of rapid and differential rotation, which is illustrated by the velocity field plots of model A4B5G5 in Figure 7.36. Contrary to model A1B3G3, here the maximum density is located at an off-center position already during contraction, and the inner core settles down to a new equilibrium state with a toroidal density structure. When the shock forms after core bounce, its initial form reflects the very oblate density structure. As the shock propagates outward, the anisotropy of the shock front increases further: Along the equatorial plane, the high density torus exhibits an almost disk-like shape in regions which have not yet been passed by the shock. Matter from these regions are subsequently being accreted by the central parts of the torus. Here the shock has to push its way through dense matter with large infall velocities, and thus propagates out comparatively slowly. On the other hand, the regions close to the rotation axis have been depleted of matter during the collapse. Here the average density is orders of magnitudes lower than close to the equatorial plane at the same radius, and the shock propagates out very rapidly. As a result of the initial anisotropy of the shock front and the focussing of the shock propagation to the polar regions due to the large density gradient in angular direction, the meridional velocity field exhibits a jet-like form, and matter is predominantly ejected from the inner core along the rotation axis.

The shock discussed above is the so-called prompt shock which obtains its energy from the hydrodynamic bounce of the inner core (cf. Section 1.3). As already indicated in the description of the physical scenario of supernova core collapse, the prompt shock stalls at a radius of a few 100 kilometers. The location where the shock comes to a halt may play an important role in a successful revival of the shock and its conversion into a neutrino-driven shock resulting in a delayed explosion. We have already discussed the impact of rotation on the shock propagation. The effects of relativistic gravity on the shock front propagation become most apparent in models which change from multiple bounce collapse type in Newtonian to regular collapse type in relativistic gravity. The higher central densities and much stronger abrupt deceleration of the inner core in a regular bounce reverse the contraction of the core into an outward shock with a much larger kinetic energy. Although the shock forms much closer to the center compared to the Newtonian multiple bounce collapse, its higher initial energy results in a higher propagation speed. At late times, the shock front is located considerably farther outside from the center, as shown for model A1B3G1 in Figure 7.37.

In the cases described above the effects of relativity on the shock front propagation can be attributed to a qualitative change of the entire collapse dynamics. The influence of relativistic gravity on the shock can be also be observed by investigating models which do not change the collapse type. In this case, however, the states of the inner core at shock formation are comparatively similar in the relativistic and the Newtonian simulation. The initial strength of the shock depends sensitively on the rapidity of contraction and the density profile of the inner core, and the effects of rotation. All these factors are subject to changes under the influence of relativity to various degrees, and thus it is hard to interpret the effects of relativistic gravity on the physical mechanisms which determine the shock strength. Therefore, we want to confine us to simply stating two general observations: By investigating models which do not change their collapse type under the influence of relativity, we have found that in all regular collapse models relativistic gravity increases the initial shock strength (defined as the jump in radial velocity across the discontinuity), whereas the initial shock is weaker in the relativistic simulations of multiple bounce collapse models. The radial velocity profiles shortly after the formation of the shock in the relativistic and Newtonian simulations of the two representative models A3B2G4 and A2B4G1 are plotted in the upper panels of Figure 7.38 and 7.39, respectively. As the deeper gravitational potential in the relativistic simulations increases the compactness of the inner core, in both models the shock forms at a radius which is smaller than the one in the Newtonian simulations. The position of the shock front long after bounce can be identified in the plots of the radial velocity profile in the lower panels of Figure 7.38 and 7.39. In the regular bounce model the shock in the relativistic simulation can never catch up with the shock in the Newtonian simulation as its velocity is lower initially and also at later times. Contrary to that, in the multiple bounce model its high initial velocity is sufficient to make up for the “head start” of the shock in Newtonian gravity. The shock front in the relativistic simulation “overtakes” the shock front in the Newtonian simulation, and later the difference between the radial locations of the shock fronts increases with time.

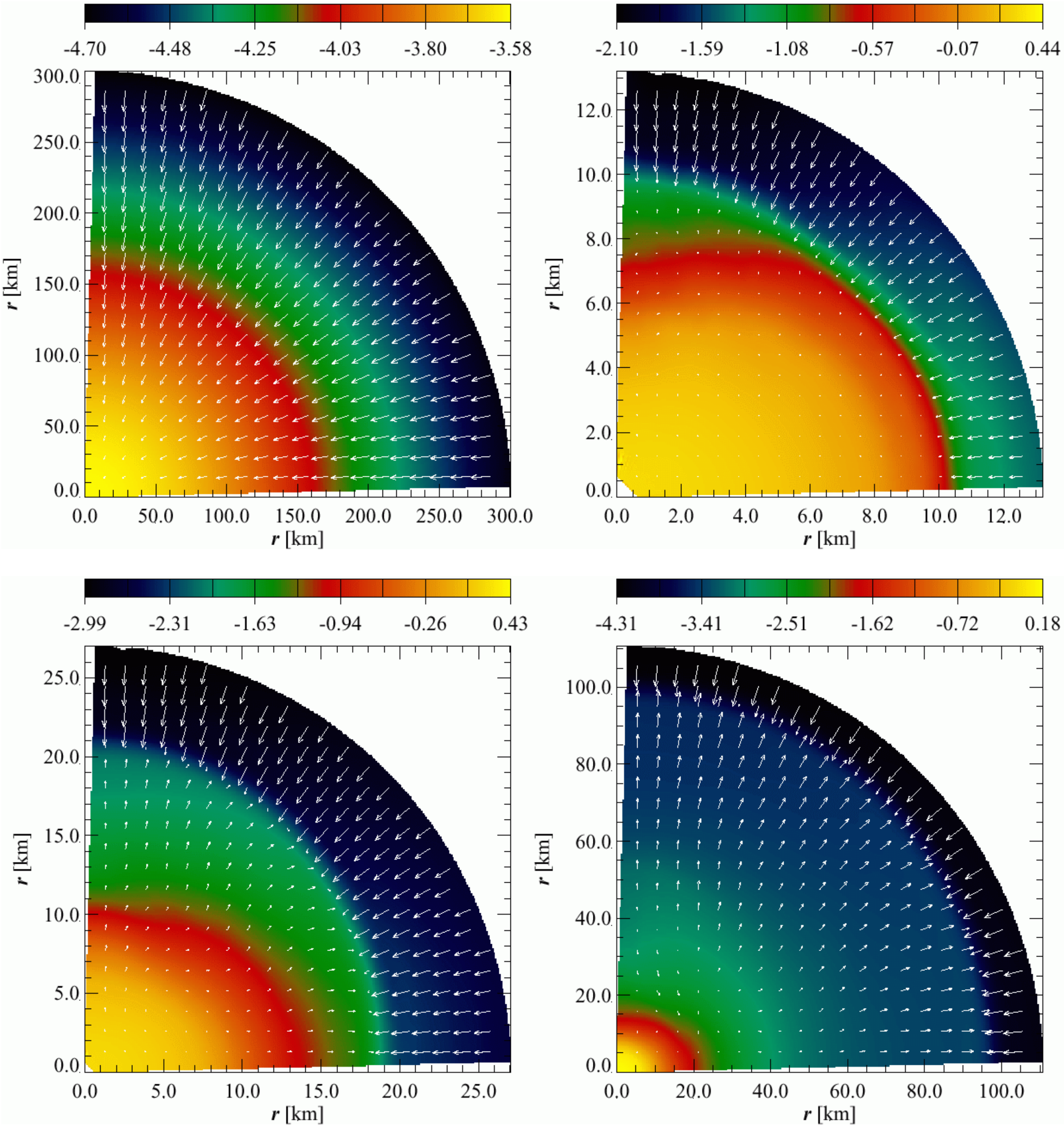

Figure 7.35: *Propagation of the shock in the regular collapse model* A1B3G3*: During the infall phase, at* $t = 30.0$ ms *(upper left panel), the velocity vector field in a meridional plane* $\vec{v}_{\mathrm{mer}}$ *(indicated by white vectors) is radial in the entire core. At* $t = 48.5$ ms *(upper right panel), the inner core comes to a halt and the shock forms at* $r \approx 10$ km*. While the inner core rebounces, the shock propagates outward to about* 20 km *at* $t = 49.0$ ms *(lower left panel); the outer layers of the core continue to fall inward. At* $t = 50.5$ ms *(lower right panel), the inner core starts to ring down; at its boundary it accretes matter from post-shock regions, while the shock front travels further outward. The velocity vectors* $\vec{v}_{\mathrm{mer}} = v_r \hat{e}^1 + v_\theta \hat{e}^2$ *are scaled to the maximum value in the plot region. The color coding shows* $\log(\rho\,[10^{14}\text{ g cm}^{-3}])$*. The radius of the plotted region and the density color coding have different scales in the various plots.*

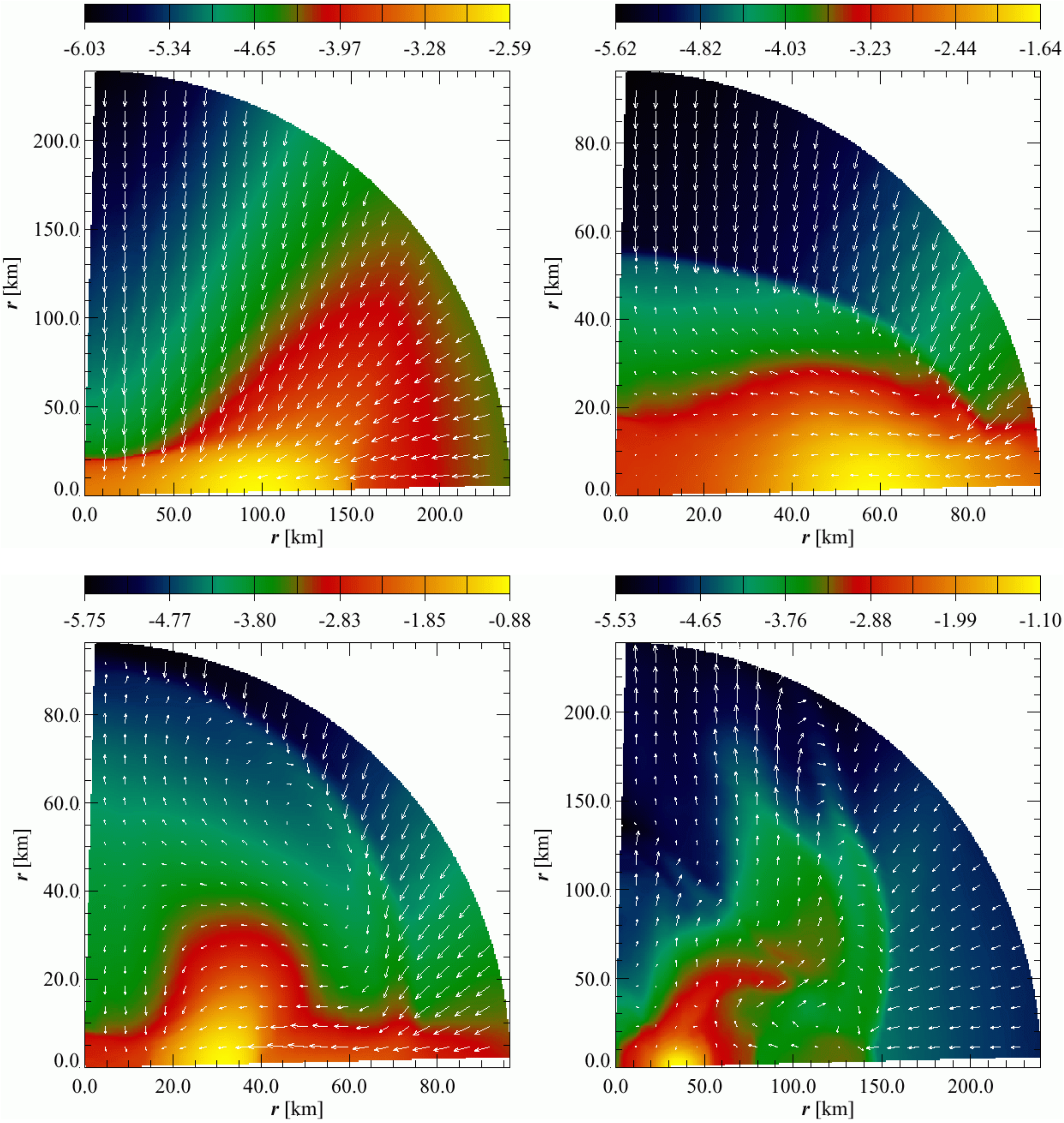

Figure 7.36: *Propagation of the shock in the extremely rapidly rotating collapse model* A4B5G5*: During the infall phase, at* $t = 25.0$ ms *(upper left panel), the velocity field in a meridional plane* v_{mer} *(indicated by white vectors) points towards an off-center region, where the collapsing matter forms a high density torus. At* $t = 28.5$ ms *(upper right panel), the inner core suffers a centrifugal bounce, which creates a strongly anisotropic shock. Due to low average densities in the polar regions, the shock propagates fastest there; at* $t = 30.0$ ms *(lower left panel), the toroidal inner core continues to accrete matter, predominantly from the equatorial plane. At* $t = 35.0$ ms *(lower right panel), the torus is surrounded by large scale velocity and density vortices; the anisotropy of the density further focuses the shock propagation towards the rotation axis. The definition of* v_{mer} *and the color coding of* ρ *are according to Figure 7.35.*

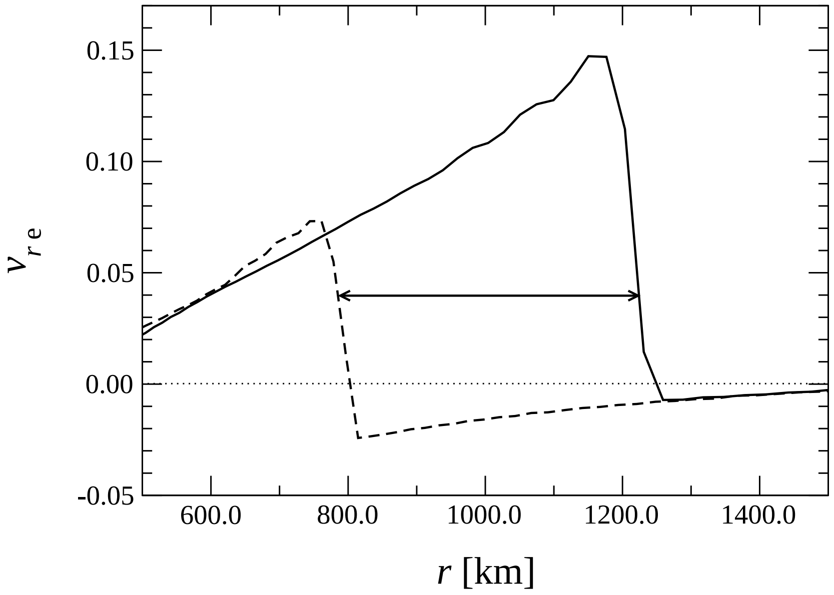

Figure 7.37: *Difference in the shock propagation for the relativistic (solid lines) and Newtonian (dotted lines) simulation of model* A1B3G1*, which changes from multiple bounce collapse type to regular collapse type in relativistic gravity: The shock is much stronger in the regular supranuclear bounce in relativistic gravity, i.e. the shock propagation velocity is higher. Thus, about* 20 ms *after core bounce, the position of the shock in the relativistic simulation is more than* 400 km *farther out from the center compared to the one in the Newtonian simulation. The radial difference in the shock position due to relativistic effects is indicated by an arrow. The velocity profiles of* $v_{r\,\mathrm{e}}$ *are evaluated along the equatorial plane.*

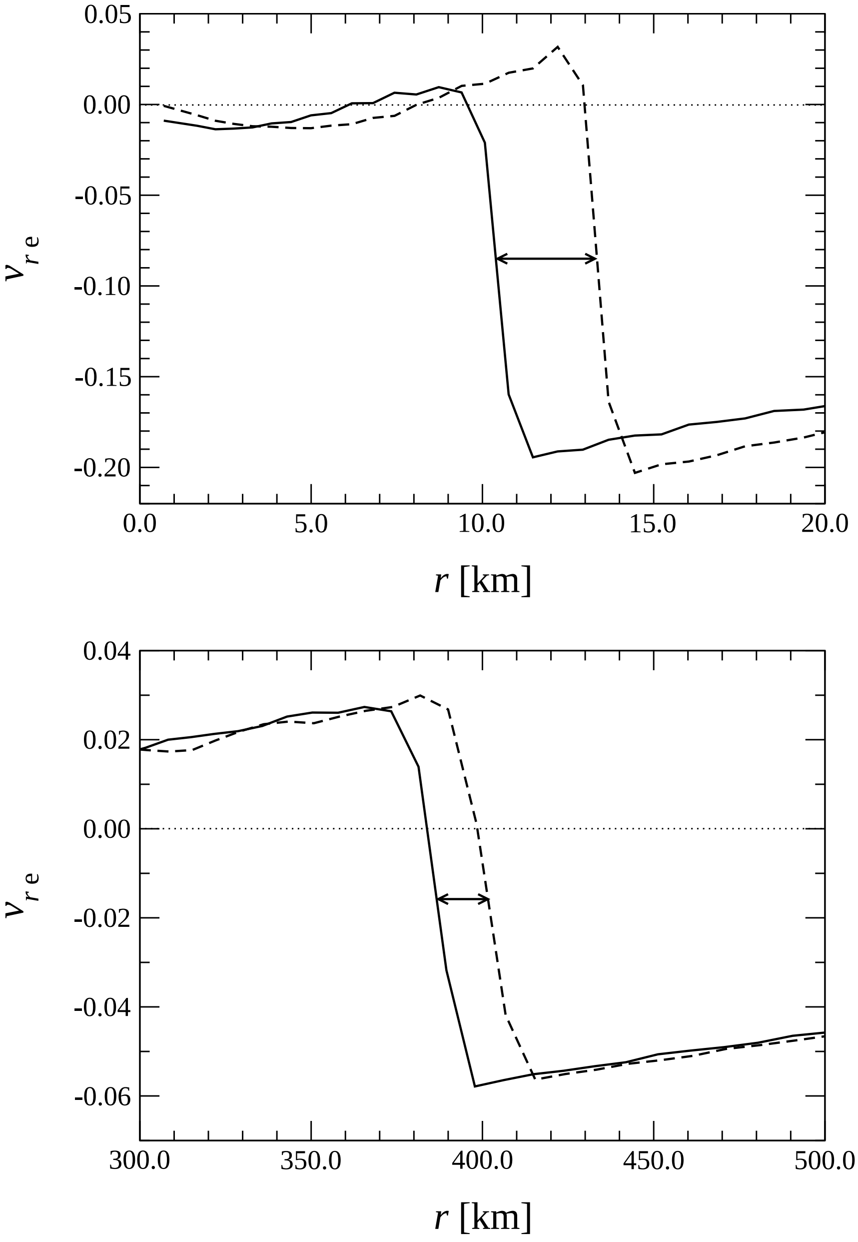

Figure 7.38: *Difference in the shock propagation for the relativistic (solid lines) and Newtonian (dotted lines) simulation of the regular collapse model* A3B2G4*: Shortly after the bounce at* $t \approx 39.25$ ms*, the shock forms at the outer boundary of the inner core. Due to the higher compactness of the central regions, the radius of shock formation is smaller in relativistic gravity (upper panel). As the speed of the shock is lower in the relativistic case at all times, the shock in the relativistic simulation cannot catch up with the shock from the Newtonian simulation of the same model. About* 20 ms *after core bounce, the difference between the shock positions has grown to almost* 20 km*. The radial differences in the shock position due to relativistic effects are indicated by arrows. The velocity profiles of* $v_{r\,\mathrm{e}}$ *are evaluated along the equatorial plane.*

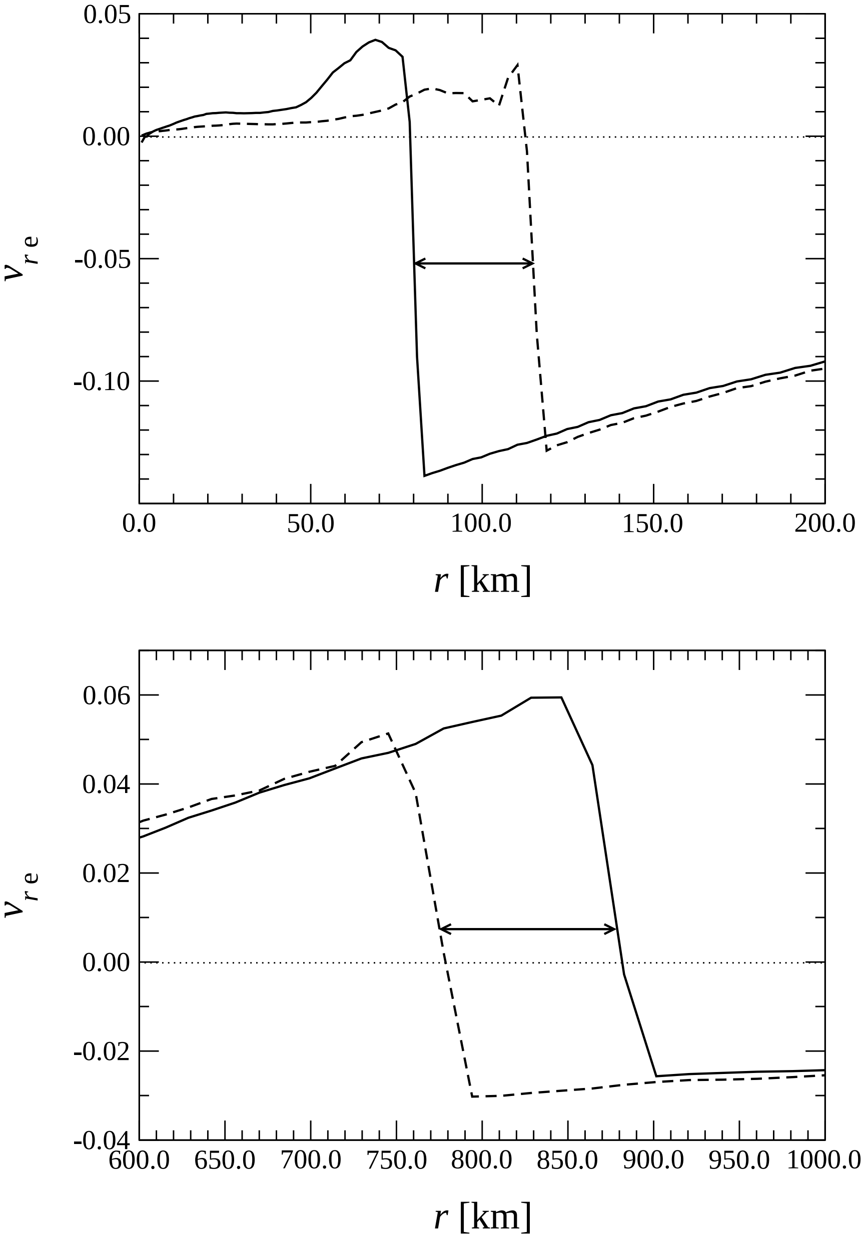

Figure 7.39: *Difference in the shock propagation for the relativistic (solid lines) and Newtonian (dotted lines) simulation of the multiple bounce collapse model* A2B4G1*: Shortly after the bounce at* $t \approx 100.0$ ms *and* $t \approx 100.75$ ms, *respectively, the shock forms at the outer boundary of the inner core. Due to the higher compactness of the central regions, the radius of shock formation is smaller in relativistic gravity (upper panel). Contrary to regular collapse models, the speed of the shock is higher in the relativistic case at all times, and the shock in the relativistic simulation quickly catches up with the shock in the Newtonian simulation of the same model. About* 30 ms *after core bounce, the shock in relativistic gravity is over* 100 km *ahead. The radial differences in the shock position due to relativistic effects are indicated by arrows. The velocity profiles of* $v_{r\,\mathrm{e}}$ *are evaluated along the equatorial plane.*

Chapter 8

Summary and Outlook

Studies of supernova core collapse are a rich and complex field of astrophysics, involving very different physical aspects. In the advent of experimental gravitational wave astronomy, the predictions from astrophysical simulations of this problem are becoming very important. In this thesis we have only touched a small section of contemporary research on supernovae. However, with the hydrodynamic code presented in this work, we were able for the first time to numerically simulate the collapse of a rotating dense stellar core to a neutron star in a fully dynamical general relativistic spacetime, from the infall of the core, via the formation and ring-down of the proto-neutron star, until the inner core assumes a new equilibrium state.

Owing to the complexity of the problem, several simplifications had to be made in our investigation. A detailed consideration of the microphysics involved in the core collapse and subsequent explosion of a supernova, which would require a multidimensional neutrino transport scheme coupled to a sophisticated equation of state (EoS) for the hydrodynamics in relativistic gravity, was beyond the scope of this work. We have shown that in the phases of core collapse which we have investigated, the microphysical behavior of the core can be modeled very well by an adiabatic EoS with thermal contributions. As we were mainly interested in the dynamics of the core, and not focussing on the propagation of the shock front and the explosion mechanism, we have neglected neutrino transport. We have further restricted our simulations to axisymmetry.

For the spacetime metric we have adopted the conformal flatness condition (CFC). This approximation significantly reduces the complexity of the hydrodynamic and metric equations. In this work, the CFC formalism has been used in a fully dynamical context for the first time. In numerous tests, including a detailed resolution study, we have demonstrated that our model and the numerical implementation is appropriate for studying rotational core collapse in general relativity. We have particularly shown that the CFC approximation of the spacetime metric is justified and that the code yields results which are sufficiently close to the exact solution of the Einstein equations. By virtue of the CFC approximation we were also able to avoid numerical instabilities which have been hampering many previous general relativistic hydrodynamic codes based on the conventional ADM formalism of calculating the spacetime metric.

For the construction of our initial models we have used the approach of Hachisu at al., who have introduced a robust and versatile method to compute rotating polytropes in general relativity. The initial models approximate the iron core of the progenitors for a core collapse supernova at the onset of the collapse. The collapse of the core was triggered by a prescribed reduction of the adiabatic index, which mimics the effects of electron capture and photodissociation. A set of 26 core collapse models with various rotation rates and profiles, and several values of the adiabatic index were evolved through all phases of the collapse until a new equilibrium configuration formed, or (in the case of multiple bounces) until several sequences of contraction and re-expansion have been simulated.

Concerning the gravitational wave signal obtained by our general relativistic simulations, we have observed the three general collapse types introduced by Zwerger in his Newtonian simulations: Regular collapse, multiple bounce collapse due to centrifugal forces, and rapid collapse. With the help of a direct comparison of our models with the corresponding models in Newtonian gravity, we were able to identify and interpret the influence of relativistic effects on rotational core collapse.

Already during the infall phase, the influence of relativity becomes apparent. Both the radial extent of the homologously collapsing inner core (where the radial infall velocity is proportional to the radius), and the mass contained therein, are significantly smaller when relativity is taken into account. Furthermore, the quality of homology on the inner core is less good when the collapse proceeds in a relativistic gravitational potential, manifesting itself in a deviation from the linear infall velocity profile in relativistic gravity.

During the bounce, when the density of the core and the gravitational wave signal amplitude are largest, relativistic effects enhance both the peak density and the average densities in the central parts of the core for all investigated models, in multiple bounce collapse models by up to 400%. These higher average and maximum densities are a direct consequence of the deeper gravitational potential well in relativistic gravity. The deeper relativistic potential also causes larger accelerations which reverse the infall velocity of the inner core during bounce. This effect is most prominent in multiple bounce collapse models, where the time intervals between the subsequent bounces are significantly shorter compared to their Newtonian counterparts.

However, the higher densities do not directly and in all models translate into a larger signal amplitude of the gravitational waves. An evaluation of the maximum absolute signal amplitudes proves that, while the maximum signal amplitudes increase by up to +70% in some models, relativistic effects result in an attenuation of the maximum gravitational wave signal by up to −70% in most models. The higher densities and accelerations during core bounce increase the predominant frequency of the wave signal in all models except one. As the gravitational wave signal amplitude is the second time derivative of the quadrupole moment, which is an integral quantity of the entire mass distribution, the interpretation of these results is not trivial.

We have found that the compactness of the central regions of the inner core in relativistic gravity is crucial for explaining the weaker gravitational wave amplitude. Although the densities close to the center are enhanced by relativistic effects, by comparing the radial density profile to Newtonian results during and after bounce we could detect a density crossing within the inner core in all models. This means that in a relativistic potential the outer parts of the inner core are (in some models significantly) less dense. In regular bounce models, which collapse to (often very high) supranuclear densities, the comparatively slow rotating central regions of the core contribute less to the quadrupole moment and its second-order time derivative than the outer regions of the core. The comparatively low average densities in the outer regions of the inner core thus explain the lower gravitational wave signal amplitudes observed in most of the relativistic simulations.

In multiple bounce collapse models the crossing between the density profiles in relativistic and Newtonian simulations also occurs, albeit at much larger radii. Therefore, the density is enhanced by relativistic effects throughout most of the inner core, and the corresponding gravitational wave signal is larger than in Newtonian gravity. Nevertheless, as the density crossing is still present, the increase in the gravitational wave signal is by far not as high as the enhancement of the central density.

Apart from these quantitative differences in the core density and gravitational wave signal of models evolved in a general relativistic spacetime, relativity also causes qualitative changes in the collapse type of many models which show multiple bounces in Newtonian gravity. Due to the relativistic enhancement of the central density and the increased compactness of the core, only a small fraction of the Newtonian multiple bounce models exhibit this collapse type also in relativistic gravity. The other models collapse to supranuclear density and behave like regular collapses. As the parameter space of models which allow for the occurrence of multiple bounces is already restricted by astrophysical reasons due to the strong and differential rotation necessary for a centrifugal bounce, relativistic effects further narrow the region of parameter space for multiple bounce models.

The suppression of multiple bounces in relativity has important consequences on the amplitude and frequency of the gravitational wave signal emitted by these models. On average, relativistic regular collapse models yield signal strengths which are smaller and have frequencies which are higher than for the corresponding model evolved in a Newtonian simulation. As both a smaller signal amplitude and a higher frequency worsen the prospects of detection by laser interferometers, the suppression of multiple bounce models in relativity may have important consequences on the detection of signals from rotational core collapse supernovae. Even in the case of relativistic multiple bounce models, where the signal amplitude increases, the higher signal frequencies compensate for this effect in terms of detectability. Despite these shifts of the position of relativistic models in the signal–frequency space, the spread and average position of the bulk of models (from about 400 cm to 3500 cm in signal amplitude, and 60 Hz to 1000 Hz in frequency) are comparable to those of the Newtonian simulations. In general, the gravitational wave signals obtained in our simulations are within the sensitivity range of modern laser interferometer detectors if the source is located within our Galaxy or in the Magellanic Clouds. A successful detection of a wave signal attributable to a core collapse supernova could, together with the waveforms obtained by our code, put important constraints on the parameter space of this event. This is particularly the case, if a signal, which is characteristic for a multiple bounce collapse, would be detected.

The rotation rate is strongly amplified during the contraction of the core due to conservation of angular momentum. This can lead to the formation of a toroidal density structure of the inner core during and after bounce for initially rapidly and differentially rotating models. Relativistic effects in general tend to increase the rotation velocities and shift the center of maximum rotation velocity in the high density torus closer towards the star's center. Such rapidly and differentially rotating proto-neutron stars may be subject to developing a triaxial instability on secular or even dynamic timescales if the rotation rate exceeds respective threshold values. Our simulations show that the maximum and average rotation rates of all 26 models increase significantly in relativistic gravity. As relativistic effects further lower the respective instability thresholds, we can infer that our models are much more prone to the development of triaxial instabilities. However, this conjecture can only be confirmed by three-dimensional simulations in general relativity.

For rapidly rotating models we observe a strongly anisotropic form of the shock front. The propagation of the shock front is also influenced by relativistic effects. The shock can either propagate faster or slower than the shock front in a Newtonian simulation.

The results presented in this thesis, particularly the waveforms of gravitational radiation emitted during the collapse, will be of use for data analysis in gravitational wave detectors. These waveforms from relativistic simulations can augment or even replace the set of waveforms obtained by Newtonian simulations. As realistic waveforms are crucially needed in interferometer data analysis for calibration of digital filtering and as templates during the actual search for events, we hope that our results can contribute to a hopefully successful detection of gravitational waves from astrophysical sources.

Appendix A

Characteristic Fields

A.1 Characteristic Structure of the Conservation Equations

When the hydrodynamic equations are formulated as a hyperbolic set of conservation laws,

$$\frac{1}{\sqrt{-g}}\left[\frac{\partial\sqrt{\gamma}\boldsymbol{F}^0}{\partial x^0}+\frac{\partial\sqrt{-g}\boldsymbol{F}^i}{\partial x^i}\right]=\boldsymbol{Q}, \tag{A.1}$$

we can use the characteristic information to analytically solve the Riemann problem (evolution of piecewise constant initial data). The Jacobi matrices corresponding to the three spatial directions are

$$\boldsymbol{B}^i=\alpha\frac{\partial\boldsymbol{F}^i}{\partial\boldsymbol{F}^0}. \tag{A.2}$$

If the Jacobians are constant (quasi-linear Riemann problem), and we can utilize the following transformation

$$\boldsymbol{B}=\boldsymbol{R}\boldsymbol{\Lambda}\boldsymbol{R}^{-1}=\boldsymbol{R}\boldsymbol{\Lambda}\boldsymbol{L}, \tag{A.3}$$

with $\boldsymbol{R}$ being the matrix of right eigenvectors, $\boldsymbol{\Lambda}$ being the diagonal matrix of eigenvalues, and $\boldsymbol{L}$ being the matrix of left eigenvectors.

From these we can calculate the numerical fluxes in a straightforward way.

A.2 Eigenvalues and Eigenvectors

The 5 eigenvalues associated to the Jacobian matrices are [11][a]:

$$\lambda_0^i = \alpha v^i - \beta^i, \qquad \text{threefold degenerate,} \tag{A.4}$$

$$\lambda_\pm^i = \frac{\alpha}{1 - v^2 c_\mathrm{s}^2} \left[v^i (1 - c_\mathrm{s}^2) \pm c_\mathrm{s}^2 \sqrt{(1 - v^2)(\gamma^{ii}(1 - v^2 c_\mathrm{s}^2) - v^i v^i (1 - c_\mathrm{s}^2))} \right] - \beta^i. \tag{A.5}$$

These are the characteristic velocities of the general relativistic hydrodynamic system, analogous to $\lambda_0^i = v^i$ and $\lambda_\pm^i = v^i \pm c_\mathrm{s}$ in Newtonian hydrodynamics.

The corresponding right-eigenvectors (columns of $\boldsymbol{R}$) in the r-direction read:

$$\boldsymbol{r}_{0,1}^1 = \begin{pmatrix} \bar{\kappa}/(hW) \\ v_1 \\ v_2 \\ v_3 \\ 1 - \bar{\kappa}/(hW) \end{pmatrix}, \quad \boldsymbol{r}_{0,2}^1 = \begin{pmatrix} W v^2 \\ 2hW^2 v_1 v^2 \\ h(1 + 2W v_2 v^2) \\ 2hW^2 v_3 v^2 \\ W v^2 (2hW - 1) \end{pmatrix}, \quad \boldsymbol{r}_{0,3}^1 = \begin{pmatrix} W v^3 \\ 2hW^2 v_1 v^3 \\ 2hW^2 v_2 v^3 \\ h(1 + 2W^2 v_3 v^3) \\ W v^3 (2hW - 1) \end{pmatrix},$$

$$\boldsymbol{r}_\pm^1 = \begin{pmatrix} 1 \\ hW \left(v_1 - \dfrac{v^1 \Lambda_\pm^1}{\gamma^{11} - v^1 \Lambda_\pm^1} \right) \\ hW v_2 \\ hW v_3 \\ hW \dfrac{\gamma^{11} - (v^1)^2}{\gamma^{11} - v^1 \Lambda_\pm^1} - 1 \end{pmatrix}, \tag{A.6}$$

with

$$\bar{\kappa} = \frac{\kappa/\rho}{\kappa/\rho - c_\mathrm{s}}, \quad \kappa = \left. \frac{\partial P}{\partial \epsilon} \right|_\rho, \quad \text{and} \quad \Lambda_\pm^i = \frac{\lambda_\pm}{\alpha} + \frac{\beta^i}{\alpha}. \tag{A.7}$$

The corresponding right-eigenvectors in the θ-direction can be obtained from the above by exchanging the indices 1 and 2, and by a permutation of rows 2 and 3:

$$\boldsymbol{r}_{0,1}^2 = \begin{pmatrix} \bar{\kappa}/(hW) \\ v_1 \\ v_2 \\ v_3 \\ 1 - \bar{\kappa}/(hW) \end{pmatrix}, \quad \boldsymbol{r}_{0,2}^2 = \begin{pmatrix} W v^1 \\ h(1 + 2W v_1 v^1) \\ 2hW^2 v_2 v^1 \\ 2hW^2 v_3 v^1 \\ W v^1 (2hW - 1) \end{pmatrix}, \quad \boldsymbol{r}_{0,3}^2 = \begin{pmatrix} W v^3 \\ 2hW^2 v_1 v^3 \\ 2hW^2 v_2 v^3 \\ h(1 + 2W^2 v_3 v^3) \\ W v^3 (2hW - 1) \end{pmatrix},$$

$$\boldsymbol{r}_\pm^2 = \begin{pmatrix} 1 \\ hW v_1 \\ hW \left(v_2 - \dfrac{v^2 \Lambda_\pm^2}{\gamma^{22} - v^2 \Lambda_\pm^2} \right) \\ hW v_3 \\ hW \dfrac{\gamma^{22} - (v^2)^2}{\gamma^{22} - v^2 \Lambda_\pm^2} - 1 \end{pmatrix}. \tag{A.8}$$

---

[a] Note that the eigenvectors stated in [11] are only valid for a diagonal three-metric (like the CFC metric). The general expressions for the eigenvectors can be found in [60] or in [37].

The left-eigenvectors are the rows of $\boldsymbol{L}$:

$$\boldsymbol{l}^1_{0,1} = \frac{W}{\bar{\kappa}-1}\begin{pmatrix} h-W \\ Wv^1 \\ Wv^2 \\ Wv^3 \\ -W \end{pmatrix}, \quad \boldsymbol{l}^1_{0,2} = \frac{1}{h(1-v_1v^1)}\begin{pmatrix} -v_2 \\ v_2v^1 \\ 1-v_1v^1 \\ 0 \\ -v_2 \end{pmatrix}, \quad \boldsymbol{l}^1_{0,3} = \frac{1}{h(1-v_1v^1)}\begin{pmatrix} -v_3 \\ v_3v^1 \\ 0 \\ 1-v_1v^1 \\ -v_3 \end{pmatrix},$$

$$\boldsymbol{l}^1_{\pm} = \mp\frac{h^2}{\Delta_1}\begin{pmatrix} hW\mathcal{A}^1_{\mp}(v_1-\gamma_{11}\Lambda^1_{\mp})-v_1-W^2(v_iv^i-v_1v^1)(2\bar{\kappa}-1)(v_1-\mathcal{A}^1_{\mp}\gamma_{11}\Lambda^1_{\mp})+\bar{\kappa}\mathcal{A}^1_{\mp}\gamma_{11}\Lambda^1_{\mp} \\ 1+W^2(v_iv^i-v_1v^1)(2\bar{\kappa}-1)(1-\mathcal{A}^1_{\mp})-\bar{\kappa}\mathcal{A}^1_{\mp} \\ W^2v^2(2\bar{\kappa}-1)\mathcal{A}^1_{\mp}(v_1-\gamma_{11}\Lambda^1_{\mp}) \\ W^2v^3(2\bar{\kappa}-1)\mathcal{A}^1_{\mp}(v_1-\gamma_{11}\Lambda^1_{\mp}) \\ -v_1-W^2(v_iv^i-v_1v^1)(2\bar{\kappa}-1)(v_1-\mathcal{A}^1_{\mp}\gamma_{11}\Lambda^1_{\mp})+\bar{\kappa}\mathcal{A}^1_{\mp}\gamma_{11}\Lambda^1_{\mp} \end{pmatrix}, \tag{A.9}$$

with

$$\mathcal{A}^i_{\pm} = \frac{1-v_iv^i}{1-v_i\Lambda^i_{\pm}}, \qquad \text{and} \quad \Delta_i = \frac{\gamma_{11}(\Lambda^i_{+}-\Lambda^i_{-})h^3W(\bar{\kappa}-1)(1-v_1v^1)^2}{(1-v_1\Lambda^1_{+})(1-v_1\Lambda^1_{-})}. \tag{A.10}$$

Again, the left-eigenvectors in the θ-direction can be obtained from the above by exchanging the indices 1 and 2, and by a permutation of rows 2 and 3:

$$\boldsymbol{l}^2_{0,1} = \frac{W}{\bar{\kappa}-1}\begin{pmatrix} h-W \\ Wv^1 \\ Wv^2 \\ Wv^3 \\ -W \end{pmatrix}, \quad \boldsymbol{l}^2_{0,2} = \frac{1}{h(1-v_2v^2)}\begin{pmatrix} -v_1 \\ 1-v_2v^2 \\ v_1v^2 \\ 0 \\ -v_1 \end{pmatrix}, \quad \boldsymbol{l}^2_{0,3} = \frac{1}{h(1-v_2v^2)}\begin{pmatrix} -v_3 \\ 0 \\ v_3v^2 \\ 1-v_2v^2 \\ -v_3 \end{pmatrix},$$

$$\boldsymbol{l}^2_{\pm} = \mp\frac{h^2}{\Delta_2}\begin{pmatrix} hW\mathcal{A}^2_{\mp}(v_2-\gamma_{22}\Lambda^2_{\mp})-v_2-W^2(v_iv^i-v_2v^2)(2\bar{\kappa}-1)(v_2-\mathcal{A}^2_{\mp}\gamma_{22}\Lambda^2_{\mp})+\bar{\kappa}\mathcal{A}^2_{\mp}\gamma_{22}\Lambda^2_{\mp} \\ W^2v^1(2\bar{\kappa}-1)\mathcal{A}^2_{\mp}(v_2-\gamma_{22}\Lambda^2_{\mp}) \\ 1+W^2(v_iv^i-v_2v^2)(2\bar{\kappa}-1)(1-\mathcal{A}^2_{\mp})-\bar{\kappa}\mathcal{A}^2_{\mp} \\ W^2v^3(2\bar{\kappa}-1)\mathcal{A}^2_{\mp}(v_2-\gamma_{22}\Lambda^2_{\mp}) \\ -v_2-W^2(v_iv^i-v_2v^2)(2\bar{\kappa}-1)(v_2-\mathcal{A}^2_{\mp}\gamma_{22}\Lambda^2_{\mp})+\bar{\kappa}\mathcal{A}^2_{\mp}\gamma_{22}\Lambda^2_{\mp} \end{pmatrix}. \tag{A.11}$$

In the flux formulas in Section 5.4.1 we use the following convention for numbering the left and right eigenvectors:

$$\begin{aligned} \boldsymbol{R} &= (\boldsymbol{r}_1, \boldsymbol{r}_2, \boldsymbol{r}_3, \boldsymbol{r}_4, \boldsymbol{r}_5) = (\boldsymbol{r}_-, \boldsymbol{r}_{0,1}, \boldsymbol{r}_{0,2}, \boldsymbol{r}_{0,3}, \boldsymbol{r}_+)\,, \\ \boldsymbol{L}^T &= (\boldsymbol{l}_1,\, \boldsymbol{l}_2,\, \boldsymbol{l}_3,\, \boldsymbol{l}_4,\, \boldsymbol{l}_5) = (\boldsymbol{l}_-,\, \boldsymbol{l}_{0,1},\, \boldsymbol{l}_{0,2},\, \boldsymbol{l}_{0,3},\, \boldsymbol{l}_+)\ . \end{aligned} \tag{A.12}$$

Analogously, the eigenvalues are numbered in this order:

$$\boldsymbol{\Lambda} = \mathrm{diag}\,(\lambda_1, \lambda_2, \lambda_3, \lambda_4, \lambda_5) = \mathrm{diag}\,(\lambda_-, \lambda_{0,2}, \lambda_{0,2}, \lambda_{0,3}, \lambda_+). \tag{A.13}$$

Appendix B

Source Terms for the Evolution Equations

The source terms in the hydrodynamic equations (2.25), which determine how the conserved quantities evolve in the curved spacetime, translate in the CFC spacetime to the following form:

$$\boldsymbol{Q} = \begin{pmatrix} 0 \\ T^{\mu\nu}\left(\dfrac{\partial g_{\nu 1}}{\partial x^{\mu}} - \Gamma^{\delta}_{\mu\nu} g_{\delta 1}\right) \\ T^{\mu\nu}\left(\dfrac{\partial g_{\nu 2}}{\partial x^{\mu}} - \Gamma^{\delta}_{\mu\nu} g_{\delta 2}\right) \\ T^{\mu\nu}\left(\dfrac{\partial g_{\nu 3}}{\partial x^{\mu}} - \Gamma^{\delta}_{\mu\nu} g_{\delta 3}\right) \\ \alpha\left(T^{\mu 0}\dfrac{\partial \ln \alpha}{\partial x^{\mu}} - T^{\mu\nu}\Gamma^{0}_{\mu\nu}\right) \end{pmatrix} = \begin{pmatrix} 0 \\ T^{1\mu}\dfrac{\partial g_{11}}{\partial x^{\mu}} - g_{11} X^{1} \\ T^{2\mu}\dfrac{\partial g_{22}}{\partial x^{\mu}} - g_{22} X^{2} \\ T^{3\mu}\dfrac{\partial g_{33}}{\partial x^{\mu}} - g_{33} X^{3} \\ T^{0\mu}\dfrac{\partial \alpha}{\partial x^{\mu}} - \alpha X^{0} \end{pmatrix}, \tag{B.1}$$

where $X^{\lambda} = T^{\mu\nu}\Gamma^{\lambda}_{\mu\nu}$.

B.1 Energy-Momentum Tensor

In the CFC metric, the energy-momentum tensor

$$T^{\mu\nu} = \rho h u^\mu u^\nu + P g^{\mu\nu} \tag{B.2}$$

for an ideal fluid has the following components:

$$T^{\mu\nu} = \begin{pmatrix} \frac{1}{\alpha^2}(\rho h W^2 - P) & \frac{1}{\alpha}\left(\frac{\beta^1 P}{\alpha} + \rho h W^2 \hat{v}^1\right) & \frac{1}{\alpha}\left(\frac{\beta^2 P}{\alpha} + \rho h W^2 \hat{v}^2\right) & \frac{1}{\alpha}\left(\frac{\beta^3 P}{\alpha} + \rho h W^2 \hat{v}^3\right) \\ \frac{1}{\alpha}\left(\frac{\beta^1 P}{\alpha} + \rho h W^2 \hat{v}^1\right) & \left(\frac{1}{\phi^4} - \frac{(\beta^1)^2}{\alpha^2}\right) P + \rho h W^2 (\hat{v}^1)^2 & -\frac{\beta^1\beta^2}{\alpha^2} P + \rho h W^2 \hat{v}^1 \hat{v}^2 & -\frac{\beta^1\beta^3}{\alpha^2} P + \rho h W^2 \hat{v}^1 \hat{v}^3 \\ \frac{1}{\alpha}\left(\frac{\beta^2 P}{\alpha} + \rho h W^2 \hat{v}^2\right) & -\frac{\beta^1\beta^2}{\alpha^2} P + \rho h W^2 \hat{v}^1 \hat{v}^2 & \left(\frac{1}{r^2\phi^4} - \frac{(\beta^2)^2}{\alpha^2}\right) P + \rho h W^2 (\hat{v}^2)^2 & -\frac{\beta^2\beta^3}{\alpha^2} P + \rho h W^2 \hat{v}^2 \hat{v}^3 \\ \frac{1}{\alpha}\left(\frac{\beta^3 P}{\alpha} + \rho h W^2 \hat{v}^3\right) & -\frac{\beta^1\beta^3}{\alpha^2} P + \rho h W^2 \hat{v}^1 \hat{v}^3 & -\frac{\beta^2\beta^3}{\alpha^2} P + \rho h W^2 \hat{v}^2 \hat{v}^3 & \left(\frac{1}{r^2 \sin^2\theta \phi^4} - \frac{(\beta^3)^2}{\alpha^2}\right) P + \rho h W^2 (\hat{v}^3)^2 \end{pmatrix}, \tag{B.3}$$

with $\hat{v}^i = v^i - \beta^i/\alpha$, and the four-velocity components $u^0 = W/\alpha$ and $u^i = W\hat{v}^i$.

The projection $S^{ij} = \rho h W^2 v^i v^j + \gamma^{ij} P$ of the energy-momentum tensor onto the three-dimensional hypersurface $\Sigma_{\hat{t}}$ is given by

$$S^{ij} = \begin{pmatrix} \rho h W^2 (v^1)^2 + \frac{P}{\phi^4} & \rho h W^2 v^1 v^2 & \rho h W^2 v^1 v^3 \\ \rho h W^2 v^1 v^2 & \rho h W^2 (v^2)^2 + \frac{P}{\phi^4 r^2} & \rho h W^2 v^2 v^3 \\ \rho h W^2 v^1 v^3 & \rho h W^2 v^2 v^3 & \rho h W^2 (v^3)^2 + \frac{P}{\phi^4 r^2 \sin^2\theta} \end{pmatrix}, \tag{B.4}$$

and the linear momenta $S^i = \rho h W^2 v^i$ read

$$S^i = \begin{pmatrix} \rho h W^2 v^1 \\ \rho h W^2 v^2 \\ \rho h W^2 v^3 \end{pmatrix}. \tag{B.5}$$

Note that in general neither $S^{ij} = T^{ij}$, nor $S_{ij} = T_{ij}$.

B.2 Christoffel Symbols

Of the 64 Christoffel symbols $\varGamma^{\lambda}_{\mu\nu}$, 40 are independent. In the numerical code, we replace the time derivative $\phi_{,t}$ by the analytic equivalent $\frac{1}{6}\phi\beta^{k}_{;k}$ (see Equation (3.34)).

$$\begin{aligned}\varGamma^{0}_{00} = -\frac{1}{\alpha^2}\Bigg[&2r^2(\beta^2)^3\phi^3\phi_{,\theta} - \alpha\alpha_{,\theta}\beta^2 + 2(\beta^1)^3\phi^3\phi_{,r} - \alpha\alpha_{,r}\beta^1 + \beta^1\beta^2\phi^4(\beta^1_{,\theta} + r^2\beta^2_{,r}) + \\ &+\beta^1(\beta^2)^2r^2\phi^4\left(\frac{1}{r} + \frac{2\phi_{,r}}{\phi}\right) - \alpha\alpha_{,t} + r^2(\beta^2)^2\phi^4\left(\beta^2_{,\theta} - \frac{2\phi_{,t}}{\phi}\right) + \\ &+(\beta^1)^2\phi^4\left(\frac{2\beta^2\phi_{,\theta}}{\phi} + \beta^1_{,r} - \frac{2\phi_{,t}}{\phi}\right) + r^2\sin^2\theta\phi^4\Bigg(\beta^2(\beta^3)^2\cot\theta + \frac{2\beta^2(\beta^3)^2\phi_{,\theta}}{\phi} + \\ &\beta^2\beta^3\beta^3_{,\theta} + \frac{\beta^1(\beta^3)^2}{r} + \beta^1\beta^3\beta^3_{,r} + \frac{2\beta^1(\beta^3)^2\phi_{,r}}{\phi} - \frac{2(\beta^3)^2\phi_{,t}}{\phi}\Bigg)\Bigg],\end{aligned}\tag{B.6}$$

$$\begin{aligned}\varGamma^{0}_{01} = -\frac{1}{2\alpha^2}\Bigg[&-2\alpha\alpha_{,r} + \phi^4\Bigg(\frac{4\beta^1\beta^2}{\phi} + \beta^2\beta^1_{,\theta} + r^2\beta^2\beta^2_{,r} + 2\beta^1\beta^1_{,r} + r^2\beta^3\beta^3_{,r}\sin^2\theta + \\ &+\frac{4(\beta^1)^2\phi_{,r}}{\phi} - \frac{4\beta^1\phi_{,t}}{\phi}\Bigg)\Bigg],\end{aligned}\tag{B.7}$$

$$\begin{aligned}\varGamma^{0}_{02} = -\frac{1}{2\alpha^2}\Bigg[&-2\alpha\alpha_{,\theta} + \phi^4\Bigg(\beta^1\beta^1_{,\theta} + 2r\beta^1\beta^2 + r^2\Bigg(\beta^1\beta^2_{,r} + \frac{4\beta^1\beta^2\phi_{,r}}{\phi} + 2\beta^2\beta^2_{,\theta} + \\ &+\beta^3\beta^3_{,\theta}\sin^2\theta + \frac{4(\beta^2)^2\phi_{,\theta}}{\phi} - \frac{\beta^2\phi_{,t}}{\phi}\Bigg)\Bigg)\Bigg],\end{aligned}\tag{B.8}$$

$$\begin{aligned}\varGamma^{0}_{03} = -\frac{1}{2\alpha^2}\Bigg[&r^2\sin^2\theta\phi^4\Bigg(\beta^2\beta^3_{,\theta} + 2\beta^2\beta^3\left(\cot\theta + \frac{2\phi_{,\theta}}{\phi}\right) + \frac{2\beta^1\beta^3}{r} + \beta^1\beta^3_{,r} + \\ &+\frac{4\beta^1\beta^3\phi_{,r}}{\phi} - \frac{4\beta^3\phi_{,t}}{\phi}\Bigg)\Bigg],\end{aligned}\tag{B.9}$$

$$\varGamma^{0}_{11} = -\frac{\phi}{\alpha^2}\left[\frac{2\beta^2\phi_{,\theta}}{\phi} + \beta^1_{,r} + \frac{2\beta^1\phi_{,r}}{\phi} - \frac{2\phi_{,t}}{\phi}\right],\tag{B.10}$$

$$\varGamma^{0}_{12} = -\frac{\phi^4}{2\alpha^2}\left[\beta^1_{,\theta} + r^2\beta^2_{,r}\right],\tag{B.11}$$

$$\varGamma^{0}_{13} = -\frac{r^2\sin^2\theta\phi^4\beta^3_{,r}}{2\alpha^2},\tag{B.12}$$

$$\varGamma^{0}_{22} = -\frac{r^2\phi^4}{\alpha^2}\left[\frac{\beta^1}{r} + \frac{2\beta^1\phi_{,r}}{\phi} + \beta^2_{,\theta} + \frac{2\beta^2\phi_{,\theta}}{\phi} - \frac{2\phi_{,t}}{\phi}\right],\tag{B.13}$$

$$\varGamma^{0}_{23} = -\frac{r^2\sin^2\theta\phi^4\beta^3_{,\theta}}{2\alpha^2},\tag{B.14}$$

$$\varGamma^{0}_{33} = -\frac{r^2\sin^2\theta\phi^4}{\alpha^2}\left[\beta^2\cot\theta + \frac{2\beta^2\phi_{,\theta}}{\phi} + \frac{\beta^1}{r} + \frac{2\beta^1\phi_{,r}}{\phi} - \frac{2\phi_{,t}}{\phi}\right],\tag{B.15}$$

$$\begin{aligned}\mathit{\Gamma}^1_{00} = {}& \frac{\alpha\alpha_{,r}}{\phi^4} - \frac{\beta^1\beta^2\alpha_{,\theta}}{\alpha} - \frac{(\beta^1)^2\alpha_{,r}}{\alpha} - \frac{\beta^1\alpha_{,t}}{\alpha} - r^2\sin^2\theta\left(\frac{(\beta^3)^2}{r} + \beta^3\beta^3_{,r} + \frac{2(\beta^3)^2\phi_{,r}}{\phi}\right) - \\ & -\beta^1\beta^1_{,r} - r^2\beta^2\beta^2_{,r} - \frac{2(\beta^1)^2\phi_{,r}}{\phi} - r^2(\beta^2)^2\left(\frac{1}{r} + \frac{2\phi_{,r}}{\phi}\right) + \beta^1_{,t} + \frac{4\beta^1\phi_{,t}}{\phi} + \\ & + \frac{\beta^1\phi^4}{\alpha^2}\left[\frac{2(\beta^1)^3\phi_{,r}}{\phi} + \beta^1\left(r(\beta^2)^2 + \beta^2\beta^1_{,\theta} + r^2\beta^2\beta^2_{,r} + \frac{2r^2(\beta^2)^2\phi_{,r}}{\phi} + \right.\right. \\ & \left. + r^2\sin^2\theta\left(\frac{(\beta^3)^2}{r} + \beta^3\beta^3_{,r} + \frac{2(\beta^3)^2\phi_{,r}}{\phi}\right)\right) + (\beta^1)^2\left(\frac{2\beta^2\phi_{,\theta}}{\phi} + \beta^1_{,r} - \frac{2\phi_{,t}}{\phi}\right) + \\ & r^2\left(\frac{2(\beta^2)^2\phi_{,\theta}}{\phi} + (\beta^2)^2\beta^2_{,\theta} - \frac{2(\beta^2)^2\phi_{,t}}{\phi}\right) + r^2\sin^2\theta(\beta^3)^2\left(\beta^2\cot\theta + \frac{\beta^2\beta^3_{,\theta}}{\beta^3} + \right. \\ & \left.\left. + \frac{2\beta^2\phi_{,\theta}}{\phi} - \frac{2\phi_{,t}}{\phi}\right)\right], \end{aligned} \tag{B.16}$$

$$\begin{aligned}\mathit{\Gamma}^1_{01} = {}& \frac{2\phi_{,t}}{\phi} - \frac{\beta^1\alpha_{,r}}{\alpha} + \frac{\phi^4}{2\alpha^2}\left[\beta^1\left(\beta^2(\beta^1_{,\theta} + r^2\beta^2_{,r}) + r^2\beta^3\sin^2\theta\beta^3_{,r}\right) + \frac{4(\beta^1)^3\phi_{,r}}{\phi} + \right. \\ & \left. + 2(\beta^1)^2\left(\frac{2\beta^2\phi_{,\theta}}{\phi} + \beta^1_{,r} - \frac{2\phi_{,t}}{\phi}\right)\right], \end{aligned} \tag{B.17}$$

$$\begin{aligned}\mathit{\Gamma}^1_{02} = {}& -\frac{\beta^1\alpha_{,\theta}}{\alpha} + \frac{1}{2}\left[\beta^1_{,\theta} + \frac{4\beta^1\phi_{,\theta}}{\phi} - r^2\beta^2\left(\frac{1}{r} + \frac{2\phi_{,r}}{\phi}\right)\right] + \frac{\beta^1\phi^4}{2\alpha^2}\left[2\beta^1\beta^2r^2\left(\frac{1}{r} + \frac{2\phi_{,r}}{\phi}\right) + \right. \\ & \left. + \beta^1\beta^1_{,\theta} + r^2\beta^1\beta^2_{,r} + r^2\left(2\beta^2\beta^2_{,\theta} + \sin^2\theta\beta^3\beta^3_{,\theta} + \frac{4(\beta^2)^2\phi_{,\theta}}{\phi} - \frac{4\beta^2\phi_{,t}}{\phi}\right)\right], \end{aligned} \tag{B.18}$$

$$\begin{aligned}\mathit{\Gamma}^1_{03} = {}& \frac{r^2\sin^2\theta}{2}\left[-\beta^3_{,r} - 2\beta^3\left(\frac{1}{r} + \frac{2\phi_{,r}}{\phi}\right) + \frac{\phi^4}{\alpha^2}\left((\beta^1)^2\beta^3_{,r} + 2(\beta^1)^2\beta^3\left(\frac{1}{r} + \frac{2\phi_{,r}}{\phi}\right) + \right.\right. \\ & \left.\left. + \beta^1\beta^2\left(2\beta^3\cot\theta + \beta^3_{,\theta} + \frac{4\beta^3\phi_{,\theta}}{\phi}\right) - \frac{4\beta^1\beta^3\phi_{,t}}{\phi}\right)\right], \end{aligned} \tag{B.19}$$

$$\mathit{\Gamma}^1_{11} = \frac{2\phi_{,r}}{\phi} + \frac{\phi^4}{\alpha^2}\left[\frac{2(\beta^1)^2\phi_{,r}}{\phi} + \beta^1\left(\frac{2\beta^2\phi_{,\theta}}{\phi} + \beta^1_{,r} - \frac{2\phi_{,t}}{\phi}\right)\right], \tag{B.20}$$

$$\mathit{\Gamma}^1_{12} = \frac{2\phi_{,\theta}}{\phi} + \frac{\phi^4}{2\alpha^2}\left[\beta^1\beta^1_{,\theta} + r^2\beta^1\beta^2_{,r}\right], \tag{B.21}$$

$$\mathit{\Gamma}^1_{13} = \frac{r^2\sin^2\theta\phi^4\beta^1\beta^3_{,r}}{2\alpha^2}, \tag{B.22}$$

$$\mathit{\Gamma}^1_{22} = -r^2\left(\frac{1}{r} + \frac{2\phi_{,r}}{\phi}\right) + \frac{r^2\phi^4}{\alpha^2}\left[(\beta^1)^2\left(\frac{1}{r} + \frac{2\phi_{,r}}{\phi}\right) + \beta^1\beta^2_{,\theta} + \frac{2\beta^1\beta^2\phi_{,\theta}}{\phi} - \frac{2\beta^1\phi_{,t}}{\phi}\right], \tag{B.23}$$

$$\mathit{\Gamma}^1_{23} = \frac{r^2\sin^2\theta\phi^4\beta^1\beta^3_{,\theta}}{2\alpha^2}, \tag{B.24}$$

$$\begin{aligned}\mathit{\Gamma}^1_{33} = {}& r^2\sin^2\theta\left[-\left(\frac{1}{r} + \frac{2\phi_{,r}}{\phi}\right) + \frac{\phi^4}{\alpha^2}\left((\beta^1)^2\left(\frac{1}{r} + \frac{2\phi_{,r}}{\phi}\right) + \beta^1\beta^2\left(\cot\theta + \frac{2\phi_{,\theta}}{\phi}\right) - \right.\right. \\ & \left.\left. - \frac{2\beta^1\phi_{,t}}{\phi}\right)\right], \end{aligned} \tag{B.25}$$

$$\begin{aligned}
\varGamma^2_{00} = {} & \frac{\alpha\alpha_{,\theta}}{r^2\phi^4} - \frac{(\beta^2)^2\alpha_{,\theta}}{\alpha} - \frac{\beta^2\alpha_{,t}}{\alpha} - \beta^2\beta^2_{,\theta} - \frac{2(\beta^2)^2\phi_{,\theta}}{\phi} + \beta^2_{,t} + \frac{4\beta^2\phi_{,t}}{\phi} - \\
& -\sin^2\theta\left((\beta^3)^2\cot\theta + \beta^3\beta^3_{,\theta} + \frac{2(\beta^3)^2\phi_{,\theta}}{\phi}\right) - \frac{\beta^1\beta^1_{,\theta}}{r^2} + \frac{2(\beta^1)^3\beta^2\phi^4\phi_{,r}}{\alpha^2\phi} - \frac{\beta^1\beta^2\alpha_{,r}}{\alpha} - \\
& -\frac{2(\beta^1)^2\phi_{,\theta}}{r^2\phi} + \frac{\phi^4}{\alpha^2}\Bigg[\beta^1\Bigg((\beta^2)^2(\beta^1_{,\theta} + r^2\beta^2_{,r}) + r^2(\beta^2)^3\left(\frac{1}{r} + \frac{2\phi_{,r}}{\phi}\right) + \\
& +r^2\sin^2\theta\left(\frac{\beta^2(\beta^3)^2}{r} + \beta^2\beta^3\beta^3_{,r} + \frac{2\beta^2(\beta^3)^2\phi_{,r}}{\phi}\right)\Bigg) + (\beta^1)^2\beta^2\left(\frac{2\beta^2\phi_{,\theta}}{\phi} + \beta^1_{,r} - \frac{2\phi_{,t}}{\phi}\right) + \\
& +r^2\beta^2\Bigg((\beta^2)^2\beta^2_{,\theta} + \frac{2(\beta^2)^3\phi_{,\theta}}{\phi} - \frac{2(\beta^2)^2\phi_{,t}}{\phi} + \sin^2\theta\Bigg(\beta^2(\beta^3)^2\cot\theta + \beta^2\beta^3\beta^3_{,\theta} + \\
& +\frac{2\beta^2(\beta^3)^2\phi_{,\theta}}{\phi} - \frac{2(\beta^3)^2\phi_{,t}}{\phi}\Bigg)\Bigg)\Bigg],
\end{aligned} \tag{B.26}$$

$$\begin{aligned}
\varGamma^2_{01} = {} & \frac{\beta^2\alpha_{,r}}{\alpha} - \frac{\beta^1_{,\theta}}{2r^2} - \frac{2\beta^1\phi_{,\theta}}{r^2\phi} + \frac{\beta^2_{,r}}{2} + \beta^2\left(\frac{1}{r} + \frac{2\phi_{,r}}{\phi}\right) + \frac{\beta^2\phi^4}{2\alpha^2}\Bigg[2\beta^1\beta^1_{,r} + \\
& +\beta^2\left(\beta^1_{,\theta} + \frac{4\beta^1\phi_{,\theta}}{\phi} + r^2\beta^2_{,r}\right) + r^2\sin^2\theta\beta^3\beta^3_{,r} + \frac{4(\beta^1)^2\phi_{,r}}{\phi} - \frac{4\beta^1\phi_{,t}}{\phi}\Bigg],
\end{aligned} \tag{B.27}$$

$$\begin{aligned}
\varGamma^2_{02} = {} & \frac{2\phi_{,t}}{\phi} - \frac{\beta^2\alpha_{,\theta}}{\alpha} + \frac{\phi^4\beta^1\beta^2\beta^1_{,\theta}}{2\alpha^2} + \frac{r^2\phi^4\beta^2}{2\alpha^2}\Bigg[2\beta^1\beta^2\left(\frac{1}{r} + \frac{2\phi_{,r}}{\phi}\right) + \beta^1\beta^2_{,r} + 2\beta^2\beta^2_{,\theta} + \\
& +\beta^3\beta^3_{,\theta}\sin^2\theta + \frac{4(\beta^2)^2\phi_{,\theta}}{\phi} - \frac{4\beta^2\phi_{,t}}{\phi}\Bigg],
\end{aligned} \tag{B.28}$$

$$\begin{aligned}
\varGamma^2_{03} = {} & \frac{\sin^2\theta}{2}\Bigg[-\beta^3_{,\theta} - 2\beta^3\left(\cot\theta + \frac{2\phi_{,\theta}}{\phi}\right) + \frac{r^2\phi^4\beta^2}{\alpha^2}\Bigg(\beta^2\left(\beta^3_{,\theta} + 2\beta^3\left(\cot\theta + \frac{2\phi_{,\theta}}{\phi}\right)\right) + \\
& +\beta^1\beta^3_{,r} - \frac{4\beta^3\phi_{,t}}{\phi} + 2\beta^1\beta^3\left(\frac{1}{r} + \frac{2\phi_{,r}}{\phi}\right)\Bigg)\Bigg],
\end{aligned} \tag{B.29}$$

$$\varGamma^2_{11} = -\frac{2\phi_{,\theta}}{r^2\phi} + \frac{\phi^4\beta^2}{\alpha^2}\left[\frac{2\beta^2\phi_{,\theta}}{\phi} + \beta^1_{,r} + \frac{2\beta^1\phi_{,r}}{\phi} - \frac{2\phi_{,t}}{\phi}\right], \tag{B.30}$$

$$\varGamma^2_{12} = \frac{1}{r} + \frac{2\phi_{,r}}{\phi} + \frac{\phi^4\beta^2}{2\alpha^2}\left[\beta^1_{,\theta} + r^2\beta^2_{,r}\right], \tag{B.31}$$

$$\varGamma^2_{13} = \frac{r^2\sin^2\theta\phi^4\beta^2\beta^3_{,r}}{2\alpha^2}, \tag{B.32}$$

$$\varGamma^2_{22} = \frac{2\phi_{,\theta}}{\phi} + \frac{r^2\phi^4}{\alpha^2}\left[\frac{2(\beta^2)^2\phi_{,\theta}}{\phi} + \beta^1\beta^2\left(\frac{1}{r} + \frac{2\phi_{,r}}{\phi}\right) + \beta^2\left(\beta^2_{,\theta} - \frac{2\phi_{,t}}{\phi}\right)\right], \tag{B.33}$$

$$\varGamma^2_{23} = \frac{r^2\sin^2\theta\phi^4\beta^2\beta^3_{,\theta}}{2\alpha^2}, \tag{B.34}$$

$$\varGamma^2_{33} = \sin^2\theta\left[-\cot\theta - \frac{2\phi_{,\theta}}{\phi} + \frac{r^2\phi^4\beta^2}{\alpha^2}\left(\beta^2\cot\theta + \frac{2\beta^2\phi_{,\theta}}{\phi} + \beta^1\left(\frac{1}{r} + \frac{2\phi_{,r}}{\phi}\right) - \frac{2\phi_{,t}}{\phi}\right)\right], \tag{B.35}$$

$$\varGamma^3_{00} = -\frac{\beta^3\alpha_{,t}}{\alpha} - \frac{\beta^2\beta^3\alpha_{,\theta}}{\alpha} - \frac{\beta^1\beta^3\alpha_{,r}}{\alpha} + \beta^3_{,t} + \frac{4\beta^3\phi_{,t}}{\phi} + \frac{\phi^4}{\alpha^2}\Bigg[\frac{2(\beta^1)^3\beta^3\phi_{,r}}{\phi} + \beta^1(\beta^3)^3 r\sin^2\theta +$$

$$
\begin{aligned}
&+\beta^1\beta^2\beta^3\beta^1_{,\theta} + (\beta^1)^2\beta^3 \Bigg(\frac{2\beta^2\phi_{,\theta}}{\phi} + \beta^1_{,r} - \frac{2\phi_{,t}}{\phi}\Bigg) + r^2 \Bigg(\frac{2(\beta^2)^3\beta^3\phi_{,\theta}}{\phi} + \beta^1\beta^2\beta^3\beta^2_{,r} + \\
&+\beta^1(\beta^2)^2\beta^3 \Bigg(\frac{1}{r} + \frac{2\phi_{,r}}{\phi}\Bigg) + (\beta^2)^2\beta^3 \Bigg(\beta^2_{,\theta} - \frac{2\phi_{,t}}{\phi}\Bigg)\Bigg) + r^2\sin^2\theta \Bigg(\beta^2(\beta^3)^3 \Bigg(\cot\theta + \frac{2\phi_{,\theta}}{\phi}\Bigg) + \\
&+\beta^2(\beta^3)^2\beta^3_{,\theta} + \beta^1(\beta^3)^2\beta^3_{,r} + \frac{2\beta^1(\beta^3)^3\phi_{,r}}{\phi} - \frac{2(\beta^3)^3\phi_{,t}}{\phi}\Bigg)\Bigg], \qquad \text{(B.36)}
\end{aligned}
$$

$$
\begin{aligned}
\mathit{\Gamma}^3_{01} = &-\frac{\beta^3\alpha_{,r}}{\alpha} + \frac{\beta^3_{,r}}{2} + \beta^3\Bigg(\frac{1}{r} + \frac{2\phi_{,r}}{\phi}\Bigg) + \frac{\phi^4\beta^3}{2\alpha^2}\Bigg[2\beta^1\beta^1_{,r} + \beta^2\Bigg(\beta^1_{,\theta} + \frac{4\beta^1\phi_{,\theta}}{\phi} + r^2\beta^2_{,r}\Bigg) + \\
&+r^2\sin^2\theta\beta^3\beta^3_{,r} + \frac{4(\beta^1)^2\phi_{,r}}{\phi} - \frac{4\beta^1\phi_{,t}}{\phi}\Bigg], \qquad \text{(B.37)}
\end{aligned}
$$

$$
\begin{aligned}
\mathit{\Gamma}^3_{02} = &-\frac{\beta^3\alpha_{,\theta}}{\alpha} + \frac{\beta^3_{,\theta}}{2} + \beta^3\Bigg(\cot\theta + \frac{2\phi_{,\theta}}{\phi}\Bigg) + \frac{\phi^4\beta^3}{2\alpha^2}\Bigg[\beta^1\Bigg(2r\beta^2 + \beta^1_{,\theta} + r^2\beta^2_{,r} + \frac{4r^2\beta^2\phi_{,r}}{\phi}\Bigg) + \\
&+r^2\Bigg(2\beta^2\beta^2_{,\theta} + \sin^2\theta\beta^3\beta^3_{,\theta} + \frac{4(\beta^2)^2\phi_{,\theta}}{\phi} - \frac{4\beta^2\phi_{,t}}{\phi}\Bigg)\Bigg], \qquad \text{(B.38)}
\end{aligned}
$$

$$
\begin{aligned}
\mathit{\Gamma}^3_{03} = &\frac{2\phi_{,t}}{\phi} + \frac{r^2\sin^2\theta\phi^4}{2\alpha^2}\Bigg[\beta^2\beta^3\Bigg(2\beta^3\cot\theta + \beta^3_{,\theta} + \frac{4\beta^3\phi_{,\theta}}{\phi}\Bigg) + \beta^1\beta^3\Bigg(\beta^3_{,r} + 2\beta^3\Bigg(\frac{1}{r} + \frac{2\phi_{,r}}{\phi}\Bigg)\Bigg) + \\
&+r^2\Bigg(2\beta^2\beta^2_{,\theta} + \sin^2\theta\beta^3\beta^3_{,\theta} + \frac{4(\beta^2)^2\phi_{,\theta}}{\phi} - \frac{4\beta^2\phi_{,t}}{\phi}\Bigg)\Bigg], \qquad \text{(B.39)}
\end{aligned}
$$

$$
\mathit{\Gamma}^3_{11} = \frac{\phi^4\beta^3}{\alpha^2}\Bigg[\frac{2\beta^2\phi_{,\theta}}{\phi} + \beta^1_{,r} + \frac{2\beta^1\phi_{,r}}{\phi} - \frac{2\phi_{,t}}{\phi}\Bigg], \qquad \text{(B.40)}
$$

$$
\mathit{\Gamma}^3_{12} = \frac{\phi^4\beta^3}{2\alpha^2}(\beta^1_{,\theta} + r^2\beta^2_{,r}), \qquad \text{(B.41)}
$$

$$
\mathit{\Gamma}^3_{13} = \frac{1}{r} + \frac{r^2\sin^2\theta\phi^4\beta^3\beta^3_{,r}}{2\alpha^2} + \frac{2\phi_{,r}}{\phi}, \qquad \text{(B.42)}
$$

$$
\mathit{\Gamma}^3_{22} = \frac{r^2\phi^4\beta^3}{\alpha^2}\Bigg[\beta^1\Bigg(\frac{1}{r} + \frac{2\phi_{,r}}{\phi}\Bigg) + \beta^2_{,\theta} + \frac{2\beta^2\phi_{,\theta}}{\phi} - \frac{2\phi_{,t}}{\phi}\Bigg], \qquad \text{(B.43)}
$$

$$
\mathit{\Gamma}^3_{23} = \cot\theta + \frac{r^2\sin^2\theta\phi^4\beta^3\beta^3_{,\theta}}{2\alpha^2} + \frac{2\phi_{,\theta}}{\phi}, \qquad \text{(B.44)}
$$

$$
\mathit{\Gamma}^3_{33} = \frac{r^2\sin^2\theta\phi^4\beta^3}{\alpha^2}\Bigg[\beta^2\Bigg(\cot\theta + \frac{2\phi_{,\theta}}{\phi}\Bigg) + \beta^1\Bigg(\frac{1}{r} + \frac{2\phi_{,r}}{\phi}\Bigg) - \frac{2\phi_{,t}}{\phi}\Bigg]. \qquad \text{(B.45)}
$$

Appendix C

Gravitational Wave Extraction

The computation of wave templates of the gravitational radiation emitted by the rotational core collapse models is one of the main objectives of this work. In this section we will introduce different approximate descriptions of the radiation field, and the numerical techniques we have implemented in our code to extract gravitational radiation. A catalogue of wave templates for all our runs can be found in Appendix D.

C.1 Multipole Expansion of the Radiation Field

Gravitational waves are in principle a highly nonlinear feature of a general relativistic spacetime. This means that they can curve spacetime, and interact with themselves and the matter in the system. Owing to this nonlinearity, it is rather difficult to specify to what extent the curvature of spacetime due to some source can be attributed to a gravitational wave rather than to the background curvature of some quasi-equilibrium solution. It is therefore much less ambiguous to define gravitational waves in the so-called wave zone, which is the part of spacetime outside the source zone and the near zone. In the source zone the gravitational waves are being generated, and in the near zone they strongly interact with the background curvature, whereas in the spacetime $g_{\mu\nu}$ of the wave zone, far away from the source, they can be regarded as a linearized metric perturbation $\tilde{h}_{\mu\nu}$ propagating on the flat background Minkowski spacetime $\eta_{\mu\nu}$ [85, 124]:

$$g_{\mu\nu} = \eta_{\mu\nu} + \tilde{h}_{\mu\nu}. \tag{C.1}$$

In the *transverse traceless* coordinate gauge, where e.g. the components $\tilde{h}_{\mu 0}$ vanish, the Einstein equations can be linearized, and one gets a wave equation for the time dependent metric perturbations $\tilde{h}_{ij}^{\mathrm{TT}}$:

$$\Box \tilde{h}_{ij}^{\mathrm{TT}} = 16\pi \tilde{T}_{ij}, \tag{C.2}$$

where $\tilde{T}_{ij}$ is the linearized energy momentum tensor in the weak field limit.

In the regime of the wave zone we can then decompose the radiation field of the gravitational wave into a multipole expansion of the transverse traceless part of the strain amplitude $\tilde{h}_{ij}^{\mathrm{TT}}$.

In the wave zone, the strain amplitude will fall off linearly with the inverse of the distance r to the source:

$$\tilde{h}_{ij}^{\mathrm{TT}} = \frac{\tilde{A}_{ij}(t-r,\theta,\varphi)}{r}. \tag{C.3}$$

For the expansion, we now absorb the angular dependence of $\tilde{A}_{ij}(t-r,\theta,\varphi)$ in a sum of pure tensor spherical harmonics $\tilde{T}_{ij}^{\mathrm{E2}\,lm}$ and $\tilde{T}_{ij}^{\mathrm{B2}\,lm}$, and we get the following expression for the radiation field:

$$\tilde{h}_{ij}^{\mathrm{TT}} = \frac{1}{r}\sum_{l=2}^{\infty}\sum_{m=-l}^{l}\left(\tilde{A}_{lm}^{\mathrm{E2}}(t-r)\tilde{T}_{ij}^{\mathrm{E2}\,lm}(\theta,\varphi) + \tilde{A}_{lm}^{\mathrm{B2}}(t-r)\tilde{T}_{ij}^{\mathrm{B2}\,lm}(\theta,\varphi)\right), \tag{C.4}$$

where the coefficients $\tilde{A}_{lm}^{\mathrm{E2}}$ and $\tilde{A}_{lm}^{\mathrm{B2}}$ are the respective amplitudes of the tensor harmonics. They are also called *electric* (E2) and *magnetic* (B2) multipoles of the radiation field.

By truncating the series (C.4), the radiation field $\tilde{h}_{ij}^{\mathrm{TT}}$ can be approximated. In the Newtonian quadrupole approximation, all terms in the expansion except the first are neglected. Additionally, for the quadrupole moments $\tilde{A}_{2m}^{\mathrm{E2}}$ and $\tilde{A}_{2m}^{\mathrm{B2}}$ the Newtonian expressions A_{2m}^{E2} and A_{2m}^{B2} are chosen. For an axisymmetric source in spherical coordinates the quadrupole field then depends only on the quadrupole moment A_{20}^{E2}, as all other quadrupole moments vanish:

$$h_{\theta\theta}^{\mathrm{TT}} = \frac{1}{r}A_{20}^{\mathrm{E2}}(t-r)T_{\theta\theta}^{\mathrm{E2}\,20}, \tag{C.5}$$

where

$$A_{20}^{\mathrm{E2}} = \frac{d^2}{dt^2}\left(\frac{32\pi^{3/2}}{\sqrt{15}}\int\rho\left(\frac{3}{2}\cos^2\theta-\frac{1}{2}\right)r^4\sin\theta dr d\theta\right). \tag{C.6}$$

The remaining tensor harmonic $T_{\theta\theta}^{\mathrm{E2}\,20}$ also exhibits a particularly simple geometrical form:

$$T_{\theta\theta}^{\mathrm{E2}\,20} = \frac{1}{8}\sqrt{\frac{15}{\pi}}\sin^2\theta. \tag{C.7}$$

In general, fully nonlinear gravitational waves are a nonlocal phenomenon. However, in the quadrupole approximation of the radiation field (C.5), the contribution of the source to the radiation field can be reduced to an integral over the mass density, which thus has compact support. This property makes this formula particularly well suited for numerical application, as the integral has to be done only over those parts of spacetime which contain matter.

In the quadrupole approximation, the only independent nonzero field component is $h_{\theta\theta}^{\mathrm{TT}}$. It is related to the other nonzero component $h_{\phi\phi}^{\mathrm{TT}}$ by $h_{\theta\theta}^{\mathrm{TT}} = -h_{\phi\phi}^{\mathrm{TT}}$.

C.2 Standard Quadrupole Formula

According to Equation (C.5), the quadrupole radiation field $h_{\theta\theta}^{\mathrm{TT}}$ of an axisymmetric source is given by

$$h_{\theta\theta}^{\mathrm{TT}} = \frac{1}{8}\sqrt{\frac{15}{\pi}} \sin^2\theta \frac{A_{20}^{\mathrm{E2}}}{r}, \tag{C.8}$$

where the radiation field quadrupole moment A_{20}^{E2} can be expressed as the second time derivative of the mass quadrupole moment M_{20}^{E2} of the source:

$$A_{20}^{\mathrm{E2}} = \frac{d^2 M_{20}^{\mathrm{E2}}}{dt^2} = \frac{d^2}{dt^2}\left(\frac{32\pi^{3/2}}{\sqrt{15}} \int \rho \left(\frac{3}{2}\cos^2\theta - \frac{1}{2}\right) r^4 \sin\theta dr d\theta\right). \tag{C.9}$$

This formulation of the radiation field as the second time derivative of M_{20}^{E2} is known as the *standard quadrupole formula* (SQF).

A numerical implementation of this formula is rather problematic. Due to the second time derivative of the mass quadrupole moment M_{20}^{E2}, discretization errors in both space and time will produce significant numerical high frequency noise in the gravitational wave signal. The amplitude of these oscillation artifacts can be higher than the total amplitude of the signal. If the signal is Fourier transformed into the frequency domain, the unphysical amplification of the high frequency portion of the gravitational wave becomes clearly visible (see Appendix C.4, or e.g. the graph for the SQF in Figure 3 in [31]).

This problematic property of the quadrupole formulation (C.9) is worsened by the fact that in this equation the density is multiplied by an r^4 weighting term. Because of this weighting, mass elements in the exterior parts of the source are strongly contributing to the signal. On the other hand, for large radii the resolution of the grid is coarser due to logarithmic spacing (see Section 5.1.1). As a consequence, the discretization errors and thus the deviation from the analytic solution become larger.

C.3 First Moment of Momentum Density Formula

To overcome the problems with the numerical implementation of the standard quadrupole formula (C.8) due to the high order time derivative, one can try to reduce the order of the derivative by analytic transformations. This can be accomplished by transforming the troublesome time derivatives into less problematic spatial derivatives. That technique has been applied to the standard quadrupole formula by Finn [31], and Blanchet et al. [14].

This reduction of the time derivative by one order can be done in different ways, for example by re-expressing the first time derivative of the mass quadrupole as the divergence of the momentum density S_i. We have chosen another approach, where the weight of the moment arm r^4 is reduced to r^3. In this *first moment of momentum density formulation*, the expression for the quadrupole moment A_{20}^{E2} in the radiation field equation (C.8) reads:

$$A_{20}^{\mathrm{E2}} = \frac{d}{dt} N_{20}^{\mathrm{E2}} = \frac{d}{dt}\left(\frac{32\pi^{3/2}}{\sqrt{15}} \int \rho \left(v_r(3\cos^2\theta - 1) - 3v_\theta \sin\theta\cos\theta\right) r^3 \sin\theta dr d\theta\right). \tag{C.10}$$

Compared to the SQF, the numerical computation of the wave signal on the basis of this formula exhibits much better properties. Because of the reduction of the order of the time derivative and the smaller effective momentum arm which emphasizes the interior parts of the matter distribution, the high frequency noise is significantly suppressed.

C.4 Stress Formula

The technique of reducing the time derivative order can be applied once more to the first moment of momentum density formulation. Then in the resulting *stress formula* for the radiation field, all time derivatives have been absorbed in spatial derivatives, and the time dependence of A_{20}^{E2} comes directly from the variation in time of the single terms in the following expression:

$$A_{20}^{\mathrm{E2}} = \frac{32\pi^{3/2}}{\sqrt{15}} \int \rho \Big(v_1 v^1 (3\cos^2\theta - 1) + v_2 v^2 (2 - 3\cos^2\theta) - v_3 v^3 - 6 r v_1 v_2 \sin\theta\cos\theta - \\ - r\frac{\partial\Phi}{\partial r}(3\cos^2\theta - 1) + 3\frac{\partial\Phi}{\partial\theta}\sin\theta\cos\theta \Big) r^2 \sin\theta dr d\theta, \qquad \text{(C.11)}$$

where Φ is the Newtonian gravitational potential, which is calculated by solving the Poisson equation with the rest mass density as source,

$$\Delta\Phi = 4\pi\rho. \qquad \text{(C.12)}$$

Note that again the weight of the moment arm has been reduced by one power to r^2. In our code we solve the Poisson equation (C.12) for the Newtonian potential Φ by means of expansion into Legendre polynomials [146].

The appearance of Φ in an equation for the gravitational waves, which are a genuinely general relativistic effect of a curved spacetime, is no contradiction: According to the post-Newtonian expansion of the metric $g_{\mu\nu}$, the Newtonian potential can be regarded as a first-order approximation of certain metric quantities. In the same spirit, the approximation of gravitational radiation as linearized perturbations of the metric leads to the above use of the Newtonian potential in the expression (C.11) for the radiation field.

We now want to compare the different methods (C.9, C.10, C.11) for numerically calculating the gravitational wave signal: For this we have applied all three formulations for extracting the signal from a typical rotational core collapse simulation. The results for the quadrupole moment A_{20}^{E2} of model A3B1G1 are shown in Figure C.1. Obviously the higher the order of time derivative involved in the calculation of A_{20}^{E2} is, the more the signal is dominated by numerical high frequency noise. However, the overall shape of the signal, which consists of the lower frequency contributions, is virtually unaffected by the choice of the wave extraction method.

This becomes particularly clear in the corresponding spectral energy distribution in the frequency domain, plotted in the upper panel of Figure C.2: Here the high order time derivatives in the first moment of momentum density formula, and especially in the standard quadrupole formula lead to an amplification of the high frequency spectrum compared to the stress formula, whereas the shape of the low frequency spectrum does not depend much on the wave extraction method. The unphysical amplification of the energy contained in high frequency oscillations is also expressed in the behavior of the radiated gravitational wave energy E_{rad} over time, which is shown in the lower panel of Figure C.2. As the calculation of the energy according to Equation (7.10) involves one more time derivative of the quadrupole moment, the energy stored in the unphysical high frequency oscillations in the signal obtained by Equation (C.10) overestimates the total radiation energy release $E_{\mathrm{rad\,tot}}$, which is the constant value of E_{rad} after ring-down at about $t \gtrsim 100$ ms, compared to the energy obtained from the stress formula by a

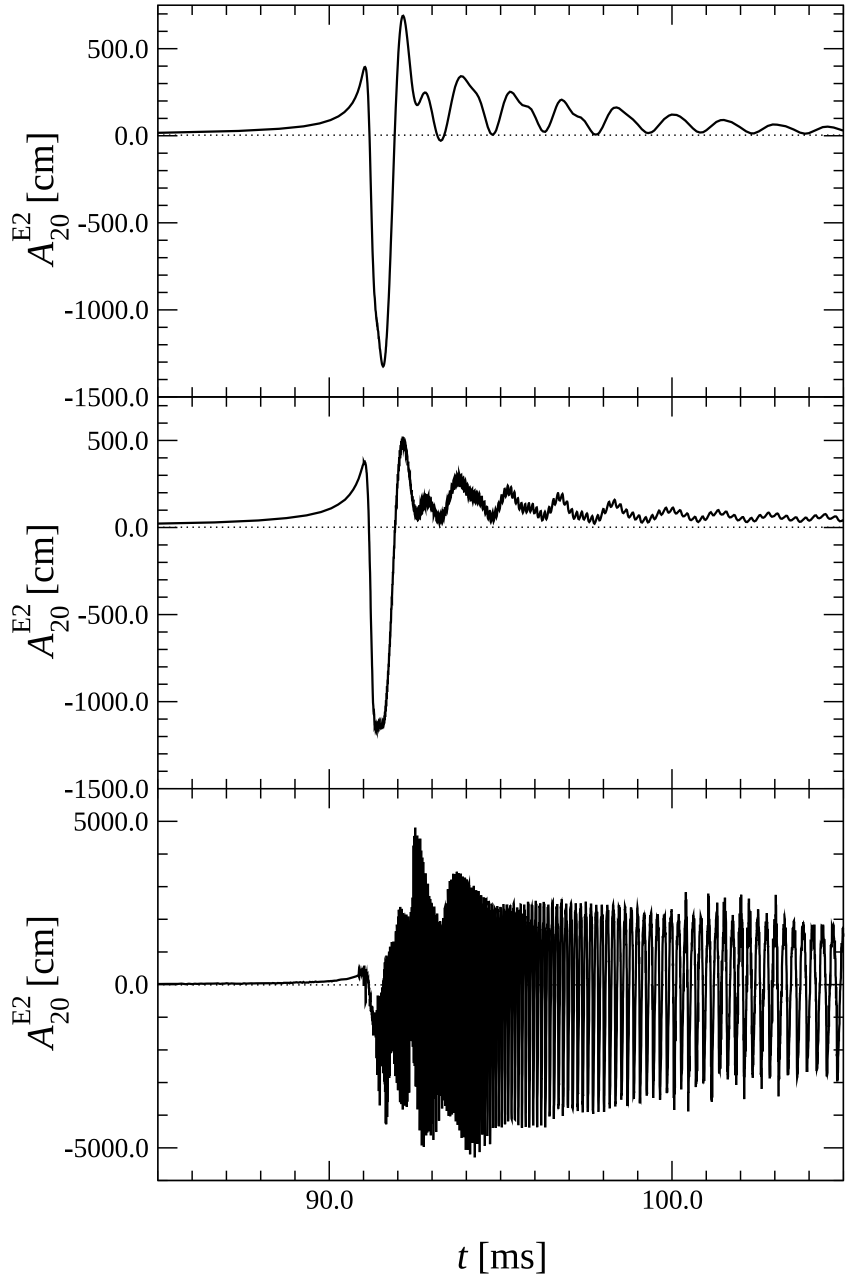

Figure C.1: *Comparison of the three numerical wave extraction methods used in our code, applied to the gravitational wave signal amplitude* A_{20}^{E2} *of model* A3B1G1*: The signal obtained by the stress formula (C.11) (upper panel) is smooth, while the signal obtained by the first moment of momentum density formula (C.10) (middle panel) exhibits unphysical high frequency noise during and after the bounce. The signal obtained by the standard quadrupole formula (C.9) (lower panel) is completely superimposed by noise with an amplitude much higher than the actual wave signal. Note that the vertical scale of the graph in the lower panel is much larger than the scale of the other two graphs.*

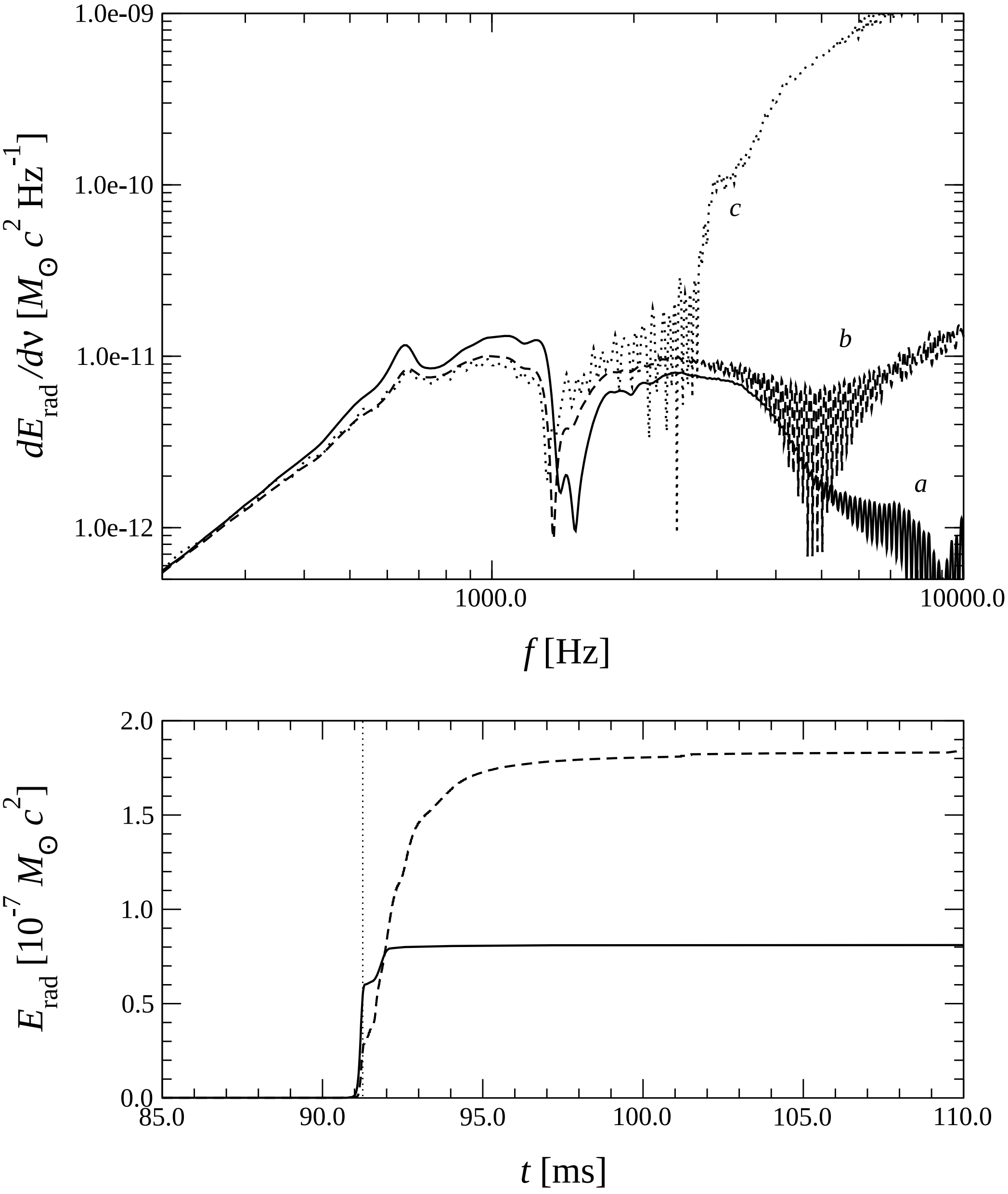

Figure C.2: *Comparison of the three numerical wave extraction methods used in our code, applied to the spectral energy distribution* $dE/d\nu$ *(upper panel) and the radiated energy* E_{rad} *over time (lower panel) of the gravitational wave signal in model* A3B1G1*: In the low frequency range the energy spectra of the signals obtained with the stress formula (solid line, a), the first moment of momentum density formula (dashed line, b), and the standard quadrupole formula (dashed-dotted line, c) coincide closely. At high frequencies, the methods involving a first and second order time derivative exhibit much higher energy contributions due to high frequency numerical noise in the wave signal, whereas for the stress formula the energy spectrum falls off exponentially. In the lower panel the time evolution of* E_{rad} *is plotted for the signal obtained with the stress formula (solid line) and with the first moment of momentum density formula (dashed line). The dotted vertical line marks the time of bounce* t_{b}.

large amount. As a result of these apparent problems with the numerical implementation of the radiation formulas involving time derivatives, we have chosen to use the stress formula (C.11) for the calculation of waveforms in all our simulations. However, we note again, that this is an entirely numerical effect, and the three Equations (C.9, C.10, C.11) are analytically equivalent. The property of the numerical implementation of the stress formula (C.11) to correctly represent the actual quadrupole wave amplitude is demonstrated for the two collapse models A3B2G4 and A3B3G1 in Figure C.3.

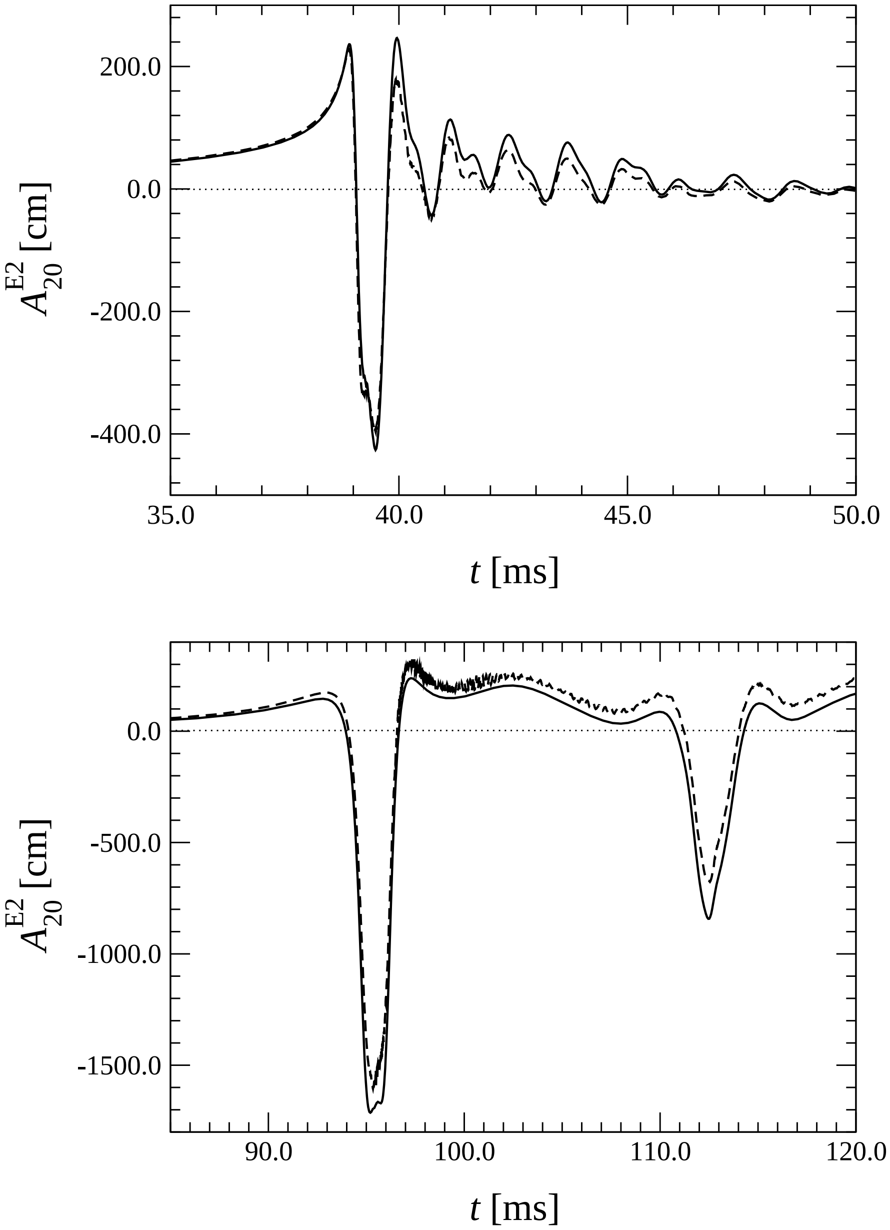

Figure C.3: *Comparison of the gravitational wave signal amplitude* A_{20}^{E2} *obtained by using the stress formula (waveform I; solid lines) and the first moment of momentum density formula (waveform II; dashed lines): In the waveform of the regular collapse model* A3B2G4 *(upper panel), all features of waveform I are very well captured by waveform II, and the amplitudes of the oscillations coincide closely for both waveforms. In this model the first moment of momentum density formula yields a waveform with very little noise. The two waveforms for the multiple bounce models* A3B3G1 *match also very well; however, during the first peak, waveform I, which is calculated using the stress formula, develops an offset compared to waveform II. Note the typical high-frequency noise in waveform II of this model right after the first bounce.*

C.5 Ambiguities of the Quadrupole Formula in Relativity

In a mathematically strict sense the multipole expansion of the radiation field (C.4) is only defined on a flat Minkowski background spacetime, on which the gravitational waves propagate as a linear perturbation. However, the multipole amplitudes and the tensor harmonics, although defined in flat spacetime, contain information about the wave source, which in general is situated in the strong field and high velocity region. This situation is resembled in our simulations, where the formulation for the gravitational waves, calculated by the different quadrupole methods, is valid only for large radii $r \gg R_{\text{iron core}}$ outside the computational domain. On the other hand, the quadrupole moment A_{20}^{E2} is computed as a spatial integral over the relativistic matter in a curved spacetime, as the metric $g_{\mu\nu}$ is certainly not Minkowskian.

However, in the Newtonian quadrupole formulation for $h_{\theta\theta}^{\text{TT}}$, the quadrupole moment A_{20}^{E2} is only the Newtonian approximation of the general moment $\tilde{A}_{20}^{\text{E2}}$ for a relativistic source. This approximation can give rise to several ambiguities in the quadrupole formula, especially in the stress formulation (which we use in the following investigation):

Covariant velocities:

In the Newtonian quadrupole formula, the physical velocities $v_i^{\text{phys}} = (v_r, v_\theta, v_\varphi)$ are used instead of the covariant three-velocity components v_i, which are the natural velocities of the general relativistic hydrodynamics. We have chosen the following natural transformation to get the physical velocities as the Newtonian limit of v_i:

$$v_i^{\text{phys}} = \sqrt{\delta_i^j v_i v^j} = \sqrt{\gamma^{ij}} v_j. \tag{C.13}$$

This formulation is equivalent to the one used in the boundary condition for the velocity components (see Equations (5.4–5.6)).

Limit of the density:

The relativistic expressions for the density ρ and $\varepsilon = \rho\epsilon$ have the same Newtonian limit ρ, which shows up in the stress formula (C.11) directly, and implicitly via the equation for the Newtonian potential Φ (C.12). In practice, the use of either of the relativistic generalizations of the Newtonian density leads to only marginal differences in the gravitational wave signal.

Radius coordinate:

Whereas in the Newtonian formulation, which is based on Euclidean geometry, the definition of the radius coordinate r is no source of ambiguity, in the Riemannian geometry of a curved spacetime the circumferential radius and the coordinate radius need not coincide. For example, we can use either the isotropic radius r, or the Schwarzschild radius $\hat{r}$ in Equation (C.11), as they have the same Newtonian limit. However, for a strongly gravitating source, whose extent R is of the order of the gravitational mass M, the deviation between r and $\hat{r}$ becomes important, which can be seen from the relation between both radial coordinates for a vacuum spacetime in Equation (5.9).

We have probed the implications of this ambiguity on the gravitational signal in our simulations. For this we consider the following transformation between the isotropic coordinate r and the Schwarzschild coordinate $\hat{r}$ in the line element of a three-metric with zero off-diagonal elements:

$$d\sigma^2 = \phi^4 dr^2 + \phi^4 r^2 d\Omega = A^2 d\hat{r}^2 + \hat{r}^2 d\Omega. \tag{C.14}$$

This yields the transformation expressions for the radial coordinates and the metric functions:

$$\hat{r} = \phi^2 r, \qquad A = \left(1 + \frac{2r}{\phi}\frac{\partial\phi}{\partial r}\right)^{-1}. \tag{C.15}$$

The use the Schwarzschild radius coordinate $\hat{r}$ instead of the isotropic radius coordinate r in the expression for the radiation quadrupole leads to an increase of the quadrupole amplitude A^{E2}_{20} of up to 5% without changing the shape and frequencies of the signal significantly. This amplification of A^{E2}_{20} is due to the effective increase in the radius $\hat{r}$ with respect to r: $\hat{r}(r) > r$.

From our point of view, there is no physical motivation to give preference to either of the two radius coordinates. The waveforms in this thesis have all been obtained using the isotropic radius, as this is the principal coordinate in our code.

Newtonian gravitational potential:

The most problematic issue in the stress formula (C.11) is the correct treatment of the Newtonian potential derivative terms, notably the expressions $\partial_r\Phi$ and $\partial_\theta\Phi$: Let us consider a rapidly rotating axisymmetric neutron star model in equilibrium. Then no matter how dense the matter distribution is, or how rapid the rotation, as long as the model is both analytically and numerically stable, the gravitational wave emission should be zero, because such a configuration, at least in perfect equilibrium, has a constant mass quadrupole moment. (In practice its gravitational wave signal will oscillate with small amplitude around zero due to numerical truncation errors.)

This vanishing gravitational wave emission is reflected in the radiation stress formula by a cancellation of the six single terms in the integral. For an equilibrium solution in Newtonian gravity, the sum of the terms will be, at least analytically, balanced out to zero. However, as the radiation stress formula in valid only in Newtonian approximation, for a relativistic neutron star model the balance between the single terms, particularly the large terms involving the rotational velocity and the derivatives of the potential Φ, need not work. This is indeed the case, as the left panel of Figure C.4 illustrates. There we plot the gravitational wave amplitude A^{E2}_{20}, obtained by using the stress formula, for the rapidly rotating neutron star equilibrium model from Section 6.2. While in a Newtonian model the wave amplitude would oscillate around zero (due to initial small density oscillations) and also be damped away to zero, for the relativistic model we see an unphysical non-negligible positive offset, which is due to the mismatch between the single terms in the radiation formula. In the formulations (C.9) and (C.10) this problem does not occur, as no large nonzero terms have to be canceled.

One strategy to get rid of this failed matching between the rotational velocity and the potential derivatives is to find a modified expression for the potential $\hat{\Phi}$ which takes into account the relativistic effects better than the Newtonian Φ. In fact there are other

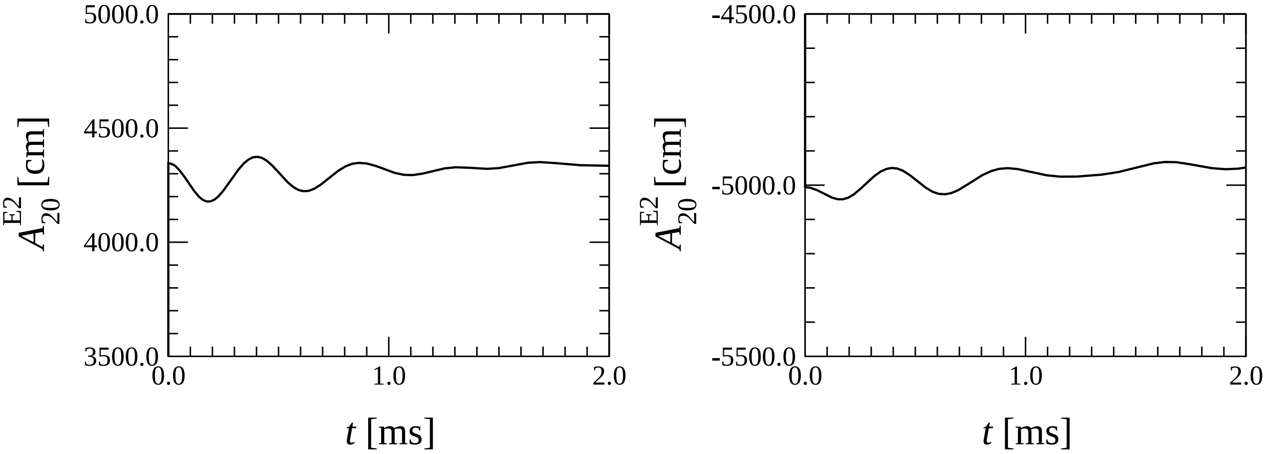

Figure C.4: *Offset in the gravitational wave amplitude* A_{20}^{E2} *of a rotating neutron star model for different formulation of the potential term in the stress formula: If the Newtonian potential* Φ *is used, the wave signal possesses a large positive offset (left panel); if the combination of metric components* $\hat{\Phi}$ *is used, the offset is even higher, but negative (right panel). Both signals initially oscillate due to small oscillatory motions in the neutron star; these oscillations are damped away within a few rotation periods.*

formulations for the gravitational potential which are equivalent up to the first post-Newtonian order [14]. One possibility is to set $-(1+2\hat{\Phi})$ equal to some metric components. Two such expressions are the following, where the metric components are the square root of the trace of $g_{\mu\nu}$, and the conformal factor ϕ^4, respectively:

$$\hat{\Phi} = \frac{1}{2}(1 - \alpha\phi^6), \qquad \hat{\Phi} = \frac{1}{2}(1 - \phi^4). \tag{C.16}$$

We have chosen to take the latter expression in Equation (C.16). Replacing Φ by $\hat{\Phi}$ in the stress formula then yields an even larger, but now negative, offset in the gravitational wave signal, as can be seen in the right panel of Figure C.4. Thus by combining Φ and $\hat{\Phi}$ as a weighted sum $\tilde{\Phi} = (\hat{\Phi} + a\Phi)/(1+a)$, we can bring the offset to zero. It turns out that the weight factor is nearly constant for a large variety of rotating neutron star models. By comparing the wave signal obtained from such a modified potential $\tilde{\Phi}$ to for example the one obtained by the SQF, one can ensure that the offset has been suppressed. This can be seen for a typical collapse waveform in Figure C.5. Additionally, with this weighting method, the amplitude and shape of the waveform is captured correctly (see Figure C.3 in Section C.4). With this method we are able to apply the numerically superior stress formula for gravitational radiation to our relativistic collapse simulations.

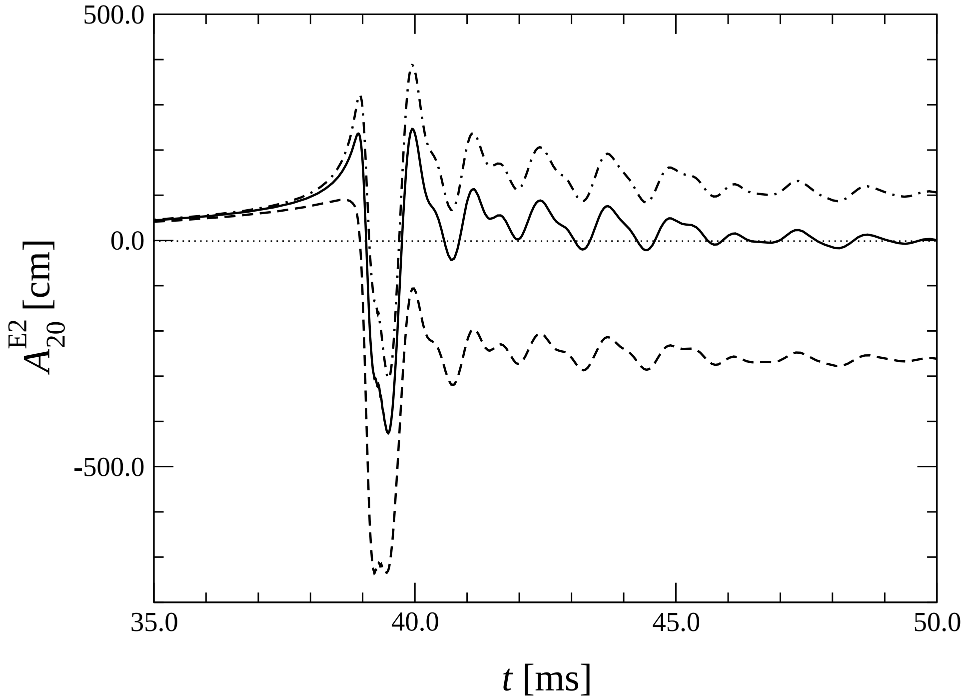

Figure C.5: *Reduction of the offset in the gravitational wave amplitude* A_{20}^{E2} *in the rotational core collapse model* A3B2G4 *with the weighting method applied to the stress formula: If the Newtonian potential* Φ *is used, the wave signal possesses a large positive offset (dashed-dotted line); if the combination of metric components* $\hat{\Phi}$ *is used, a large negative offset occurs (dashed line). A weighted sum of these two signals yields a waveform with practically zero offset (solid line). This combined signal exhibits no high frequency noise, as its constituents have been obtained using the stress formula.*

Appendix D

Density Evolution and Gravitational Wave Signal Catalogue

In this chapter we present plots of the evolution of the central density ρ_c (or, for the toroidal A4 runs with $A = 10^7$ cm, the maximum density ρ_max), and the gravitational wave signal amplitude A_{20}^E2 for all 26 simulations in both relativistic and Newtonian gravity.

The corresponding maxima of ρ_c and A_{20}^E2 are listed in Tables 7.1–7.3 and Tables 7.4–7.6, respectively.

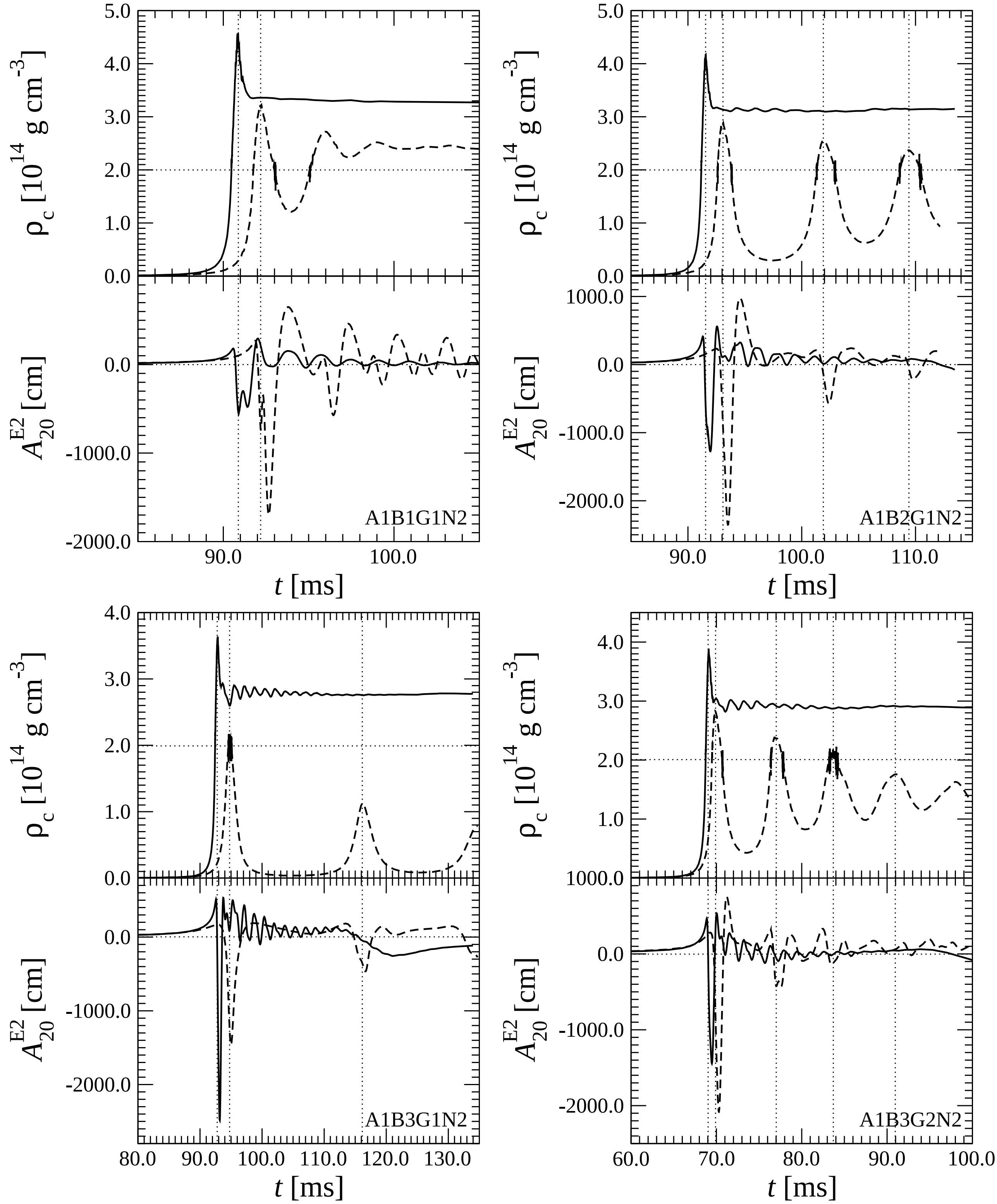

Figure D.1: *Evolution of the central density and gravitational wave signal in the relativistic (solid lines) and Newtonian (dashed lines) simulation of models* A1B1G1 *(upper left panel),* A1B2G1 *(upper right panel),* A1B3G1 *(lower left panel), and* A1B3G2 *(lower right panel): The central density* ρ_c *is plotted in the upper graphs, the signal amplitude* A^{E2}_{20} *in the lower graphs. The horizontal dotted lines in the density plots mark the nuclear density, the vertical dotted lines mark the times of maximum central density* t_b.

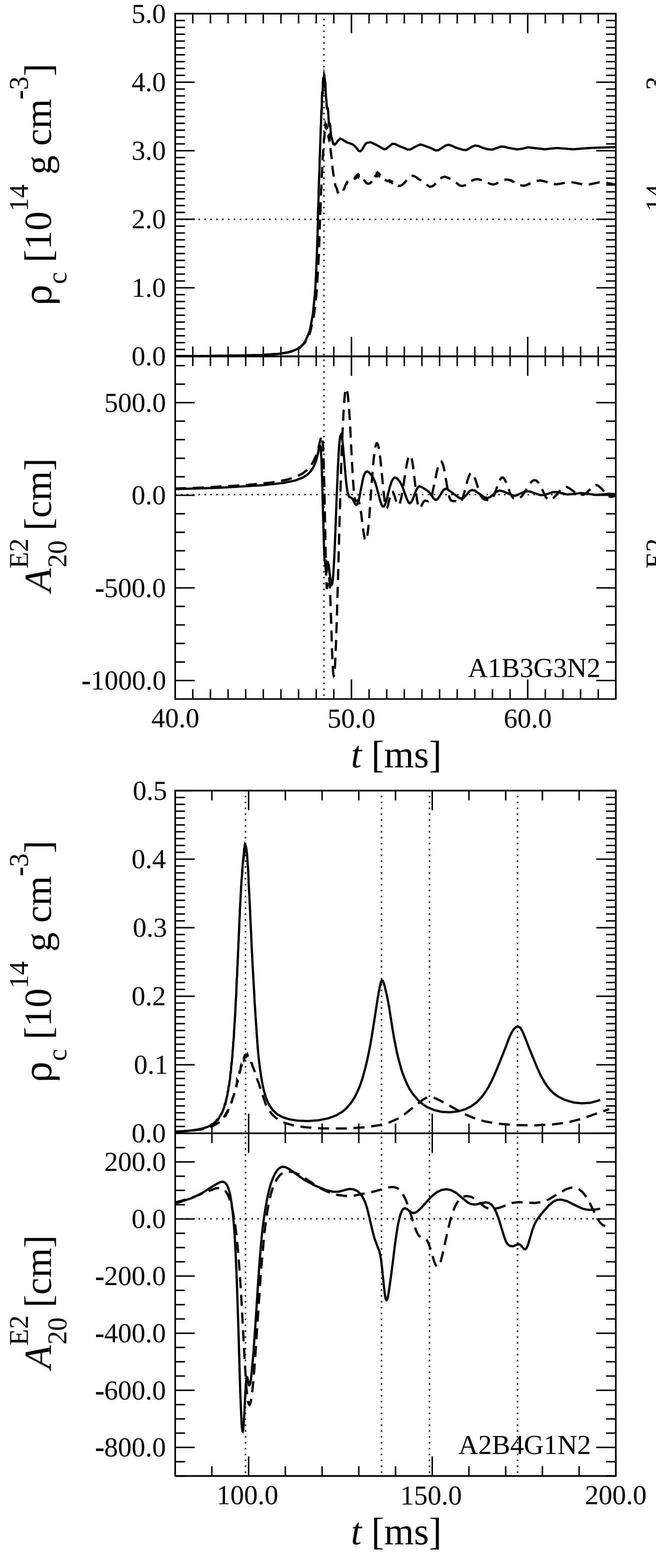

Figure D.2: *Evolution of the central density and gravitational wave signal in the relativistic (solid lines) and Newtonian (dashed lines) simulation of models* A1B3G3 *(upper left panel),* A1B3G5 *(upper right panel), and* A2B4G1 *(lower left panel): The central density ρ_{c} is plotted in the upper graphs, the signal amplitude A_{20}^{E2} in the lower graphs. The horizontal dotted lines in the density plots mark the nuclear density, the vertical dotted lines mark the times of maximum central density t_{b}.*

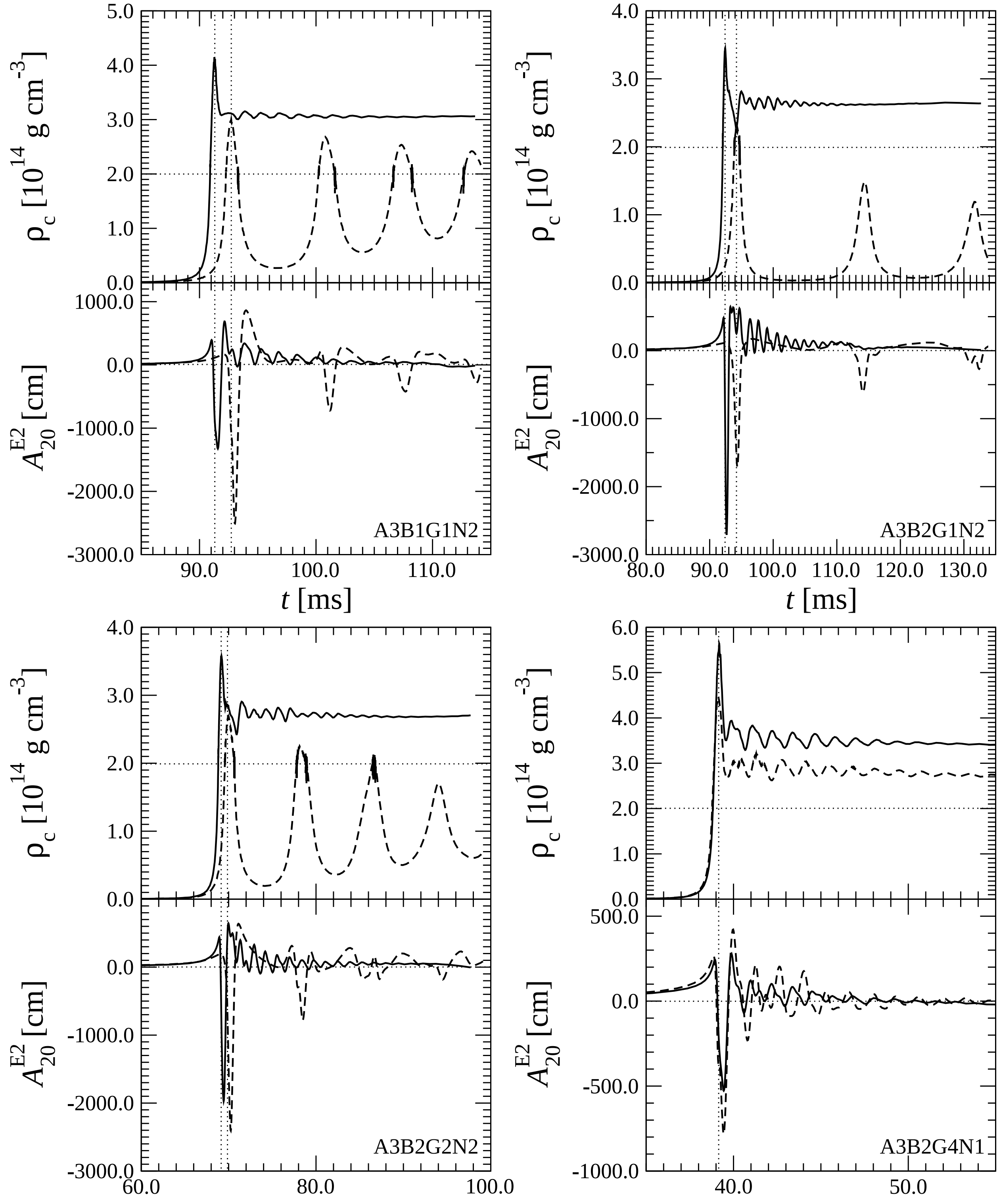

Figure D.3: *Evolution of the central density and gravitational wave signal in the relativistic (solid lines) and Newtonian (dashed lines) simulation of models* A3B1G1 *(upper left panel),* A3B2G1 *(upper right panel),* A3B2G2 *(lower left panel), and* A3B2G4$_{\mathrm{soft}}$ *(lower right panel): The central density* ρ_{c} *is plotted in the upper graphs, the signal amplitude* A_{20}^{E2} *in the lower graphs. The horizontal dotted lines in the density plots mark the nuclear density, the vertical dotted lines mark the times of maximum central density* t_{b}.

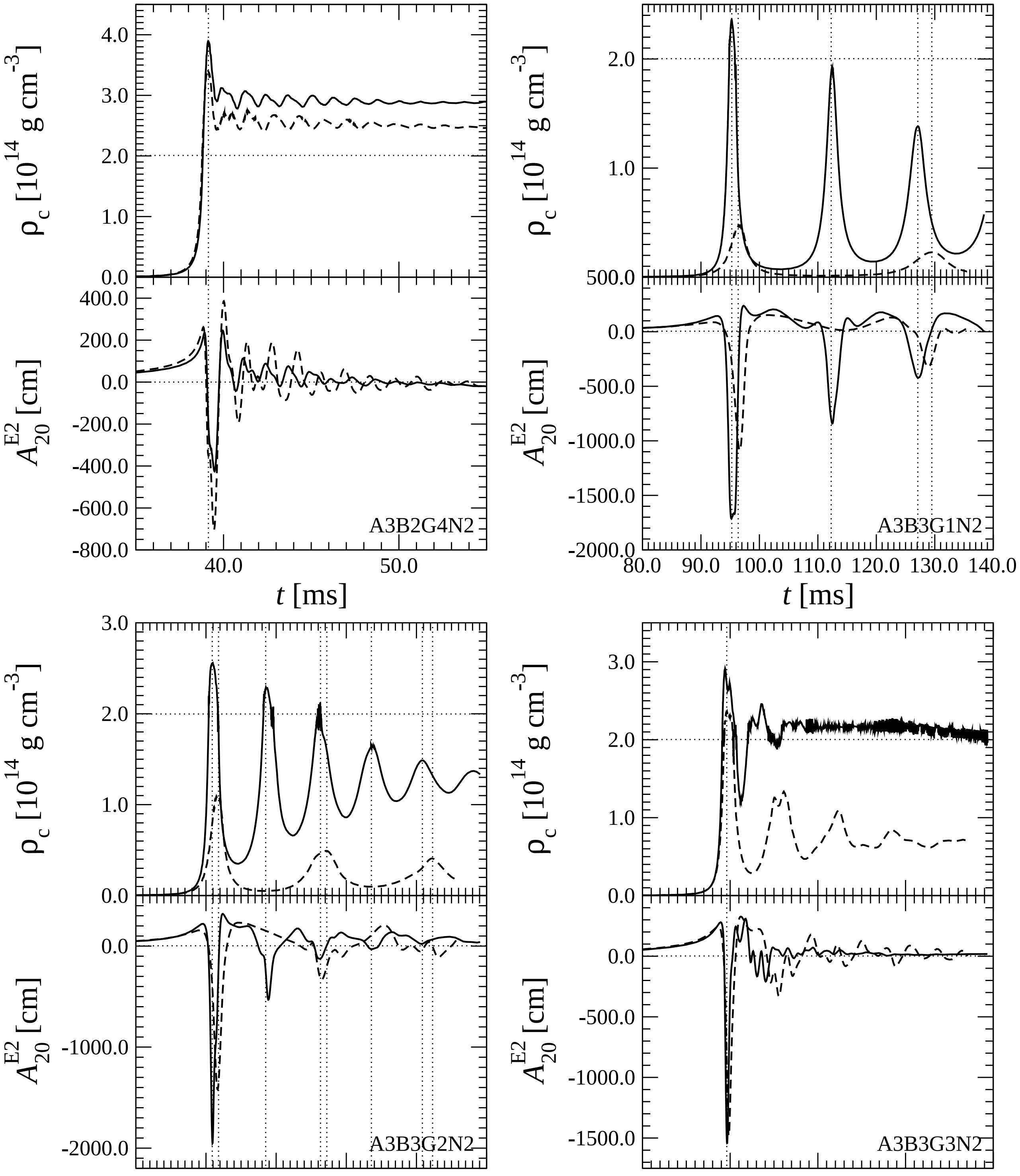

Figure D.4: *Evolution of the central density and gravitational wave signal in the relativistic (solid lines) and Newtonian (dashed lines) simulation of models* A3B2G4 *(upper left panel),* A3B3G1 *(upper right panel),* A3B3G2 *(lower left panel), and* A3B3G3 *(lower right panel): The central density ρ_c is plotted in the upper graphs, the signal amplitude A^E2_{20} in the lower graphs. The horizontal dotted lines in the density plots mark the nuclear density, the vertical dotted lines mark the times of maximum central density t_b.*

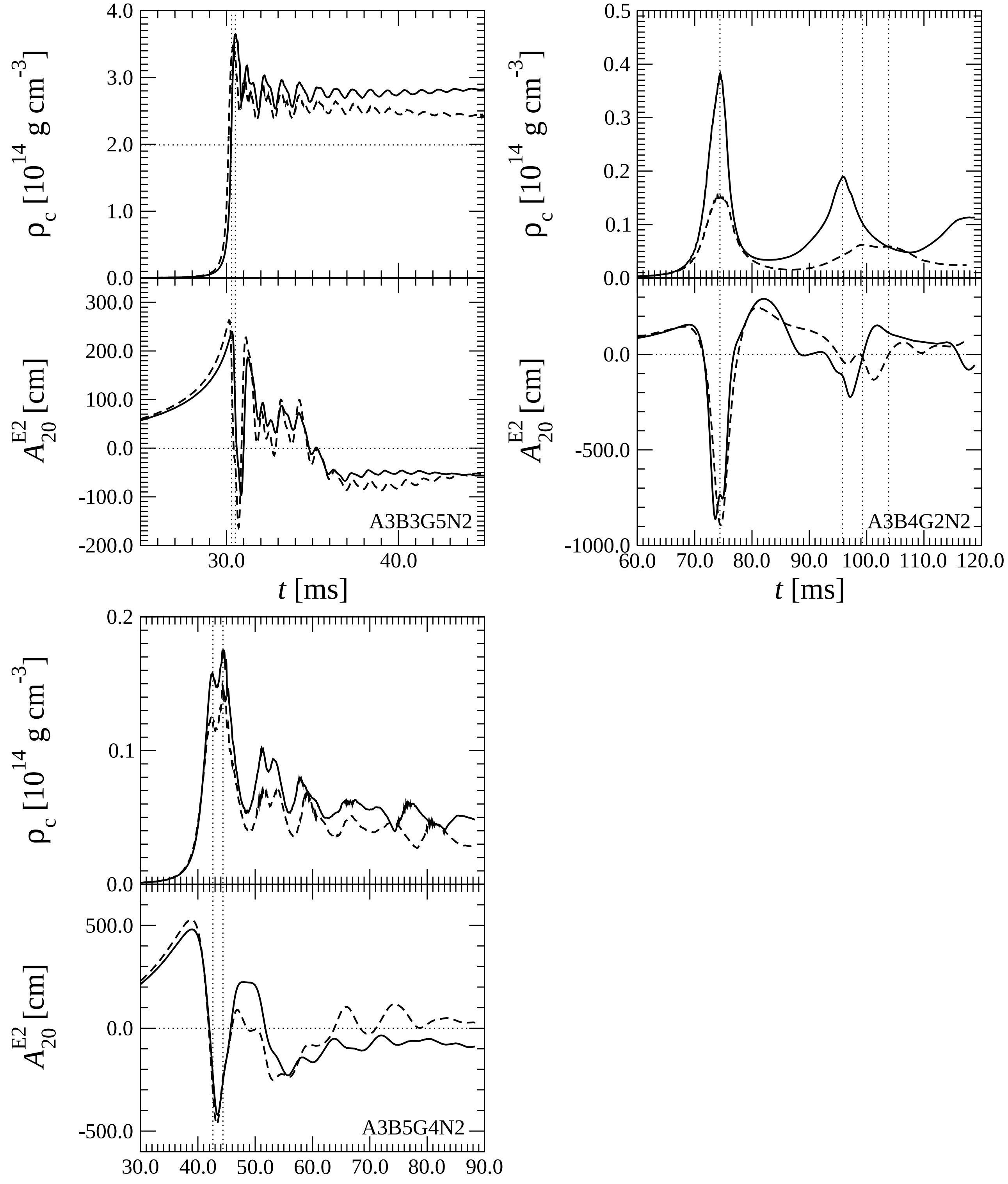

Figure D.5: *Evolution of the central density and gravitational wave signal in the relativistic (solid lines) and Newtonian (dashed lines) simulation of models* A3B3G5 *(upper left panel),* A3B4G2 *(upper right panel), and* A3B5G4 *(lower left panel): The central density* ρ_c *is plotted in the upper graphs, the signal amplitude* A^{E2}_{20} *in the lower graphs. The horizontal dotted lines in the density plots mark the nuclear density, the vertical dotted lines mark the times of maximum central density* t_b.

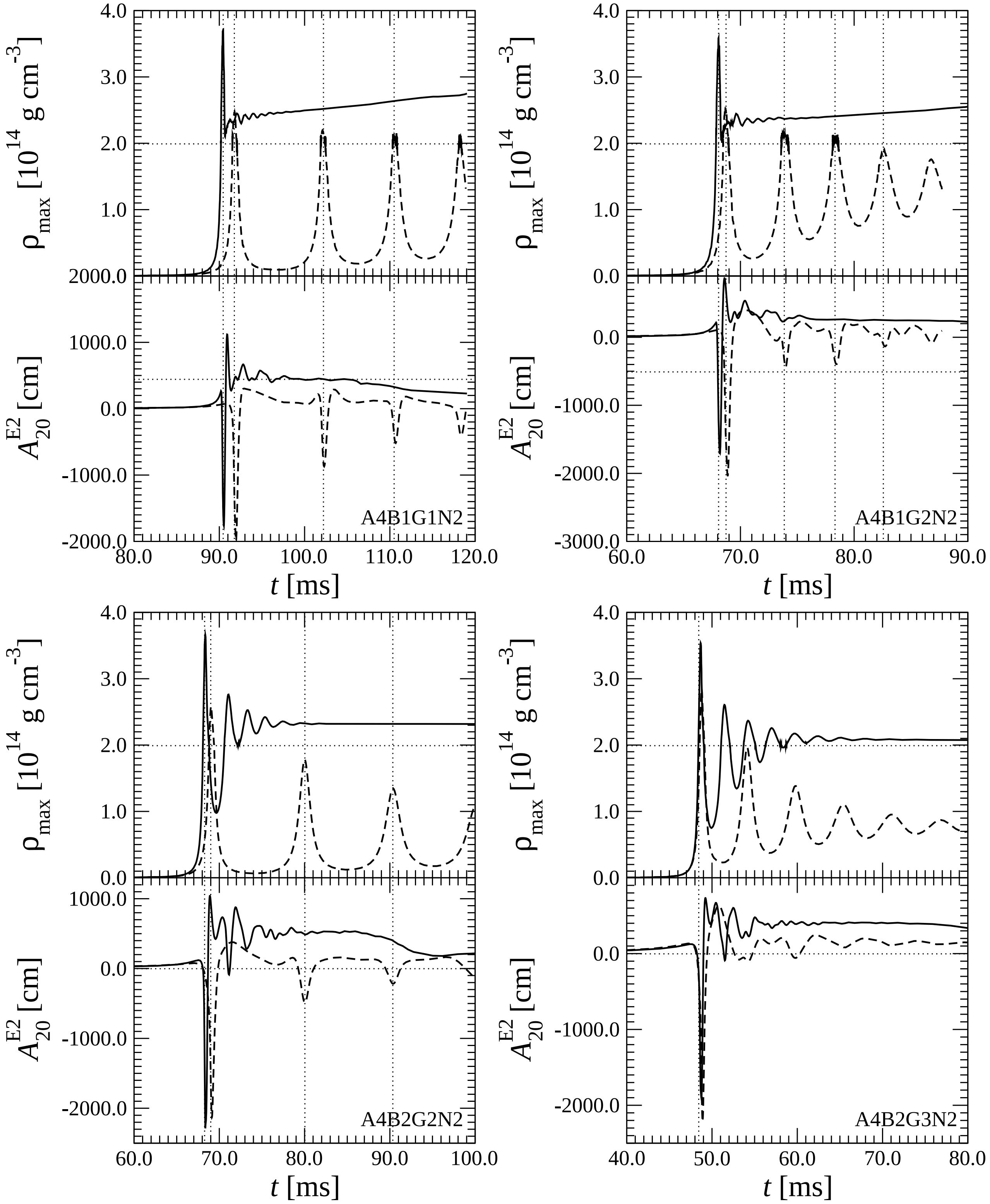

Figure D.6: *Evolution of the central density and gravitational wave signal in the relativistic (solid lines) and Newtonian (dashed lines) simulation of (the toroidal) models* A4B1G1 *(upper left panel),* A4B1G2 *(upper right panel),* A4B2G2 *(lower left panel), and* A4B2G3 *(lower right panel): The central density* ρ_c *is plotted in the upper graphs, the signal amplitude* A^E2_{20} *in the lower graphs. The horizontal dotted lines in the density plots mark the nuclear density, the vertical dotted lines mark the times of maximum central density* t_b.

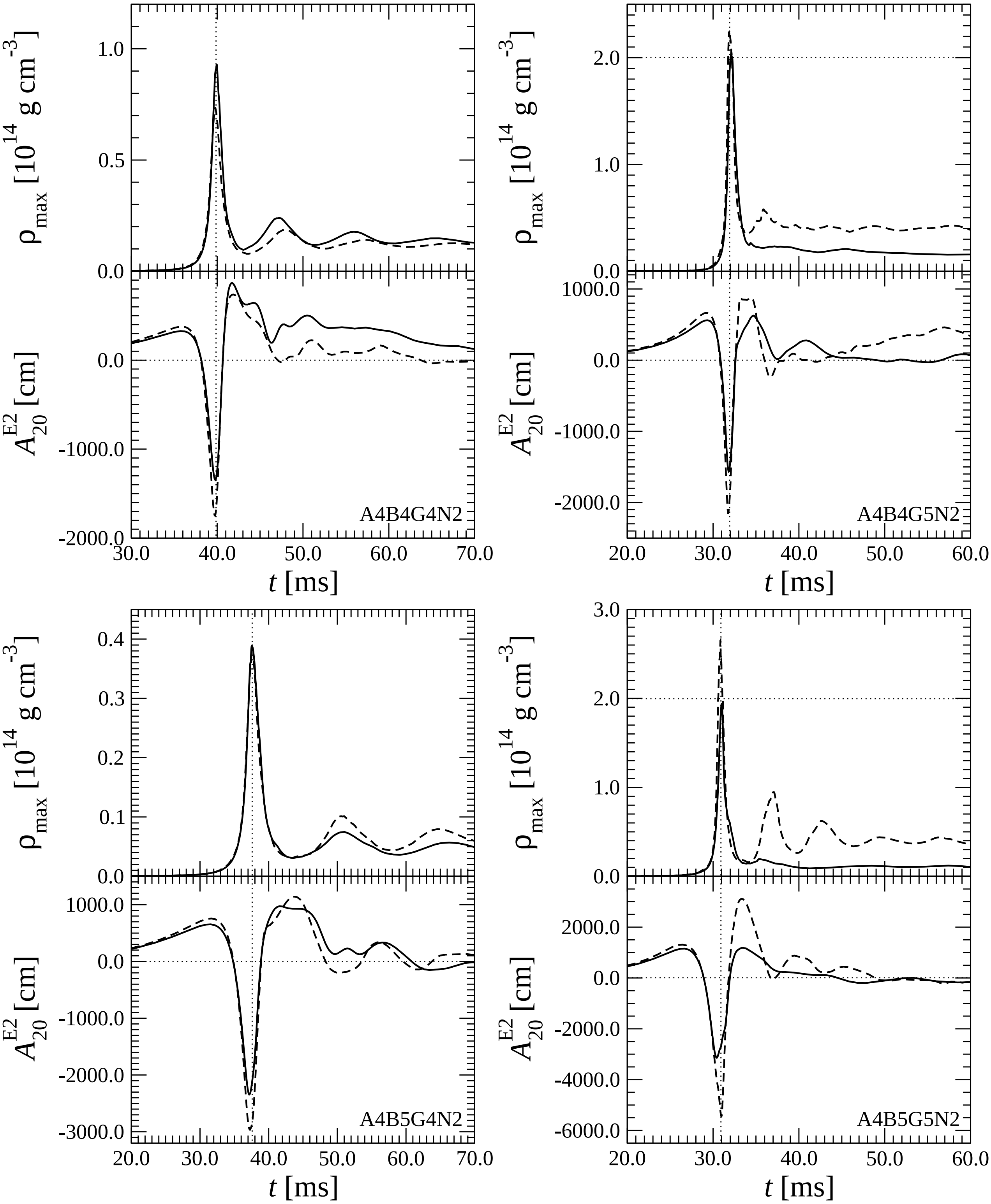

Figure D.7: *Evolution of the central density and gravitational wave signal in the relativistic (solid lines) and Newtonian (dashed lines) simulation of (the toroidal) models* A4B4G4 *(upper left panel),* A4B4G5 *(upper right panel),* A4B5G4 *(lower left panel), and* A4B5G5 *(lower right panel): The central density* ρ_c *is plotted in the upper graphs, the signal amplitude* A_{20}^{E2} *in the lower graphs. The horizontal dotted lines in the density plots mark the nuclear density, the vertical dotted lines mark the times of maximum central density* t_b.

Appendix E

Acknowledgments

Many people have contributed to making this thesis a success. First of all, I would like to thank my parents for their continuous love and support, and their tolerance with my sometimes unconventional lifestyle.

I am deeply indebted to my advisor E. Müller, whose door was always open to my numerous visits. His scientific expertise and friendly company have helped to guide me in the course of this project, while he has managed to leave me enough freedom to experiment on my own. I also want to thank him for his thorough proof-reading of the thesis.

J.A. Font's profound knowledge of relativistic hydrodynamics has cleared many obstacles put in my way by the unfathomable mysteries of general relativity and tensor calculus. He has always managed to cheer me up in the sometimes depressing moments resulting from codes being unstable and full of bugs. (Now the code is bug-free. Period.)

I also want to gratefully acknowledge J.Mª Ibáñez for suggesting this project, and G. Schäfer for introducing us to the CFC formalism. At the Max-Planck-Institut für Astrophysik, among others particularly W. Hillebrandt, T. Janka, M. Rampp, K. Kifonidis, and M.A. Aloy have contributed significantly to this work with many discussions, helpful suggestions and by sharing with me their tricks of the trade.

I am also very grateful to Y. Eriguchi for providing me with his code for constructing rotating polytropes in relativity, which has become the basis of my initial data solver, and to N. Stergioulas, whose RNS code I have used for calibration purposes. The discussions with M. Bruni have enabled me to get a grip on quantifying the accuracy of the CFC approximation. R. Fischer from NEC has made very helpful suggestions during my early attempts to solve the system of metric equations.

My various office mates have also made my time at the institute very enjoyable. They have generously overlooked my little peculiarities. Last but not least I want to express my appreciation for the financial support by the Max-Planck-Institut für Astrophysik and the Max-Planck-Gesellschaft, especially for the generous travel program.

Bibliography

[1] Abramowitz, M., and Stegun, I., *Handbook of mathematical functions*, (Dover, 1974).

[2] Alcubierre, M., Allen, G., Brügmann, B., Lanfermann, G., Seidel, E., Suen, W.-M., and Tobias, M., "Gravitational collapse of gravitational waves in 3D numerical relativity", *Phys. Rev. D*, **61**, 041501, (2000).

[3] Alcubierre, M., Brügmann, B., Dramlitsch, T., Font, J.A., Papadopoulos, P., Seidel, E., Stergioulas, N., and Takahashi, R., "Towards a stable numerical evolution of strongly gravitating systems in general relativity: The conformal treatments", *Phys. Rev. D*, **62**, 044034, (2000).

[4] Allen, G., Anderson, N., Kokkotas, K., and Schutz, B., "Gravitational waves from pulsating stars: Evolving the perturbation equations for a relativistic star", *Phys. Rev. D*, **58**, 124012, (1998).

[5] Aloy, M.A., Ibáñez, J.M$^{\underline{a}}$, Martí, J.M$^{\underline{a}}$, Gómez, J.L., and Müller, E., "High-resolution three-dimensional simulations of relativistic jets", *Astrophys. J.*, **523**, L125–L128, (1999).

[6] Aloy, M.A., Müller, E., Ibáñez, J.M$^{\underline{a}}$, Martí, J.M$^{\underline{a}}$, and MacFadyen, A., "Relativistic jets from collapsars", *Astrophys. J. Lett.*, **531**, L119–L122, (2000).

[7] Arnett, W.D., Bahcall, J.N., Kirshner, R.P., and Woosley, S.E., "Supernova 1987A", *Ann. Rev. Astron. Astrophys.*, **27**, 629–700, (1989).

[8] Arnowitt, R., Deser, S., and Misner, C.W., "The dynamics of general relativity", in Witten, L., ed., *Gravitation: An introduction to current research*, 227–265, (Wiley, New York, U.S.A., 1962).

[9] Bahcall, N., Ostriker, J.P., Perlmutter, S., and Steinhardt, P.J., "The cosmic triangle: Revealing the state of the Universe", *Science*, **284**, 1481–1488, (1999).

[10] Baker, J., Brandt, S., Campanelli, M., Lousto, C.O., Seidel, E., and Takahashi, R., "Nonlinear and perturbative evolution of distorted black holes. II. Odd-parity modes", *Phys. Rev. D*, **62**, 127701, (2000).

[11] Banyuls, F., Font, J.A., Ibáñez, J.M$^{\underline{a}}$, Martí, J.M$^{\underline{a}}$, and Miralles, J.A., "Numerical $\{3+1\}$ general relativistic hydrodynamics: A local characteristic approach", *Astrophys. J.*, **476**, 221–231, (1997).

[12] Baumgarte, T.W., and Shapiro, S.L., "On the numerical integration of Einstein's field equations", *Phys. Rev. D*, **59**, 024007, (1999).

[13] Bethe, H.A., and Wilson, J.R., "Revival of stalled supernova shock by neutrino heating", *Astrophys. J.*, **295**, 14–23, (1985).

[14] Blanchet, L., Damour, T., and Schäfer, G., "Post-Newtonian hydrodynamics and post-Newtonian gravitational wave generation for numerical relativity", *Mon. Not. R. Astron. Soc.*, **242**, 289–305, (1990).

[15] Brandt, S.R., and Seidel, E., "Evolution of distroted rotating black holes. I. Methods and tests", *Phys. Rev. D*, **52**, 856–869, (1995).

[16] Burrows, A., Hayes, J., and Fryxell, B.A., "On the nature of core-collapse supernova explosions", *Astrophys. J.*, **450**, 830–850, (1995).

[17] Butterworth, E.M., and Ipser, J.R., "On the structure and stability of rapidly rotating fluid bodies in general relativity: I. The numerical method for computing structure and its application to uniformly rotating homogenous bodies", *Astrophys. J.*, **204**, 200–223, (1976).

[18] Cardall, C.Y., Mezzacappa, A., and Liebendoerfer, M., "NewtonPlus: Approximate relativity for supernova simulations", *Phys. Rev. D*, submitted, (2001).

[19] Colella, P., and Woodward, P.R., "The piecewise parabolic method (PPM) for gas-dynamical simulations", *J. Comput. Phys.*, **54**, 174–201, (1984).

[20] Colgate, S.A., and White, R.H., "The hydrodynamical behavior of supernovae explosions", *Astrophys. J.*, **143**, 626–681, (1966).

[21] Cook, G.B., "Initial data for numerical relativity", *Living Reviews in Relativity*, **3**, (2000). URL: http://www.livingreviews.org/Articles/Volume3/2000-5cook/.

[22] Cook, G.B., Shapiro, S.L., and Teukolsky, S.A., "Testing a simplified version of Einstein's equations for numerical relativity", *Phys. Rev. D*, **53**, 5533–5540, (1996).

[23] Dimmelmeier, H., *Numerical calculations of hydrodynamic gravitational collapse and its observational consequences in scalar-tensor theories of gravity*, Diploma thesis, (Universität Regensburg, Regensburg, Germany, 1998).

[24] Donat, R., and Marquina, A., "Capturing shock reflections: An improved flux formula", *J. Comput. Phys.*, **125**, 42–58, (1996).

[25] Eddington, R.S., *The mathematical theory of relativity*, (Cambridge University Press, Cambridge, U.K., 1923).

[26] Eriguchi, Y., and Müller, E., "A general computational method for obtaining equilibria of self-gravitating and rotating gases", *Astron. Astrophys.*, **146**, 260–268, (1985).

[27] Eulderink, F., and Mellema, G., "General relativistic hydrodynamics with a Roe solver", *Astron. Astrophys. Suppl. Ser.*, **110**, 587–623, (1995).

[28] Evans, C.R., “An approach for calculating axisymmetric gravitational collapse”, in Centrella, J.M., ed., *Dynamical spacetimes and numerical relativity*, 3–39, (Cambridge University Press, Cambridge, U.K., 1986).

[29] Filippenko, A.V., “Optical spectra of supernovae”, *Ann. Rev. Astron. Astrophys.*, **35**, 309–355, (1997).

[30] Filippenko, A.V., “Optical observations of core-collapse supernovae”, in Holt, S.S., ed., *Young supernova remnants*, (American Institute of Physics, New York, U.S.A., 2001). to appear.

[31] Finn, L.S., “Supernovae, gravitational radiation, and the quadrupole formula”, in Evans, C.R., Finn, S.L., and Hobill, D.W., eds., *Frontiers in numerical relativity*, 126–145, (Cambridge University Press, Cambridge, U.K., 1989).

[32] Flanagan, É.É., “Possible explanation for star-crushing effect in binary neutron star simulations”, *Phys. Rev. Lett.*, **82**, 1354–1357, (1999).

[33] Flanagan, É.É., and Hughes, S.A., “Measuring gravitational waves from binary black hole coalescences: I. Signal to noise for inspiral, merger, and ringdown”, *Phys. Rev. D*, **57**, 4535–4565, (1998).

[34] Font, J.A., “Numerical hydrodynamics in general relativity”, *Living Reviews in Relativity*, **3**, (2000). URL: http://www.livingreviews.org/Articles/Volume3/2000-2font/.

[35] Font, J.A., Dimmelmeier, H., Gupta, A., and Stergioulas, N, “Axisymmetric modes of rotating relativistic stars in the Cowling approximation”, *Mon. Not. R. Astron. Soc.*, (2001). To appear.

[36] Font, J.A., Ibáñez, J.Mª, and Papadopoulos, P., “Non-axisymmetric relativistic Bondi-Hoyle accretion on to a Kerr black hole”, *Mon. Not. R. Astron. Soc.*, **305**, 920–936, (1999).

[37] Font, J.A., Miller, M., Suen, W.-M., and Tobias, M., “Three-dimensional numerical general relativistic hydrodynamics: Formulations, methods, and code tests”, *Phys. Rev. D*, **61**, 044011, (2000).

[38] Font, J.A., Stegioulas, N., and Kokkotas, K.D., “Nonlinear hydrodynamical evolution of rotating relativistic stars: Numerical methods and code tests”, *Mon. Not. R. Astron. Soc.*, **313**, 678–688, (2000).

[39] Frauendiener, J., “Numerical treatment of the hyperboloidal initial value problem for the vacuum Einstein equations. II. The evolution equations”, *Phys. Rev. D*, **58**, 064003, (1998).

[40] Friedman, J.L., Ipser, J.R., and Parker, L., “Rapidly rotating neutron star models”, *Astrophys. J.*, **304**, 115–139, (1986).

[41] Friedrich, H., “On the regular and the asymptotic characteristic initial value problem for Einstein’s vacuum field equations”, *Proc. R. Soc. London, Ser. A*, **375**, 169–184, (1981).

[42] Friedrich, H., and Rendall, A., "The Cauchy problem for the Einstein equations", *Lect. Notes Phys.*, **540**, 127, (2000).

[43] Fuller, G.M., "Neutron shell blocking of electron capture during gravitational collapse", *Astrophys. J.*, **252**, 741–764, (1982).

[44] Garat, A., and Price, R.H., "Nonexistence of conformally flat slices of the Kerr spacetime", *Phys. Rev. D*, **61**, 124011, (2000).

[45] Godunov, S.K., Zabrodin, A.V., and Prokopov, G.P., "A computational scheme for two-dimensional non stationary problems of gas dynamics and calculation of the flow from a shock wave approaching a stationary state", *Zh. vych. mat.*, **1**, 1020–1050, (1961).

[46] Goldreich, P., and Weber, S.V., *Astrophys. J.*, **238**, 991–997, (1980).

[47] Gourgoulhon, E., private communication.

[48] Gourgoulhon, E., Grandclement, P., and Bonazzola, S., "Binary black holes in circular orbits. I. A global spacetime approach", *Phys. Rev. D*, (2001). Submitted.

[49] Hachisu, I., "A versatile method for obtaining structures of rapidly rotating stars", *Astrophys. J.*, **61**, 479–507, (1986).

[50] Harten, A., "On a class of high resolution total-variation-stable finite-difference schemes", *SIAM J. Numer. Analysis*, **21**, 1–23, (1984).

[51] Heger, A., Langer, N., and Woosley, S.E., "Presupernova evolution of rotating massive stars. I. Numerical method and evolution of the internal stellar structure", *Astrophys. J.*, **528**, 368–396, (2000).

[52] Herant, M., Benz, W., Hix, W.R., Fryes, C.L., and Colgate, S.A., "Inside the supernova: A powerful convective engine", *Astrophys. J.*, **435**, 339–361, (1994).

[53] Hillebrandt, W., "The equation of state of supernova and neutron star matter", in Eliezer, S., and Ricci, R.A., eds., *Proceedings of the international school of physics "Enrico Fermi" – Course CXIII*, 399–437, (North–Holland, Amsterdam, Netherlands, 1991).

[54] Hobill, D., Seidel, E., Smarr, L.L., and Suen, W.-M., "The head-on collision of two equal mass black holes", *Phys. Rev. D*, **52**, 2044–2058, (1995).

[55] Hough, J., and Rowan, S., "Gravitational wave detection by interferometry (Ground and space)", *Living Reviews in Relativity*, **3**, (2000). URL: http://www.livingreviews.org/Articles/Volume3/2000-3hough/.

[56] Hübner, P., "Method for calculating the global structure of (singular) spacetimes", *Phys. Rev. D*, **53**, 701–721, (1996).

[57] Hübner, P., "Numerical calculation of conformally smooth hyperboloidal data", *Class. Quantum Grav.*, **18**, 1421–1440, (2001).

[58] Hulse, R.A., "The discovery of the binary pulsar (PSR 1913+16)", *Rev.Mod.Phys.*, **66**, 699–710, (1994).

[59] Hulse, R.A., and Taylor, J.H., “Discovery of a pulsar in a binary system”, *Astrophys. J.*, **195**, L51–L53, (1975).

[60] Ibáñez, J.Mª, Aloy, M.A., Font, J.A., Martí, J.Mª, Miralles, J.A., and Pons, J.A., “Riemann solvers in general relativistic hydrodynamics”, in Toro, E.F., ed., *Godunov methods: theory and applications*, (Oxford, U.K., 2001).

[61] Janka, H.-T., Kifonidis, K., and Rampp, M., “Supernova explosions and neutron star formation”, in Blaschke, D., Glendenning, N.K., and Sedrakian, A.D., eds., *Proceedings of the Workshop on Physics of Neutron Star Interiors*, (Springer, Berlin, Germany). In press.

[62] Kifonidis, K., Müller, E., and Plewa, T., “Non-spherical core collapse supernovae and nucleosynthesis”, in *Nucl. Phys. A – Proceedings of the conference ”Nuclei in the Cosmos 2000”*. To appear.

[63] Kifonidis, K., Plewa, T., Janka, H.-T., and Müller, E., “The first five minutes of a core collapse supernova: Multidimensional hydrodynamic models”, to appear, (2001).

[64] Kley, W., and Schäfer, G., “Relativistic dust disks and the Wilson-Mathews approach”, *Phys. Rev. D*, **60**, 027501, (1999).

[65] Komatsu, H., Eriguchi, Y., and Hachisu, I., “Rapidly rotating general relativistic stars – I. Numerical method and its application to uniformly rotating polytropes”, *Mon. Not. R. Astron. Soc.*, **237**, 355–379, (1989).

[66] Komatsu, H., Eriguchi, Y., and Hachisu, I., “Rapidly rotating general relativistic stars – II. Differentially rotating polytropes”, *Mon. Not. R. Astron. Soc.*, **239**, 153–171, (1989).

[67] Landau, L.D., and Lifshitz, E.M., *The classical theory of fields – Course of theoretical physics, volume 2*, (Butterworth–Heinemann, 1997), 4 edition.

[68] LeVeque, R.J., *Numerical methods for conservation laws*, (Birkhäuser, Basel, Switzerland, 1992), 2nd edition.

[69] LeVeque, R.J., “Nonlinear conservation laws and finite volume methods”, in Steiner, O., and Gautschy, A., eds., *Computational methods for astrophysical fluid flow. Saas-Fee Advanced Course 27*, 1–159, (Springer, Berlin, Germany, 1998).

[70] Lichnerovicz, A., “L’integration des équations de la gravitation relativiste et le problème des n corps”, *J. Math. Pures Appl.*, **23**, 37–63, (1944).

[71] Liebendoerfer, M., Mezzacappa, A., Thielemann, F.-K., Messer, O.E.B., Hix, W.R., and Bruenn, S.W., “Probing the gravitational well: No supernova explosion in spherical symmetry with general relativistic Boltzmann neutrino transport”, *Phys. Rev. D*, **63**, 103004, (2001).

[72] Linke, F., Font, J.A., Janka, H.-T., Müller, E., and Papadopoulos, P., “Spherical collapse of supermassive stars: neutrino emission and gamma-ray bursts”, *Astron. Astrophys.*, (2001). In press.

[73] Lorimer, D.R., "Binary and millisecond pulsars at the new millennium", *Living Reviews in Relativity*, **4**, (2001). URL: http://www.livingreviews.org/Articles/Volume4/2001-5lorimer/.

[74] MacFadyen, A.I., Woosley, S.E., and Heger, A., "Supernovae, jets, and collapsars", *Astrophys. J.*, **550**, 410–425, (2001).

[75] Martí, J.Mª, Ibáñez, J.Mª, and Miralles, J.A., "Numerical relativistic hydrodynamics: Local characteristic approach", *Phys. Rev. D*, **43**, 3794–3801, (1991).

[76] Martí, J.Mª, and Müller, E., "The analytical solution of the Riemann problem in relativistic hydrodynamics", *J. Fluid Mech.*, **258**, 317–333, (1994).

[77] Martí, J.Mª, and Müller, E., "Extension of the piecewise parabolic method to one-dimensional relativistic hydrodynamics", *J. Comput. Phys.*, **123**, 1–14, (1996).

[78] Martí, J.Mª, Müller, E., Font, J.A., and Ibáñez, J.Mª, "Morphology and Dynamics of Highly Supersonic Relativistic Jets", *Astrophys. J. Lett.*, **448**, L105–L109, (1995).

[79] Mathews, G.J., and Wilson, J.R., "Revised relativistic hydrodynamical model for neutron-star binaries", *Phys. Rev. D*, **61**, 127304, (2000).

[80] May, M.M., and White, R.H., "Hydrodynamic calculations of general-relativistic collapse", *Phys. Rev.*, **141**, 1232–1241, (1966).

[81] May, M.M., and White, R.H., "Stellar dynamics and gravitational collapse", in *Methods in computational physics*, volume 7, 219–258, (Academic Press, New York, U.S.A., 1967).

[82] Meier, D.L., Koide, S., and Uchida, Y., "Magnetohydrodynamic production of relativistic jets", *Science*, **291**, 84–92, (2001).

[83] Miller, M., private communication.

[84] Misner, C.W., and Sharp, D.H., "Relativistic equations for adiabatic, spherically symmetric gravitational collapse", *Phys. Rev.*, **136**, B571–B576, (1964).

[85] Misner, C.W., Thorne, K.S., and Wheeler, J.A, *Gravitation*, (W.H. Freeman, San Francisco, U.S.A., 1973).

[86] Mönchmeyer, R., Schäfer, G., Müller, E., and Kates, R.E., "Gravitational waves from the collapse of rotating stellar cores", *Astron. Astrophys.*, **246**, 417–440, (1991).

[87] Müller, E., "Simulation of astrophysical fluid flow", in Steiner, O., and Gautschy, A., eds., *Computational methods for astrophysical fluid flow. Saas-Fee Advanced Course 27*, 343–494, (Springer, Berlin, Germany, 1998).

[88] Müller, E., and Hillebrandt, W., "A magnetohydrodynamical supernova model", *Astron. Astrophys.*, **80**, 147–154, (1979).

[89] Müller, E., and Hillebrandt, W., "The collapse of rotating stellar cores", *Astron. Astrophys.*, **103**, 358–366, (1981).

[90] Müller, E., and Janka, H.-T., "Gravitational radiation from convective instabilities in type II supernova explosions", *Astron. Astrophys.*, **317**, 140–163, (1997).

[91] Murdin, P., and Murdin, L., *Supernovae*, (Cambridge University Press, Cambridge, U.K., 1978).

[92] Nakamura, K., Kajita, T., and Nakahata, M., "Kamiokande", in Fukugita, M., and Suzuki, A., eds., *Physics and astrophysics of neutrinos*, 249–387, (Springer, Tokyo, Japan, 1994).

[93] Nakamura, T., "General relativistic collapse of axially symmetric stars leading to the formation of rotating black holes", *Prog. Theor. Phys.*, **65**, 1876–1890, (1981).

[94] Norman, M.L., and Winkler, K.-H.A., "Why ultrarelativistic hydrodynamics is difficult", in Norman, M.L., and Winkler, K.-H.A, eds., *Astrophysical Radiation Hydrodynamics*, 449–476, (Reidel, Dordrecht, Netherlands, 1986).

[95] Papadopoulos, P., and Font, J.A., "Matter flows around black holes and gravitational radiation", *Phys. Rev. D*, **59**, 044014, (1999).

[96] Papadopoulos, P., and Font, J.A., "Relativistic hydrodynamics on spacelike and null surfaces: Formalism and computations of spherically symmetric", *Phys. Rev. D*, **61**, 024015, (2000).

[97] Penrose, R., *Phys. Rev. Lett.*, **10**, 21, (1963).

[98] Pons, J.A., Font, J.A., Ibáñez, J.Mª, Martí, J.Mª, and Miralles, J.A., "General relativistic hydrodynamics with special relativistic Riemann solvers", *Astron. Astrophys.*, **339**, 638–642, (1998).

[99] Pradier, T., Arnaud, N., Bizouard, M.-A., Cavalier, F., Davier, M., and Hello, P., "An efficient filter for detecting gravitational wave bursts in interferometric detectors", *LANL Preprint Server*, gr–qc/0010037, (2000).

[100] Press, W.H., Teukolsky, S.A., Vetterling, W.T., and Flannery, B.P., *Numerical recipes in C: The art of scientific programming*, (Cambridge University Press, Cambridge, U.K., 1992).

[101] Rampp, M., and Janka, H.-T., "Spherically symmetric simulation with Boltzmann neutrino transport of core collapse and post-bounce evolution of a 15 $M_\odot$ star", *Astrophys. J. Lett.*, **539**, L33–L36, (2000).

[102] Rampp, M., Müller, E., and Ruffert, M., "Simulations of non-axisymmetric rotational core collapse", *Astron. Astrophys.*, **332**, 969–983, (1998).

[103] Roe, P.L., "Approximate Riemann solvers, parameter vectors and difference schemes", *J. Comput. Phys.*, **43**, 357–372, (1981).

[104] Romero, J.V., Ibáñez, J.Mª, Martí, J.Mª, and Miralles, J.A., "A new spherically symmetric general relativistic hydrodynamical code", *Astrophys. J.*, **462**, 839–854, (1996).

[105] Saad, Y., and van der Vorst, H.A., “Iterative solution of linear systems in the 20-th century”, *J. Comp. Appl. Math.*, **123**, 1–33, (2000).

[106] Seidel, E., “Gravitational radiation from even-parity perturbations of stellar collapse: Mathematical formalism and numerical methods”, *Phys. Rev. D*, **42**, 1884–1907, (1990).

[107] Seidel, E., and Moore, T., “Gravitational radiation from realistic relativistic stars: Odd-parity fluid perturbations”, *Phys. Rev. D*, **35**, 2287–2296, (1987).

[108] Seidel, E., and Suen, W.-M., “Numerical relativity as a tool for computational astrophysics”, *J. Comput. Appl. Math.* Submitted.

[109] Shapiro, S.L., and Teukolsky, S.A., *Black holes, white dwarfs, and neutron stars*, (Wiley, New York, U.S.A., 1983).

[110] Shapiro, S.L., and Teukolsky, S.A., “Relativistic stellar dynamics on the computer”, in Centrella, J.M., ed., *Dynamical spacetimes and numerical relativity*, 74–100, (Cambridge University Press, Cambridge, U.K., 1986).

[111] Shibata, M., “Axisymmetric simulations of rotating stellar collapse in full general relativity – Criteria for prompt collapse to black holes”, *Prog. Theor. Phys.*, **104**, (2000).

[112] Shibata, M., and Nakamura, T., “Evolution of three-dimensional gravitational waves: Harmonic slicing case”, *Phys. Rev. D*, **52**, 5428–5444, (1995).

[113] Shu, C.W., and Osher, S.J., “Efficient implementation of essentially non-oscillatory shock-capturing schemes, II”, *J. Comput. Phys.*, **83**, 32–78, (1989).

[114] Siebel, F., Font, J.A., and Müller, E., “Characteristic numerical relativity applied to hydrodynamic studies of neutron stars”, *Electronic proceedings of the 9th Marcel Grossmann Meeting.* URL: http://www.icra.it/MG/mg9/mg9.htm.

[115] Siegler, S., and Riffert, H., “Smoothed particle hydrodynamics simulations of ultrarelativistic shocks with artificial viscosity”, *Astrophys. J.*, **531**, 1053–1066, (2000).

[116] Smarr, L.L., and York Jr., J.W., “Kinematical conditions in the construction of spacetime”, *Phys. Rev. D*, **17**, 2529–2551, (1978).

[117] Stark, R.F., and Piran, T., “A general relativistic code for rotating axisymmetric configurations and gravitational radiation: Numerical methods and tests”, *Comp. Phys. Rep.*, **5**, 221–264, (1987).

[118] Stergioulas, N., “Rotating stars in relativity”, *Living Reviews in Relativity*, **1**, (1998). URL: http://www.livingreviews.org/Articles/Volume1/1998-8stergio/.

[119] Stergioulas, N., and Font, J.A., “Nonlinear r-modes in rapidly rotating relativistic stars”, *Phys. Rev. Lett.*, **86**, 1148–1151, (2001).

[120] Stergioulas, N., and Friedman, J.L., “Comparing models of rapidly rotating relativistic stars constructed by two numerical methods”, *Astrophys. J.*, **444**, 306–311, (1995).

[121] Symbalisty, E.M.D., "Magnetorotational iron core collapse", *Astrophys. J.*, **285**, 729–746, (1984).

[122] Tassoul, J.-L., *Theory of rotating stars*, (Princeton University Press, Princeton, U.S.A., 1978).

[123] The Binary Black Hole Grand Challenge Alliance, "Stable characteristic evolution of generic 3-dimensional single-black-hole spacetimes", *Phys. Rev. Lett.*, **80**, 3915–3918, (1998).

[124] Thorne, K.S., "Multipole expansions of graviational radiation", *Rev. Mod. Phys.*, **52**, 299–339, (1980).

[125] Thorne, K.S., "Gravitational radiation – a new window onto the universe", *Rev. Mod. Astron.*, **10**, 1–28, (1997).

[126] Toro, E.F., *Riemann solvers and numerical methods for fluid dynamics – a practical introduction*, (Springer, Berlin, Germany, 1997).

[127] Totani, T., Sato, K., Dalhed, H.E., and Wilson, J.R., "Future detection of supernova neutrino burst and explosion mechanism", *Astrophys. J.*, **496**, 216–225, (1998).

[128] Tubbs, D., and Schramm, D., "Neutrino opacities at high temperatures and densities", *Astrophys. J.*, **201**, 467–488, (1975).

[129] van Leer, B.J., "Towards the ultimate conservative difference scheme. V. A second order sequel to Godunov's method", *J. Comput. Phys.*, **32**, 101–136, (1979).

[130] van Riper, K.A., "The hydrodynamics of stellar collapse", *Astrophys. J.*, **221**, 304–319, (1978).

[131] van Riper, K.A., "General relativistic hydrodynamics and the adiabatic collapse of stellar cores", *Astrophys. J.*, **232**, 558–571, (1979).

[132] von Neumann, J., and Richtmyer, R.D., "A method for the numerical calculation of hydrodynamic shocks", *J. Appl. Phys.*, **21**, 232–237, (1950).

[133] Wald, R., *General relativity*, (University of Chicago Press, Chicago, U.S.A., 1984).

[134] White, S.D.M., "Formation and evolution of galaxies", in Schaeffer, R., Silk, J., Spiro, M., and Zinn-Justin, J., eds., *Cosmology and large scale structure: Les Houches session LX, 1993*, 349–430, (Elsevier, Amsterdam, Netherlands, 1996).

[135] Will, C.M., *Theory and experiment in gravitational physics*, (Cambridge University Press, Cambridge, U.K., 1993), 2nd edition.

[136] Wilson, J.R., "A numerical study of gravitational stellar collapse", *Astrophys. J.*, **163**, 209–219, (1971).

[137] Wilson, J.R., "Numerical study of fluid flow in a Kerr space", *Astrophys. J.*, **173**, 431–438, (1972).

[138] Wilson, J.R., “Coherent neutrino scattering and stellar collapse”, *Phys. Rev. Lett.*, **32**, 849–852, (1974).

[139] Wilson, J.R., “A numerical method for relativistic hydrodynamics”, in Smarr, L.L., ed., *Sources of gravitational radiation*, 423–445, (Cambridge University Press, Cambridge, U.K., 1979).

[140] Wilson, J.R., “Supernovae and post-collapse behavior”, in Centrella, J.M., LeBlanc, J.M., and Bowers, R.L., eds., *Numerical Astrophysics*, 422–434, (Jones and Bartlett Publishers, Boston, U.S.A., 1985).

[141] Wilson, J.R., Mathews, G.J., and Marronetti, P., “Relativistic numerical model for close neutron-star binaries”, *Phys. Rev. D*, **54**, 1317–1331, (1996).

[142] Winicour, J., “Characteristic evolution and matching”, *Living Reviews in Relativity*, **4**, (2001). URL: http://www.livingreviews.org/Articles/Volume4/2001-3winicour/.

[143] Woosley, S.E., and Weaver, T.A., “The physics of supernova explosions”, *Ann. Rev. Astron. Astrophys.*, **24**, 205–253, (1986).

[144] Yahil, A., and Lattimer, J.M., “Supernovae for pedestrians”, in Rees, M.J., and Stoneham, R.J., eds., *Proceedings of the Advanced Study Institute, Cambridge: Supernovae: A Survey of Current Research*, 53–70, (Reidel, Dordrecht, Netherlands, 1982).

[145] York Jr., J.W., “Kinematics and dynamics of general relativity”, in Smarr, L.L., ed., *Sources of gravitational radiation*, 83–126, (Cambridge University Press, Cambridge, U.K., 1979).

[146] Zwerger, T., *Der Gravitationskollaps rotierender Polytrope*, PhD thesis, (Technische Universität München, München, Germany, 1995).

[147] Zwerger, T., and Müller, E., “Dynamics and gravitational wave signature of axisymmetric rotational core collapse”, *Astron. Astrophys.*, **320**, 209–227, (1997).